NONLINEAR FINITE ELEMENT MODELLING AND ADAPTIVE SLIDING MODE CONTROL OF PIEZOELECTRIC TUBE ACTUATOR

CHUNG SUI HONG

M.Phil

THE HONG KONG POLYTECHNIC UNIVERSITY

2011

THE HONG KONG POLYTECHNIC UNIVERSITY

DEPARTMENT OF MECHANICAL ENGINEERING

NONLINEAR FINITE ELEMENT MODELLING AND ADAPTIVE SLIDING MODE CONTROL OF PIEZOELECTRIC TUBE ACTUATOR

CHUNG SUI HONG

A thesis submitted in partial fulfilment of the requirements for the degree of Master of Philosophy

August 2010

CERTIFICATE OF ORIGINALITY

I hereby declare that this thesis is my own work and that, to the best of my knowledge and belief, it reproduces no material previously published or written, nor material that has been accepted for the award of any other degree or diploma, except where due acknowledgement has been made in the text.

_____ (Signed)

CHUNG SUI HONG (Name of Student)

ABSTRACT

The piezoelectric tube actuator is a compact device, which realizes three dimensional nano-scale scanning on the sample in Atomic Force Microscope (AFM). However, nonlinearities, including creep and hysteresis, together with coupling effect significantly limit the accuracy of AFM. The main goal of this research is to design a controller to minimize the tracking error due to coupling effect, creep and hysteresis, and also increase the stability for the piezoelectric tube actuator with electrode dislocation.

An accurate model of piezoelectric tube actuator which can fully describe the dynamic properties and nonlinear phenomena is a pre-requisite for model-based controller design. The first objective is to develop a reduced order nonlinear finite element (FE) model for controller design and computer simulation. The key point for developing a nonlinear model is to implement Prandtl-Ishlinskii hysteresis operators and Kelvin-Voigt creep operators into constitutive equations. The order of the nonlinear FE model in state space form is reduced by the balanced model truncation via Schur method in order that the model is feasible for controller design and computer simulation.

The working operation of the piezoelectric tube actuator is simulated in such a way that the cantilever is desired to scan the sample surface in a raster pattern. The simulation results of the open loop nonlinear system reveal that coupling effect,

creep and hysteresis can lead to significant tracking errors. Simulations on the closed loop nonlinear system with electrode dislocation using the proportional-integral (PI) controller and the output feedback controller (OFC) show that creep cannot be compensated and the tracking errors in Y direction diverge.

The second objective is to develop an adaptive sliding mode controller (ASMC) for the piezoelectric tube actuator. The piezoelectric tube actuator is characterized as a multiple-input-multiple-output (MIMO) nonlinear time-varying system. The design of controller is based on the reduced order nonlinear FE model. A continuous-time dynamic model assists the design process such that part of hysteresis can be extracted as known design information. The remaining part of hysteresis together with coupling effect and creep are considered as uncertainties. Walcott Zak observer is adopted to estimate the unmeasurable states. Lyapunov criterion is stated to guarantee the theoretical stability of the closed loop system. Adaptive scheme is used to search for the unknown controller gains.

The simulation of the piezoelectric tube actuator using the ASMC is performed. It shows that the ASMC can reduce more tracking error due to adverse effects and is relatively more stable than the PI controller and the OFC. The performance of the ASMC with the same settings is further investigated in piezoelectric tube actuator with different creep properties and hysteresis properties in addition to electrode dislocation. The results are evident that the proposed ASMC can tolerate certain changes of nonlinearity properties. The ASMC is the best candidate for AFM among the controllers investigated in this research.

PUBLICATIONS ARISING FROM THE PRESENT WORK

Chung S H and Fung E H K 2009 Modeling Piezoelectric Tube Scanner with Hysteresis and Creep by Finite Element Method *Proceedings of 2009 ASME International Mechanical Engineering Congress and Exposition* **10** 377-84

Chung S H and Fung E H K 2010 A Nonlinear Finite Element Model of a Piezoelectric Tube Actuator with Hysteresis and Creep *Smart Materials and Structures* **19** Article number 045028

Chung S H and Fung E H K 2010 Adaptive Sliding Mode Control of Piezoelectric Tube Actuator with Hysteresis, Creep and Coupling Effect *Proceedings of 2010 ASME International Mechanical Engineering Congress and Exposition* Paper No. IMECE2010-37637

ACKNOWLEDGMENTS

I would like to express special thanks to my supervisor, Dr. Eric H. K. Fung, for his support, guidance, encouragement throughout my study period. He was always available when I needed help and I do not have enough words to express my gratitude for that.

I wish to acknowledge the Research Committee of The Hong Kong Polytechnic University for funding in the form of research studentship.

TABLE OF CONTENTS

Certificate of Originality iii
Abstract iv
Publications Arising from the Present Work vi
Acknowledgments vii
Table of Contents viii
List of Figures xi
List of Tables xvii
Nomenclature xix

Chapter 1. Introduction 1
1.1 Background 1
1.2 Motivation for Research 6
1.3 Research Objective 10
1.4 Thesis Organization 13

Chapter 2. Literature Review 14
2.1 Introduction 14
2.2 Mathematical Modelling 14
2.3 Controller Design 19

Chapter 3. Dynamic Model Development of Piezoelectric Tube Actuator 24
3.1 Introduction 24
3.2 Assumptions and Conditions 25
3.3 Finite Element Formulation 26
3.3.1 Finite Element Discretization 28
3.3.2 Kelvin-Voigt Creep Operator 33
3.3.3 Prandtl-Ishlinskii Hysteresis Operator 35
3.3.4 Constitutive Equations 37
3.3.5 Energy Approach 39
3.3.6 Hamilton's Principle 42
3.3.7 State Space Equation 45

3.3.8 Reduction Method 47
3.4 Program Development 49
3.5 Parameter Identification and Validation 50
3.5.1 Rayleigh Constants 51
3.5.2 Parameters of Kelvin-Voigt Creep Operator 52
3.5.3 Parameters of Prandtl-Ishlinskii Hysteresis Operators 54
3.5.4 Full Model Validation 56
3.6 Model Reduction 57
3.6.1 Procedures 57
3.6.2 Reduced Order Model Validation 58
3.7 Summary 61

Chapter 4. Performance of Typical Controllers 63
4.1 Introduction 63
4.2 Simulation Conditions 64
4.3 Simulation Results of Open Loop System 66
4.3.1 Effect of Creep and Hysteresis 66
4.3.2 Coupling Effect 71
4.4 Simulation Results of Closed Loop System using Typical Controllers 73
4.4.1 Proportional-Integral Controller 73
4.4.2 Output Feedback Controller 84
4.5 Summary 104

Chapter 5. Development and Performance of Adaptive Sliding Mode Controller 106
5.1 Introduction 106
5.2 Assumptions and Conditions 108
5.3 Controller Design 109
5.3.1 Hysteresis Model for Controller Design 109
5.3.2 Adaptive Sliding Mode Controller 111
5.3.3 Sliding Mode Observer 117
5.3.4 Lyapunov Criterion 121
5.4 Program Development 127
5.5 Simulation Results of Closed Loop System with Adaptive Sliding Mode Controller 128
5.6 Summary 145

Chapter 6. Performance of Controllers under Various Nonlinearity Properties 147
6.1 Introduction 147
6.2 Simulation Conditions 148
6.3 Simulation Results of Systems with Various Hysteresis Properties 149
6.4 Simulation Results of Systems with Various Creep Properties 156
6.5 Summary 163

Chapter 7. Discussions and Conclusions 165
7.1 Discussions 165
7.2 Conclusions 172
7.3 Contributions 174
7.4 Suggestions for Future Research 175

Appendix A: Derivation of $[A]^e$ and $[B]^e$ 178

Appendix B: Formulation of $[Q_E]^e$ 183

Appendix C: Balanced Model Truncation via Schur Method 187

Appendix D: Optimal Control for Reference Model 190

Appendix E: Derivation of Error Dynamics on Sliding Surface 194

Appendix F: Plottings of Estimated States 196

Appendix G: Block Connections in MATLAB/Simulink 198

Appendix H: Main Program for Formulation of Reduced Order Finite Element Model 201

References 207

LIST OF FIGURES

Figure 1-1	Scanning Module of AFM	4
Figure 1-2	Physical Object of Piezoelectric Tube Actuator	6
Figure 3-1	Schematic Diagram of Piezoelectric Tube Actuator	27
Figure 3-2	Discretized Piezoelectric Tube Actuator	29
Figure 3-3	Local Node Number of Element	29
Figure 3-4	Characteristic of Prandtl-Ishlinskii Hysteresis Operator	36
Figure 3-5	Step Response of Linear FE Model in Short Time	51
Figure 3-6	Block Diagram of Open Loop System	52
Figure 3-7	Step Response of Nonlinear FE Model in Extended Time	53
Figure 3-8	Response of Nonlinear FE Model with Periodic Input	55
Figure 3-9	Hankel Singular Values of Full Nonlinear FE Model	58
Figure 3-10a	Simulations of Reduced Order Nonlinear FE Models with Different Number of Retained States (10 States – 25 States)	59
Figure 3-10b	Simulations of Reduced Order Nonlinear FE Models with Different Number of Retained States (30 States – 40 States)	60
Figure 4-1	Desired X Displacement	64
Figure 4-2	Desired Y Displacement	65
Figure 4-3	Illustration of Covering Angles	65
Figure 4-4	X Input to Open Loop Nonlinear System	67
Figure 4-5	Y Input to Open Loop Nonlinear System	67
Figure 4-6	X Displacements of Open Loop Nonlinear System	68
Figure 4-7	Y Displacements of Open Loop Nonlinear System	68

Figure 4-8	X Errors of Open Loop Nonlinear System	69
Figure 4-9	Y Errors of Open Loop Nonlinear System	69
Figure 4-10	Block Diagram of Closed Loop System using PI Controller	74
Figure 4-11	X Inputs of Closed Loop Nonlinear System without Electrode Dislocation using PI Controller	75
Figure 4-12	Y Inputs of Closed Loop Nonlinear System without Electrode Dislocation using PI Controller	76
Figure 4-13	X Displacements of Closed Loop Nonlinear System without Electrode Dislocation using PI Controller	76
Figure 4-14	Y Displacements of Closed Loop Nonlinear System without Electrode Dislocation using PI Controller	77
Figure 4-15	X Errors of Closed Loop Nonlinear System without Electrode Dislocation using PI Controller	77
Figure 4-16	Y Errors of Closed Loop Nonlinear System without Electrode Dislocation using PI Controller	78
Figure 4-17	RMSEs of Closed Loop Nonlinear System without Electrode Dislocation using PI Controller	79
Figure 4-18	X Input of Closed Loop Nonlinear System with Electrode Dislocation using PI Controller	80
Figure 4-19	Y Input of Closed Loop Nonlinear System with Electrode Dislocation using PI Controller	81
Figure 4-20	X Displacement of Closed Loop Nonlinear System with Electrode Dislocation using PI Controller	81
Figure 4-21	Y Displacement of Closed Loop Nonlinear System with Electrode Dislocation using PI Controller	82
Figure 4-22	X Error of Closed Loop Nonlinear System with Electrode Dislocation using PI Controller	82
Figure 4-23	Y Error of Closed Loop Nonlinear System with Electrode Dislocation using PI Controller	83
Figure 4-24	Block Diagram of Closed Loop System using OFC	85
Figure 4-25a	X Inputs of Closed Loop Nonlinear System without Electrode Dislocation using OFC (Set A – Set C)	87

Figure 4-25b X Inputs of Closed Loop Nonlinear System without Electrode Dislocation using OFC (Set D – Set F) 87

Figure 4-25c X Inputs of Closed Loop Nonlinear System without Electrode Dislocation using OFC (Set G – Set J) 88

Figure 4-26a Y Inputs of Closed Loop Nonlinear System without Electrode Dislocation using OFC (Set A – Set C) 88

Figure 4-26b Y Inputs of Closed Loop Nonlinear System without Electrode Dislocation using OFC (Set D – Set F) 89

Figure 4-26c Y Inputs of Closed Loop Nonlinear System without Electrode Dislocation using OFC (Set G – Set J) 89

Figure 4-27a X Displacements of Closed Loop Nonlinear System without Electrode Dislocation using OFC (Set A – Set C) 90

Figure 4-27b X Displacements of Closed Loop Nonlinear System without Electrode Dislocation using OFC (Set D – Set F) 90

Figure 4-27c X Displacements of Closed Loop Nonlinear System without Electrode Dislocation using OFC (Set G – Set J) 91

Figure 4-28a Y Displacements of Closed Loop Nonlinear System without Electrode Dislocation using OFC (Set A – Set C) 91

Figure 4-28b Y Displacements of Closed Loop Nonlinear System without Electrode Dislocation using OFC (Set D – Set F) 92

Figure 4-28c Y Displacements of Closed Loop Nonlinear System without Electrode Dislocation using OFC (Set G – Set J) 92

Figure 4-29a X Errors of Closed Loop Nonlinear System without Electrode Dislocation using OFC (Set A – Set C) 93

Figure 4-29b X Errors of Closed Loop Nonlinear System without Electrode Dislocation using OFC (Set D – Set F) 93

Figure 4-29c X Errors of Closed Loop Nonlinear System without Electrode Dislocation using OFC (Set G – Set J) 94

Figure 4-30a Y Errors of Closed Loop Nonlinear System without Electrode Dislocation using OFC (Set A – Set C) 94

Figure 4-30b Y Errors of Closed Loop Nonlinear System without Electrode Dislocation using OFC (Set D – Set F) 95

Figure 4-30c Y Errors of Closed Loop Nonlinear System without Electrode Dislocation using OFC (Set G – Set J) 95

Figure 4-31	X Errors of Closed Loop Nonlinear System without Electrode Dislocation using OFC (Set A – Set J)	98
Figure 4-32	X Input of Closed Loop Nonlinear System with Electrode Dislocation using OFC	99
Figure 4-33	Y Input of Closed Loop Nonlinear System with Electrode Dislocation using OFC	99
Figure 4-34	X Displacement of Closed Loop Nonlinear System with Electrode Dislocation using OFC	100
Figure 4-35	Y Displacement of Closed Loop Nonlinear System with Electrode Dislocation using OFC	100
Figure 4-36	X Error of Closed Loop Nonlinear System with Electrode Dislocation using OFC	101
Figure 4-37	Y Error of Closed Loop Nonlinear System with Electrode Dislocation using OFC	101
Figure 5-1	Block Diagram of Closed Loop System using ASMC	127
Figure 5-2	Desired and Reference X Displacements	133
Figure 5-3	Desired and Reference Y Displacements	133
Figure 5-4	X Input of Closed Loop Nonlinear System with Electrode Dislocation using ASMC	137
Figure 5-5	Y Input of Closed Loop Nonlinear System with Electrode Dislocation using ASMC	138
Figure 5-6	Estimated Sliding Surfaces of ASMC	138
Figure 5-7a	(1,1) Element of Estimates of Control Gains of Equivalent Control $\left[\hat{K}_1\right]$	139
Figure 5-7b	(1,1) Element of Estimates of Control Gains of Equivalent Control $\left[\hat{K}_2\right]$	139
Figure 5-7c	(1,1) Element of Estimates of Control Gains of Equivalent Control $\left[\hat{K}_3\right]$	140
Figure 5-8	X Displacement of Closed Loop Nonlinear System with Electrode Dislocation using ASMC	140

Figure 5-9	Y Displacement of Closed Loop Nonlinear System with Electrode Dislocation using ASMC	141
Figure 5-10	X Error of Open Loop and Closed Loop Nonlinear System with Electrode Dislocation	141
Figure 5-11	Y Error of Open Loop and Closed Loop Nonlinear System with Electrode Dislocation	142
Figure 6-1	X Input of Closed Loop Nonlinear System with Electrode Dislocation (Hysteresis Slope decreased by 8%)	150
Figure 6-2	Y Input of Closed Loop Nonlinear System with Electrode Dislocation (Hysteresis Slope decreased by 8%)	150
Figure 6-3	X Error of Closed Loop Nonlinear System with Electrode Dislocation (Hysteresis Slope decreased by 8%)	151
Figure 6-4	Y Error of Closed Loop Nonlinear System with Electrode Dislocation (Hysteresis Slope decreased by 8%)	151
Figure 6-5	X Input of Closed Loop Nonlinear System with Electrode Dislocation (Hysteresis Slope decreased by 9% and Hysteresis Backlash-distance increased by 10%)	152
Figure 6-6	Y Input of Closed Loop Nonlinear System with Electrode Dislocation (Hysteresis Slope decreased by 9% and Hysteresis Backlash-distance increased by 10%)	153
Figure 6-7	X Error of Closed Loop Nonlinear System with Electrode Dislocation (Hysteresis Slope decreased by 9% and Hysteresis Backlash-distance increased by 10%)	153
Figure 6-8	Y Error of Closed Loop Nonlinear System with Electrode Dislocation (Hysteresis Slope decreased by 9% and Hysteresis Backlash-distance increased by 10%)	154
Figure 6-9	X Input of Closed Loop Nonlinear System with Electrode Dislocation (Creep Parameters increased by 10%)	157
Figure 6-10	Y Input of Closed Loop Nonlinear System with Electrode Dislocation (Creep Parameters increased by 10%)	157
Figure 6-11	X Error of Closed Loop Nonlinear System with Electrode Dislocation (Creep Parameters increased by 10%)	158
Figure 6-12	Y Error of Closed Loop Nonlinear System with Electrode Dislocation (Creep Parameters increased by 10%)	158

Figure 6-13	X Input of Closed Loop Nonlinear System with Electrode Dislocation (Creep Parameters increased by 25%)	159
Figure 6-14	Y Input of Closed Loop Nonlinear System with Electrode Dislocation (Creep Parameters increased by 25%)	160
Figure 6-15	X Error of Closed Loop Nonlinear System with Electrode Dislocation (Creep Parameters increased by 25%)	160
Figure 6-16	Y Error of Closed Loop Nonlinear System with Electrode Dislocation (Creep Parameters increased by 25%)	161
Figure B-1	Illustration of r_{inner}, r_{outer}, r_v and Θ	184
Figure F-1	Estimated States (State 1 – 5)	196
Figure F-2	Estimated States (State 6 – 10)	196
Figure F-3	Estimated States (State 11 – 15)	197
Figure F-4	Estimated States (State 16 – 20)	197
Figure G-1	Block Connection of Plant Model in MATLAB/Simulink	198
Figure G-2	Block Connection of Closed Loop System using ASMC in MATLAB/Simulink	199
Figure G-3	Block Connection of Walcott Zak Observer in MATLAB/Simulink	200

LIST OF TABLES

Table 3-1	Material Properties of Piezoelectric Material PZT-4 (Sridhar *et al.*, 1999)	27
Table 3-2	Parameters of Kelvin-Voigt Creep Operators	53
Table 3-3	Parameters of Prandtl-Ishlinskii Hysteresis Operators	55
Table 3-4	RMSE of Reduced Order Nonlinear FE Models with Different Number of Retained States	59
Table 4-1	RMSE of Open Loop Nonlinear System	67
Table 4-2	Settings of PI Controller and Corresponding RMSEs of Closed Loop Nonlinear System without Electrode Dislocation	75
Table 4-3	RMSEs of Closed Loop Nonlinear System with Electrode Dislocation	80
Table 4-4	Settings of OFC and Corresponding RMSEs of Closed Loop Nonlinear System without Electrode Dislocation	86
Table 5-1	Model Parameters for Controller Design	130
Table 5-2	Control Parameters and RMSEs for Reference Model	132
Table 5-3	Settings for ASMC and Walcott Zak Observer	135
Table 5-4	Initial Estimates of Control Gains	136
Table 5-5	RMSEs of Open Loop Nonlinear System and Closed Loop Nonlinear System with Electrode Dislocation	137
Table 6-1	RMSEs of Open Loop Nonlinear System and Closed Loop Nonlinear System with Electrode Dislocation (Hysteresis Slope decreased by 8%)	149
Table 6-2	RMSEs of Open Loop Nonlinear System and Closed Loop Nonlinear System with Electrode Dislocation (Hysteresis Slope decreased by 9% and Hysteresis Backlash-distance increased by 10%)	152

Table 6-3 RMSEs of Open Loop Nonlinear System and Closed Loop Nonlinear System with Electrode Dislocation (Creep Parameters increased by 10%) 156

Table 6-4 RMSEs of Open Loop Nonlinear System and Closed Loop Nonlinear System with Electrode Dislocation (Creep Parameters increased by 25%) 159

NOMENCLATURE

$[0]$	zero matrix in appropriate size
$[\breve{A}_{1,2,3,4,5,6}]^e$	components of $[A]^e$
$[A]^e$	connection matrix of elemental displacement vector and elemental strain vector
$[A_m]$	reference system matrix
$[A_s]$	full order system matrix
$[A]$	reduced order system matrix
A_E	total area of an electrode
A_e	area of electrode attached surface of an element
a_f	proportional constant of f -th Kelvin-Voigt creep operator
$[\breve{B}_{1,2,3}]^e$	components of $[B]^e$
$[B]^e$	connection matrix of elemental electric potential vector and elemental electric field vector
$[\overline{B}_1]$	modified input matrix for controller design
$[B_g]$	gravitational force distribution matrix
$[B_m]$	reference input matrix
$[B_n]$	reduced order input matrix with nonlinear distribution
$[B_s]$	full order input matrix
$[B_1]$	true modified input matrix
$[B]$	reduced order input matrix
$[\Delta B_1]$	perturbation for modified input matrix
b_j	proportional constant of j -th Prandtl-Ishinskii hysteresis operator
$[C]^{e,g}$	elemental / global damping matrices
$[C_s]$	full order output matrix
$[C_1],[C_2],[C_3]$	adaptive gains for $[K_1]$, $[K_2]$ and $[K_3]$ respectively
$[C]$	reduced order output matrix
$[c_E]^e$	elastic modulus
$[D]^e$	electric displacement vector
$[D_s]$	full order feedforward matrix
$[D_1]$	bounded time varying nonlinear uncertainty
$[D_{1m}]$	matched bounded time varying nonlinear uncertainty
$[D_2]$	overall uncertainty

$[D_{2m}]$	matched overall uncertainty
$[D]$	reduced order feedforward matrix
$D_{r,\theta,z}$	electric displacements in r,θ,z directions
d_h	bounded time-varying uncertain part of continuous-time dynamic model
d_{hVX}	bounded time varying nonlinear uncertainty of continuous-time dynamic model due to voltage at X-pair electrode
d_{31}	piezoelectric coefficient of r-direction to z-direction relation
$[E]^e$	elemental electric field vector
$[E_G]$	error between full order transfer function and reduced order transfer function
$E_{r,\theta,z}$	electric fields in r,θ,z directions
$[e]^e$	piezoelectric coefficients
$[\hat{e}_s]$	estimated state error vector
$[e_s]$	state error vector
$[e_y]$	output error vector
$e_{X,Y}$	displacement errors in x, y directions
e_{n_e}	error at n_e-th time step
$[\overline{F}]^g$	part of force vector unrelated to gravitational force
$[F]^{e,g}$	elemental / global force vectors
$[F_o]$	observer sliding surface design matrix
$[f]^e$	gravitational force per unit volume
f_g	gravitational force
fo	order of full model
$[\tilde{G}_{transfer}]$	reduced order transfer function
$[G_{transfer}]$	full order transfer function
$[G]$	nonlinear distribution matrix
H	output of continuous-time dynamic model
h_j	output of Prandtl-Ishinskii hysteresis operator
h	height of piezoelectric tube actuator
$[I_q]^e$	current vector
$[I]$	identity matrix in appropriate size
$I_{X,Y}$	Integral Gains of PI Controller
$[J]$	Jacobian matrix
J_c	performance index

$\left[K_{qq,q\Phi,\Phi\Phi}\right]^{e,g}$	elemental / global stiffness matrices, electro-mechanical coupling matrices and capacitance matrices
$\left[\overline{K}_g\right]$	constant term due to gravity for controller design
$\left[\hat{K}_1\right],\left[\hat{K}_2\right],\left[\hat{K}_3\right]$	estimates of control gains of equivalent control $\left[K_1\right]$, $\left[K_2\right]$ and $\left[K_3\right]$ respectively
$\left[\tilde{K}_1\right],\left[\tilde{K}_2\right],\left[\tilde{K}_3\right]$	estimation errors of control gains of equivalent control $\left[K_1\right]$, $\left[K_2\right]$ and $\left[K_3\right]$ respectively
$\left[\hat{K}_1\right]_{initial}$	initial estimates of control gains of equivalent control $\left[K_1\right]$
$\left[\hat{K}_2\right]_{initial}$	initial estimates of control gains of equivalent control $\left[K_2\right]$
$\left[\hat{K}_3\right]_{initial}$	initial estimates of control gains of equivalent control $\left[K_3\right]$
$\left[K_g\right]$	constant term due to gravity
$\left[K_m\right]$	feedback gain for reference model
$\left[K_s\right]$	sliding mode matrix
$\left[K_1\right],\left[K_2\right],\left[K_3\right]$	true control gains of equivalent control
$\left[\Delta K_g\right]$	perturbation for constant term due to gravity
KE	kinetic energy
$\left[k_{fb}\right]$	feedback gain of OFC
$k_{XX,XY,YX,YY}$	components of feedback gains of OFC $\left[k_{fb}\right]$
k_{ff}	feedforward gain of open loop system
k_h	slope of linear part of continuous-time dynamic model
k_o	static gain
k	discrete time
Δk_{n_e}	time interval of n_e-th time step
$\left[L_o\right]$	observer gain
L	Lagrangian
$\left[M\right]^{e,g}$	elemental / global mass matrices
$\left[M_1\right],\left[M_2\right],\left[M_3\right]$	Lyapunov matrix for estimation errors of control gains of equivalent control $\left[\tilde{K}_1\right]$, $\left[\tilde{K}_2\right]$ and $\left[\tilde{K}_3\right]$ respectively
$\left[\overline{N}_{C1X,C1Y,C2X,C2Y}\right]^g$	constant parts of global nonlinear matrix due to creep with voltage at X-pair / Y-pair electrode
$\left[\overline{N}_{hX,hY}\right]^g$	constant parts of global nonlinear matrix due to hysteresis with voltage at X-pair / Y-pair electrode
$\left[N_{C1,C2}\right]^{e,g}$	elemental / global nonlinear matrices due to creep
$\left[N_h\right]^{e,g}$	elemental / global nonlinear matrices due to hysteresis
$\left[N\right]^e$	assembly of shape functions for interpolation of displacements

$[N_{ff}]$	feedforward gain of OFC
$[N_m]$	feedforward gain for reference model
N_F	total number of Kelvin-Voigt creep operators
N_J	total number of Prandtl-Ishlinskii operators
N_e	total number of time step
N_i	shape function
$[n]^e$	assembly of shape functions for interpolation of electric potentials
n	order of reduced order system
n_e	n_e -th time step
$[P]^e$	remnant polarization vector
$[P_m]$	Riccati matrix
$[P_o]$	Lyapunov matrix for observer error $[\varepsilon_o]$
$[P_r]$	reachability Grammian
PE	potential energy
$p_{VX,VY}$	remnant polarizations due to voltage at X-pair / Y-pair electrode
$p_{r,\theta,z}$	remnant polarizations in r,θ,z directions
p	remnant polarization
$[\overline{Q}_{EX,EY}]^g$	constant parts of global charge input vector with voltage at X-pair / Y-pair electrodes
$[Q_E]^{e,g}$	elemental / global charge input vectors
$[Q_m]$	design matrix for reference states
$[Q_o]$	observability Grammian
$[Q]$	design matrix for observer
$[q]^{e,g,n}$	elemental / global / nodal displacement vectors
q_E	total surface charge
$q_{ri,\theta i,zi}$	displacements of i -th node in r,θ,z directions
$q_{X,Y}$	horizontal motions of sample in X direction and Y direction
$[R]^e$	nodal r coordinates of an element
$[R_m]$	design matrix for input to reference model
$RMSE$	root mean square error
$[r]$	desired output vector
r^e	r coordinate of an arbitrary point
$r_{X,Y}$	desired X displacement and desired Y displacement
r,θ,z	position variables in global cylindrical coordinate system
r_i	nodal r coordinate of i -th node
$r_{inner,outer}$	inner radius and outer radius of piezoelectric tube actuator
r_v	radius

$[S_{L,BIG}]$, $[S_{R.BIG}]$	left and right transformations for reduced order model
$[\hat{s}]$	estimated sliding surface
$[s]$	sliding surface
$[T_c]$	nonsingular matrix
T_s	sampling period
t_{wall}	wall thickness of piezoelectric tube actuator
t	time
$[u]^e$	displacement vector of an arbitrary point
$[u_E]$	input vector
$[u_{eq}]$	equivalent control
$[u_m]$	input to the reference model
u_c	input of Kelvin-Voigt creep operator
u_h	input of hysteresis operator
u_m	input to reference model.
$u_{r,\theta,z}$	displacements of an arbitrary point in r,θ,z directions
$\overline{V_E}$	potential difference of outer electrode and inner electrode and divided by number of elements across both electrodes
V_E	potential difference of outer electrode and inner electrode
$V_{EX,EY}$	voltages applied to X-pair electrodes and Y-pair electrodes
V_L	Lyapunov equation
V	volume
W_e	electrical energy
$[\hat{w}_c]$	estimated unit vector nonlinear control
$[w_c]$	unit vector nonlinear control
$[w_o]$	unit vector dynamics of the sliding mode observer
w_f	weighting factor of f -th Kelvin-Voigt creep operator
$[\hat{x}]$	estimated state vector
$[x_m]$	reference state vector
$[x]$	state vector
x_f	state of f -th Kelvin-Voigt creep operator
$[y_m]$	reference output vector
$[y]$	output vector
α_h	switching rate of continuous-time dynamic model
α,β	Rayleigh constants
γ_c	chattering constant for controller
γ_o	chattering constant for observer
$\gamma_{\theta r,zr,z\theta}$	shear strains in $\theta-r,z-r,z-\theta$ directions

δ	design scalar
$[\varepsilon_c]^e$	creep strain vector
$[\varepsilon_l]^e$	strain vector due to mechanical stress and piezoelectric effect
$[\varepsilon_t]^e$	total strain vector
$[\varepsilon]^e$	elemental strain vector
$[\varepsilon_o]$	observer error
ε_c	creep strain
$\varepsilon_{cVX,cVY}$	creep strains due to voltage at X-pair / Y-pair electrode
ε_l	strain due to mechanical stress and piezoelectric effect
$\varepsilon_{r,\theta,z}$	strains in r,θ,z directions
ε_t	total strain
Θ	covering angle of electrode
κ_h	threshold of continuous-time dynamic model
κ_j	threshold of Prandtl-Ishlinskii operator
$[\Lambda_1]$	partial differentiations of assembly of shape functions for interpolation of displacements
$[\Lambda_2]$	partial differentiations of assembly of shape functions for interpolation of electric potentials
$\lambda_{\min}$	eigenvalue with minimum real part
λ	eigenvalue
μ	mass per unit volume
ξ_i,η_i,ζ_i	coordinates of i-th node in local coordinate system
ξ,η,ζ	position variables in local coordinate system
ρ_c	controller reaching gain
$\rho_{inner},\rho_{outer}$	surface charge density of inner and outer electrode respectively
ρ_o	observer reaching gain
$[\Sigma_n]$	truncated $[\Sigma_M]$
$[\Sigma_M]$	diagonal matrix with its diagonal containing all σ_{eig}
$[\sigma]^e$	stress vector
σ_{eig}	square root of eigenvalues
$\sigma_{r,\theta,z}$	tensile stresses in r,θ,z directions
$[\upsilon]^e$	electric flux linkage
υ_h	input of hysteresis operator for integration
τ	time variable for integration
$[\Phi]^{e,g}$	elemental / global electric potential vectors.
Φ^n	nodal electric potential
Φ_i	electric potential of i-th node

$[\varphi]^e$	dielectric coefficients
ϕ^e	electric potential of an arbitrary point
$\Psi_{A,D}$	orthogonal real transformations which order Schur forms in ascending / descending order
$\Psi_{L,BIG,L,SMALL}$	left orthogonal transformations with big / small eigenvalues of $P_r Q_o$
$\Psi_{R,BIG,R,SMALL}$	right orthogonal transformations with big / small eigenvalues of $P_r Q_o$
$[\Omega_M], [U_M]$	singular value decompositions $[\Psi_{L,BIG}]^T [\Psi_{R,BIG}]$

Superscripts

T	transpose
e	elemental vector or matrix
g	global vector or matrix
n	nodal vector

Subscripts

f	f -th Kelvin-Voigt creep operator
i	i -th node
j	j -th Prandtl-Ishlinskii hysteresis operator
k	k -th eigenvalue of $P_r Q_o$
n_e	n_e -th time step
r, θ, z	components in r, θ, z directions

CHAPTER 1

INTRODUCTION

1.1 BACKGROUND

Piezoelectric tube actuator, which is a compact smart device, is well-known for realizing nano-scale positioning and fabrication for Atomic Force Microscope (AFM). Afterward imaging technology of AFM is extended to the application of data storage. The storage instrument, using this technology, called Micro-electro-mechanical-system (MEMS)-based scanning-probe data-storage device has advantages over its peers with ultra-high density (1 Tb/in^2) and low access time (Pantazi *et al.,* 2007). Getting back to AFM, it was developed by Binnig *et al.* (1986) based on scanning tunneling microscope, which has extremely high resolution (between several 100 μm to 10 pm). AFM can provide information about three dimensional configurations as well as crystal structures of macromolecules. The packing order of molecular adsorption on a surface of metals or minerals can be investigated, thus, the types of forces can be determined. Moreover, AFM is so versatile that it possesses different features when equipped with specific cantilevers (probes) such as detecting light (fluorescence, infrared, ultraviolet and visible light), current, magnetic field and pressure. With appreciation of the high resolution and the attractive functions, AFM is widely adopted in the fields of biology (biomolecules, biosensors, cell tracking, DNA

analysis and enzyme activities), chemistry (chromatography), industry (contact lens manufacturing, lithography, lubrication, microelectronics, microfabrication techniques, nanoetching, nanomachining and production of semiconductor integrated circuits), material science (ceramic or metal surface investigation, mineral surface morphology and single-molecule studies) and medicine (peptides, vaccines and virus) (Birdi, 2003).

AFM is eminent in various aspects in microscopy. The conventional optical microscope obtains the image of the sample surface by receiving the reflected light through lenses. The basic problem is the interaction of the probe, a photon, with the sample. The resolution is restricted by diffraction limit, which is not better than 250 nm. Although adjustment of the shape or index of refraction of the lens can achieve improvement, it can cause large changes in the instrument response. Unlike the optical microscope, AFM uses the interaction force to image a sample surface. Therefore, diffraction limit is not the restriction for AFM. It explains that AFM has higher resolution than optical microscope. Scanning Electron Microscope (SEM), which is an advanced instrument for metrology, has insignificant diffraction effect. Its resolution is comparable to AFM. However, the incident beam may be uncontrollably deflected if the sample potential changes through charging. Also, sample must be put in vacuum. Regarding to the cost, SEM is more expensive than AFM by double. Moreover, for both the optical microscope and SEM, high resolution cannot be achieved in all three dimensions simultaneously. The special imaging method allows AFM overcoming those drawbacks of optical microscope and SEM.

The schematic diagram of the scanning module of AFM in sample-on-actuator design is shown in Fig. 1-1 (Magonov and Whangbo, 1996). The characteristic of this design is that the sample is placed on the top of the piezoelectric tube actuator, and the cantilever is fixed. Alternatively, AFM can be in the cantilever-on-actuator design for which the cantilever is attached to the piezoelectric tube actuator, and the sample is fixed (El Rifai and Youcef-Toumi, 2003). The discussion throughout the thesis is based on the former design. In general, an AFM has two main operating modes, namely, contact (El Rifai and Youcef-Toumi, 1999) and tapping (Sebastian *et al.*, 2007). For contact mode, a cantilever scans the sample surface by exerting a vertical force on the sample surface by cantilever sharp tip, keeping the force constant at a very close separation and dragging across the sample surface in raster pattern. Usually, the interaction forces between the cantilever tip and the sample surface (repulsive force and Van der Waals' forces described by the Lennard-Jones type behavior (Agarwal and Salapaka, 2008)) is kept between 0.5 and 0.1 nN for the cantilever with the force constant 0.06 N/m. The interaction force causes the cantilever to deflect. The resulting deflection is detected by emitting a laser beam to the back of the cantilever and then reflected to the optical sensor. For tracking improvement, capacitive sensors can be implemented to independently measure the actuator tip position or the sample position for feedback. Alternatively, instead of using a pair of electrodes for actuation (double-actuation), it is a possible way to sacrifice one of the actuating electrodes to act as a sensor (single-actuation) (Moheimani and Yong, 2008). Sample position measurement can be realized by detecting the voltage existing on the sensing electrode. Single-actuation can overcome the problem of capacitive sensors which is significantly influenced by noise at high scanning frequency. But this method

reduces the operating range by half and causes the piezoelectric tube not driving symmetrically. In this thesis, double-actuation is considered. For tapping mode, the cantilever is kept vibrating at the resonant frequency. The separation between the cantilever tip and the sample surface is kept constant by measuring the vibration of the cantilever with the fact that the vibration is damped as the sample comes closer to the cantilever tip. The necessary information can be obtained by determining amplitude, phase or frequency of the response of the cantilever. Tapping mode enables AFM scanning a matter in liquid phase such as actin, cells, DNA and lysozyme (Colton *et al.*, 1998), which is not possibly performed in contact mode. In contrary, the advantage of contact mode over the tapping mode is that the force constant of the cantilever used in contact mode is much smaller than that used in tapping mode, hence, the cantilever tip drags across the sample surface with less damage.

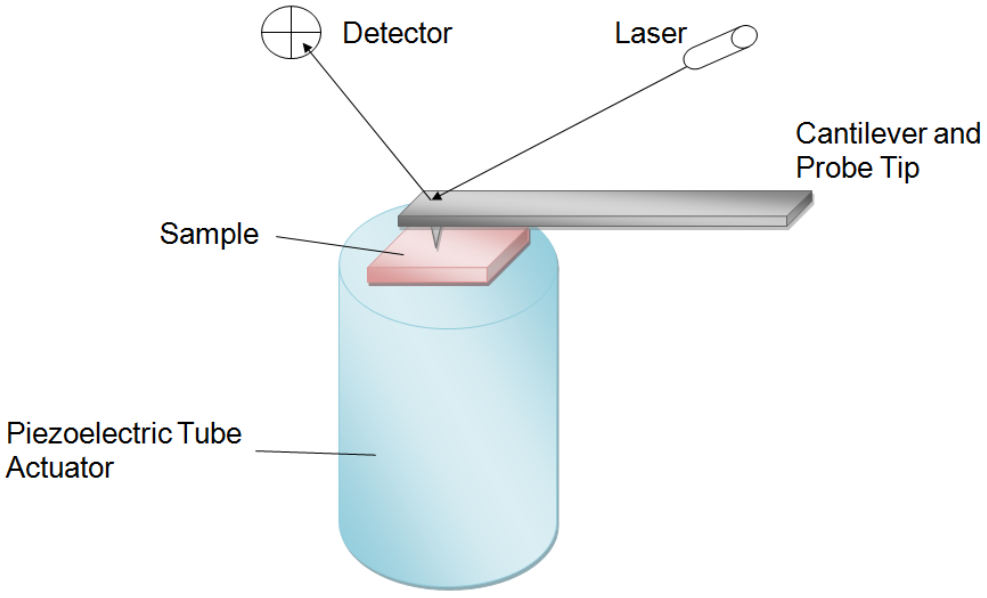

Figure 1-1. Scanning Module of AFM

AFM being an outstanding metrology tool is attributed to beneficial characteristics of the piezoelectric tube actuator including fast response, good mechanical durability, high resolution, large output force and low power consumption (Haertling, 1999; and Niezrechi *et al.*, 2001). Piezoelectric tube actuator was invented by Binnig and Smith (1986). The merit of this actuator design is that the piezoelectric tube actuator is fabricated by just a single material for application of three dimensional scanning; therefore, complicated structures or components are avoided. The physical object of piezoelectric tube actuator is shown in Fig. 1-2. It is made of outward polarized piezoelectric material in cylindrical shape attached with copper made quartered outer electrodes and a copper made inner electrode. When voltage is applied to the electrodes, a potential difference exists between the outer electrode and the inner electrode. Due to converse piezoelectric effect, the piezoelectric tube actuator deforms and bends accordingly. Therefore, the lateral and longitudinal movements of the sample can be controlled by input voltage on appropriate electrodes in order that the cantilever can scan across the sample surface. Since feedback control of longitudinal movement involves interaction of piezoelectric tube actuator and cantilever, it is preferred to separate controller design of longitudinal movement from lateral movements to reduce the complexity of controller. In this thesis, the controller design for lateral movements is considered. A number of previous researchers have contributed to the control of longitudinal movement with different types of controller such as robust controller (Hsu and Fu, 1999) and adaptive regulator (Li *et al.*, 2009). The control of longitudinal movement is out of the scope of this research.

Figure 1-2. Physical Object of Piezoelectric Tube Actuator

1.2 MOTIVATION FOR RESEARCH

There are numerous factors for degrading accuracy of AFM regarding cantilever, piezoelectric tube actuator, sample and sensor. Frictional force between the cantilever tip and the sample surface not only causes cantilever tip to flex but also hinders the movement of tip of piezoelectric tube actuator especially in contact mode. Some nonideal characteristics such as cantilever tip-shape artifacts, cantilever tip contamination and sample damage exist due to careless handling and repeatedly use (Barrett and Quate, 1991a). Sensor noise which disturbs the measured signal is unavoidably present in any kind of sensor. Imperfectly constructed capacitive sensor on the tip of the actuator or bending of the piezoelectric tube actuator during scanning cause nonlinear behavior in

measurement because two plates of the capacitive sensor are not in parallel but forming a relative tilt (Griffith and Grigg, 1993). Directly proportion between the output voltage and the capacitor spacing is no longer valid. Moreover, the properties of the piezoelectric material change gradually with time after polarization in manufacturing process. In other words, the piezoelectric material exhibits aging. Most of the undesired effects mentioned before can be avoided by either good maintenance or advanced instrument. The nonlinearities of the piezoelectric material including creep and hysteresis also limit the accuracy of AFM significantly. The piezoelectric tube actuator scans in forward and backward directions giving different position outputs on the same scanning path. The maximum error that hysteresis can create is as large as 15% of the total displacement range (Mokaberi and Requicha, 2008). It is quite a large error for nanopositioning and nanomanipulation. Creep happens obviously in such a way that when a step input is applied to the piezoelectric tube actuator, the displacement increases with time even the step input is steady. The accuracy is reduced with increase in scanning time. Since most of AFM are operating at a moderately low speed, its adverse effect on the accuracy is noticeable (Moheimani, 2008; and Mokaberi and Requicha, 2008). Lastly, coupling effect, which is caused by abnormal size of electrodes, cross-coupling deformation, dislocated electrodes and eccentricity, cannot be overlooked (Maess *et al.*, 2008a; 2008b). Coupling effect happens in such a way that an input or a displacement of one axis reluctantly induces unnecessary motions in another axis. In this research, the coupling effect due to electrode dislocation is the interest. Machining imperfection in the manufacturing process is an inevitable cause of electrode dislocation. Electrode dislocation of piezoelectric tube actuator can be different from each other.

Therefore, coupling effect due to electrode dislocation can be considered as uncertainties of the system. It is an interesting and challenging topic of compensation of nonlinearities and coupling effect for piezoelectric tube actuator.

Approaches which tackle the problems of piezoelectric tube actuator in AFM can be classified into four categories including calibration of the actuator, linearization by charge input, postimaging software image correction and real time correction via control system (Tamer and Dahleh, 1994). Calibration is a compulsory and fundamental method carried out by manufacturer but it cannot solve the repeatability problems such as creep. Post-imaging software image correction achieves limited improvement of imaging (Barrett and Quate, 1991b). This approach allows fast imaging; however, it has the following drawbacks. First, large number of data is required to be collected and stored. Second, there is a delay between scanning and image display during the correcting software running. Therefore, it is not applicable to real time application such as manipulation since correction is performed after scanning. Charge input has been proven that it does not induce nonlinearities significantly (Fleming and Moheimani, 2005; 2006; Bhikkaji *et al.*, 2007; and Ashley *et al.*, 2008). This approach can work with controller jointly (Clayton *et al.*, 2008). However, the necessary instrument, charge amplifier which converts the input signal into the charge input, is costly. On the contrary, the benefits of implementation of feedback controller are real time compensation of creep, hysteresis, thermal drift and vibrations. It is also easy to perform implementation, maintenance and modification since most of control applications are based on computer (digital control).

There are a number of works done by previous researchers on control of piezoelectric devices (Croft *et al.*, 2001; Tien *et al.* 2005; Shakir *et al.*, 2007; Payam and Abdel-Rahman, 2008; and Berghuis *et al.*, 1993). Their works are reviewed in Chapter 2 in detail. Although the previously proposed controllers are good choices for tracking error minimization of the piezoelectric tube actuator, the current literature related to this area have the following gaps: (i) a mathematical model which demonstrates not only dynamic responses but also coupling effect, creep and hysteresis has not yet been developed for simulation and controller design purposes; (ii) tasks related to controller design only concerns one or two of the adverse effects including coupling effect, creep or hysteresis but not a combination of them. The controllers proposed by former researchers have not yet shown to compensate all the adverse effects simultaneously; (iii) comparison between the performance of the previously proposed controllers and the controller currently used in AFM has not yet been made.

In order to bridge the gaps, this thesis proposes a reduced order nonlinear finite element (FE) model and a robust controller. It is remarked that a nonlinear model or a nonlinear system means that a model or a system exhibits creep and hysteresis. FE method is chosen because its formulation process can be handled by computer automatically and systematically. By implementing creep and hysteresis models to the FE formulation, the proposed FE model can exhibit creep and hysteresis in simulation. Based on the proposed FE model, an adaptive sliding mode controller (ASMC) is designed. The sliding mode controller is a practical version of the variable structure control which was found to be insensitive to parameter perturbations and uncertainties (Utkin, 1977). It can force the tracking

error of the piezoelectric tube actuator with coupling effect, creep and hysteresis to converge to zero. Lyapunov equation is formulated to state the theoretical stability of the closed loop nonlinear system with electrode dislocation. The performance of the ASMC, including error minimization ability and stability improvement ability, is examined and compared with that of typical controllers including the proportional-integral (PI) controller and the output feedback controller (OFC). They are chosen as comparison candidates because PI controller is commercially used in piezoelectric tube actuator in AFM (Abramovitch *et al.*, 2007). OFC which contains coupling control gains can reduce the tracking error caused by coupling effect.

1.3 RESEARCH OBJECTIVE

The main objective of this research is to propose a controller for the piezoelectric tube actuator to minimize error due to coupling effect, creep and hysteresis, and enhance stability when tracking a scanning trajectory of AFM (a raster pattern). It is remarked that the studies are based on simulation results only. It is outside the scope of this research to conduct the experimental verification.

In order to achieve the objective mentioned above, the following major tasks have been accomplished and listed below:

(1) To establish a nonlinear FE model of piezoelectric tube actuator

An accurate model which is not only able to characterize the dynamic properties but also exhibit creep and hysteresis phenomena is indispensable for both simulation and controller design. The Kelvin-Voigt creep operator and the Prandtl-Ishlinskii hysteresis operator are implemented in the FE model formulation process to enable the FE model to exhibit nonlinearities. The order of the nonlinear FE model is reduced so that simulation and controller design are feasible. Parameters of the nonlinear operators are identified. The simulated responses of the full and reduced nonlinear FE models are compared with the experiment result obtained from other literature for validation.

(2) To develop an ASMC for the piezoelectric tube actuator

An ASMC is chosen because it has an advantage that it is insensitive to coupling effect, creep and hysteresis. The ASMC is developed in such a way that the reduced order nonlinear FE model is used for developing the observer and the controller, and a continuous-time dynamic model of backlash-like hysteresis is utilized in the controller design in order that the performance on the compensation of hysteresis can be improved. The sliding mode observer is designed for estimating the unmeasurable states. Lyapunov criterion is stated to guarantee the stability of the closed loop system theoretically.

(3) To investigate the performance of the ASMC

The controller commands the system to track a raster pattern. Raster pattern is a standard trajectory used in scanning operation of AFM. The output responses of the closed loop nonlinear system with electrode dislocation using the ASMC are obtained by simulations. By investigating the results, the performance including error minimization ability and stability improvement ability is assessed. The performance of closed loop nonlinear system with electrode dislocation using the ASMC is compared to that of the open loop nonlinear system with electrode dislocation, and the closed loop nonlinear system with electrode dislocation using the PI controller and the OFC. Open loop system means a system without implementation of controller.

(4) To evaluate the effects of different creep properties and different hysteresis properties on the controller performance

The reason for evaluation is to assess the ability of the controllers on enduring biases of the creep properties and the hysteresis properties. Because of bias measure of hysteresis properties, rate dependent hysteresis properties (Yu *et al.*, 2002), thermal dependent creep properties (Motamedi *et al.*, 2009), and changes of hysteresis properties and creep properties due to different treatments on the piezoelectric tube actuator, creep and hysteresis parameters can be different from those original values considered in controller design. Performance comparisons are made between the ASMC, the PI controller and the OFC.

1.4 THESIS ORGANIZATION

This thesis consists of seven chapters:

Chapter 1 contains background information, motivation for research and research objective.

Chapter 2 presents a comprehensive literature review.

Chapter 3 demonstrates the formulation of full and reduced order nonlinear FE models. The parameters identification and the validation are performed.

Chapter 4 shows the effects of coupling, creep and hysteresis on the open loop system. Then, the performance of typical controllers on the piezoelectric tube actuator with electrode dislocation is investigated.

Chapter 5 presents the formulation of the ASMC. The performance of the ASMC on the piezoelectric tube actuator with electrode dislocation is studied and compared to that of typical controllers.

Chapter 6 studies the controllers' ability of tolerating the biases of creep and hysteresis properties.

Chapter 7 discusses and concludes the work done in this thesis, and gives suggestions for the future work.

CHAPTER 2

LITERATURE REVIEW

2.1 INTRODUCTION

In recent years, the control problems of piezoelectric tube actuator have received much attention, and a number of controllers have been proposed. In this chapter, the related literature are reviewed in detail, which provide necessary information, ingenious theory and remarkable discussion for inspiration of the work in this thesis. According to the main objective of this research, the review is separated in two sections, namely, mathematical modelling and controller design.

2.2 MATHEMATICAL MODELLING

A mathematical model of a piezoelectric tube actuator which can simulate the response accurately is important for studying the effect of nonlinearities and the performance of the controllers. For model-based controller, a mathematical model is a pre-requisite in controller design process. Some researchers have developed model for piezoelectric devices by analytical formulation. Low and Guo (1995) formulated a nonlinear analytical model with hysteresis for piezoelectric bimorph

beam. The structure of the piezoelectric bimorph beam consists of a metal shim sandwiched in between two piezoelectric plates. A hysteresis model described by a differential equation was implemented in the analytical model as an external excitation. By the proposed model, the vertical displacement of piezoelectric bimorph beam can be calculated. Royston and Houston (1998) developed a nonlinear analytical model for 1-3 piezoelectric ceramic composite sandwiched by two plexiglass layers. 1-3 piezoelectric ceramic composite is a number of vertical piezoelectric rods embedded in the polymer. Maxwell resistive capacitor model was used for approximating the hysteresis occurring between electric field and electric displacement of 1-3 piezoelectric ceramic composite. The displacement of the plexiglass layer can be calculated by the dynamic equation of the plexiglass layer with the nonlinear deformation of 1-3 piezoelectric ceramic composite. Wu *et al.* (2006; 2007) proposed a model which provides three-dimensional solutions for the static analysis of multilayered piezoelectric tube actuator. The procedures of model formulation are nondimensionlization, asymptotic expansion and successive integration in sequence. It is remarked that this proposed model does not take the nonlinear behaviors in account. The benefit of analytical formulation is that accurate solution can be obtained. However, the weakness of this method is that it is not applicable to the system with complicated shape or structure. Also, difficulty of mathematical formulation is high. By the way, the literature in this paragraph give ideas of nonlinear model implementation and three-dimensional model formulation.

To overcome the problems of analytical formulation, the FE method, which is a type of the numerical formulation, is a good choice. FE method is better than

finite difference (FD) method because FE method can handle objects with complex geometry and has higher accuracy. Although model obtained by FE method provides approximate solution, the formulation is unrestricted by shape of object because discretization is performed at the initial stage. The formulation process which can be handled by computer is also an attractive advantage. Lim *et al.* (1997) developed a three-dimensional linear FE model of piezoelectric ceramic sensors embedded in a micro-cantilever for transient analysis. It is remarked that a linear model or a linear system means that a model or a system does not exhibit creep and hysteresis. Afterward, Lim *et al.* (1999) applied similar FE method to model a smart structure which is an aluminum plate with discrete piezoelectric sensors and actuators attached. A multi-input-multi-output (MIMO) linear quadratic controller, which is a type of optimal controller, was designed based on the FE model, and its performances on vibration and noise control of the system were studied in simulation. Hau and Fung (2004) proposed a reduced order FE model for a clamp-free beam with partial active constrained layer damping (ACLD). In ACLD, patches consisting of piezoelectric layer and viscoelastic material (VEM) layer were attached on the beam for active damping and passive damping respectively. The Golla-Hughes-McTavish (GHM) method was adopted to FE formulation to account for the frequency dependent characteristic of VEM. The effect of different ACLD treatment configuration on the frequency response was investigated. For piezoelectric tubes, Carr (1988) first constructed a linear model by FE method. The magnitudes of the three-dimensional motion were investigated with different tube materials and tube dimensions. Berg *et al.* (2004) proposed a linear FE model for piezoelectric thin-walled cylindrical shell with shell theory. In this theory, only dielectric displacements in the radial direction were considered. Admittance, axial

displacements and eigenmodes of the piezoelectric shell were investigated in simulation. The advantage of approximating a tube as a shell is that the complexity of FE formulation is reduced but the accuracy decreases. Santos *et al.* (2008) further extends the FE formulation with shell theory for piezoelectric tube in axisymmetric case. The development of this model is further simplified; however, analysis of bending and free vibrations is limited to axisymmetric excitation. Kumar *et al.* (2008) applied FE method with shell theory to the formulation of laminated composite (graphite epoxy) shell with piezoelectric patches including actuators and sensors attached. This model can simulate the responses of the laminated shell subjected to electrical, mechanical and thermal loadings. A negative velocity feedback control was applied and simulation showed that location of piezoelectric patches affected the performance of controller. In the review of this paragraph, the formulations of linear FE model of piezoelectric plate and tube are studied.

Nonlinear modelling is in fact an essential area of study because piezoelectric material exhibits nonlinear behaviors in reality. Concerning hysteresis, the physical models called thermodynamically consistent models (Kamlah and Bhle, 2001; and Landis, 2004) can describe the underlying physics of hysteresis but are still in development. Thermodynamically consistent models are based on a macroscopic view to describe microscopic phenomena. However, they suffer from computational inefficiency and cumbersome mathematics for controller design. In contrary, the mathematical models, which are usually formulated by dynamics of a combination of mechanical components, are conceptually simpler and more mathematically elegant. A classical Preisach model (Mayergoyz, 1991) is the most

popular one for modelling hysteresis because of its accuracy. Its applications, not limited to modelling, extend to feedforward control for piezoelectric actuator (Ge and Jouaneh, 1996; and Galinaitis and Rogers, 1998). Prandtl-Ishlinskii hysteresis operator is simpler than Preisach model and can easily extend to include creep model (Krejci and Kuhnen, 2001; and Mokaberi and Requicha, 2008). Concerning creep, there are no physical models but only mathematical models available in the current literature. One of creep models is expressed in logarithmic function (Jung and Gweon, 2000). Its expression is rather simple but its accuracy on modelling creep behavior of piezoelectric material receiving a signal other than step input has never been investigated, therefore, it is not guaranteed. A creep operator which is modelled by superposition of parallel connections of a damper and a spring called Kelvin-Voigt operators (expressed in the form of first order differential equation) was validated together with superposition of Prandtl-Ishlinskii hysteresis operators when the piezoelectric actuator is receiving an irregular input signal (Krejci and Kuhnen, 2001). The two nonlinear operators, i.e. Prandtl-Ishlinskii hysteresis operator and Kelvin-Voigt creep operator, are adopted in nonlinear modelling for simulation purpose in this research.

It is a good idea to fuse the nonlinear operators into FE formulation in order to take advantages of both of them. However, seldom literature are related to formulate nonlinear FE model in this way. Kusculuoglu and Royston (2008) developed a nonlinear FE model for piezoeletric laminated plates using Mindlin plate theory. The piezoeletric laminated plates arranged as a piezoelectric patch were bonded to the aluminum plate. Ishlinskii hysteresis operator was implemented into FE formulation in such a way that it models hysteresis behavior existing

between electric field and electric displacement. However, the state space form of this nonlinear FE model has a nonlinear term embedded in the system matrix and this nonlinear term is hard to be separated out. This makes the existing numerical solvers difficult to compute the solution. Also, it is not available for controller design.

In this section, the advantages and the disadvantages of different mathematical models are reviewed. It is pointed out that a mathematical model which can demonstrate coupling effect, creep and hysteresis has not been developed. It is also found that implementing the mathematical nonlinear operators into FE formulation is a relatively convenient and simple way to formulate an accurate nonlinear model for piezoelectric tube actuator for controller design and simulation purposes. By adopting a continuous-time dynamic model of backlash-like hysteresis (Su *et al.*, 2000), the nonlinear FE model becomes available for designing an ASMC design with enhanced ability in compensation of hysteresis, which will be discussed in Chapter 5.

2.3 CONTROLLER DESIGN

As discussed in Chapter 1, feedback control has numerous advantages so it is chosen for error minimization and stability improvement of piezoelectric tube actuator. In this section, various kinds of controllers used for piezoelectric devices in current literatures are reviewed to study their advantages and disadvantages. Many researchers have worked on design of inverse feedforward controllers. The

inverse feedforward controller constructed by inversing creep or hysteresis model releases an input signal to cancel the effect of the corresponding nonlinear behavior. Croft *et al.* (2001) inversed the creep dynamics, the Preisach hysteresis model and the vibration dynamics to compensate corresponding adverse effects of piezoelectric tube actuator. The performance of the controller was tested in AFM for imaging. Janocha and Kuhnen (2000) used inverse of Kelvin-Voigt creep operator and inverse of Prandtl-Ishlinskii hysteresis operator while Krejci and Kuhnen (2001) used Kelvin-Voigt creep operator and inverse of Prandtl-Ishlinskii hysteresis operator to create the inverse feedforward controller. The performances of the proposed controllers were examined in piezoelectric stage and the tracking error is reduced by approximately one order of magnitude. Mokaberi and Requicha (2008) assessed the performance of the controller proposed by Krejci and Kuhnen (2001) on AFM for manipulation. Among the literature, their differences are on the types of creep or hysteresis model used for inverse feedforward controller design.

The inverse feedforward controller has the following advantages. First, additional sensor for the output is not necessary for compensation purposes of the pure feedforward controller so the complexity and the cost of the control setup are reduced (Krejci and Kuhnen, 2001). Second, this controller is available for combining with the feedback controller to provide further improvement for the performance of the closed loop system. However, the creep operator-based feedforward controller has the disadvantage that the sensitivity to unconsidered external disturbances is introduced (Krejci and Kuhnen, 2001). For instance, the creep is thermal dependent. The step response exhibits creep 15% more when the temperature increases from 25 ˚C to 49 ˚C (Motamedi *et al*., 2009). The thermal

dependent property of creep is not characterized in the Kelvin-Voigt creep operator. The error of the system using feedforward controller may even larger than that without using it when the temperature change is large.

Iterative control is a digital control method, which generates a control signal based on the information of the control signal and the error at the last time step. Its benefits are that the control law is rather simple and no intensive calculations are needed for computer. The stability of iterative control is higher than feedforward control. Tien *et al.* (2005) proposed iterative control for compensation of coupling effect between lateral axis and longitudinal axis. Wu and Zou (2007) based on the work of Tien *et al.* (2005) combines a Preisach hysteresis model and vibration dynamics with iterative control to enable the controller to compensate the corresponding effects. Ashley *et al.* (2008) proposed inversed Preisach hysteresis model combined with iterative control to allow compensation of hysteresis. All of the works, Tien *et al.* (2005), Wu and Zou (2007), and Ashley *et al.* (2008), demonstrated the performance of the proposed controllers on compensation of coupling effect, hysteresis or vibration by performing experiment on AFM. The disadvantage of the iterative control is that the iteration can be influenced by disturbances and uncertainties.

Other controllers such as optimal PI controller (Shakir *et al.*, 2007) and proportional derivative fuzzy controller (Payam and Abdel-Rahman, 2008) were developed. The former one was proposed for the experimental study of the piezoelectric positioning system while the latter one was proposed for the simulation study of the AFM. The advantage of the optimal PI controller is ease of

selection of controller parameters while the advantage of the proportional derivative fuzzy controller is that it is not necessary to understand the model of the system clearly. Maess *et al.* (2008c) developed a MIMO feedforward feedback controller for a piezoelectric tube actuator. The feedforward controller was designed by FE model to compensate vibration and the feedback controller was used for compensation of coupling effect due to tube eccentricity. The simulation was carried out to track a raster pattern to assess the performance of the controller on AFM.

As discussed in Chapter 1, ASMC, which belongs to the class of robust control, is chosen for achieving the objective of this research, i.e. minimizing error due to coupling effect, creep and hysteresis, and enhancing stability for piezoelectric tube actuator, because it is insensitive to parameter perturbations and uncertainties. In the past two decades, the robust adaptive controller is popular in researches (Berghuis *et al.*, 1993; Chiu *et al.*, 2004; and Li *et al.*, 2007; 2008a; 2008b) for robot motion control to tackle disturbances and modelling errors. For application of piezoelectric devices, Sabanovic *et al* (2006), and Zhong and Yao (2008) proposed a MIMO and a single-input-single-output (SISO) adaptive robust controller respectively for piezoelectric stack actuator. The proposed controllers were shown to be effective in dealing with unknown model parameters and compensating hysteresis.

After reviewing the controllers proposed in previous research, the following deficiencies are identified. First, the researchers concerned only one or two of the adverse effects of piezoelectric tube actuator including coupling effect, creep and

hysteresis. However, the outputs of the overall system with the controllers proposed by previous researchers can be undesirable when all of the adverse effects exist simultaneously. Hence, it is necessary to develop a controller which demonstrates its effectiveness in compensating all the adverse effects. Second, the performances of the controllers proposed by previous researchers were seldom compared with typical controllers, especially the one used in current AFM, the PI controller. Through the comparison, the value of the proposed controller in this thesis applied to AFM can be clarified. The reviewed literature provide a full picture of control of piezoelectric tube actuator and give directions to carry out the present research.

CHAPTER 3

DYNAMIC MODEL DEVELOPMENT OF PIEZOELECTRIC TUBE ACTUATOR

3.1 INTRODUCTION

The formulation procedures of the nonlinear FE model of piezoelectric tube actuator are presented in this chapter. The FE method is chosen for modelling because the algorithm of FE discretization, dynamic equation formulation and global assembly can be executed by computer. First of all, the piezoelectric tube actuator is discretized into isoparametric elements in cylindrical coordinates. Next, Kelvin-Voigt creep operators and Prandtl-Ishlinskii hysteresis operators are introduced into the constitutive equations of the piezoelectric material. Then, the nonlinear FE model is formulated by energy approach and Hamilton's Principle. Finally, the balanced model truncation via Schur method is adopted to reduce the order of the FE model. Thus, simulation and controller design are feasible with the reduced order nonlinear FE model. The damping matrix, the parameters of the Kelvin-Voigt creep operators and the parameters of the Prandtl-Ishlinskii hysteresis operators are identified by matching the simulation results and experimental results of the other research (Leang and Devasia, 2007). Hence, the full nonlinear FE model and the reduced order nonlinear FE models are validated by comparing the

simulation results with the experiment results of other research (Leang and Devasia, 2007).

3.2 ASSUMPTIONS AND CONDITIONS

The FE model is developed based on the following assumptions:

(1) The charges supplied by the input voltage are uniform throughout the electrode.

(2) The charges on the electrodes induced by the piezoelectric material are much less than those supplied by the external voltage.

(3) Energy loss of motion of the piezoelectric tube actuator is negligible.

(4) The physical properties are uniform over the whole tube.

(5) The electrode is so thin that its dynamics is negligible.

The FE model is developed based on the following conditions:

(1) The inner electrode is grounded.

(2) The bottom of the piezoelectric tube actuator is firmly fixed to the stationary support.

(3) The sample is placed on top of the piezoelectric tube actuator during scanning in actual application. The effect of the sample on the piezoelectric tube actuator is not considered in simulation.

3.3 FINITE ELEMENT FORMULATION

The piezoelectric tube actuator used in AFM is radially outward polarized with evenly quartered outer electrodes (+X electrode, –X electrode, +Y electrode and –Y electrode) and a complete inner electrode (Z electrode). In this thesis, the FE model is built based on the piezoelectric tube actuator used by Leang and Devasia (2007). In addition, Leang and Devasia (2007) referred the sectored lead-zirconate-titanate (PZT) piezoelectric tube actuator used in their experiment to Chen (1992). According to Chen (1992), the piezoelectric tube actuator is made of PZT-4, and the length, outer diameter and wall thickness are 25.4 mm, 12.7 mm and 0.5 mm respectively. The material properties of the piezoelectric material PZT-4 are shown in Table 3-1 (Sridhar *et al*., 1999). The schematic diagram of the piezoelectric tube actuator is shown in Fig. 3-1. +X electrode and –X electrode belong to X-pair electrodes. Similarly, +Y electrode and –Y electrode belong to Y-pair electrodes. In this research, piezoelectric tube actuator actuated by a pair of electrodes (double-actuation) is considered. Double-actuation means that when a voltage is applied on the +X electrode, the same magnitude but opposite sign of voltage is applied on the –X electrode. Similarly, when a voltage is applied on the +Y electrode, the same magnitude but opposite sign of voltage is applied on the –Y electrode. Due to the converse piezoelectric effect, the voltages applied to the X-pair electrodes (V_{EX}) and Y-pair electrodes (V_{EY}) control the bendings of the piezoelectric tube actuator in the X direction and Y direction respectively. Hence, the displacements in X direction and Y direction of the sample can be controlled. The displacement of the sample in Z direction which is controlled by voltage applied on Z electrode is not the focus in the current research and will be

considered in the future development. The voltage applied on the Z electrode is always equal to zero in this research (Chapter 3 Condition 1).

Table 3-1. Material Properties of Piezoelectric Material PZT-4 (Sridhar *et al.*, 1999)

$c_{E,11}$(Pa)	1.39×10^{11}	e_{31}(C/m^2)	-5.2
$c_{E,12}$(Pa)	7.78×10^{10}	e_{32}(C/m^2)	-5.2
$c_{E,13}$(Pa)	7.43×10^{10}	e_{33}(C/m^2)	15.1
$c_{E,22}$(Pa)	1.39×10^{11}	e_{24}(C/m^2)	12.7
$c_{E,23}$(Pa)	7.43×10^{10}	e_{15}(C/m^2)	12.7
$c_{E,33}$(Pa)	1.15×10^{11}	φ_{11}(F/m)	6.461×10^{-9}
$c_{E,44}$(Pa)	2.56×10^{10}	φ_{22}(F/m)	6.461×10^{-9}
$c_{E,55}$(Pa)	2.56×10^{10}	φ_{33}(F/m)	5.620×10^{-9}
$c_{E,66}$(Pa)	3.06×10^{10}	Density (kg/ m^3)	7500

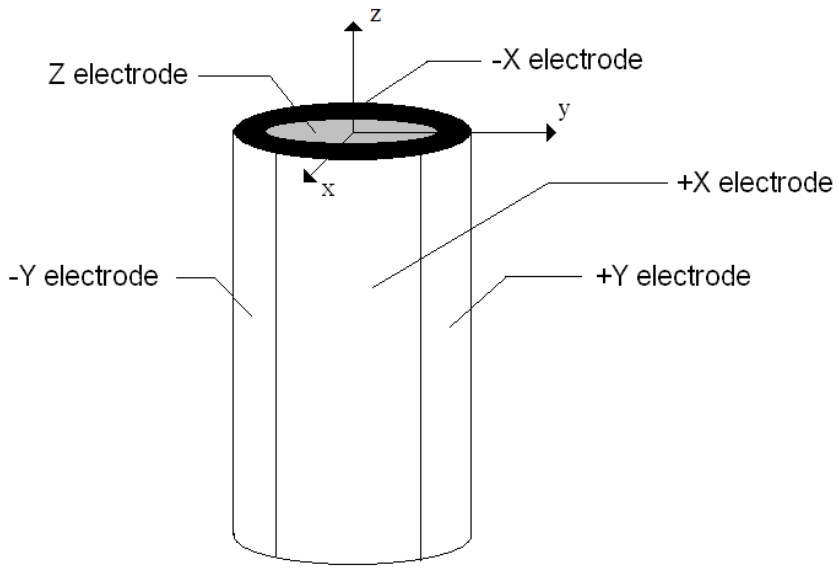

Figure 3-1. Schematic Diagram of Piezoelectric Tube Actuator

3.3.1 Finite Element Discretization

The piezoelectric tube actuator is discretized into 192 elements for FE analysis which is shown in Fig. 3-2. An isoparametric element is used for FE discretization in cylindrical coordinates (Danielson and Noor, 1997). 8-node brick type element is chosen. Therefore, there are totally 336 nodes in the discretized piezoelectric tube actuator. The global node number (1-336) is labeled starting from the node marked "*" shown in Fig. 3-2. The labeling sequence is in counter-clockwise direction, from outer round to inner round, from lower layer to upper layer. A shape function is used for interpolation of displacement, interpolation of electric potential and interpolation of position. The following shape function is adopted (Chandrupatla and Belegundu, 2002):

$$N_i = \frac{1}{8}(1+\xi_i\xi)(1+\eta_i\eta)(1+\zeta_i\zeta), \tag{3.1}$$

where ξ, η and ζ are the coordinates of an arbitrary point in the local coordinate system which are analogue to position variables r, θ, z in the global cylindrical coordinate system. ξ_i, η_i and ζ_i denote the coordinates of i-th node respectively. Each node of an element has local node number 1-8. A labeled element is shown in Fig. 3-3.

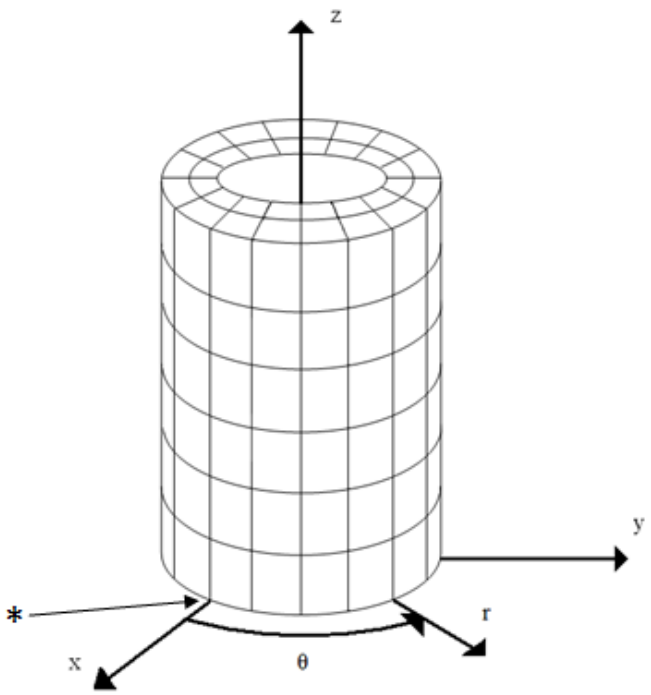

Figure 3-2. Discretized Piezoelectric Tube Actuator

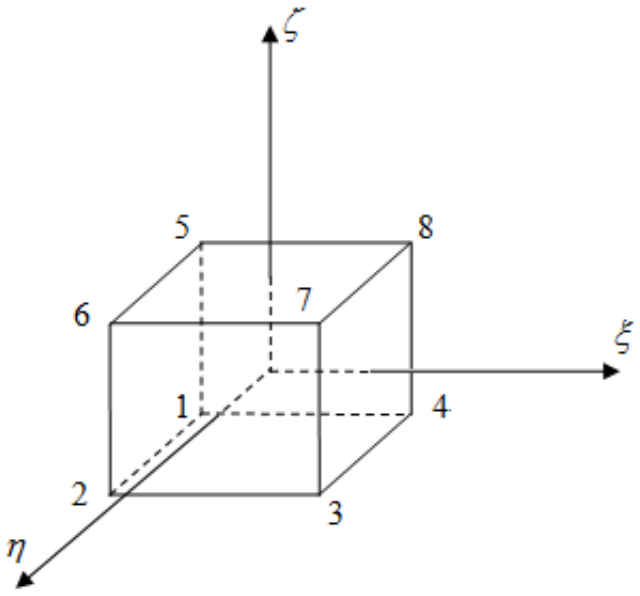

Figure 3-3. Local Node Number of Element

Each node has four degrees of freedom which are nodal displacements and nodal electric potential. Nodal displacements are expressed as:

$$[q]^n = [q_{ri} \quad q_{\theta i} \quad q_{zi}]^T \tag{3.2}$$

and nodal electric potential is given by:

$$\Phi^n = \Phi_i . \tag{3.3}$$

The superscript 'n' denotes the nodal vector. $[q]^n \in \Re^3$ denotes the nodal displacements. Φ^n denotes the nodal electric potential. q_{ri}, $q_{\theta i}$ and q_{zi} denote the nodal displacements of i-th node in r, θ and z directions respectively. Φ_i denotes the nodal electric potential of i-th node.

The nodal displacements of an element are expressed as:

$$[q]^e = [q_{r1} \quad q_{\theta 1} \quad q_{z1} \quad q_{r2} \quad q_{\theta 2} \quad q_{z2} \quad \cdots \quad q_{r8} \quad q_{\theta 8} \quad q_{z8}]^T \tag{3.4a}$$

$$= [q_1 \quad q_2 \quad q_3 \quad q_4 \quad q_5 \quad q_6 \quad \cdots \quad q_{22} \quad q_{23} \quad q_{24}]^T . \tag{3.4b}$$

The superscript 'e' denotes the elemental vector. $[q]^e \in \Re^{24}$ denotes the nodal displacements of an element. The number 'i' in the subscripts of q_{ri}, $q_{\theta i}$ and q_{zi} in Eq. (3.4a) specifies the node. The subscripts of Eq. (3.4a) are rewritten as Eq. (3.4b) for convenience. Displacements at an arbitrary point are defined (Danielson and Noor, 1997):

$$[u]^e = [u_r \quad u_\theta \quad u_z]^T , \tag{3.5a}$$

where:

$$u_r = N_1 q_1 + N_2 q_4 + N_3 q_7 + \cdots + N_8 q_{22} \tag{3.5b}$$

$$u_\theta = N_1 q_2 + N_2 q_5 + N_3 q_8 + \cdots + N_8 q_{23} \tag{3.5c}$$

$$u_z = N_1 q_3 + N_2 q_6 + N_3 q_9 + \cdots + N_8 q_{24}, \tag{3.5d}$$

where $[u]^e \in \Re^3$ denotes the displacements at an arbitrary point. u_r, u_θ and u_z denote displacement of an arbitrary point in r, θ and z directions respectively. Eq. (3.5a) can be rearranged as:

$$[u]^e = [N]^e [q]^e, \tag{3.5e}$$

where

$$[N]^e = \begin{bmatrix} N_1 & 0 & 0 & N_2 & 0 & 0 & \cdots & N_8 & 0 & 0 \\ 0 & N_1 & 0 & 0 & N_2 & 0 & \cdots & 0 & N_8 & 0 \\ 0 & 0 & N_1 & 0 & 0 & N_2 & \cdots & 0 & 0 & N_8 \end{bmatrix}. \tag{3.5f}$$

$[N]^e \in \Re^{3\times 24}$ denotes assembly of shape functions for interpolation of displacements. Strains of an element are given (Santos *et al.*, 2008):

$$[\varepsilon]^e = [\varepsilon_z \quad \varepsilon_\theta \quad \varepsilon_r \quad \gamma_{\theta r} \quad \gamma_{zr} \quad \gamma_{z\theta}]^T \tag{3.6a}$$

$$= \left[\frac{\partial u_z}{\partial z} \quad \frac{1}{r}\left(\frac{\partial u_\theta}{\partial \theta} + u_r\right) \quad \frac{\partial u_r}{\partial r} \quad \frac{\partial u_\theta}{\partial r} - \frac{u_\theta}{r} + \frac{1}{r}\frac{\partial u_r}{\partial \theta} \quad \frac{\partial u_z}{\partial r} + \frac{\partial u_r}{\partial z} \quad \frac{\partial u_\theta}{\partial z} + \frac{1}{r}\frac{\partial u_z}{\partial \theta} \right]^T, \tag{3.6b}$$

where $[\varepsilon]^e \in \Re^6$ denotes the strains of an element. ε_r, ε_θ and ε_z denote the tensile strain in r, θ and z directions respectively. $\gamma_{\theta r}$, γ_{zr} and $\gamma_{z\theta}$ denote the shear strain in θr, zr and $z\theta$ directions respectively. By relating Eq. (3.5e) and Eq. (3.6b) and using Jacobian matrix, the relation between the nodal displacements of an element $[q]^e$ and the strains of an element $[\varepsilon]^e$ is obtained:

$$[\varepsilon]^e = [A]^e [q]^e, \tag{3.6c}$$

where $[A]^e \in \Re^{6\times 24}$ which is function of ξ, η and ζ denotes the connection matrix. The detail of derivation of Eq. (3.6c) is shown in Appendix A.

Similarly, the nodal electric potential of an element can be expressed as:

$$\left[\Phi\right]^e = \left[\Phi_1 \quad \Phi_2 \quad \Phi_3 \quad \Phi_4 \quad \Phi_5 \quad \Phi_6 \quad \Phi_7 \quad \Phi_8\right]^T, \tag{3.7}$$

where $\left[\Phi\right]^e \in \Re^8$ denotes the nodal electric potential of an element. Electric potential at an arbitrary point is defined as:

$$\phi^e = N_1\Phi_1 + N_2\Phi_2 + N_3\Phi_3 + \cdots + N_8\Phi_8, \tag{3.8a}$$

where ϕ^e denotes the electric potential at an arbitrary point. Eq. (3.8a) can be rearranged as:

$$\phi^e = \left[n\right]^e\left[\Phi\right]^e, \tag{3.8b}$$

where

$$\left[n\right]^e = \left[N_1 \quad N_2 \quad N_3 \quad N_4 \quad N_5 \quad N_6 \quad N_7 \quad N_8\right]. \tag{3.8c}$$

$\left[n\right]^e \in \Re^8$ denotes assembly of shape functions for interpolation of electric potentials. Electric fields of an element are given (Santos *et al.*, 2008):

$$\left[E\right]^e = \left[E_z \quad E_\theta \quad E_r\right]^T \tag{3.9a}$$

$$= \left[-\frac{\partial\phi^e}{\partial z} \quad -\frac{1}{r}\frac{\partial\phi^e}{\partial\theta} \quad -\frac{\partial\phi^e}{\partial r}\right]^T, \tag{3.9b}$$

where $\left[E\right]^e \in \Re^3$ denotes the electric fields of an element. E_r, E_θ and E_z denote the electric fields in r, θ and z directions respectively. By relating Eq. (3.8b) and Eq. (3.9b) and using Jacobian matrix, the relation between the nodal electric potential of an element $\left[\Phi\right]^e$ and the electric fields of an element $\left[E\right]^e$ is obtained:

$$\left[E\right]^e = \left[B\right]^e\left[\Phi\right]^e, \tag{3.9c}$$

where $\left[B\right]^e \in \Re^{3\times 8}$ which is function of ξ, η and ζ denotes the connection

matrix. The detail of derivation of Eq. (3.9c) is shown in Appendix A.

3.3.2 Kelvin-Voigt Creep Operator

In order to allow the FE model exhibiting creep phenomenon, it is necessary to implement the creep operator in the FE formulation. In this section, the Kelvin-Voigt creep operator is introduced. It is represented by a linear first order differential equation (Krejci and Kuhnen, 2001; and Mokaberi and Requicha, 2008):

$$\frac{1}{w_f}\dot{x}_f(t) + x_f(t) = u_c(t), \tag{3.10a}$$

where u_c denotes the input of the creep operator, x_f denotes the state of f-th creep operator, t denotes the time variable and w_f denotes the weighting factor of f-th Kelvin-Voigt creep operator. By solving Eq. (3.10a) for the state of f-th Kelvin-Voigt creep operator w_f, the explicit integral formula is obtained (Krejci and Kuhnen, 2001):

$$x_f = e^{-w_f t}x_f(0) + w_f\int_0^t e^{w_f(\tau-t)}u_c(\tau)d\tau. \tag{3.10b}$$

The state of the operator x_f is function of time t and input u_c. The discrete form of the Kelvin-Voigt creep operator is used for computation. By rectangular approximation, Eq. (3.10b) is expressed as below (Krejci and Kuhnen, 2001; and Mokaberi and Requicha, 2008):

$$x_f(k) = e^{-w_f T_s}x_f(k-1) + (1-e^{-w_f T_s})u_c(k-1), \tag{3.11}$$

where T_s denotes the sampling period and k denotes discrete time.

The creep strain is given below (Krejci and Kuhnen, 2001; and Mokaberi and Requicha, 2008):

$$\varepsilon_c(k) = \sum_{f=1}^{N_F} a_f x_f(k), \tag{3.12}$$

where ε_c denotes the strain due to creep and a_f is the proportional constant for the Kelvin-Voigt creep operator. N_F denotes total number of Kelvin-Voigt creep operators. The purpose of using superposition of Kelvin-Voigt creep operators is to improve modelling of the creep. The input of the Kelvin-Voigt creep operator is given below:

$$u_c = \overline{V}_E, \tag{3.13}$$

where $\overline{V}_E$ denotes the potential difference between the outer electrode and the inner electrode and divided by number of rounds of elements across the both electrodes. It is remarked that voltage is defined as positive when the potential at the outer electrode is higher than inner electrode. When a positive voltage V_E is applied, the portion of the piezoelectric material covered by the electrode will contract since the poling direction is radially outward. Positive V_E gives negative creep strain ε_c. Therefore, a_f is negative. The total strain ε_t is given by:

$$\varepsilon_t = \varepsilon_l + \varepsilon_c, \tag{3.14a}$$

where ε_l denotes the strain due to mechanical stress or piezoelectric effect. Rearranging Eq. (3.14a):

$$\varepsilon_l = \varepsilon_t - \varepsilon_c. \tag{3.14b}$$

3.3.3 Prandtl-Ishlinskii Hysteresis Operator

The hysteresis phenomenon of the piezoelectric material has backlash-like property (Bashash and Jalili, 2009) which can be modelled by Prandtl-Ishlinskii hysteresis operator. It is implemented into the FE formulation to allow the FE model exhibiting hysteresis phenomenon. In this section, the Prandtl-Ishlinskii hysteresis operator is introduced. The Prandtl-Ishlinskii hysteresis operator consists of three regions (Krejci and Kuhnen, 2001):

$$\dot{h}_j(t) = \dot{u}_h(t), \qquad u_h(t) = h_j(t) - \kappa_j \tag{3.15a}$$

$$\dot{h}_j(t) = 0, \qquad h_j(t) - \kappa_j < u_h(t) < h_j(t) + \kappa_j \tag{3.15b}$$

$$\dot{h}_j(t) = \dot{u}_h(t), \qquad u_h(t) = h_j(t) + \kappa_j, \tag{3.15c}$$

where h_j denotes the output of the hysteresis operator, u_h denotes the input of the hysteresis operator and κ_j denotes threshold of the hysteresis operator. The threshold determines the backlash-distance of the hysteresis phenomenon. The characteristic of the Prandtl-Ishlinskii hysteresis operator is shown in Fig. 3-4. The output h_j is function of time t and input u_h. The equivalent discrete form of the Prandtl-Ishlinskii hysteresis operator is given (Krejci and Kuhnen, 2001):

$$h_j(k) = u_h(k) + \kappa_j, \qquad u_h(k) \le h_j(k-1) - \kappa_j \tag{3.16a}$$

$$h_j(k) = h_j(k-1), \qquad h_j(k-1) - \kappa_j < u_h(k) < h_j(k-1) + \kappa_j \tag{3.16b}$$

$$h_j(k) = u_h(k) - \kappa_j, \qquad u_h(k) \ge h_j(k-1) + \kappa_j. \tag{3.16c}$$

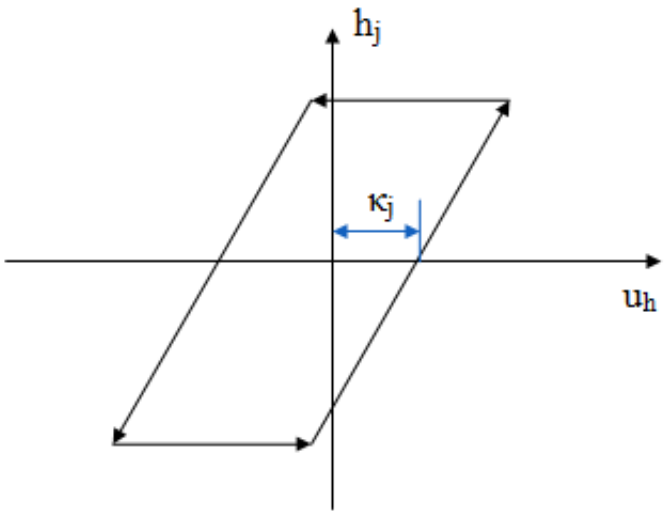

Figure 3-4. Characteristic of Prandtl-Ishlinskii Hysteresis Operator

The remnant polarization p (C/m^2), sometimes called irreversible polarization, exhibits hysteresis when a voltage is applied. The remnant polarization p can be modelled by the superposition of Prandtl-Ishlinskii hysteresis operators with different threshold κ_j and proportional constant b_j (Krejci and Kuhnen, 2001; and Mokaberi and Requicha, 2008):

$$p(k) = \sum_{j=1}^{N_J} b_j h_j(k), \tag{3.17}$$

where b_j denotes the proportional constant for the Prandtl-Ishlinskii hysteresis operator. N_J denotes total number of Prandtl-Ishlinskii hysteresis operators. Superposition of Prandtl-Ishlinskii hysteresis operators can improve modelling. The input of the Prandtl-Ishlinskii hysteresis operator is given below:

$$u_h = \overline{V}_E. \tag{3.18}$$

When a positive V_E is applied, the remnant polarization will point to the negative r direction. Therefore, the proportional constant b_j is negative. It is remarked

that the sum of the proportional constants for the Kelvin-Voigt creep operator a_f and the sum of the proportional constants for the Prandtl-Ishlinskii hysteresis operator b_j are not necessary equal to one (Krejci and Kuhnen, 2001).

3.3.4 Constitutive Equations

The linear constitutive equations of piezoelectric material are expressed in Eq. (3.19a) and Eq. (3.20a):

$$[\sigma]^e = [c_E]^e [\varepsilon_l]^e - [e^T]^e [E]^e \tag{3.19a}$$

or

$$\begin{bmatrix} \sigma_z \\ \sigma_\theta \\ \sigma_r \\ \tau_{\theta r} \\ \tau_{zr} \\ \tau_{z\theta} \end{bmatrix} = \begin{bmatrix} c_{11} & c_{12} & c_{13} & 0 & 0 & 0 \\ c_{12} & c_{22} & c_{23} & 0 & 0 & 0 \\ c_{13} & c_{23} & c_{33} & 0 & 0 & 0 \\ 0 & 0 & 0 & c_{44} & 0 & 0 \\ 0 & 0 & 0 & 0 & c_{55} & 0 \\ 0 & 0 & 0 & 0 & 0 & c_{66} \end{bmatrix} \begin{bmatrix} (\varepsilon_l)_z \\ (\varepsilon_l)_\theta \\ (\varepsilon_l)_r \\ (\gamma_l)_{\theta r} \\ (\gamma_l)_{zr} \\ (\gamma_l)_{z\theta} \end{bmatrix} - \begin{bmatrix} 0 & 0 & e_{31} \\ 0 & 0 & e_{32} \\ 0 & 0 & e_{33} \\ 0 & e_{24} & 0 \\ e_{15} & 0 & 0 \\ 0 & 0 & 0 \end{bmatrix} \begin{bmatrix} E_z \\ E_\theta \\ E_r \end{bmatrix} \tag{3.19b}$$

and

$$[D]^e = [e]^e [\varepsilon_l]^e + [\varphi]^e [E]^e \tag{3.20a}$$

or

$$\begin{bmatrix} D_z \\ D_\theta \\ D_r \end{bmatrix} = \begin{bmatrix} 0 & 0 & 0 & 0 & e_{15} & 0 \\ 0 & 0 & 0 & e_{24} & 0 & 0 \\ e_{31} & e_{32} & e_{33} & 0 & 0 & 0 \end{bmatrix} \begin{bmatrix} (\varepsilon_l)_z \\ (\varepsilon_l)_\theta \\ (\varepsilon_l)_r \\ (\gamma_l)_{\theta r} \\ (\gamma_l)_{zr} \\ (\gamma_l)_{z\theta} \end{bmatrix} + \begin{bmatrix} \varphi_{11} & 0 & 0 \\ 0 & \varphi_{22} & 0 \\ 0 & 0 & \varphi_{33} \end{bmatrix} \begin{bmatrix} E_z \\ E_\theta \\ E_r \end{bmatrix}, \tag{3.20b}$$

where $[c_E]^e \in \Re^{6\times6}$ is elastic modulus (N/m^2), $[e]^e \in \Re^{3\times6}$ is piezoelectric coefficients (C/m^2), $[\varphi]^e \in \Re^{3\times3}$ is dielectric coefficients (F/m), $[\sigma]^e \in \Re^6$ is stress (N/m^2), $[\varepsilon_l]^e \in \Re^6$ is strain due to mechanical stress and piezoelectric effect, $[D]^e \in \Re^3$ is electric displacement (C/m^2) and $[E]^e \in \Re^3$ is electric field (NC^{-1}).

The nonlinear constitutive equations of piezoelectric material are developed by substituting Eq. (3.14b) into linear constitutive equations Eq. (3.19a) and Eq. (3.20a) and adding remnant polarization p to Eq. (3.20a):

$$[\sigma]^e = [c_E]^e \left\{ [\varepsilon_t]^e - [\varepsilon_c]^e \right\} - [e^T]^e [E]^e \tag{3.21a}$$

or

$$\begin{bmatrix} \sigma_z \\ \sigma_\theta \\ \sigma_r \\ \tau_{\theta r} \\ \tau_{zr} \\ \tau_{z\theta} \end{bmatrix} = \begin{bmatrix} c_{11} & c_{12} & c_{13} & 0 & 0 & 0 \\ c_{12} & c_{22} & c_{23} & 0 & 0 & 0 \\ c_{13} & c_{23} & c_{33} & 0 & 0 & 0 \\ 0 & 0 & 0 & c_{44} & 0 & 0 \\ 0 & 0 & 0 & 0 & c_{55} & 0 \\ 0 & 0 & 0 & 0 & 0 & c_{66} \end{bmatrix} \left\{ \begin{bmatrix} (\varepsilon_t)_z \\ (\varepsilon_t)_\theta \\ (\varepsilon_t)_r \\ (\gamma_t)_{\theta r} \\ (\gamma_t)_{zr} \\ (\gamma_t)_{z\theta} \end{bmatrix} - \begin{bmatrix} (\varepsilon_c)_z \\ (\varepsilon_c)_\theta \\ (\varepsilon_c)_r \\ (\gamma_c)_{\theta r} \\ (\gamma_c)_{zr} \\ (\gamma_c)_{z\theta} \end{bmatrix} \right\} - \begin{bmatrix} 0 & 0 & e_{31} \\ 0 & 0 & e_{32} \\ 0 & 0 & e_{33} \\ 0 & e_{24} & 0 \\ e_{15} & 0 & 0 \\ 0 & 0 & 0 \end{bmatrix} \begin{bmatrix} E_z \\ E_\theta \\ E_r \end{bmatrix} \tag{3.21b}$$

and

$$[D]^e = [e]^e \left\{ [\varepsilon_t]^e - [\varepsilon_c]^e \right\} + [\varphi]^e [E]^e + [P]^e \tag{3.22a}$$

or

$$\begin{bmatrix} D_z \\ D_\theta \\ D_r \end{bmatrix} = \begin{bmatrix} 0 & 0 & 0 & 0 & e_{15} & 0 \\ 0 & 0 & 0 & e_{24} & 0 & 0 \\ e_{31} & e_{32} & e_{33} & 0 & 0 & 0 \end{bmatrix} \left\{ \begin{bmatrix} (\varepsilon_t)_z \\ (\varepsilon_t)_\theta \\ (\varepsilon_t)_r \\ (\gamma_t)_{\theta r} \\ (\gamma_t)_{zr} \\ (\gamma_t)_{z\theta} \end{bmatrix} - \begin{bmatrix} (\varepsilon_c)_z \\ (\varepsilon_c)_\theta \\ (\varepsilon_c)_r \\ (\gamma_c)_{\theta r} \\ (\gamma_c)_{zr} \\ (\gamma_c)_{z\theta} \end{bmatrix} \right\} + \begin{bmatrix} \varphi_{11} & 0 & 0 \\ 0 & \varphi_{22} & 0 \\ 0 & 0 & \varphi_{33} \end{bmatrix} \begin{bmatrix} E_z \\ E_\theta \\ E_r \end{bmatrix} + \begin{bmatrix} p_z \\ p_\theta \\ p_r \end{bmatrix}, \tag{3.22b}$$

where $[\varepsilon_c]^e \in \Re^6$ is creep strain, $[\varepsilon_t]^e \in \Re^6$ is total strain and $[P]^e \in \Re^3$ is

remnant polarization vector (C/m^2).

Because the electrodes locate at the circumferences of the piezoelectric tube actuator, input voltage is only applied across the piezoelectric tube actuator in r direction. Therefore, there are no strains due to creep and no remnant polarizations due to hysteresis in θ and z directions:

$$(\varepsilon_c)_z = (\varepsilon_c)_\theta = (\gamma_c)_{\theta r} = (\gamma_c)_{zr} = (\gamma_c)_{z\theta} = 0 \tag{3.23}$$

and

$$p_z = p_\theta = 0. \tag{3.24}$$

3.3.5 Energy Approach

By the energy approach, the Lagrangian is obtained (Preumont, 2006):

$$L = -PE + W_e + KE, \tag{3.25}$$

where L is the Lagrangian, PE is the potential energy, W_e is the electrical energy and KE is the kinetic energy.

$$PE = \frac{1}{2}\int_V [\sigma]^{eT}[\varepsilon]^e dV - \int_V [u]^{eT}[f]^e dV \tag{3.26}$$

$$W_e = \frac{1}{2}\int_V [E]^{eT}[D]^e dV \tag{3.27}$$

$$KE = \frac{1}{2}\int_V [\dot{u}]^{eT}[\dot{u}]^e \mu dV = \frac{1}{2}[\dot{q}]^{eT}[M]^e[\dot{q}]^e. \tag{3.28}$$

For the linear case which does not consider creep and hysteresis, by substituting Eq. (3.19a) into Eq. (3.26), the potential energy can be expressed:

$$PE = \frac{1}{2}\int_V \left(\left[c_E\right]^e \left[\varepsilon_l\right]^e - \left[e^T\right]^e \left[E\right]^e \right)^T \left[\varepsilon_l\right]^e dV - \int_V \left[u\right]^{eT} \left[f\right]^e dV \tag{3.29a}$$

$$= \frac{1}{2}\int_V \left[\varepsilon_l\right]^{eT} \left[c_E\right]^e \left[\varepsilon_l\right]^e dV - \frac{1}{2}\int_V \left[E\right]^{eT} \left[e\right]^e \left[\varepsilon_l\right]^e dV - \int_V \left[u\right]^{eT} \left[f\right]^e dV . \tag{3.29b}$$

By substituting Eq. (3.6c) and Eq. (3.9c) into Eq. (3.29b), the following equation is obtained:

$$PE = \frac{1}{2}\left[q\right]^{eT} \left[K_{qq}\right]^e \left[q\right]^e - \frac{1}{2}\left[\Phi\right]^{eT} \left[K_{\Phi q}\right]^e \left[q\right]^e - \left[q\right]^{eT} \left[F\right]^e . \tag{3.29c}$$

By substituting Eq. (3.20a) into Eq. (3.27), the electrical energy can be obtained:

$$W_e = \frac{1}{2}\int_V \left[E\right]^{eT} \left[e\right]^e \left[\varepsilon_l\right]^e dV + \frac{1}{2}\int_V \left[E\right]^{eT} \left[\varphi\right]^e \left[E\right]^e dV . \tag{3.30a}$$

By substituting Eq. (3.6c) and Eq. (3.9c) into Eq. (3.30a), the following equation is obtained:

$$W_e = \frac{1}{2}\left[\Phi\right]^{eT} \left[K_{\Phi q}\right]^e \left[q\right]^e + \frac{1}{2}\left[\Phi\right]^{eT} \left[K_{\Phi\Phi}\right]^e \left[\Phi\right]^e . \tag{3.30b}$$

Therefore, by Eq. (3.25), the Lagrangian can be expressed:

$$\begin{aligned} L = &-\frac{1}{2}\left[q\right]^{eT} \left[K_{qq}\right]^e \left[q\right]^e + \left[\Phi\right]^{eT} \left[K_{\Phi q}\right]^e \left[q\right]^e + \left[q\right]^{eT} \left[F\right]^e + \frac{1}{2}\left[\Phi\right]^{eT} \left[K_{\Phi\Phi}\right]^e \left[\Phi\right]^e \\ &+ \frac{1}{2}\left[\dot{q}\right]^{eT} \left[M\right]^e \left[\dot{q}\right]^e , \end{aligned} \tag{3.31}$$

where the matrices $\left[K_{qq}\right]^e \in \Re^{24\times 24}$, $\left[K_{\Phi q}\right]^e \in \Re^{8\times 24}$, $\left[K_{\Phi\Phi}\right]^e \in \Re^{8\times 8}$, $\left[F\right]^e \in \Re^{24}$ and $\left[M\right]^e \in \Re^{24\times 24}$ are constant.

For the nonlinear case with both creep and hysteresis, by substituting Eq. (3.21a) into Eq. (3.26), the potential energy can be expressed:

$$PE = \frac{1}{2}\int_V \left([c_E]^e [\varepsilon_t]^e - [c_E]^e [\varepsilon_c]^e - [e^T]^e [E]^e \right)^T [\varepsilon_t]^e \, dV - \int_V [u]^{eT} [f]^e \, dV \tag{3.32a}$$

$$\begin{aligned} &= \frac{1}{2}\int_V [\varepsilon_t]^{eT} [c_E]^e [\varepsilon_t]^e \, dV - \frac{1}{2}\int_V [\varepsilon_c]^{eT} [c_E]^e [\varepsilon_t]^e \, dV \\ &\quad - \frac{1}{2}\int_V [E]^{eT} [e]^e [\varepsilon_t]^e \, dV - \int_V [u]^{eT} [f]^e \, dV . \end{aligned} \tag{3.32b}$$

By substituting Eq. (3.6c) and Eq. (3.9c) into Eq. (3.32b), the following equation is obtained:

$$PE = \frac{1}{2}[q]^{eT} [K_{qq}]^e [q]^e - [q]^{eT} [N_{C1}]^e - \frac{1}{2}[\Phi]^{eT} [K_{\Phi q}]^e [q]^e - [q]^{eT} [F]^e . \tag{3.32c}$$

By substituting Eq. (3.22a) into Eq. (3.27), the electrical energy can be expressed:

$$\begin{aligned} W_e &= \frac{1}{2}\int_V [E]^{eT} [e]^e [\varepsilon_t]^e \, dV - \frac{1}{2}\int_V [E]^{eT} [e]^e [\varepsilon_c]^e \, dV + \frac{1}{2}\int_V [E]^{eT} [\varphi]^e [E]^e \, dV \\ &\quad + \frac{1}{2}\int_V [E]^{eT} [P]^e dV . \end{aligned} \tag{3.33a}$$

By substituting Eq. (3.6c) and Eq. (3.9c) into Eq. (3.33a), the following equation is obtained:

$$W_e = \frac{1}{2}[\Phi]^{eT} [K_{\Phi q}]^e [q]^e - [\Phi]^{eT} [N_{C2}]^e + \frac{1}{2}[\Phi]^{eT} [K_{\Phi\Phi}]^e [\Phi]^e + [\Phi]^{eT} [N_h]^e . \tag{3.33b}$$

Therefore, the Lagrangian can be expressed:

$$\begin{aligned} L = &-\frac{1}{2}[q]^{eT} [K_{qq}]^e [q]^e + [q]^{eT} [N_{C1}]^e + [\Phi]^{eT} [K_{\Phi q}]^e [q]^e - [\Phi]^{eT} [N_{C2}]^e \\ &+ [q]^{eT} [F]^e + \frac{1}{2}[\Phi]^{eT} [K_{\Phi\Phi}]^e [\Phi]^e + [\Phi]^{eT} [N_h]^e + \frac{1}{2}[\dot{q}]^{eT} [M]^e [\dot{q}]^e , \end{aligned} \tag{3.34}$$

where the matrix which relates to hysteresis operator is $[N_h]^e \in \Re^8$ and the matrices which relate to creep operator are $[N_{C1}]^e \in \Re^{24}$ and $[N_{C2}]^e \in \Re^8$.

$[N_h]^e$, $[N_{C1}]^e$ and $[N_{C2}]^e$ are nonlinear terms. Two-point Gaussian Quadrature is adopted for numerical integration.

3.3.6 Hamilton's Principle

The dynamic equations of the piezoelectric tube actuator are formulated by Hamilton's Principle. Hamilton's Principle for mechanical coordinates and electrical coordinates are shown in Eq. (3.35) and Eq. (3.36) respectively (Preumont, 2006):

$$\frac{d}{dt}\left(\frac{\partial L}{\partial [\dot{q}]^e}\right) - \frac{\partial L}{\partial [q]^e} = [0] \tag{3.35}$$

$$\frac{d}{dt}\left(\frac{\partial L}{\partial [\dot{\upsilon}]^e}\right) - \frac{\partial L}{\partial [\upsilon]^e} = [I_q]^e, \tag{3.36}$$

where $[\upsilon]^e \in \Re^8$ is called electric flux linkage and $[\dot{\upsilon}]^e = [\Phi]^e$. $[I_q]^e \in \Re^8$ denotes current.

For the linear case, by differentiating Eq. (3.31) according to Eq. (3.35) and Eq. (3.36), the following equations are obtained:

$$\frac{\partial L}{\partial [\dot{q}]^e} = [M]^e [\dot{q}]^e \tag{3.37a}$$

$$\frac{d}{dt}\left(\frac{\partial L}{\partial [\dot{q}]^e}\right) = [M]^e [\ddot{q}]^e \tag{3.37b}$$

$$\frac{\partial L}{\partial [q]^e} = -[K_{qq}]^e [q]^e + [K_{\Phi q}]^{eT} [\Phi]^e + [F]^e \tag{3.38}$$

$$\frac{\partial L}{\partial [\dot{\upsilon}]^e} = [K_{\Phi\Phi}]^e [\dot{\upsilon}]^e + [K_{\Phi q}]^e [q]^e \tag{3.39}$$

$$\frac{\partial L}{\partial [\upsilon]^e} = [0]. \tag{3.40}$$

By substituting Eq. (3.37b) and Eq. (3.38) into Eq. (3.35) and adding damping term, the following equation is obtained:

$$[M]^e [\ddot{q}]^e + [C]^e [\dot{q}]^e + [K_{qq}]^e [q]^e - [K_{\Phi q}]^{eT} [\Phi]^e = [F]^e, \tag{3.41}$$

where $[C]^e \in \Re^{24\times 24}$ denotes damping matrix. The damping matrix is obtained (Maess *et al.*, 2008b):

$$[C]^e = \alpha [M]^e + \beta [K_{qq}]^e, \tag{3.42}$$

where α and β are the Rayleigh constants. By substituting Eq. (3.39) and Eq. (3.40) into Eq. (3.36), the following equations are obtained:

$$\frac{d}{dt}\left([K_{\Phi\Phi}]^e [\dot{\upsilon}]^e + [K_{\Phi q}]^e [q]^e\right) = [I_q]^e \tag{3.43a}$$

$$[K_{\Phi q}]^e [q]^e + [K_{\Phi\Phi}]^e [\Phi]^e = [Q_E]^e. \tag{3.43b}$$

Eq. (3.41) and Eq. (3.43b) are the local linear dynamic equations. $[Q_E]^e \in \Re^8$ denotes the charge input vector. The detail of formulation of $[Q_E]^e$ is shown in Appendix B.

For the nonlinear case with both creep and hysteresis, by differentiating Eq. (3.34) according to Eq. (3.35) and Eq. (3.36), the following equation are obtained:

$$\frac{\partial L}{\partial [\dot{q}]^e} = [M]^e [\dot{q}]^e \tag{3.44a}$$

$$\frac{d}{dt}\left(\frac{\partial L}{\partial [\dot{q}]^e}\right) = [M]^e[\ddot{q}]^e \tag{3.44b}$$

$$\frac{\partial L}{\partial [q]^e} = -[K_{qq}]^e[q]^e + [N_{C1}]^e + [K_{\Phi q}]^{eT}[\Phi]^e + [F]^e \tag{3.45}$$

$$\frac{\partial L}{\partial [\dot{\upsilon}]^e} = [K_{\Phi\Phi}]^e[\dot{\upsilon}]^e + [K_{\Phi q}]^e[q]^e - [N_{C2}]^e + [N_h]^e \tag{3.46}$$

$$\frac{\partial L}{\partial [\upsilon]^e} = [0]. \tag{3.47}$$

By substituting Eq. (3.44b) and Eq. (3.45) into Eq. (3.35) and adding damping matrix $[C]^e$, the following equation is obtained:

$$[M]^e[\ddot{q}]^e + [C]^e[\dot{q}]^e + [K_{qq}]^e[q]^e - [K_{\Phi q}]^{eT}[\Phi]^e = [F]^e + [N_{C1}]^e. \tag{3.48}$$

By substituting Eq.(3.46) and Eq. (3.47) into Eq. (3.36), the following equations are obtained:

$$\frac{d}{dt}\left([K_{\Phi\Phi}]^e[\dot{\upsilon}]^e + [K_{\Phi q}]^e[q]^e - [N_{C2}]^e + [N_h]^e\right) = [I_q]^e \tag{3.49a}$$

$$[K_{\Phi q}]^e[q]^e + [K_{\Phi\Phi}]^e[\Phi]^e = [Q_E]^e + [N_{C2}]^e - [N_h]^e. \tag{3.49b}$$

Eq. (3.48) and Eq. (3.49b) are the local nonlinear dynamic equations with both creep and hysteresis. The local nonlinear dynamic equations have three terms more than the local linear dynamic equations. They are the nonlinear terms $[N_h]^e$, $[N_{C1}]^e$ and $[N_{C2}]^e$.

The local dynamic equations in linear case and nonlinear case are assembled to global form according to the local node number and the global node number (Chandrupatla and Belegundu, 2002). The global matrices and vectors are identified by a superscript ‘g’. For the linear FE model, the global dynamic

equations are given:

$$[M]^g[\ddot{q}]^g + [C]^g[\dot{q}]^g + [K_{qq}]^g[q]^g - [K_{\Phi q}]^{gT}[\Phi]^g = [F]^g \tag{3.50}$$

$$[K_{\Phi q}]^g[q]^g + [K_{\Phi\Phi}]^g[\Phi]^g = [Q_E]^g. \tag{3.51}$$

For the nonlinear FE model with both creep and hysteresis, the global dynamic equations are given:

$$[M]^g[\ddot{q}]^g + [C]^g[\dot{q}]^g + [K_{qq}]^g[q]^g - [K_{\Phi q}]^{gT}[\Phi]^g = [F]^g + [N_{C1}]^g \tag{3.52}$$

$$[K_{\Phi q}]^g[q]^g + [K_{\Phi\Phi}]^g[\Phi]^g = [Q_E]^g + [N_{C2}]^g - [N_h]^g. \tag{3.53}$$

The electrical and mechanical boundary conditions are applied by elimination approach.

3.3.7 State Space Equation

The state space equation is compatible to numerical solvers provided by computer software. It is a benefit to express the dynamic equation in state space form. For the nonlinear FE model, Eq. (3.53) is substituted into Eq. (3.52) and the following equation is obtained:

$$\begin{aligned}
&[M]^g[\ddot{q}]^g + [C]^g[\dot{q}]^g + [K]^g[q]^g = [K_{\Phi q}]^{gT}[K_{\Phi\Phi}]^{g-1}[\overline{Q}_{EX}]^g V_{EX} \\
&+ [K_{\Phi q}]^{gT}[K_{\Phi\Phi}]^{g-1}[\overline{Q}_{EY}]^g V_{EY} + \left([\overline{N}_{C1X}]^g + [K_{\Phi q}]^{gT}[K_{\Phi\Phi}]^{g-1}[\overline{N}_{C2X}]^g\right)\varepsilon_{cVX} \\
&+ \left([\overline{N}_{C1Y}]^g + [K_{\Phi q}]^{gT}[K_{\Phi\Phi}]^{g-1}[\overline{N}_{C2Y}]^g\right)\varepsilon_{cVY} - [K_{\Phi q}]^{gT}[K_{\Phi\Phi}]^{g-1}[\overline{N}_{hX}]^g p_{VX} \\
&- [K_{\Phi q}]^{gT}[K_{\Phi\Phi}]^{g-1}[\overline{N}_{hY}]^g p_{VY} + [\overline{F}]^g f_g \\
&= [R_1]^g V_{EX} + [R_2]^g V_{EY} + [R_3]^g \varepsilon_{cVX} + [R_4]^g \varepsilon_{cVY}
\end{aligned} \tag{3.54a}$$

$$-[R_5]^g p_{VX} - [R_6]^g p_{VY} + [\bar{F}]^g f_g, \tag{3.54b}$$

where

$$[K]^g = [K_{qq}]^g + [K_{\Phi q}]^{gT} [K_{\Phi\Phi}]^{g-1} [K_{\Phi q}]^g \tag{3.54c}$$

and f_g is the gravitational force. In Eq. (3.54b), $[Q_E]^g$, $[N_{C1}]^g$, $[N_{C2}]^g$ and $[N_h]^g$ are divided into constant parts and variable parts. Moreover, they are separated into two groups, one has variable part which is function of V_{EX} and the another group has variable part which is function of V_{EY}. ε_{cVX} and ε_{cVY} are $(\varepsilon_c)_r$ due to V_{EX} and V_{EY} respectively. p_{VX} and p_{VY} are p_r due to V_{EX} and V_{EY} respectively. It is remarked that the terms $[R_3]^g \varepsilon_{cVX}$, $[R_4]^g \varepsilon_{cVY}$, $[R_5]^g p_{VX}$ and $[R_6]^g p_{VY}$ are zero for linear model. Eq. (3.54b) is expressed in state space form. For the linear model, the state equation is given:

$$\begin{bmatrix} [\dot{q}]^g \\ [\ddot{q}]^g \end{bmatrix} = \begin{bmatrix} [0] & [I] \\ -[M]^{g-1}[K]^g & -[M]^{g-1}[C]^g \end{bmatrix} \begin{bmatrix} [q]^g \\ [\dot{q}]^g \end{bmatrix}$$
$$+ \begin{bmatrix} [0] & [0] & [0] \\ [M]^{g-1}[R_1]^g & [M]^{g-1}[R_2]^g & [M]^{g-1}[\bar{F}]^g \end{bmatrix} \bullet [V_{EX} \quad V_{EY} \quad f_g]^T. \tag{3.55}$$

For the nonlinear model, the state equation is given:

$$\begin{bmatrix} [\dot{q}]^g \\ [\ddot{q}]^g \end{bmatrix} = \begin{bmatrix} [0] & [I] \\ -[M]^{g-1}[K]^g & -[M]^{g-1}[C]^g \end{bmatrix} \begin{bmatrix} [q]^g \\ [\dot{q}]^g \end{bmatrix}$$
$$+ \begin{bmatrix} [0] & [0] & [0] & [0] & [0] & [0] & [0] \\ [M]^{g-1}[R_1]^g & [M]^{g-1}[R_2]^g & [M]^{g-1}[R_3]^g & [M]^{g-1}[R_4]^g & -[M]^{g-1}[R_5]^g & -[M]^{g-1}[R_6]^g & [M]^{g-1}[\bar{F}]^g \end{bmatrix}$$
$$\bullet [V_{EX} \quad V_{EY} \quad \varepsilon_{cVX} \quad \varepsilon_{cVY} \quad p_{VX} \quad p_{VY} \quad f_g]^T. \tag{3.56}$$

Since the nodal displacements of 241-th node and 245-th node in r direction are equivalent to the horizontal motions of the sample in X direction and Y direction

respectively, the output equation is formed for both linear model and nonlinear model:

$$\begin{bmatrix} q_X \\ q_Y \end{bmatrix} = \left[\begin{array}{ccc|c|ccc|c|ccc} 0 & \cdots & 0 & \overset{721st}{1} & 0 & \cdots & 0 & \overset{733rd}{0} & 0 & \cdots & 0 \\ 0 & \cdots & 0 & 0 & 0 & \cdots & 0 & 1 & 0 & \cdots & 0 \end{array}\right] \begin{bmatrix} [q]^g \\ [\dot{q}]^g \end{bmatrix}. \tag{3.57}$$

For convenience, q_X and q_Y which denote horizontal motions of sample in X direction and Y direction respectively are simply called X displacement and Y displacement respectively.

3.3.8 Reduction Method

The order of the state space model shown in Eq. (3.56) and Eq. (3.57) is too high for computer simulation and controller design because the dynamic equations are formulated by FE method. It is necessary to perform model order reduction. The reduction method which is called the balanced model truncation via Schur method (Safonov and Chiang, 1989) is chosen and the detail is given in Appendix C. By the reduction method, the reduced order model can be obtained:

$$[A] = [S_{L,BIG}]^T [A_s][S_{R,BIG}] \tag{3.58}$$

$$[B_n] = [S_{L,BIG}]^T [B_s] \tag{3.59}$$

$$[C] = [C_s][S_{R,BIG}] \tag{3.60}$$

$$[D] = [D_s] = [0], \tag{3.61}$$

where $[S_{L,BIG}] \in \Re^{fo \times n}$ and $[S_{R,BIG}] \in \Re^{fo \times n}$ denote left and right transformations for reduced order model respectively. $[A] \in \Re^{n \times n}$ denotes the reduced order system matrix. $[B_n] \in \Re^{n \times 7}$ denotes the reduced order input matrix with nonlinear

distribution. $[C] \in \Re^{2\times n}$ denotes the reduced order output matrix. $[D] \in \Re^{2\times 7}$ denotes the reduced order feedforward matrix. The reduced order model Eq. (3.58)-(3.61) can be rearranged so that nonlinearities are expressed explicitly:

$$[\dot{x}] = [A][x] + [B][u_E] + [G][\chi] + [B_g] f_g \tag{3.62a}$$

$$[\dot{x}] = [A][x] + [B][u_E] + [G][\chi] + [K_g] \tag{3.62b}$$

$$[y] = [C][x], \tag{3.63}$$

where

$$[B_n] = [[B] \quad [G] \quad [B_g]] \tag{3.64a}$$

$$[u_E] = \begin{bmatrix} V_{EX} \\ V_{EY} \end{bmatrix} \tag{3.64b}$$

$$[\chi] = [\varepsilon_{cVX} \quad \varepsilon_{cVY} \quad p_{VX} \quad p_{VY}]^T \tag{3.64c}$$

$$[y] = \begin{bmatrix} q_X \\ q_Y \end{bmatrix}. \tag{3.64d}$$

$[x] \in \Re^n$ is the state vector, $[u_E] \in \Re^2$ is the input vector, $[y] \in \Re^2$ is the output vector and $[K_g] \in \Re^n$ is the constant term due to gravity. $[B] \in \Re^{n\times 2}$ denotes the reduced order input matrix. $[G] \in \Re^{n\times 4}$ denotes the nonlinear distribution matrix. $[B_g] \in \Re^n$ denotes the gravitational force distribution matrix. For convenience, the voltages applied to the X-pair electrodes (V_{EX}) and Y-pair electrodes (V_{EY}) are simply called X input and Y input respectively. The reduced order nonlinear model shown in Eq. (3.62b) and Eq. (3.63) is available for computer simulation and controller design if appropriate order 'n' is selected. It is remarked that the reduced order linear model does not contain the term '$[G][\chi]$' in Eq. (3.62b). Therefore:

$$[\dot{x}] = [A][x] + [B][u_E] + [K_g]. \tag{3.65}$$

3.4 PROGRAM DEVELOPMENT

The codes for building the full linear FE model (Eq. (3.55) and Eq. (3.57)) and the full nonlinear FE model (Eq. (3.56) and Eq. (3.57)) of the piezoelectric tube actuator are programmed by the engineering software MATLAB R2010a. The Hankel singular values of the full nonlinear FE model (Eq. (3.56) and Eq. (3.57)) is determined by MATLAB command "hankelsv". The order reduction is then performed by MATLAB command "schurmr", and the reduced order linear FE model (Eq. (3.63) and Eq. (3.65)) and the reduced order nonlinear FE model (Eq. (3.62b) and Eq. (3.63)) are obtained. The simulation is carried out by MATLAB/SIMULINK 7.5. The connection of the blocks of the plant model is shown in Fig G-1 in Appendix F. For simulation of reduced order nonlinear FE model, Eq. (3.62a) and Eq. (3.63) are implemented into "State-Space" block. Eq. (3.16a)-(3.16c) and Eq. (3.17) are implemented into "Hysteresis" block. Eq. (3.11) and Eq. (3.12) are implemented into "Creep" Block. The fifth order ode15s solver (Shampine and Reichelt, 1997) which is a code of numerical differentiation formulas with backwards differences is chosen. It is efficient to solve stiff model.

Stiff model means the difference between the maximum and the minimum value of the absolute of the real part of the eigenvalue of the system is large. In the FE model developed in the thesis, the difference is up to a magnitude of 10^5 times.

If a solver not specifically tackling stiff system is used, for example, all the fixed step solvers, the time required for the simulation is very long.

The step size of the ode15s solver is variable and the minimum step size is set as 0.1 μs. This setting can increase simulation speed and does not cause numerical instability. However, the sampling time of an experiment can be larger than the step size in simulation. For example, the maximum settling time of the D/A converter of dSPACE PCI Controller Card DS1104 is 10 μs. The sampling time is limited by this maximum settling time (if the computational time is short enough). Since the sampling time (10 μs) is larger than the minimum step size (0.1 μs) in the simulation (numerical instability may occur when the minimum step size is set as 10 μs), the controller performs less effectively in the experiment than in the simulation. Larger errors and lower stability may be observed in the experiment.

3.5 PARAMETER IDENTIFICATION AND VALIDATION

In this section, the Rayleigh constants, the parameters of the Kelvin-Voigt creep operators and the parameters of the Prandtl-Ishlinskii hysteresis operators are identified by choosing appropriate values of parameters in order that the simulation results were close to the experimental results. The experimental results are obtained from the literature (Leang and Devasia, 2007). It is remarked that single input (X input) and single output (X displacement) are used only for parameter identification and validation.

3.5.1 Rayleigh Constants

The step response of the full linear FE model (Eq. (3.55) and Eq. (3.57)) shows fairly good agreement with the experimental result obtained from Leang and Devasia (2007) as shown in Fig. 3-5 when Rayleigh constants are selected as $\alpha = 1.8$ and $\beta = 6 \times 10^{-7}$. The reason for using linear FE model to identify the Rayleigh constants is that the parameters of the Kelvin-Voigt creep operators and the parameters of the Prandtl-Ishlinskii hysteresis operators are not yet identified. The creep and hysteresis phenomena are not dominant with step input in short time.

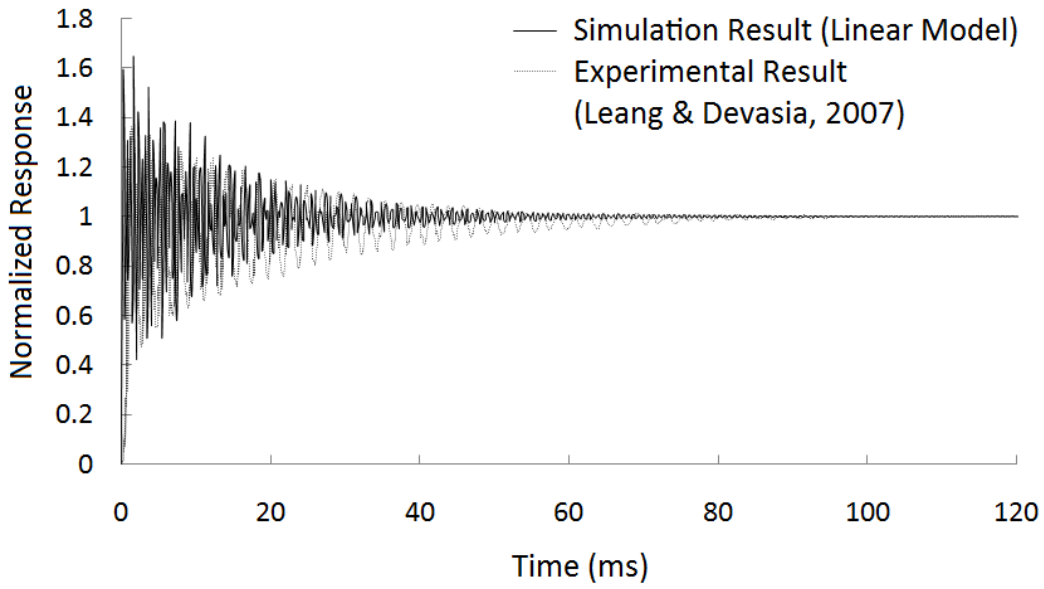

Figure 3-5. Step Response of Linear FE Model in Short Time

3.5.2 Parameters of Kelvin-Voigt Creep Operator

The static gain of the full linear FE model (Eq. (3.55) and Eq. (3.57)) is determined as 3.37 nm/V by step response. The block diagram of the open loop system is shown in Fig. 3-6. The input signal is given:

$$[u_E] = \begin{bmatrix} V_{EX} \\ V_{EY} \end{bmatrix} = \begin{bmatrix} r_X \times k_{ff} \\ r_Y \times k_{ff} \end{bmatrix}, \tag{3.66}$$

where r_X and r_Y denote the desired X displacement and the desired Y displacement respectively. k_{ff} denotes feedforward gain of the open loop system. k_{ff} = 1/3.37 = 0.30 V/nm. It is remarked that the block diagram shown in Fig. 3-6 is for MIMO system. For SISO system, r_Y is simply set to zero.

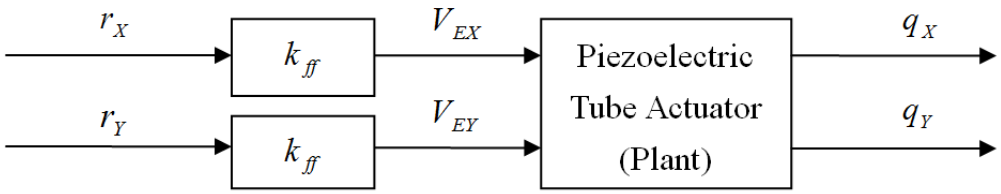

Figure 3-6. Block Diagram of Open Loop System

The simulation of full nonlinear FE model (Eq. (3.56) and Eq. (3.57)) is performed with step input in extended time. In extended time, creep is dominant. It is reasonable to set the undetermined parameters of Prandtl-Ishlinskii hysteresis operators to zero. Superposition of three Kelvin-Voigt creep operators is adopted in the simulation. It is shown in Fig. 3-7 that the simulation result matches with the experimental one obtained from Leang and Devasia (2007). The proportional

constants of creep operator a_f and the weighting factors of creep operator w_f adopted in the simulation are shown in Table 3-2.

Table 3-2. Parameters of Kelvin-Voigt Creep Operators

w_1	0.15	a_1	-1.78×10^{-6}
w_2	5.00×10^{-3}	a_2	-8.57×10^{-7}
w_3	3.80×10^{-4}	a_3	-1.70×10^{-6}

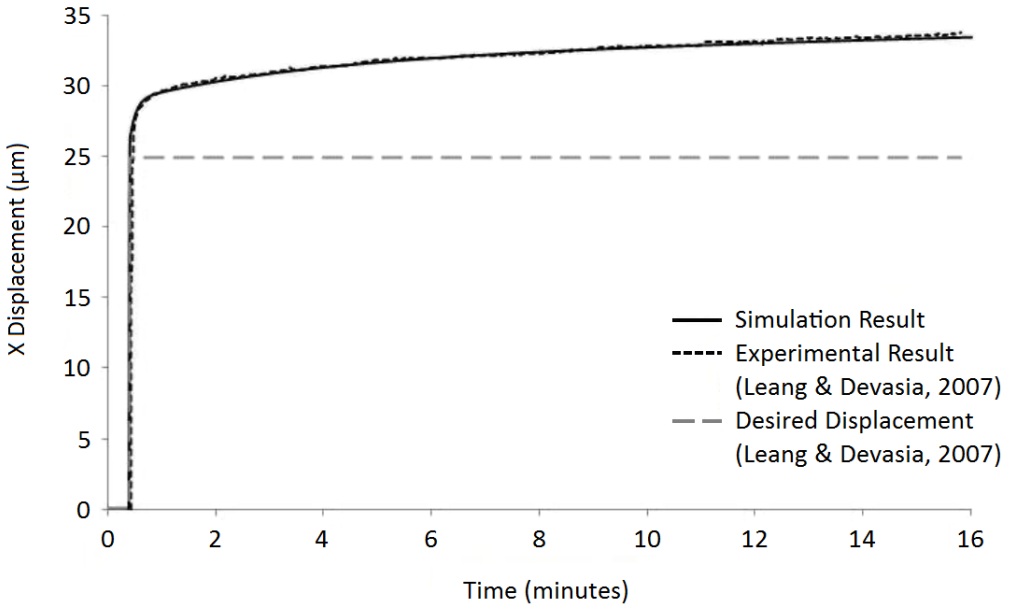

Figure 3-7. Step Response of Nonlinear FE Model in Extended Time

The analytic static gain of a piezoelectric tube actuator with double-actuation can be calculated by the following equation (Chen, 1992):

$$k_o = \frac{q_x}{V_{EX}} = \frac{\sqrt{2}d_{31}h^2}{\pi r_{inner}t_{wall}}, \tag{3.67}$$

where k_o denotes the analytic static gain (m/V). h and t_{wall} denote the height and the wall thickness of the piezoelectric tube actuator respectively (m). d_{31} denotes the piezoelectric coefficient of r direction to z direction relation (m/V).

d_{31} is equivalent to e_{31} shown in Eq. (3.20b) but they are in different units. By experiment, d_{31} is found as 1.05×10^{-10} m/V (Chen, 1992). Therefore, the static gain k_o is calculated as 4.99 nm/V by experiment result. It is fairly agreed with the static gain of the full nonlinear FE model (Eq. (3.56) and Eq. (3.57)) which is found as 4.51 nm/V by the step response shown in Fig. 3-7. It is remarked that the static gain of full nonlinear FE model (Eq. (3.56) and Eq. (3.57)) varies with time and 4.51 nm/V is determined by its maximum value.

3.5.3 Parameters of Prandtl-Ishlinskii Hysteresis Operators

The simulation of the full nonlinear FE model (Eq. (3.56) and Eq. (3.57)) is performed with periodic input. Hysteresis is dominant with periodic input. Superposition of eight Prandtl-Ishlinskii hysteresis operators is adopted in the simulation. Superposition of three Kelvin-Voigt creep operators with parameters determined in Section 3.5.2 is also adopted in the simulation. It is shown in Fig. 3-8 that the simulation result matches with the experimental one obtained from Leang and Devasia (2007). The threshold values κ_j and the proportional constants of Prandtl-Ishlinskii hysteresis operators b_j adopted in the simulation are shown in Table 3-3.

Table 3-3. Parameters of Prandtl-Ishlinskii Hysteresis Operators

κ_1	700	κ_5	3892
κ_2	1498	κ_6	4690
κ_3	2296	κ_7	5488
κ_4	3094	κ_8	6300
b_1 to b_8	-1.94×10^{-6}		

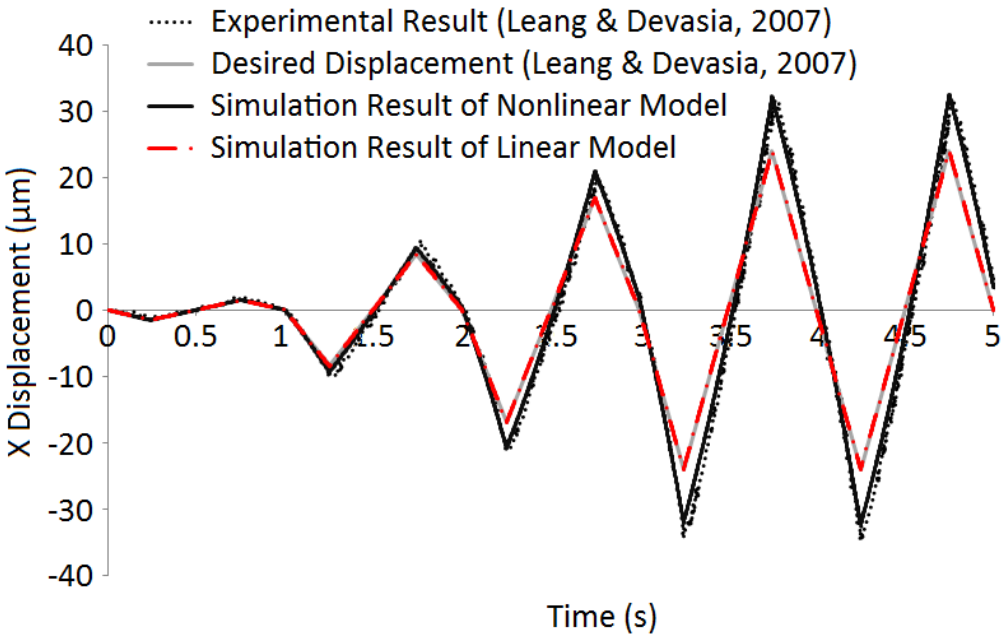

Figure 3-8. Response of Nonlinear FE Model with Periodic Input

3.5.4 FULL MODEL VALIDATION

For validation, the root-mean-square error (RMSE) between the displacement of the full nonlinear FE model (Eq. (3.56) and Eq. (3.57)) and the experimental result obtained from Leang and Devasia (2007) is determined as 0.362 μm. The RMSE is defined as:

$$RMSE = \sqrt{\frac{\sum_{n_e=1}^{N_e} e_{n_e}^2 \times \Delta k_{n_e}}{\sum_{n_e=1}^{N_e} \Delta k_{n_e}}}, \tag{3.68}$$

where e_{n_e} denotes error at the n_e-th time step, Δk_{n_e} denotes the time interval of the n_e-th time step and N_e denotes total number of time step. For comparison, the simulation result of the full linear FE model (Eq. (3.55) and Eq. (3.57)) is also plotted in Fig. 3-8. It is observed that the simulation result of the full nonlinear FE model (Eq. (3.56) and Eq. (3.57)) is closer to the simulation result obtained from Leang and Devasia (2007) than that of the full linear FE model (Eq. (3.55) and Eq. (3.57)). The RMSE of the full nonlinear FE model (Eq. (3.56) and Eq. (3.57)) (0.362 μm) is much smaller than that of the full linear FE model (Eq. (3.55) and Eq. (3.57)) (4.021 μm). It reveals that the full nonlinear FE model (Eq. (3.56) and Eq. (3.57)) is more accurate than the full linear FE model (Eq. (3.55) and Eq. (3.57)).

3.6 MODEL REDUCTION

The full FE nonlinear model (Eq. (3.56) and Eq. (3.57)) has 1728 states in state space form. It is necessary to reduce its order so that it is available for controller design and simulation purposes.

3.6.1 PROCEDURES

The first step of the model reduction process is to find the Hankel singular value of each state of the state space model. It can be performed by the MATLAB command “hankelsv”. The singular values of the states of the full nonlinear FE model (Eq. (3.56) and Eq. (3.57)) are plotted in Fig. 3-9 (1-st – 106-th states are shown only). Discarding a state with large Hankel singular value causes large modelling error. By observing the Hankel singular values (Fig. 3-9), it is safe to retain 40 states (1688 states discarded) in order that the modelling error is kept small. The second step is to use the balanced model truncation via Schur method to reduce the order of the state space model. It can be performed by the MATLAB command “schurmr”.

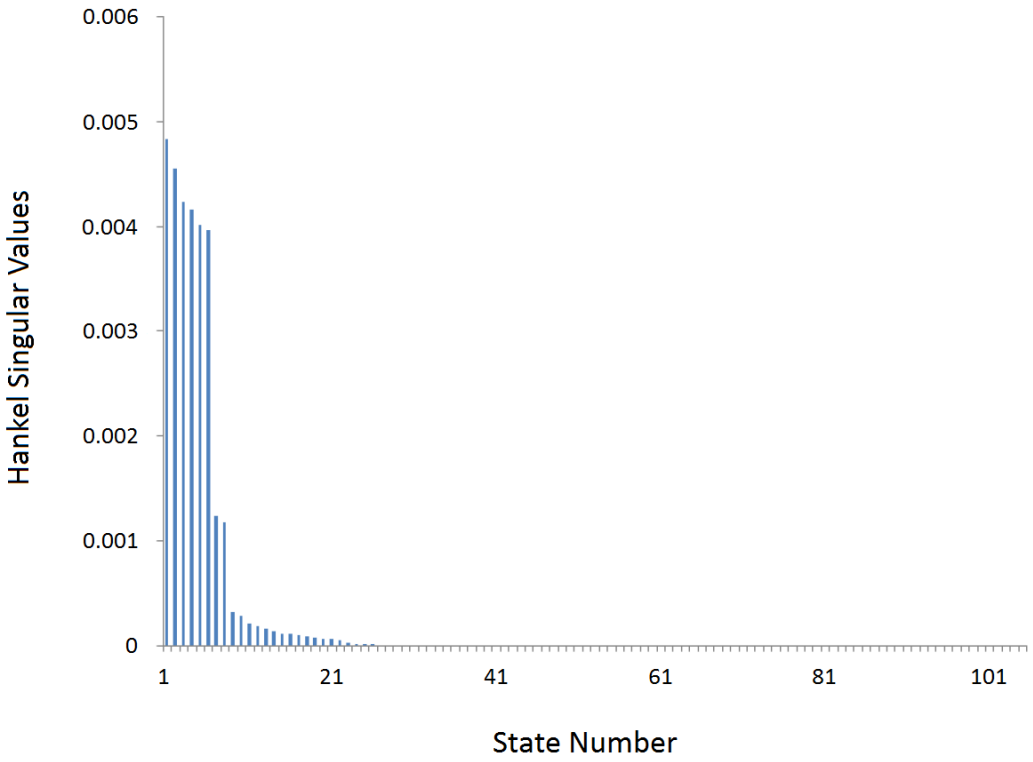

Figure 3-9. Hankel Singular Values of Full Nonlinear FE Model

3.6.2 REDUCED ORDER MODEL VALIDATION

Totally, seven different retained sizes, 10, 15, 20, 25, 30, 35 and 40, were tried. The displacement of the reduced order nonlinear FE models (Eq. (3.62b) and Eq. (3.63)) with different number of retained states and the displacement of the full nonlinear FE model (Eq. (3.56) and Eq. (3.57)) are plotted in Fig. 3-10a and Fig. 3-10b for comparison. For validation, the RMSEs between the displacement of the reduced order nonlinear FE models (Eq. (3.62b) and Eq. (3.63)) with different number of retained states and that of the full order nonlinear FE model (Eq. (3.56) and Eq. (3.57)) are shown in Table 3-4. It is observed that the reduced order nonlinear FE model (Eq. (3.62b) and Eq. (3.63)) with 35 retained states has the smallest RMSE (0.044 μm) and the reduced order nonlinear FE model (Eq. (3.62b)

and Eq. (3.63)) with 20 retained states has the second smallest RMSE (0.099 μm). Hence, the reduced order nonlinear FE models (Eq. (3.62b) and Eq. (3.63)) with 20 or 35 retained states are accurate enough for simulation and controller design.

Table 3-4. RMSE of Reduced Order Nonlinear FE Models with Different Number of Retained States

No. of States Retained	10	15	20	25	30	35	40
RMSE (μm)	0.259	0.940	0.099	0.540	0.170	0.044	0.125

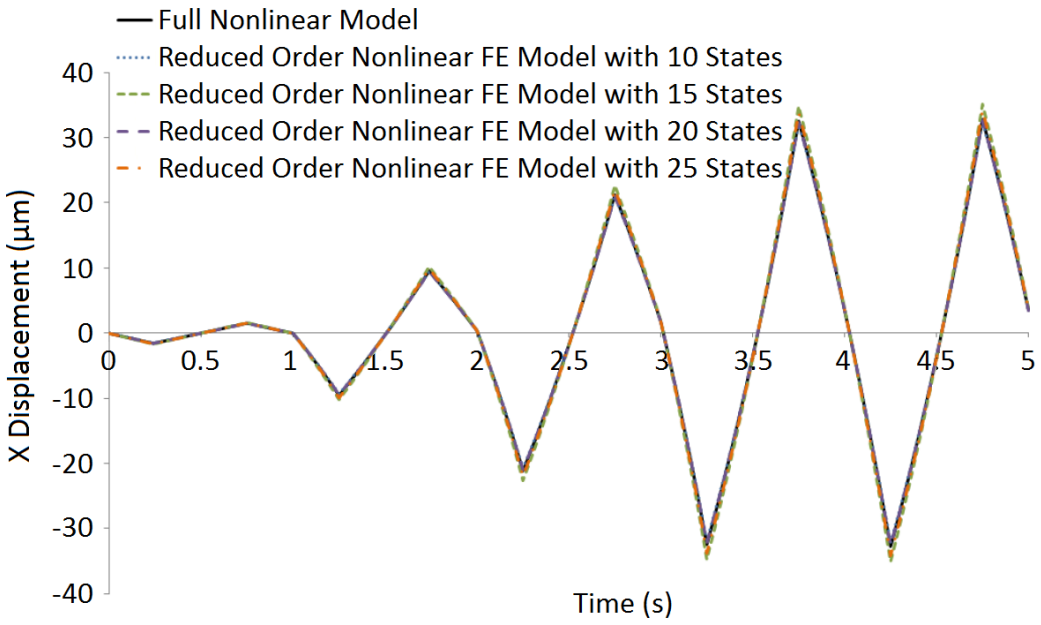

Figure 3-10a. Simulations of Reduced Order Nonlinear FE Models with Different Number of Retained States (10 States – 25 States)

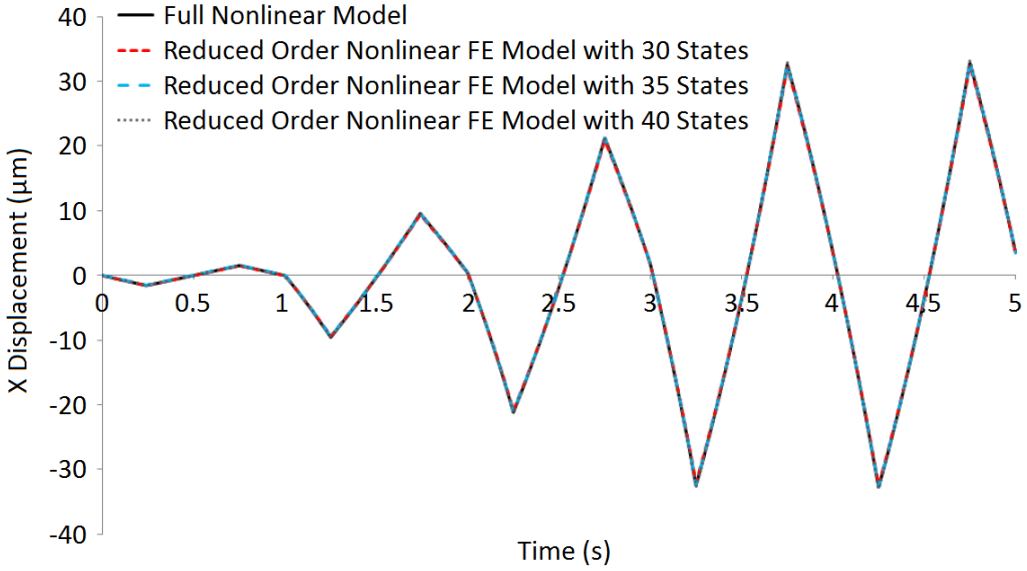

Figure 3-10b. Simulations of Reduced Order Nonlinear FE Models with Different Number of Retained States (30 States – 40 States)

In the Table 3-4, there is a big difference between the reduced order system with 30 states and 35 states. According to the balanced model truncation via Schur method (Safonov and Chiang, 1989), the error between the full order transfer function and the reduced order transfer function $[E_G] \in \Re^{2\times 2}$ is bounded such that:

$$\|[E_G]\| = \left\|[G_{transfer}] - [\tilde{G}_{transfer}]\right\| \le 2\sum_{n+1}^{fo} \sigma_{eig,i}(P_r Q_o), \tag{3.69a}$$

where

$$[G_{transfer}] = [D_s] + [C_s]\{[I]s - [A_s]\}^{-1}[B_s] \tag{3.69b}$$

$$[\tilde{G}_{transfer}] = [D] + [C]\{[I]s - [A]\}^{-1}[B_n] \tag{3.69c}$$

$$\sigma_{eig,i}(P_r Q_o) \ge 0\,. \tag{3.69d}$$

$[G_{transfer}] \in \Re^{2\times 2}$ denotes the full order transfer function. $[\tilde{G}_{transfer}] \in \Re^{2\times 2}$ denotes the reduced order transfer function. Eq. (3.69a) shows that the bound is larger with smaller order of the reduced order system n. Since the norm of the error $\|[E_G]\|$

can be any value within the bound, an extreme case may exist such that for the reduced order system with an order n_1, the norm of the error $\|[E_G]\|$ is close to the bound while for the other reduced order system with order n_2 which $n_2 \neq n_1$, the norm of the error $\|[E_G]\|$ is close to the zero. This reason accounts for the big difference observed in Table 3-4.

As a remark, the magnitude of the inputs used in the simulations should be correct since the comparisons indicate that both the static gain (Section 3.5.2) and the displacement output (Section 3.5.4 and Section 3.6.2) of the nonlinear FE model are close to the experimental results from other researchers (Chen, 1992; and Leang and Devasia, 2007).

3.7 SUMMARY

The works of this chapter are summarized as follows:

(i) A nonlinear FE model has been developed through discretization, implementation of the Kelvin-Voigt creep operators and the Prandtl-Ishlinskii hysteresis operators, energy approach, Hamilton's principle and globalization in sequence.

(ii) The Rayleigh constants, the parameters of Kelvin-Voigt creep operators and the parameters of the Prandtl-Ishlinskii hysteresis operators are identified by comparing the simulation result with the experimental one obtained from Leang and Devasia (2007).

(iii) The full nonlinear FE model (Eq. (3.56) and Eq. (3.57)) is validated by means of a periodic input. The RMSE between the response of full nonlinear FE model (Eq. (3.56) and Eq. (3.57)) and the experimental result obtained from Leang and Devasia (2007) is 0.362 μm.

(iv) The reduced order nonlinear FE models (Eq. (3.62b) and Eq. (3.63)) are obtained by the balanced model truncation via Schur method. Again, they are validated using a periodic input. The RMSE between the simulation result of the full nonlinear FE model (Eq. (3.56) and Eq. (3.57)) and the simulation result of the reduced order nonlinear FE model (Eq. (3.62b) and Eq. (3.63)) with 20 retained states is 0.099 μm. The RMSE between the full nonlinear FE model (Eq. (3.56) and Eq. (3.57)) and the reduced order nonlinear FE model (Eq. (3.62b) and Eq. (3.63)) with 35 retained states is 0.044 μm. These reduced order nonlinear FE models (Eq. (3.62b) and Eq. (3.63)) are accurate enough for controller design and simulation purposes.

CHAPTER 4

PERFORMANCE OF TYPICAL CONTROLLERS

4.1 INTRODUCTION

It has been discussed that coupling effect, creep and hysteresis of the piezoelectric tube actuator induce tracking error, hence, image distortion occurs. Since AFMs are originally not equipped with controller, it is important to investigate open loop error caused by coupling effect, creep and hysteresis in the scanning operation of the piezoelectric tube actuator in AFM. For several models of AFM (e.g. Dimension Icon Atomic Force Microscope manufactured by Veeco), typical controller (e.g. The NanoScope V-PI controller manufactured by Veeco) is served as an add-in component for tracking improvement. Controller can modify the dynamic properties of a closed loop system in order that the output response of the closed loop system can be altered. The typical controllers which are PI controller and OFC applied on the piezoelectric tube actuator with coupling effect, creep and hysteresis are chosen for performance investigation in this research. Their performance will be compared with the performance of the ASMC in Chapter 5 to determine which controller is most suitable for AFM.

4.2 SIMULATION CONDITIONS

In AFM, the piezoelectric tube actuator scans a sample surface in raster pattern by running a zigzag path (Moheimani, 2008). The desired X displacement and the desired Y displacement should be a triangular pattern (Fig. 4-1) and a pseudo-step (Fig. 4-2) respectively in order that the piezoelectric tube actuator scans in zigzag path. In the simulation, the piezoelectric tube actuator scans a sample surface area 24 μm × 24 μm with a moderate frequency 1 Hz normally used in practice. It is remarked that only first ten periods are simulated. The reduced order nonlinear FE model (Eq. (3.62b) and Eq. (3.63)) with 35 retained states is used for the plant model in simulation. The term, covering angle, should be stated to represent the degree of electrode dislocation. The covering angle is defined as the angle which the outer electrode covers the circumference of the piezoelectric tube actuator. It is illustrated in Fig. 4-3. Θ_{+X}, Θ_{-X}, Θ_{+Y} and Θ_{-Y} are the covering angle of +X, –X, +Y and –Y electrode respectively. It is noted that the simulations are based on the assumptions and conditions stated in Chapter 3.

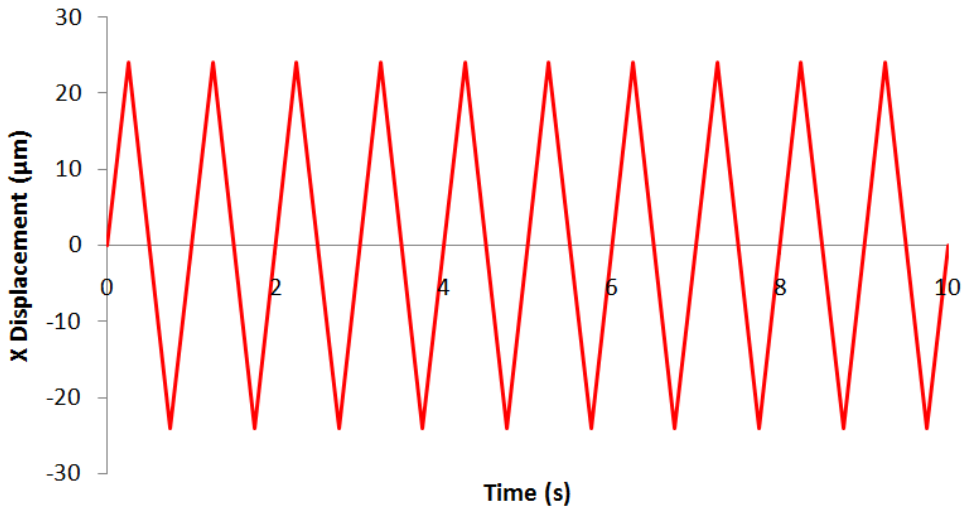

Figure 4-1. Desired X Displacement

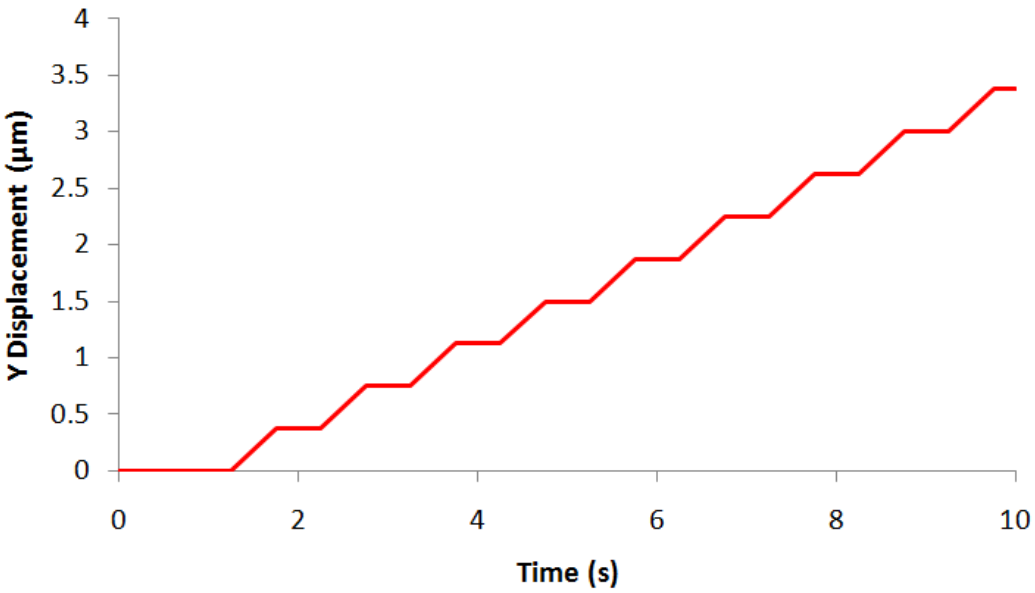

Figure 4-2. Desired Y Displacement

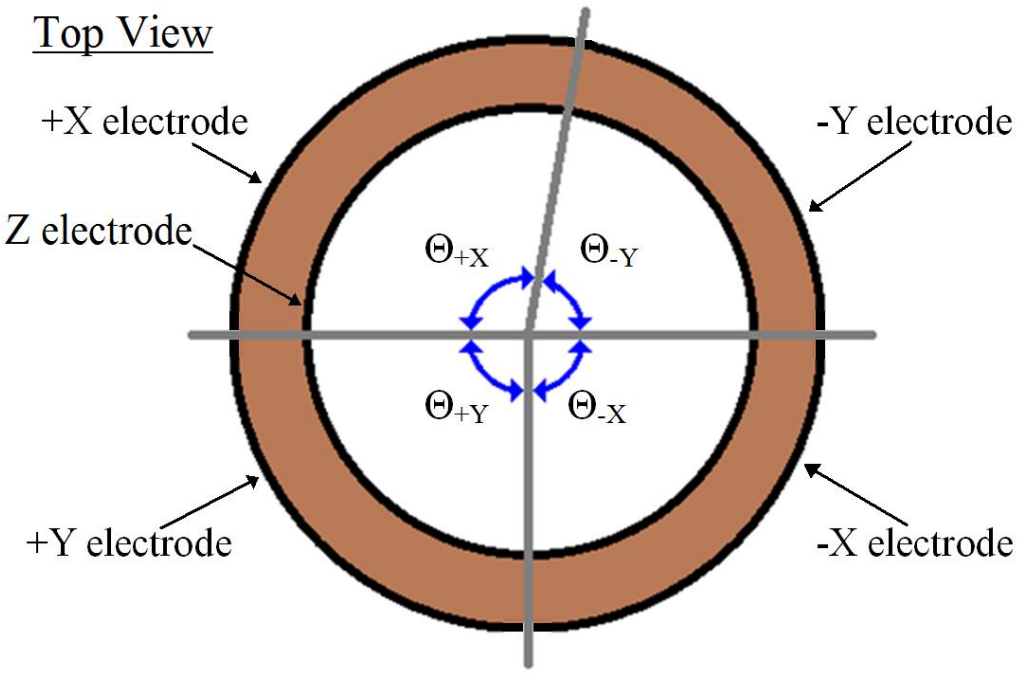

Figure 4-3. Illustration of Covering Angles

4.3 SIMULATION RESULTS OF OPEN LOOP SYSTEM

4.3.1 Effect of Creep and Hysteresis

In this section, the effects of creep and hysteresis on scanning operation of the open loop piezoelectric tube actuator without electrode dislocation (covering angles Θ_{+X} = 90˚, Θ_{-X} = 90˚, Θ_{+Y} = 90˚ and Θ_{-Y} = 90˚) are investigated. The block diagram of the open loop system is shown in Fig. 3-7.

The X input and the Y input to the open loop nonlinear system without electrode dislocation are shown in Fig. 4-4 and Fig. 4-5 respectively. The X displacement and the Y displacement of the open loop nonlinear system without electrode dislocation are shown in Fig. 4-6 and Fig. 4-7 respectively. The tracking error of the open loop nonlinear system without electrode dislocation in X direction (X error) and in Y direction (Y error) are shown in Fig. 4-8 and Fig. 4-9 respectively. The RMSE in X direction (X RMSE) and in Y direction (Y RMSE) are shown in Table 4-1. For convenience, the tracking error in X direction is simply called X error and the tracking error in Y direction is simply called Y error. The RMSE in X direction is simply called X RMSE and the RMSE in Y direction is simply called Y RMSE.

Table 4-1. RMSE of Open Loop Nonlinear System

	X RMSE (μm)	Y RMSE (μm)
Open Loop Nonlinear System without Electrode Dislocation	5.693	0.259
Open Loop Nonlinear System with Electrode Dislocation	5.619	0.678

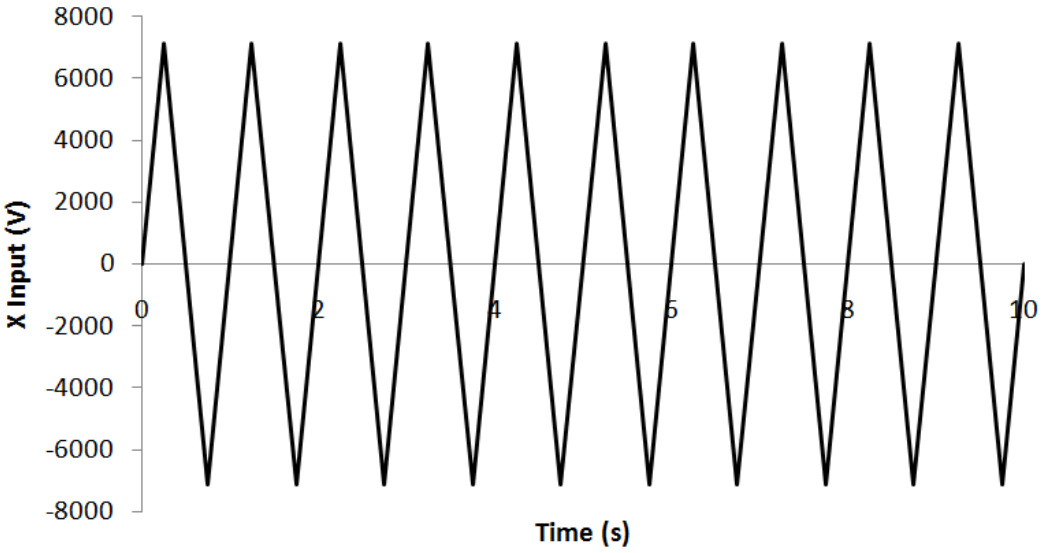

Figure 4-4. X Input to Open Loop Nonlinear System

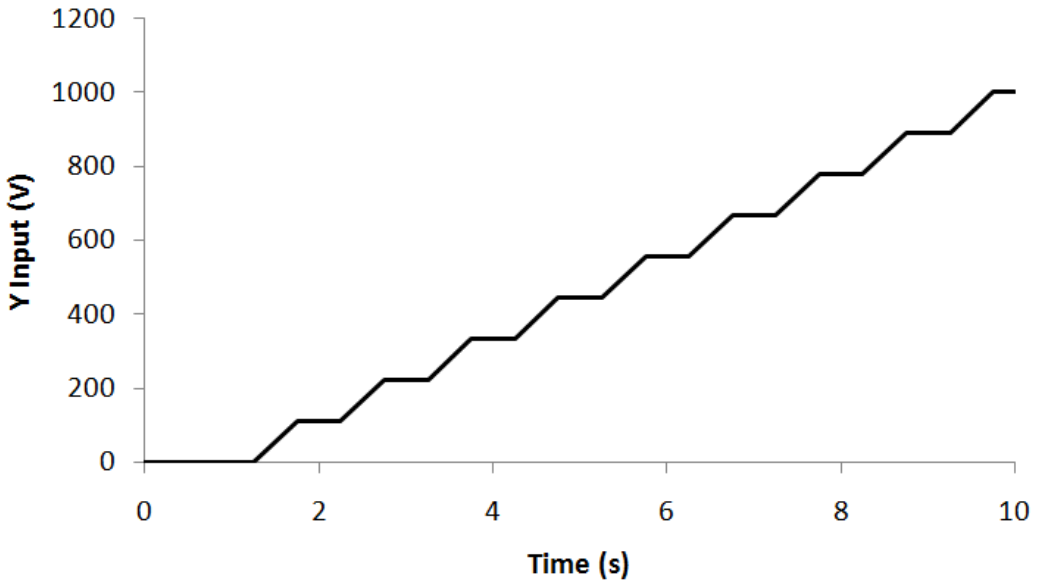

Figure 4-5. Y Input to Open Loop Nonlinear System

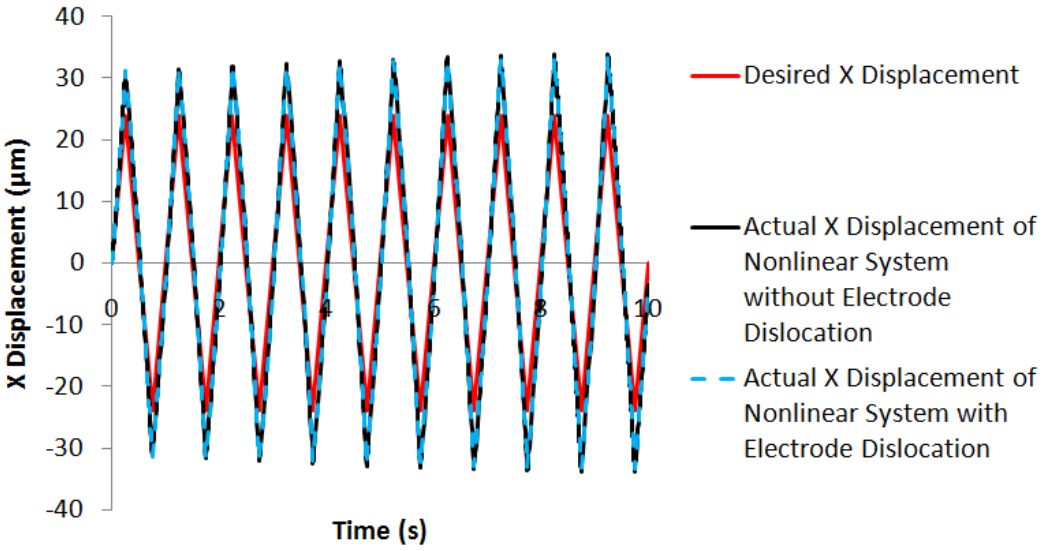

Figure 4-6. X Displacements of Open Loop Nonlinear System

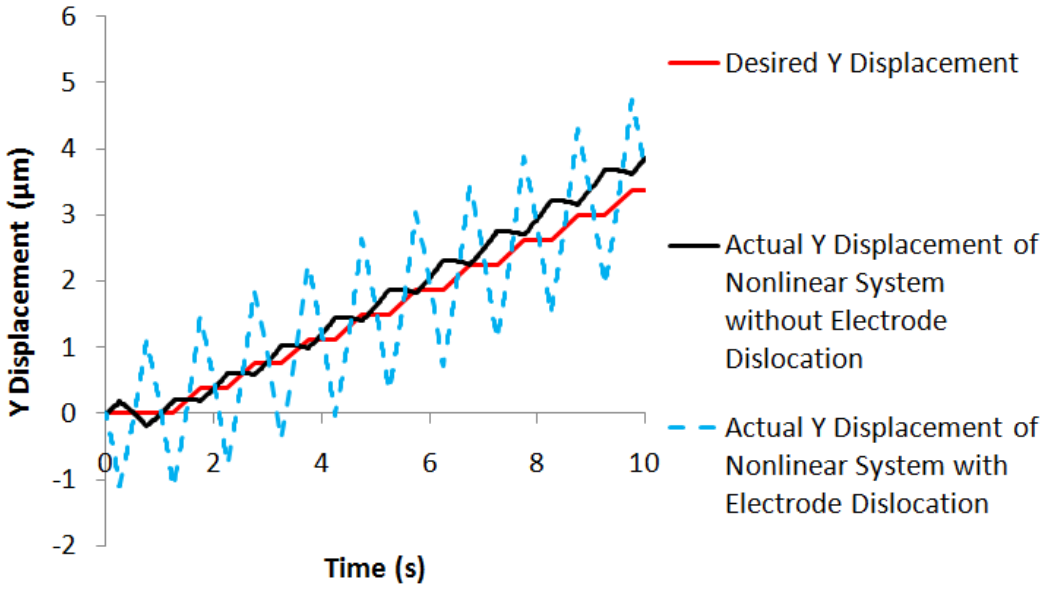

Figure 4-7. Y Displacements of Open Loop Nonlinear System

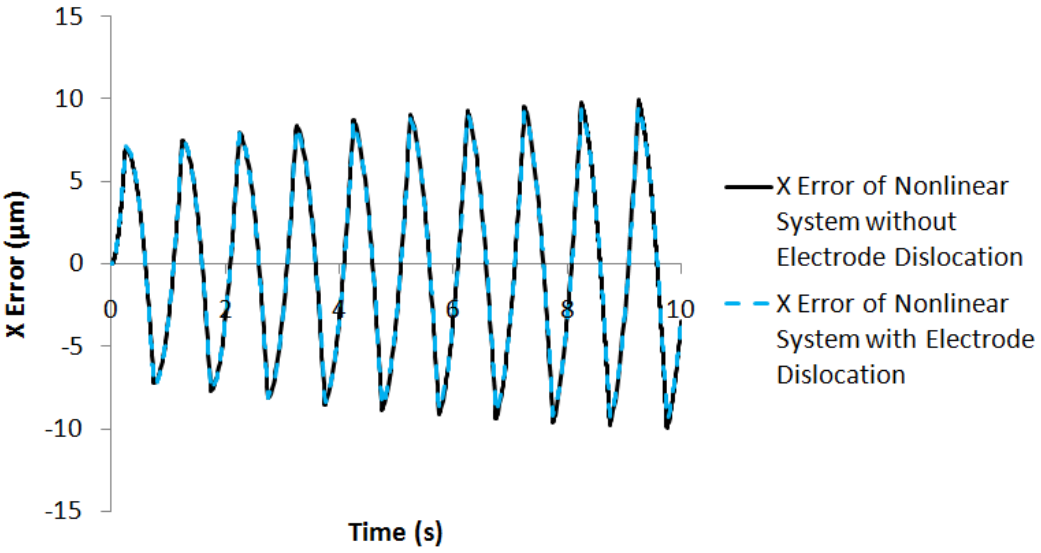

Figure 4-8. X Errors of Open Loop Nonlinear System

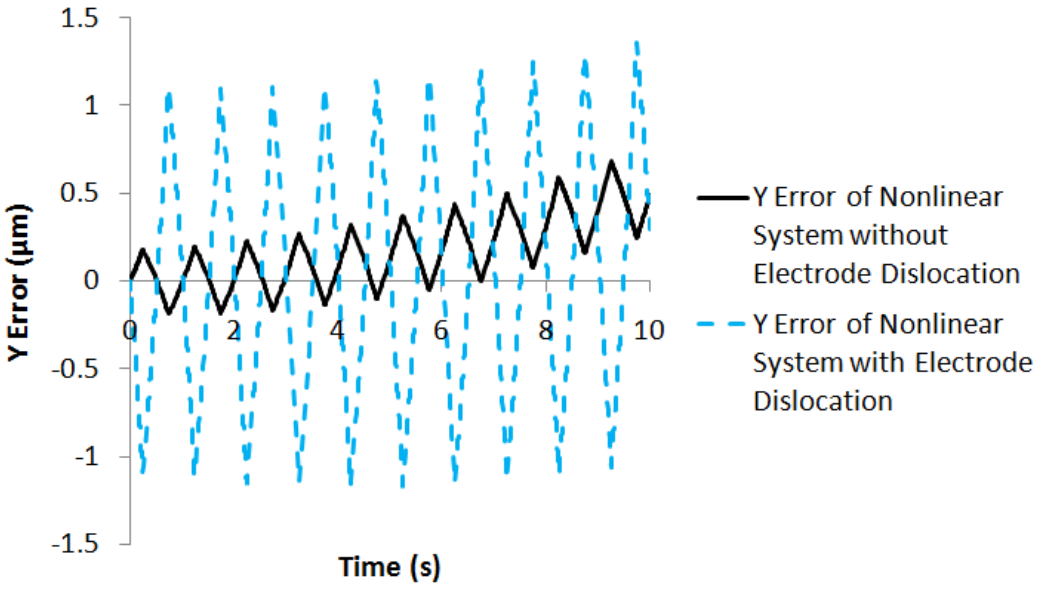

Figure 4-9. Y Errors of Open Loop Nonlinear System

Hysteresis is dominated in periodic input. In Fig. 4-6, it is observed that the X displacement of the open loop nonlinear system without electrode dislocation is larger than the desired X displacement due to hysteresis. In Fig. 4-8, it is observed that the X error of the open loop nonlinear system without electrode dislocation is in wave pattern. It implies that the X displacement of the open loop nonlinear system without electrode dislocation is distorted to wave pattern which is also due to hysteresis. Therefore, hysteresis causes the system gain to become larger and varying. In Table 4-1, the X RMSE of the open loop nonlinear system without electrode dislocation is 5.693 μm which is mainly due to hysteresis.

In Fig. 4-7, it is observed that the trajectory of the open loop nonlinear system without electrode dislocation in Y direction goes away from the desired Y displacement. Therefore, in Fig. 4-9, it is observed that the Y error of the open loop nonlinear system without electrode dislocation increases with time. The observed phenomenon is due to creep. Creep causes the system gain increases with time. In Table 4-1, the Y RMSE of the open loop nonlinear system without electrode dislocation is 0.259 μm which is mainly caused by creep. Although the Y RMSE is not large, the tracking error is significant when the scanning lasts long because creep causes the Y error of the open loop nonlinear system without electrode dislocation to increase in positive direction as shown in Fig. 4-9.

In Fig. 4-8, it is observed that the X error of the open loop nonlinear system without electrode dislocation diverges. In addition, it is observed from Fig. 4-9 that the Y error of the open loop nonlinear system without electrode dislocation increases in positive direction due to creep as mentioned before. It is revealed that

the open loop nonlinear system without electrode dislocation is unstable in both X direction and Y direction.

4.3.2 Coupling Effect

In this section, the coupling effect during scanning operation of the open loop piezoelectric tube actuator in AFM is investigated. The simulation is performed based on the open loop nonlinear model with electrode dislocation (Θ_{+X} = 100˚, Θ_{-X} = 90˚, Θ_{+Y} = 90˚ and Θ_{-Y} = 80˚).

The simulation results are plotted together with the desired outputs and the output responses of the open loop nonlinear system without electrode dislocation for comparison. The simulation in this section applies the same inputs used in Section 4.2.1 (the X input and the Y input shown in Fig. 4-4 and Fig. 4-5 respectively) to the open loop nonlinear model with electrode dislocation. The X displacement and the Y displacement of the open loop nonlinear system with electrode dislocation are shown in Fig. 4-6 and Fig. 4-7 respectively. The X error and the Y error of the open loop nonlinear system with electrode dislocation are shown in Fig. 4-8 and Fig. 4-9 respectively. The X RMSE and the Y RMSE of the open loop nonlinear system with electrode dislocation are shown in Table 4-1.

In Fig. 4-6, it is observed that the X displacement of the open loop nonlinear system with electrode dislocation is similar to that of the open loop nonlinear system without electrode dislocation. In Table 4-1, the X RMSE of the open loop

nonlinear system with electrode dislocation (5.619 μm) is close to that of the open loop nonlinear system without electrode dislocation (5.693 μm). In Fig. 4-7, it is observed that the Y displacement of the open loop nonlinear system with electrode dislocation exhibits triangular pattern which is due to coupling effect. In Fig. 4-11, it is observed that the peak-to-peak amplitude of the triangular pattern of the Y error of the open loop nonlinear system with electrode dislocation (2.3 μm) is larger than that of the open loop nonlinear system without electrode dislocation (0.4 μm). It is shown that the coupling effect from Y-axis to X-axis is unobvious but that from X-axis to Y-axis is significant. It is because the magnitude of the X input is about an order of magnitude larger than that of the Y input. In Table 4-1, the Y RMSE of the open loop nonlinear system with electrode dislocation (0.678 μm) is larger than that of the open loop nonlinear system without electrode dislocation (0.259 μm).

In Fig. 4-8, it is observed that the X error of the open loop nonlinear system with electrode dislocation diverges. In addition, it is observed from Fig. 4-9 that the Y error of the open loop nonlinear system with electrode dislocation increases in the positive direction. Therefore, the open loop nonlinear system with electrode dislocation is unstable in both X direction and Y direction. As a remark, it is observed in Fig. 4-7 that the Y displacement of the open loop nonlinear system without electrode dislocation also exhibits triangular pattern but the amplitude is smaller than that of the open loop nonlinear system with electrode dislocation. The coupling effect exhibiting in the open loop nonlinear system without electrode dislocation is due to deformation of the piezoelectric tube actuator. Based on the significant errors and instability in both X direction and Y direction, it is concluded

that the performance of the open loop nonlinear system is unsatisfactory.

4.4 SIMULATION RESULTS OF CLOSED LOOP SYSTEM USING TYPICAL CONTROLLERS

4.4.1 Proportional-Integral Controller

In this section, the performance of the PI controller on the piezoelectric tube actuator with electrode dislocation is assessed. The control law of the PI controller is given (Ogata, 2001):

$$V_{EX} = P_X e_X + I_X \int_0^t e_X d\tau , \tag{4.1a}$$

where

$$e_X = r_X - q_X , \tag{4.1b}$$

and

$$V_{EY} = P_Y e_Y + I_Y \int_0^t e_Y d\tau , \tag{4.2a}$$

where

$$e_Y = r_Y - q_Y , \tag{4.2b}$$

where P_X and P_Y are the proportional gains of the PI controller for tracking in X direction and Y direction respectively. I_X and I_Y are the integral gains of the PI controller for tracking in X direction and Y direction respectively. e_X and e_Y are X error and Y error respectively. The block diagram of the PI controller is shown in Fig. 4-10. The proportional term of the proportional-integral controller allows

changing the location of the closed loop system poles in order that the closed loop system dynamics can be modified. The integral term of the proportional-integral controller improves the steady state error. The derivative term is not implemented into the proportional-integral controller because the desired X displacement is in triangular pattern. Differentiating at the sharp corner induces very high input which causes large vibration, excites unmodelled dynamics and may even cause instability. Because different piezoelectric tube actuator has various covering angle and covering angle is considered as unknown, it is objective to tune the PI controller based on the reduced order nonlinear FE model (Eq. (3.62b) and Eq. (3.63)) without electrode dislocation. The PI controller gains are tuned by trial-and-error method. Then the PI controller with fine tuned gains is applied to the reduced order nonlinear FE model (Eq. (3.62b) and Eq. (3.63)) with electrode dislocation for investigation.

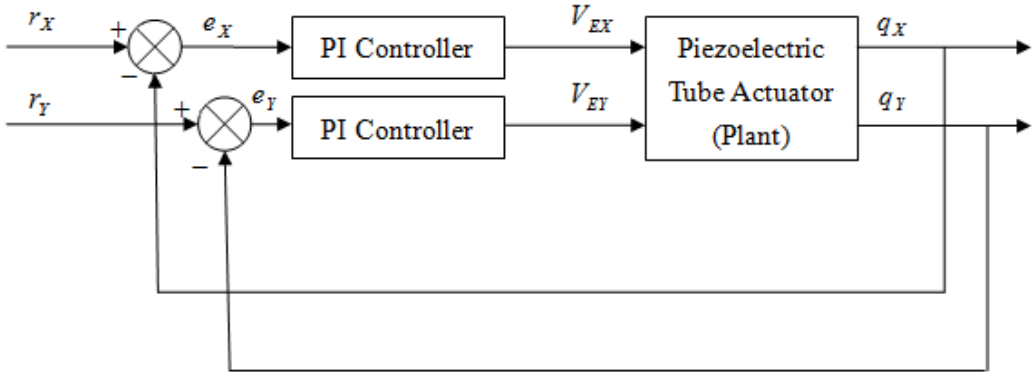

Figure 4-10. Block Diagram of Closed Loop System using PI Controller

Six sets of different PI controller gains (Set 1 – 6) and corresponding X RMSE and Y RMSE of the closed loop nonlinear model without electrode dislocation using the PI controller are shown in Table 4-2. The X inputs and the Y inputs to the

closed loop nonlinear system without electrode dislocation using the PI controller generated by Eq. (4.1a) and Eq. (4.2a) are shown in Fig. 4-11 and Fig. 4-12 respectively. The X displacements and the Y displacements of the closed loop nonlinear system without electrode dislocation using the PI controller are shown in Fig. 4-13 and Fig. 4-14 respectively. The X errors and the Y errors of the closed loop nonlinear system without electrode dislocation using the PI controller are shown in Fig. 4-15 and Fig. 4-16 respectively.

Table 4-2. Settings of PI Controller and Corresponding RMSEs of Closed Loop Nonlinear System without Electrode Dislocation

Set	P_X $\times 10^6$	I_X $\times 10^3$	P_Y $\times 10^6$	I_Y $\times 10^3$	X RMSE (μm)	Y RMSE (μm)
1	50	1	50	1	11.437	1.581
2	80	1	80	1	10.110	1.446
3	100	1	100	1	9.560	1.350
4	300	1	300	1	6.087	0.874
5	600	1	600	1	3.882	0.572
6	1000	1	1000	1	2.587	0.391

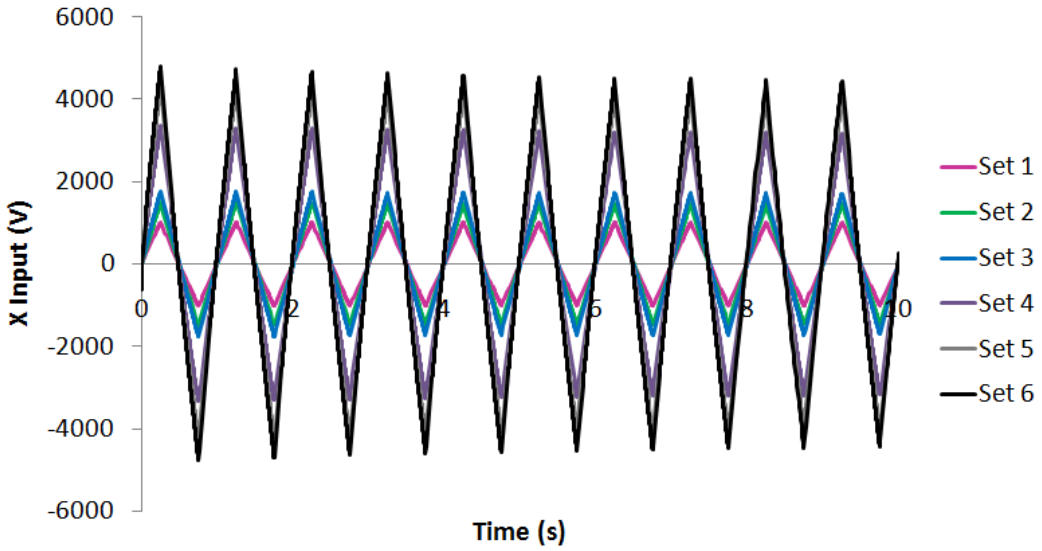

Figure 4-11. X Inputs of Closed Loop Nonlinear System without Electrode Dislocation using PI Controller

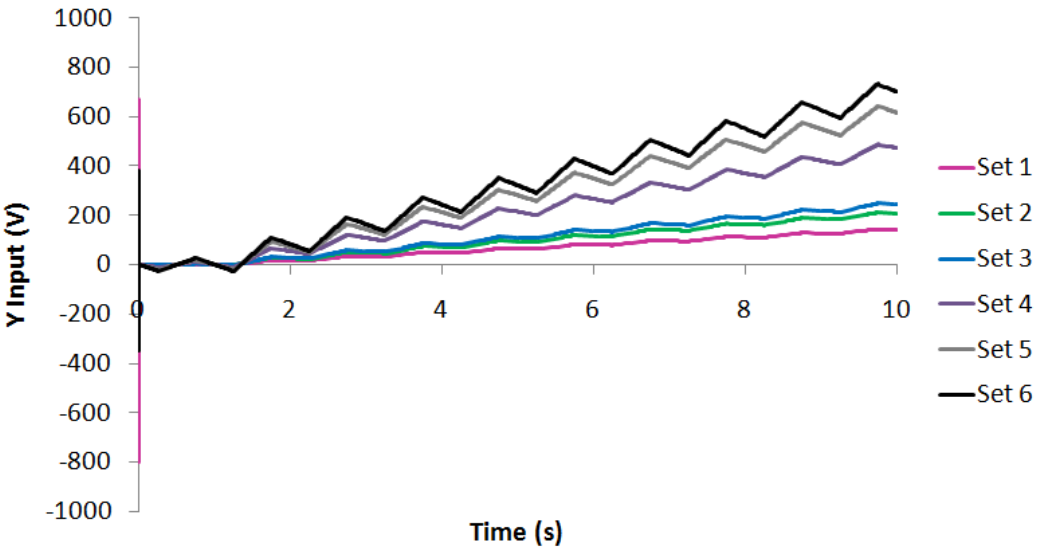

Figure 4-12. Y Inputs of Closed Loop Nonlinear System without Electrode Dislocation using PI Controller

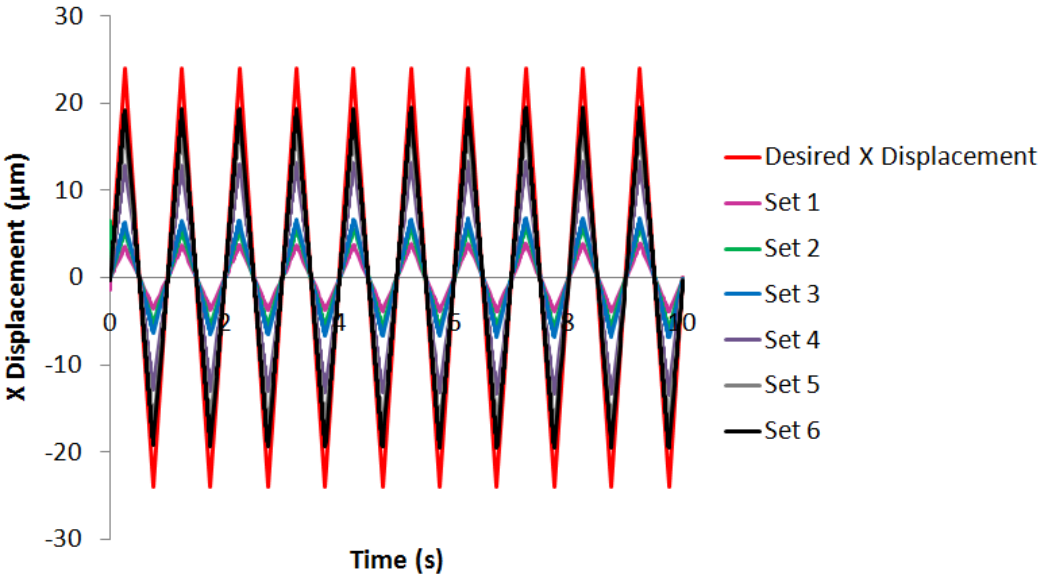

Figure 4-13. X Displacements of Closed Loop Nonlinear System without Electrode Dislocation using PI Controller

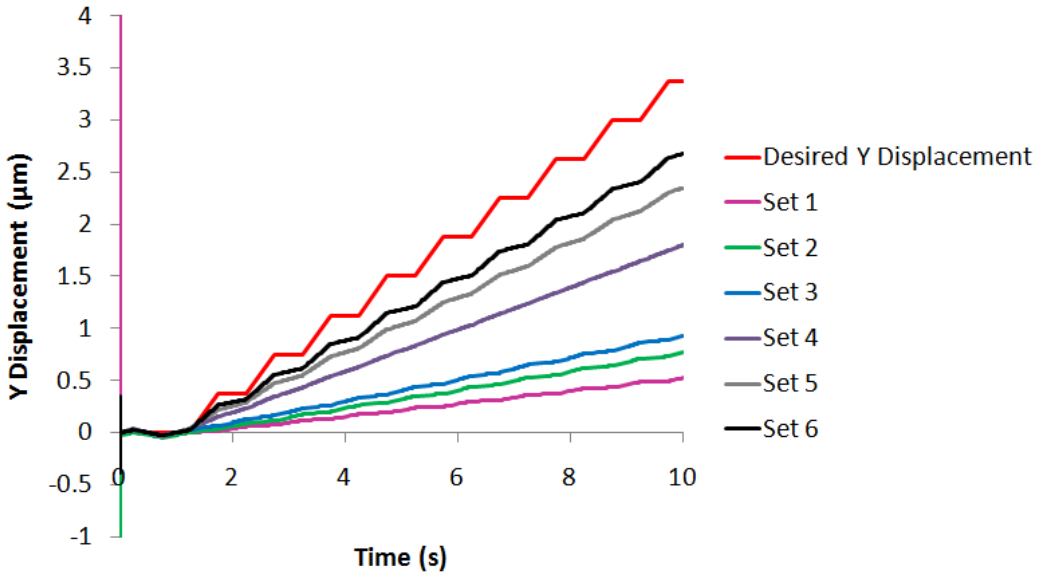

Figure 4-14. Y Displacements of Closed Loop Nonlinear System without Electrode Dislocation using PI Controller

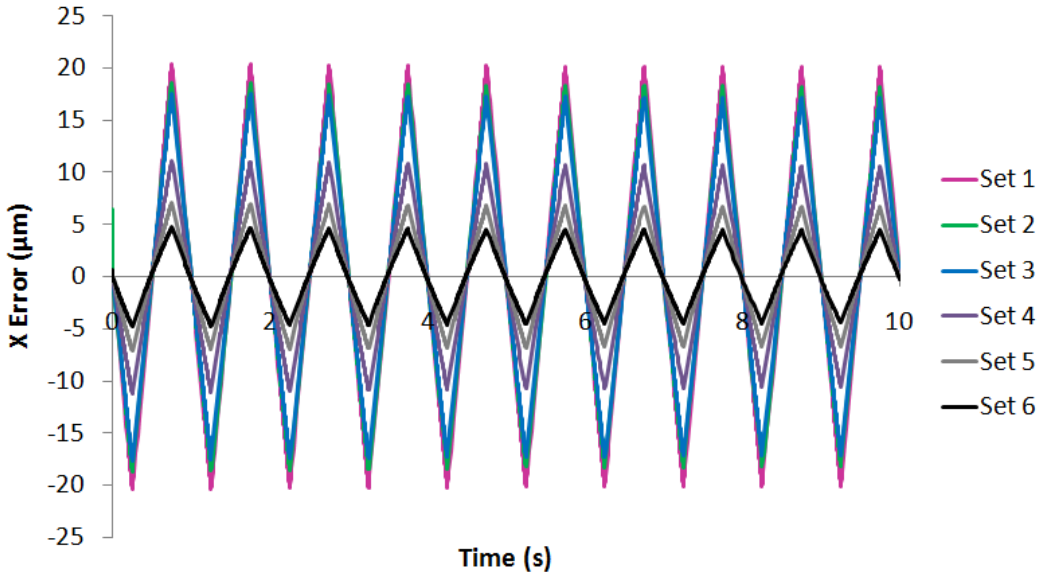

Figure 4-15. X Errors of Closed Loop Nonlinear System without Electrode Dislocation using PI Controller

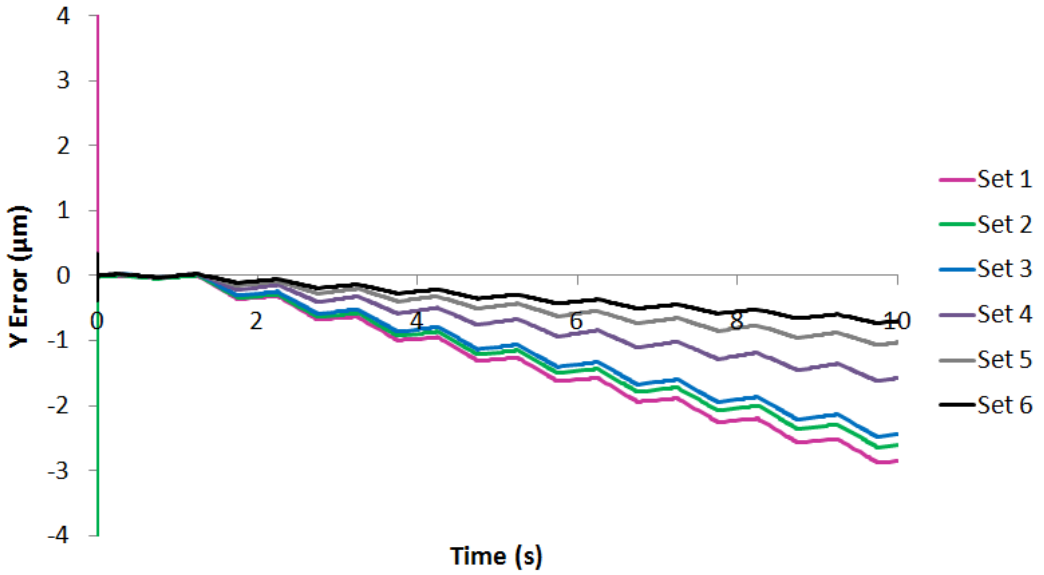

Figure 4-16. Y Errors of Closed Loop Nonlinear System without Electrode Dislocation using PI Controller

In Fig. 4-13 and Fig. 4-14, it is observed that the X displacement and the Y displacement of the closed loop nonlinear system without electrode dislocation using the PI controller are closer to the desired X displacement and the desired Y displacement respectively with larger proportional gains of the PI controller. Therefore, it can be observed in Fig. 4-15 and Fig. 4-16 that the X error and the Y error of the closed loop nonlinear system without electrode dislocation using the PI controller are smaller with larger proportional gains of the PI controller. In Table 4-2, the X RMSE and the Y RMSE of the closed loop nonlinear system without electrode dislocation using the PI controller are smaller with larger proportional gains of the PI controller. It implies that larger proportional gains of the PI controller are preferred. However, by observing the trend of the X RMSEs and the Y RMSEs of the closed loop nonlinear system without electrode dislocation using the PI controller in Fig. 4-17, the X RMSEs and the Y RMSEs converge to some values. The reductions of the X RMSE and the Y RMSE are not significantly improved by further increasing the proportional gains of the PI controller. Also,

large proportional gain of PI controller is not suggested because it may cause saturation of actuator or voltage amplifier, and instability in practice. Therefore, the PI controller gains (the Set 6), which give RMSEs close to the converged values, is used to investigate the performance of the PI controller on the piezoelectric tube actuator with electrode dislocation.

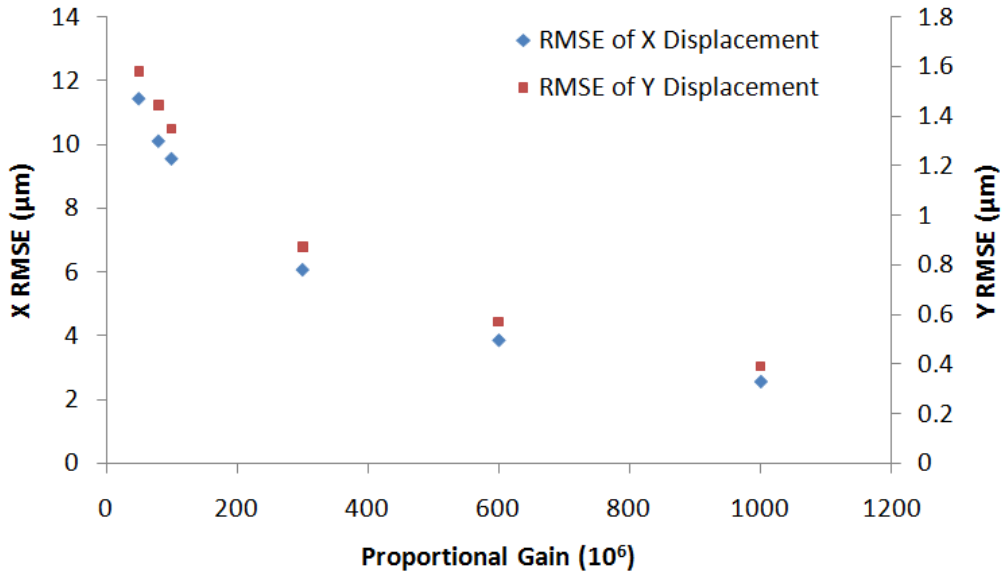

Figure 4-17. RMSEs of Closed Loop Nonlinear System without Electrode Dislocation using PI Controller

The Set 6 controller gains are used in the PI controller to investigate the case that the piezoelectric tube actuator has electrode dislocation. The X input and the Y input to the closed loop nonlinear system with electrode dislocation using the PI controller generated by Eq. (4.1a) and Eq. (4.2a) are shown in Fig. 4-18 and Fig. 4-19 respectively. The X displacement and the Y displacement of the closed loop nonlinear system with electrode dislocation using the PI controller gains are shown in Fig. 4-20 and Fig. 4-21 respectively. The X error and the Y error of the closed loop nonlinear system with electrode dislocation using the PI controller are shown in Fig. 4-22 and Fig. 4-23 respectively. The X RMSE and the Y RMSE of the

closed loop nonlinear system with electrode dislocation using the PI controller are shown in Table 4-3.

Table 4-3. RMSEs of Closed Loop Nonlinear System with Electrode Dislocation

	X RMSE (μm)	Y RMSE (μm)
PI Controller	2.908	0.409
OFC	2.003	0.465

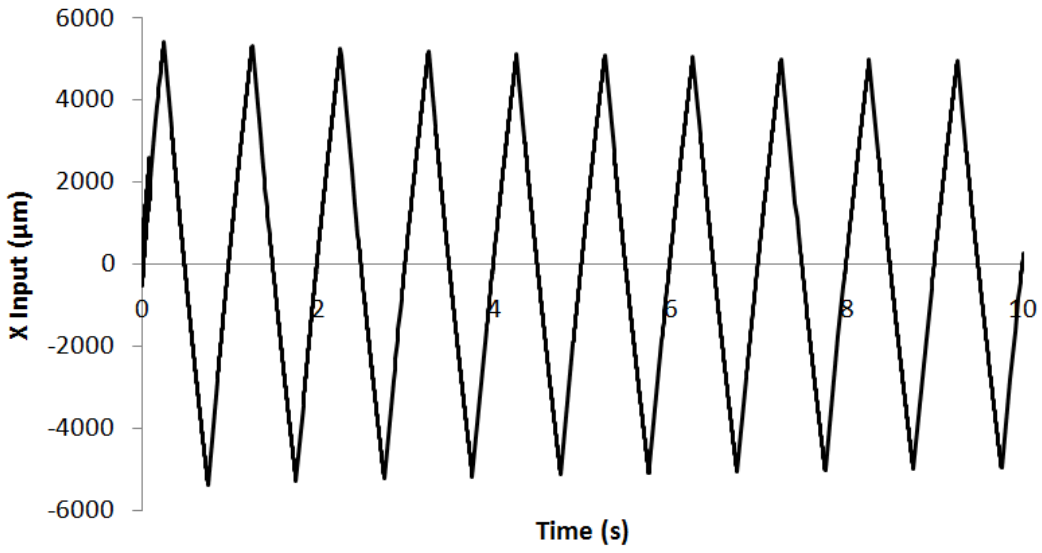

Figure 4-18. X Input of Closed Loop Nonlinear System with Electrode Dislocation using PI Controller

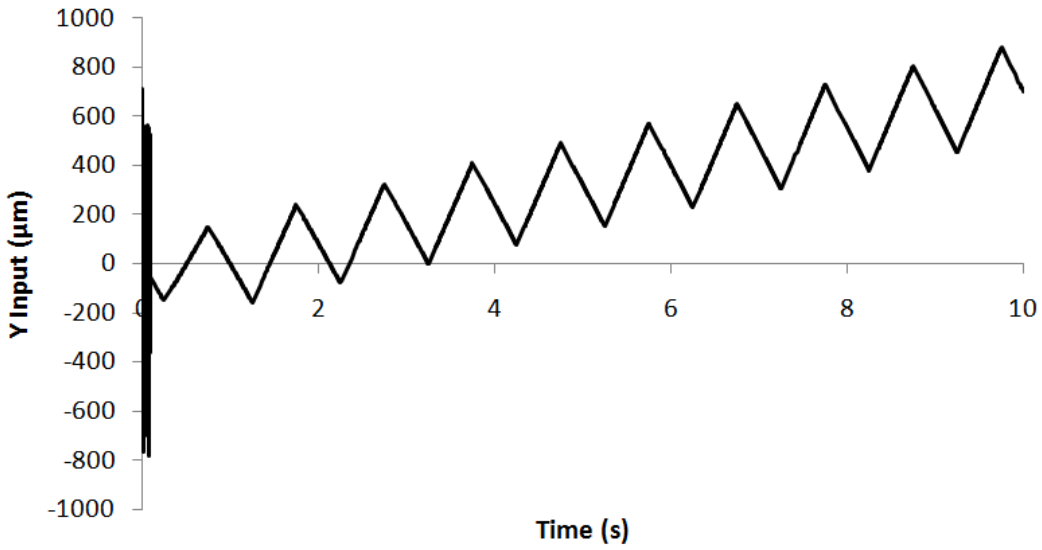

Figure 4-19. Y Input of Closed Loop Nonlinear System with Electrode Dislocation using PI Controller

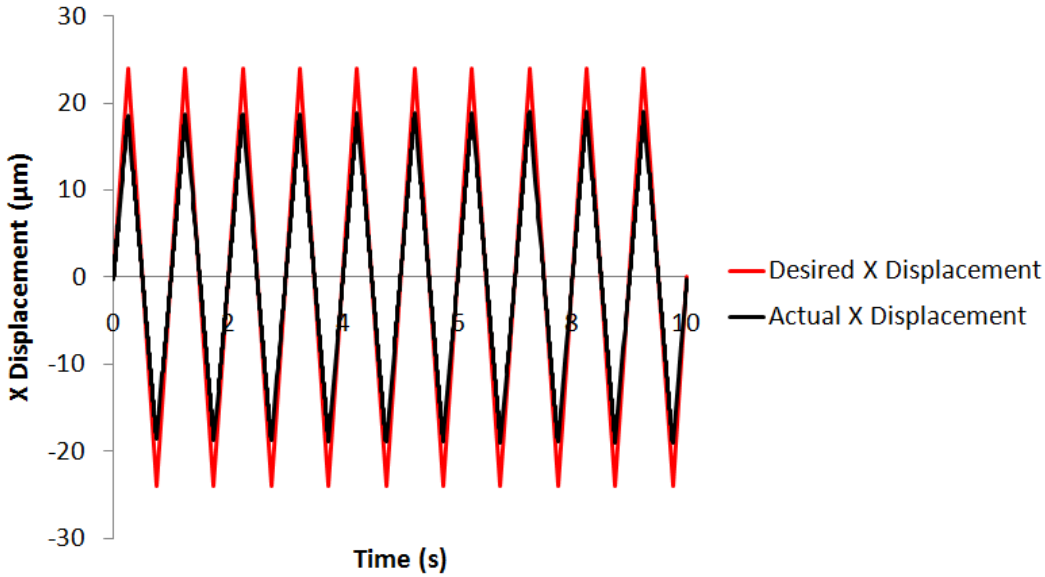

Figure 4-20. X Displacement of Closed Loop Nonlinear System with Electrode Dislocation using PI Controller

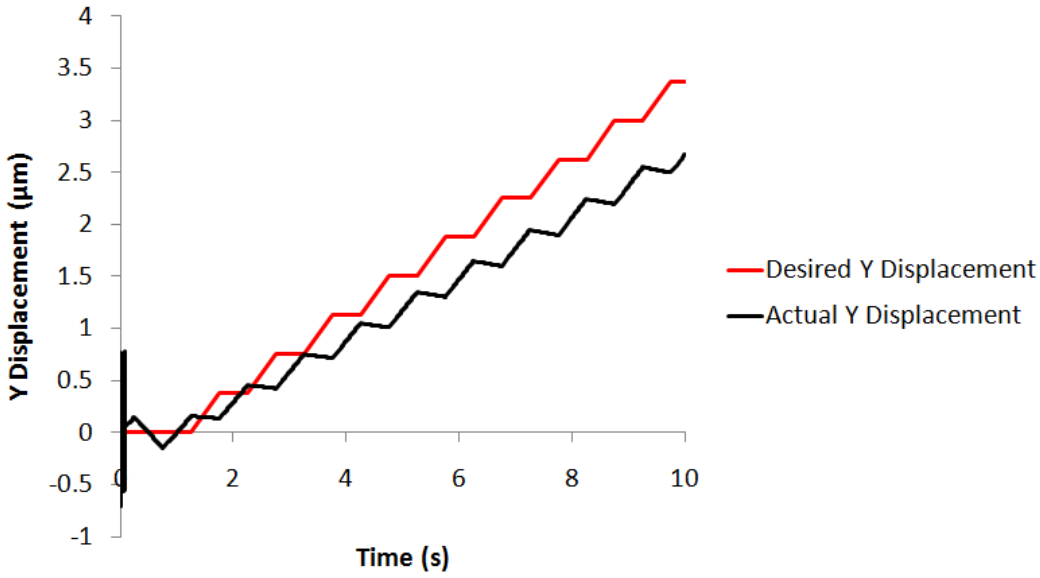

Figure 4-21. Y Displacement of Closed Loop Nonlinear System with Electrode Dislocation using PI Controller

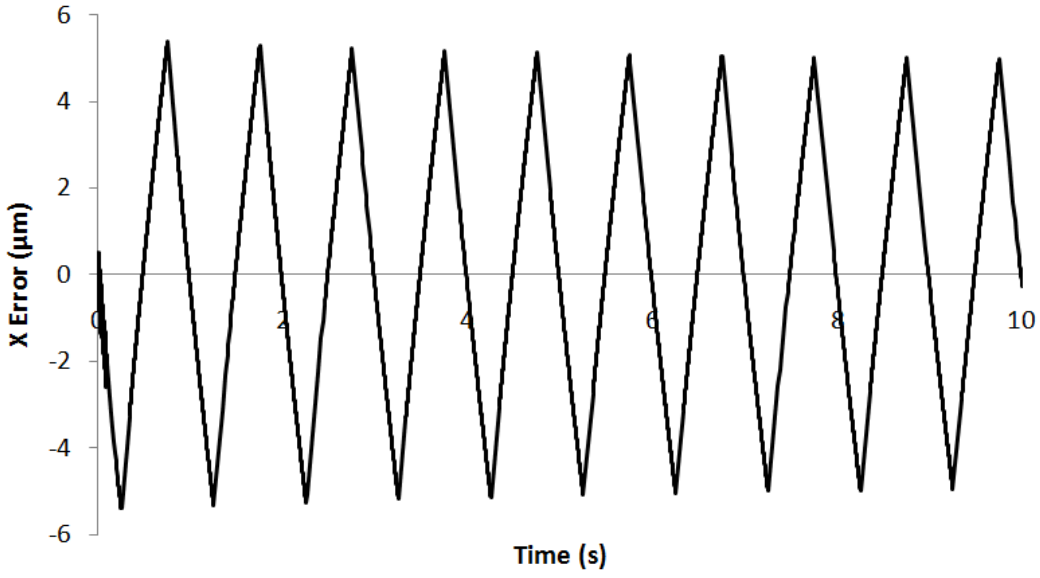

Figure 4-22. X Error of Closed Loop Nonlinear System with Electrode Dislocation using PI Controller

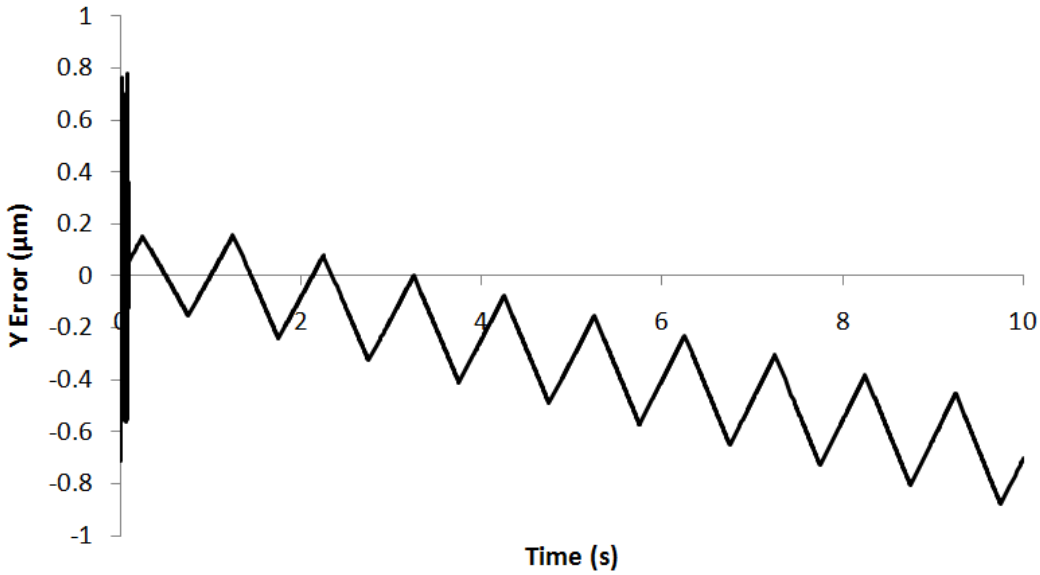

Figure 4-23. Y Error of Closed Loop Nonlinear System with Electrode Dislocation using PI Controller

In Fig. 4-20, it is observed that the amplitude of the X displacement of the closed loop nonlinear system with electrode dislocation using the PI controller is reduced and it is smaller than that of the open loop nonlinear system with electrode dislocation shown in Fig. 4-6. The X RMSE of the closed loop nonlinear system with electrode dislocation using the PI controller (2.908 μm in Table 4-3) is smaller than that of the open loop nonlinear system with electrode dislocation (5.619 μm in Table 4-1). In Fig. 4-21, it is observed that the amplitude of the triangular pattern due to coupling effect exhibited in the Y displacement of the closed loop nonlinear system with electrode dislocation using the PI controller is smaller than that of the open loop nonlinear system with electrode dislocation shown in Fig. 4-7. Therefore, it is observed in Fig. 4-9 and Fig. 4-23 that the peak-to-peak amplitude of the triangular pattern of the Y error of the closed loop nonlinear system with electrode dislocation using the PI controller (0.6 μm) is smaller than that of the open loop nonlinear system with electrode dislocation (2.3 μm). It is concluded that the PI controller can reduce the tracking error induced by coupling effect and hysteresis.

In Table 4-1 and Table 4-3, it is shown that comparing to the open loop nonlinear system with electrode dislocation, the X RMSE of the closed loop nonlinear system with electrode dislocation using the PI controller reduced from 5.619 μm to 2.908 μm and the Y RMSE of the closed loop nonlinear system with electrode dislocation using the PI controller reduced from 0.678 μm to 0.409 μm. In Fig. 4-22, the X error of the closed loop nonlinear system with electrode dislocation using the PI controller slightly converges. Therefore, the closed loop nonlinear system with electrode dislocation using the PI controller is more stable than the open loop system with electrode dislocation. Overall, the PI controller improves the stability and reduces the error caused by coupling effect and hysteresis.

4.4.2 Output Feedback Controller

In this section, the performance of the OFC on the piezoelectric tube actuator with electrode dislocation is assessed. The control law of the OFC is given (Jairath, 2008):

$$[u_E] = [N_{ff}][r] - [k_{fb}][y], \tag{4.3a}$$

where

$$[N_{ff}] = \begin{bmatrix} N_{XX} & N_{XY} \\ N_{YX} & N_{YY} \end{bmatrix} \tag{4.3b}$$

$$[k_{fb}] = \begin{bmatrix} k_{XX} & k_{XY} \\ k_{YX} & k_{YY} \end{bmatrix} \tag{4.3c}$$

$$[r] = \begin{bmatrix} r_X \\ r_Y \end{bmatrix}. \tag{4.3d}$$

$[N_{ff}] \in \Re^{2\times 2}$ and $[k_{fb}] \in \Re^{2\times 2}$ denotes the feedforward gain and feedback gain of the OFC respectively. N_{XX}, N_{XY}, N_{YX} and N_{YY} are the components of $[N_{ff}]$. k_{XX}, k_{XY}, k_{YX} and k_{YY} are the components of $[k_{fb}]$. $[r] \in \Re^2$ is the desired output vector. The block diagram of the OFC is shown in Fig. 4-24. The feedforward gain allows modification of the magnitude of the feedforward signal. The feedback gain allows change of location of the closed loop poles in order that the closed loop system dynamics can be modified. With the same reason as the PI controller, the OFC is tuned based on the reduced order nonlinear FE model (Eq. (3.62b) and Eq. (3.63)) without electrode dislocation. The controller gains of the OFC are also tuned by trial-and-error method. Then the OFC with tuned gains is applied to the reduced order nonlinear FE model (Eq. (3.62b) and Eq. (3.63)) with electrode dislocation for investigation.

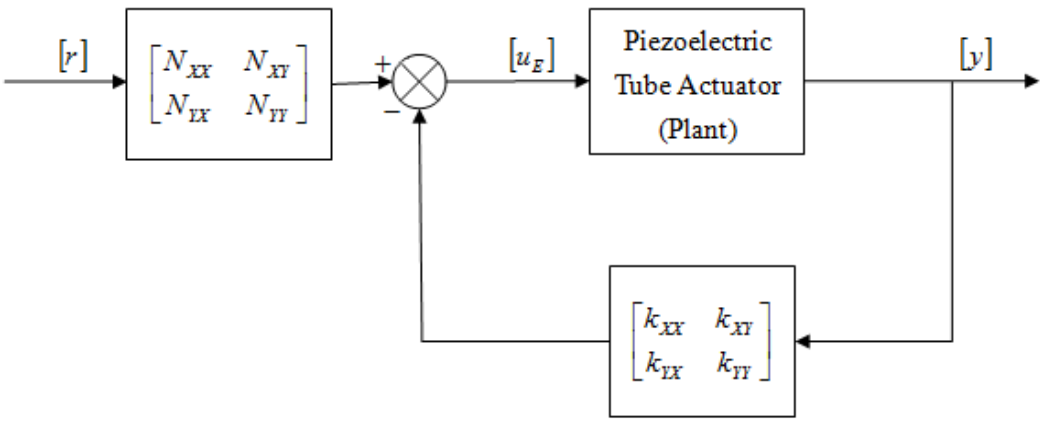

Figure 4-24. Block Diagram of Closed Loop System using OFC

Ten sets of different OFC gains (Set A – Set J) and corresponding X RMSE and Y RMSE of the closed loop nonlinear system without electrode dislocation using the OFC are shown in Table 4-4. The X inputs to the closed loop nonlinear

system without electrode dislocation using the OFC generated by Eq. (4.3a) are shown in Fig. 4-25a – Fig. 4-25c. The Y inputs to the closed loop nonlinear system without electrode dislocation using the OFC generated by Eq. (4.3a) are shown in Fig. 4-26a – Fig. 4-26c. The X displacements of the closed loop nonlinear system without electrode dislocation using the OFC are shown in Fig. 4-27a – Fig. 4-27c. The Y displacements of the closed loop nonlinear system without electrode dislocation using the OFC are shown in Fig. 4-28a – Fig. 4-28c. The X errors of the closed loop nonlinear system without electrode dislocation using the OFC are shown in Fig. 4-29a – Fig. 4-29c. The Y errors of the closed loop nonlinear system without electrode dislocation using the OFC are shown in Fig. 4-30a – Fig. 4-30c.

Table 4-4. Settings of OFC and Corresponding RMSEs of Closed Loop Nonlinear System without Electrode Dislocation

Set	N_{XX} $\times 10^6$	N_{XY} $\times 10^6$	N_{YX} $\times 10^6$	N_{YY} $\times 10^6$	k_{XX} $\times 10^6$	k_{XY} $\times 10^6$	k_{YX} $\times 10^6$	k_{YY} $\times 10^6$	X RMSE (μm)	Y RMSE (μm)
A	400	0	0	200	10	-10	-10	10	12.303	1.219
B	200	0	0	400	10	-10	-10	10	2.767	0.980
C	300	-50	50	300	10	-10	-10	10	5.145	3.301
D	300	50	-50	300	10	-10	-10	10	4.807	1.739
E	297	0	0	297	10	-10	-10	10	4.733	0.772
F	297	0	0	297	100	-10	-10	10	1.720	0.539
G	297	0	0	297	10	-0.5	-10	10	4.733	0.772
H	297	0	0	297	10	-10	10	10	4.657	0.559
I	297	0	0	297	10	-10	-10	80	4.725	0.676
J	297	0	0	297	70	-1	0	20	1.190	0.118

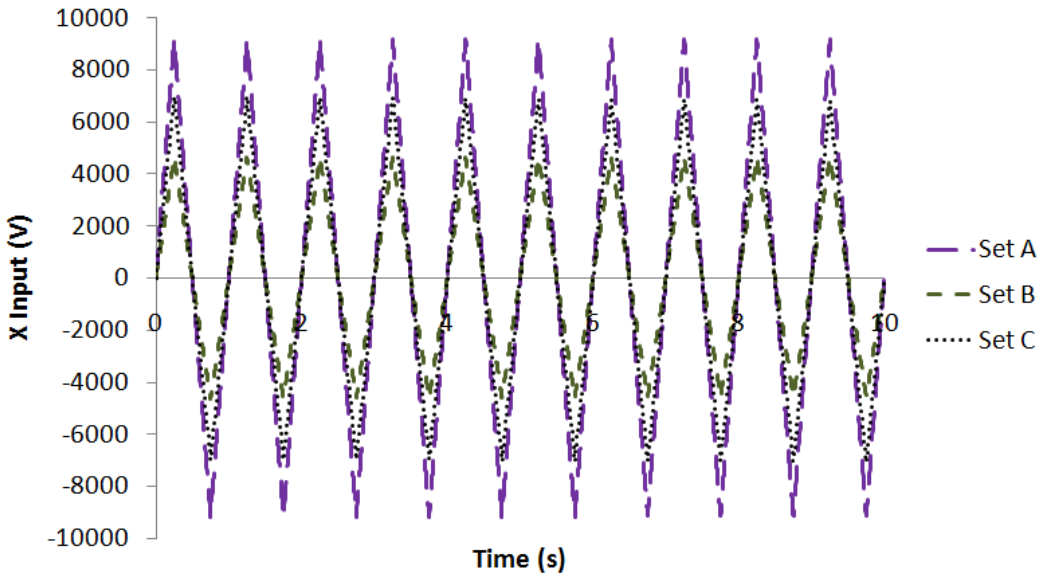

Figure 4-25a. X Inputs of Closed Loop Nonlinear System without Electrode Dislocation using OFC (Set A – Set C)

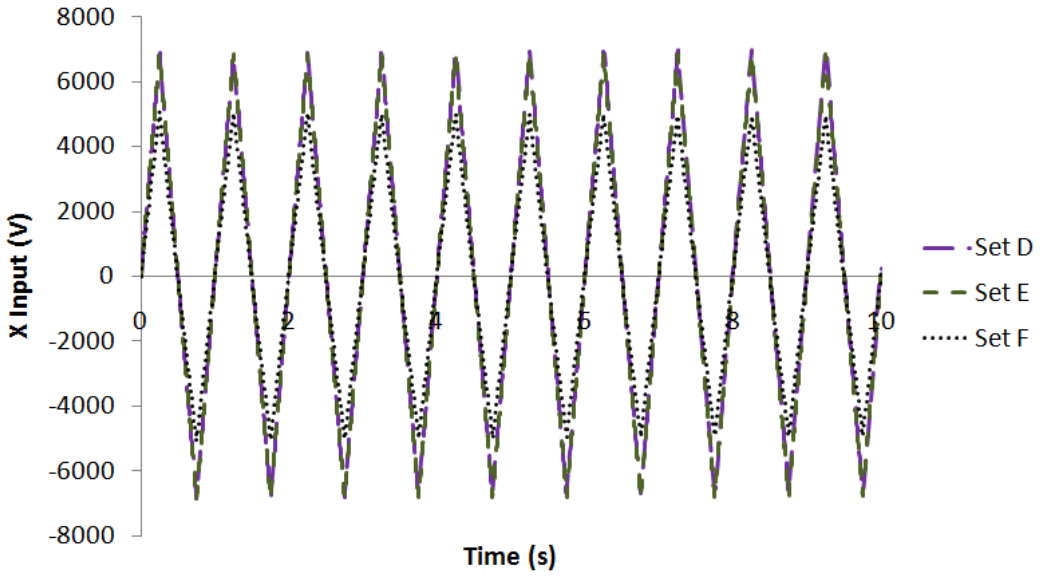

Figure 4-25b. X Inputs of Closed Loop Nonlinear System without Electrode Dislocation using OFC (Set D – Set F)

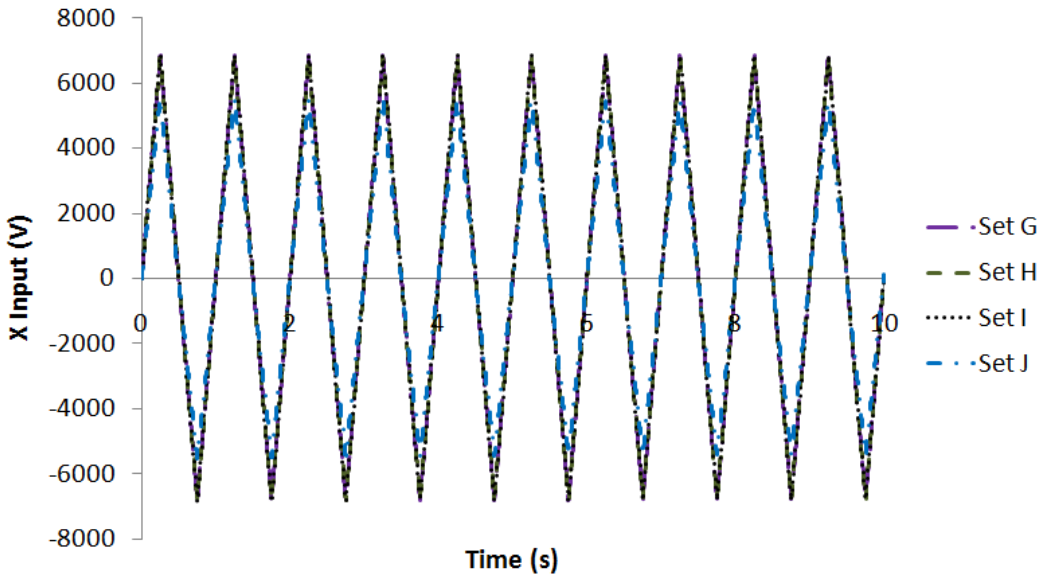

Figure 4-25c. X Inputs of Closed Loop Nonlinear System without Electrode Dislocation using OFC (Set G – Set J)

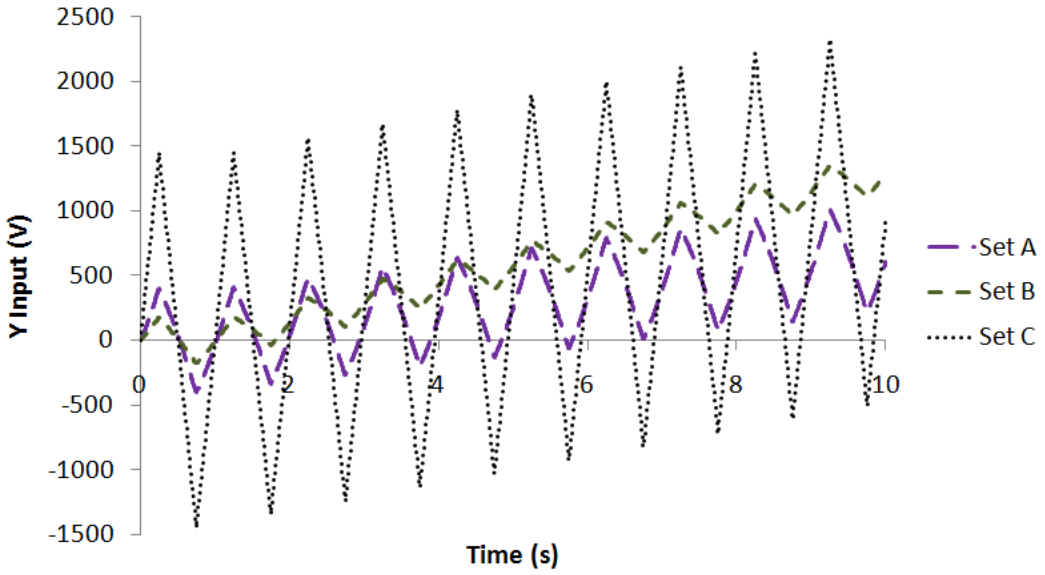

Figure 4-26a. Y Inputs of Closed Loop Nonlinear System without Electrode Dislocation using OFC (Set A – Set C)

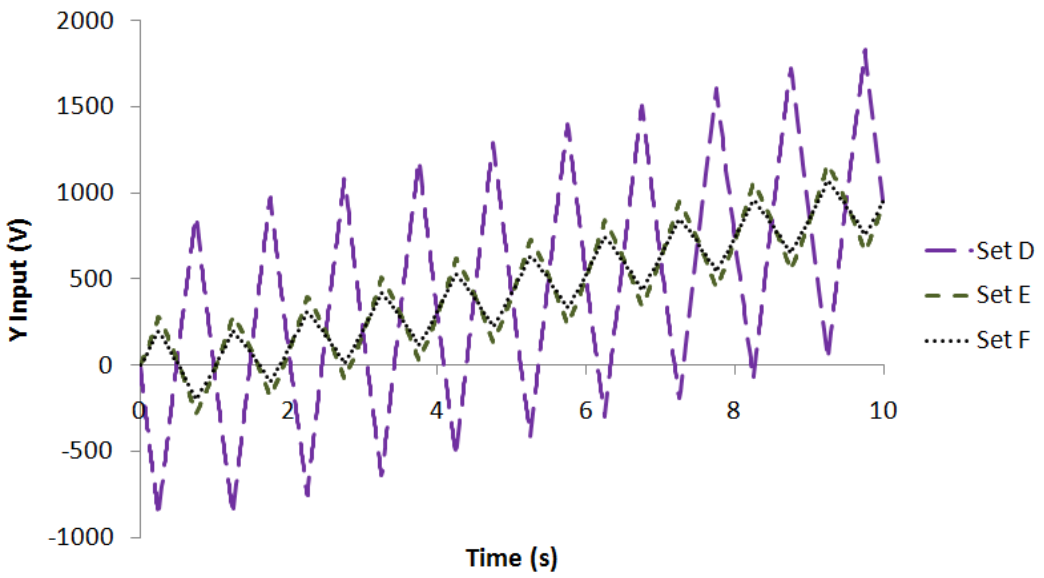

Figure 4-26b. Y Inputs of Closed Loop Nonlinear System without Electrode Dislocation using OFC (Set D – Set F)

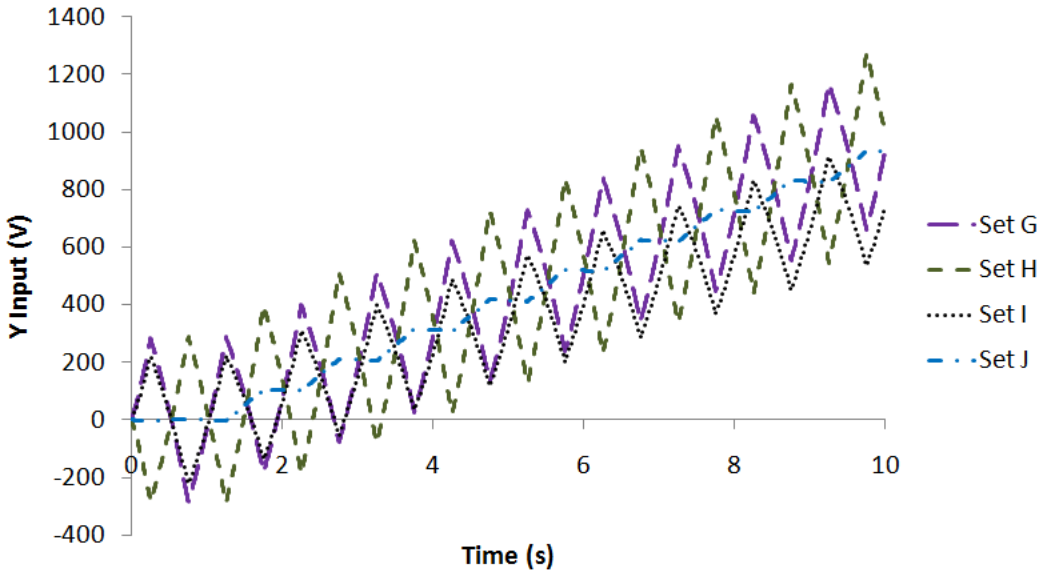

Figure 4-26c. Y Inputs of Closed Loop Nonlinear System without Electrode Dislocation using OFC (Set G – Set J)

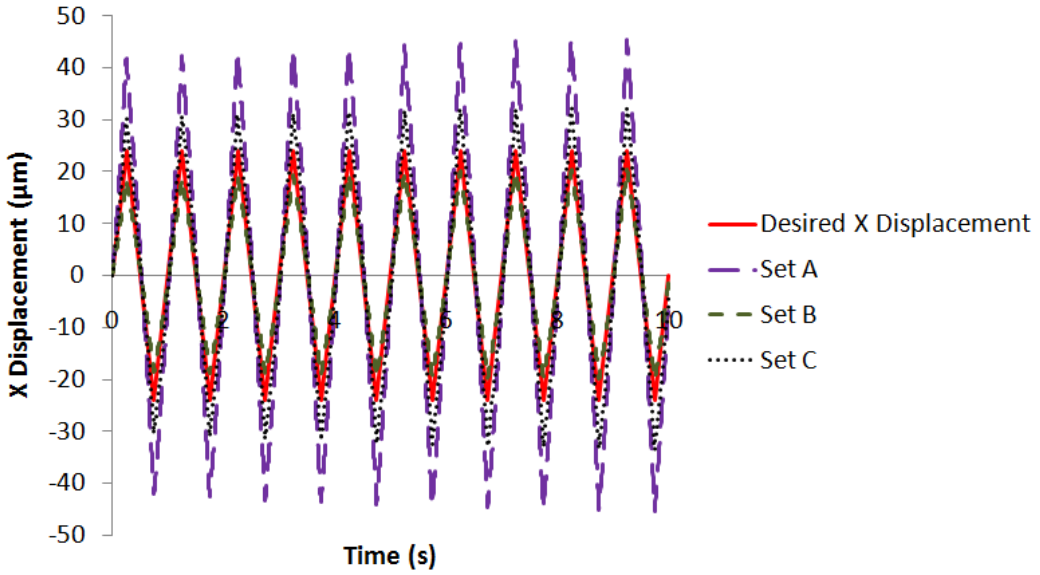

Figure 4-27a. X Displacements of Closed Loop Nonlinear System without Electrode Dislocation using OFC (Set A – Set C)

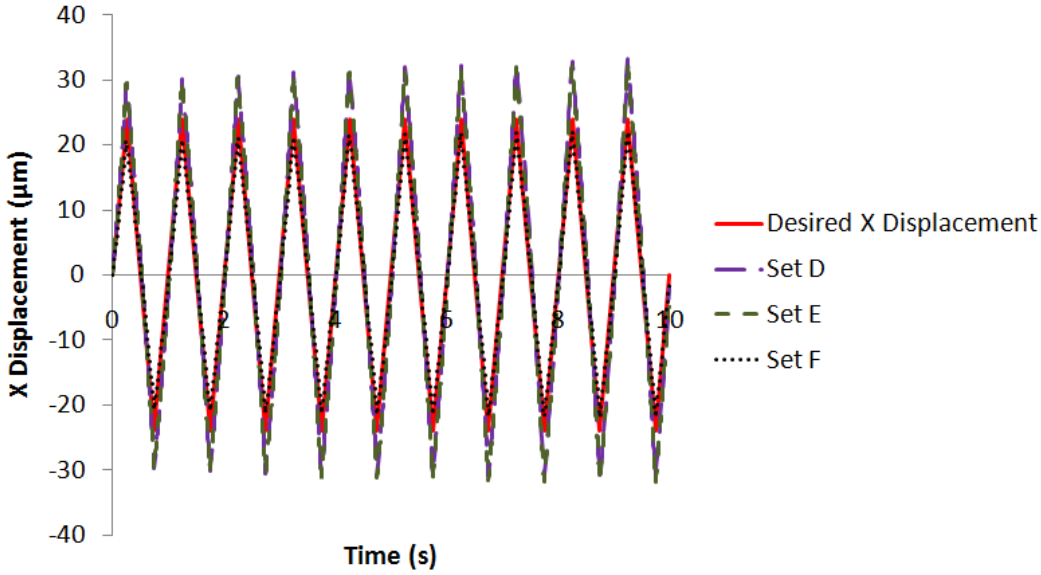

Figure 4-27b. X Displacements of Closed Loop Nonlinear System without Electrode Dislocation using OFC (Set D – Set F)

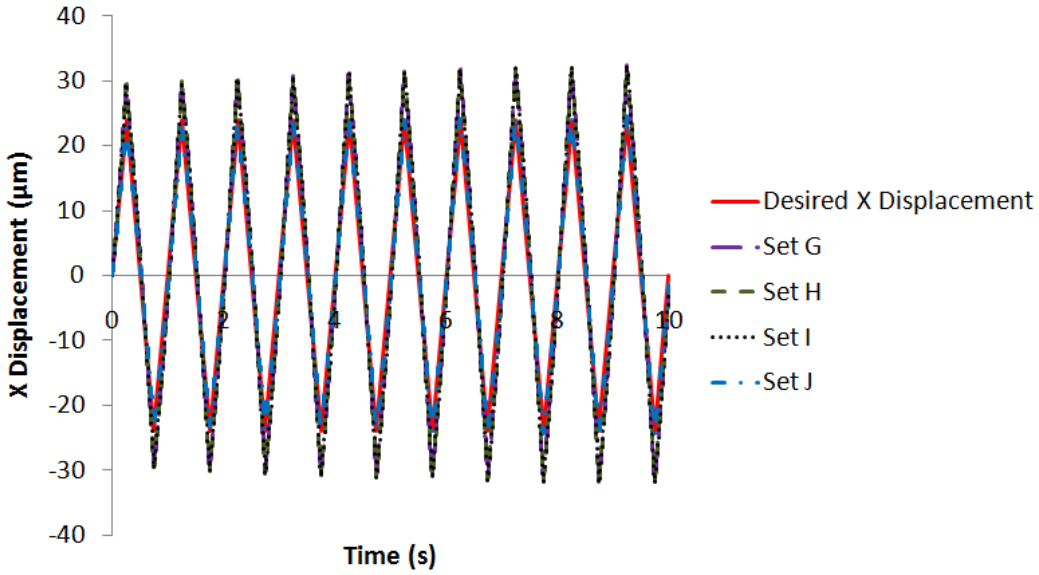

Figure 4-27c. X Displacements of Closed Loop Nonlinear System without Electrode Dislocation using OFC (Set G – Set J)

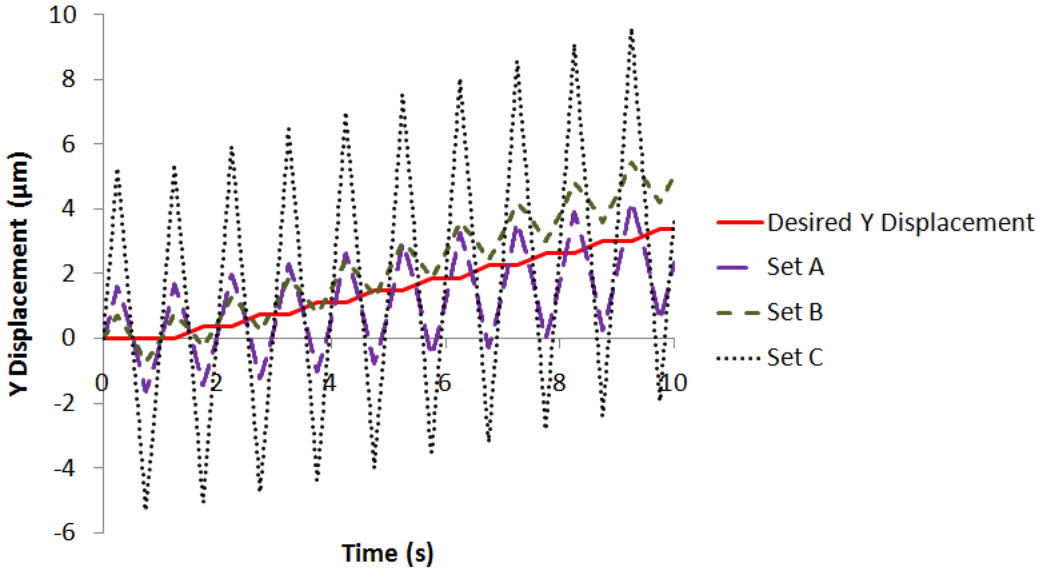

Figure 4-28a. Y Displacements of Closed Loop Nonlinear System without Electrode Dislocation using OFC (Set A – Set C)

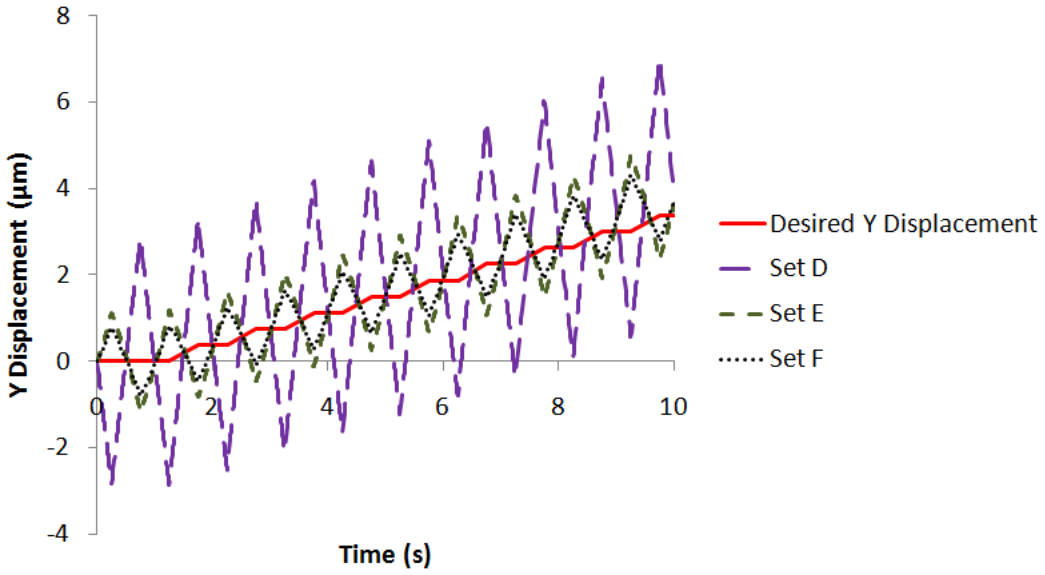

Figure 4-28b. Y Displacements of Closed Loop Nonlinear System without Electrode Dislocation using OFC (Set D – Set F)

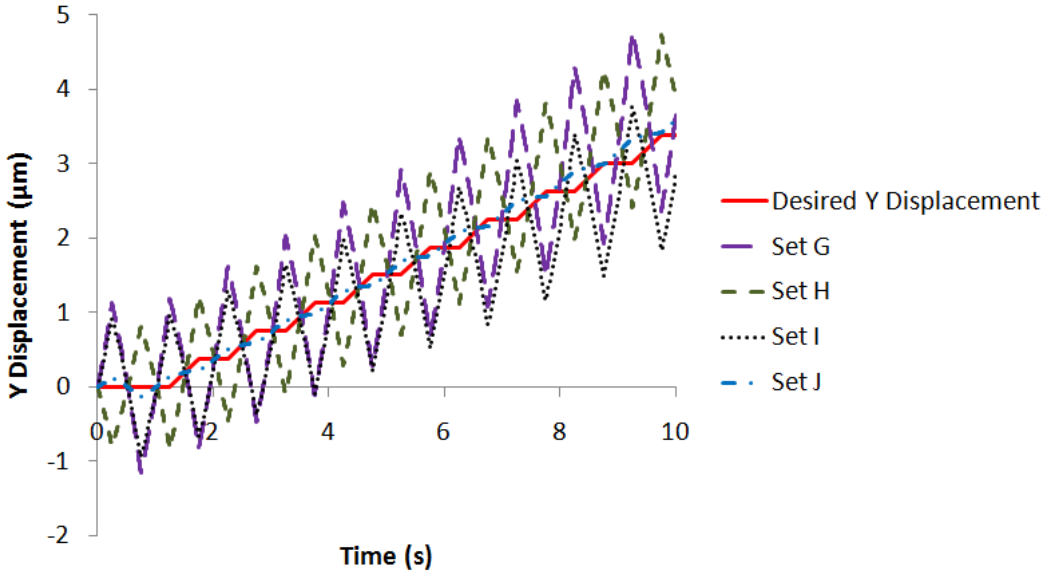

Figure 4-28c. Y Displacements of Closed Loop Nonlinear System without Electrode Dislocation using OFC (Set G – Set J)

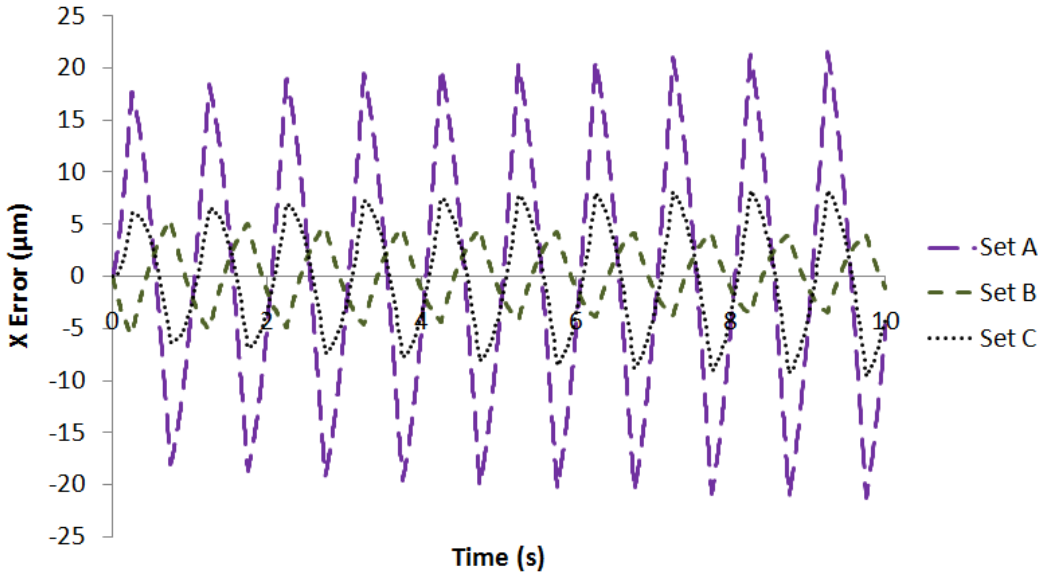

Figure 4-29a. X Errors of Closed Loop Nonlinear System without Electrode Dislocation using OFC (Set A – Set C)

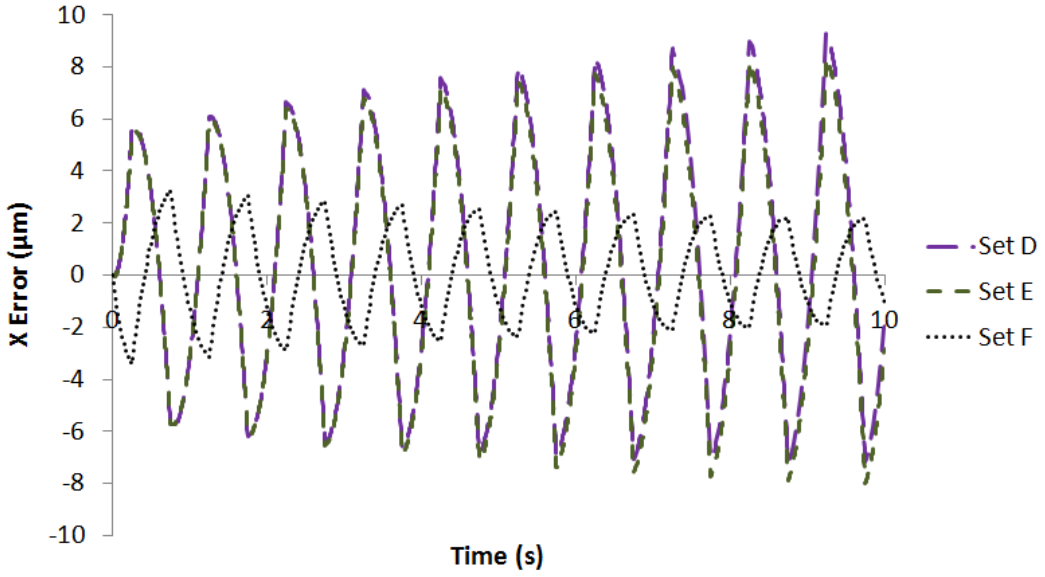

Figure 4-29b. X Errors of Closed Loop Nonlinear System without Electrode Dislocation using OFC (Set D – Set F)

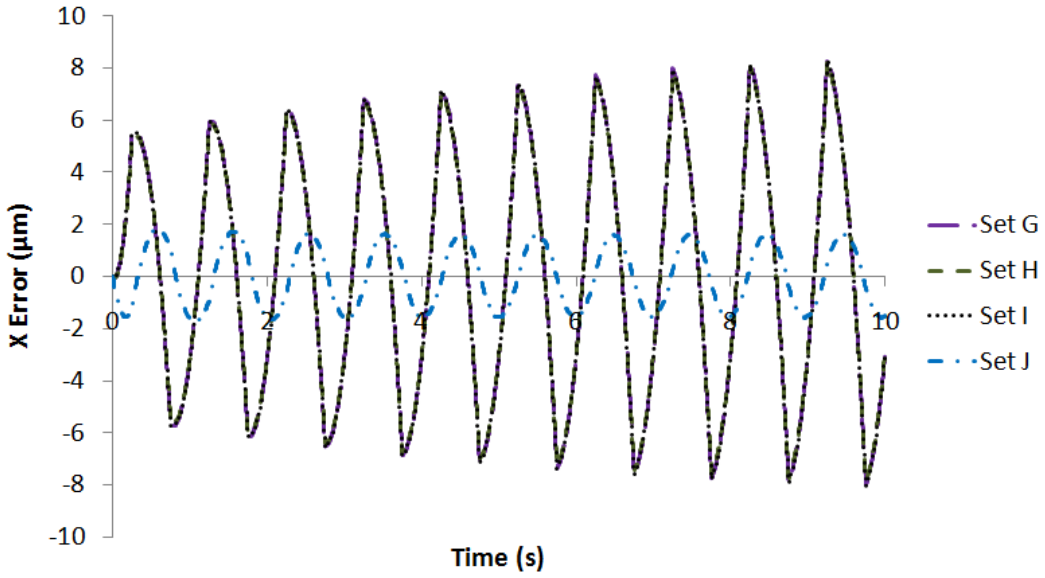

Figure 4-29c. X Errors of Closed Loop Nonlinear System without Electrode Dislocation using OFC (Set G – Set J)

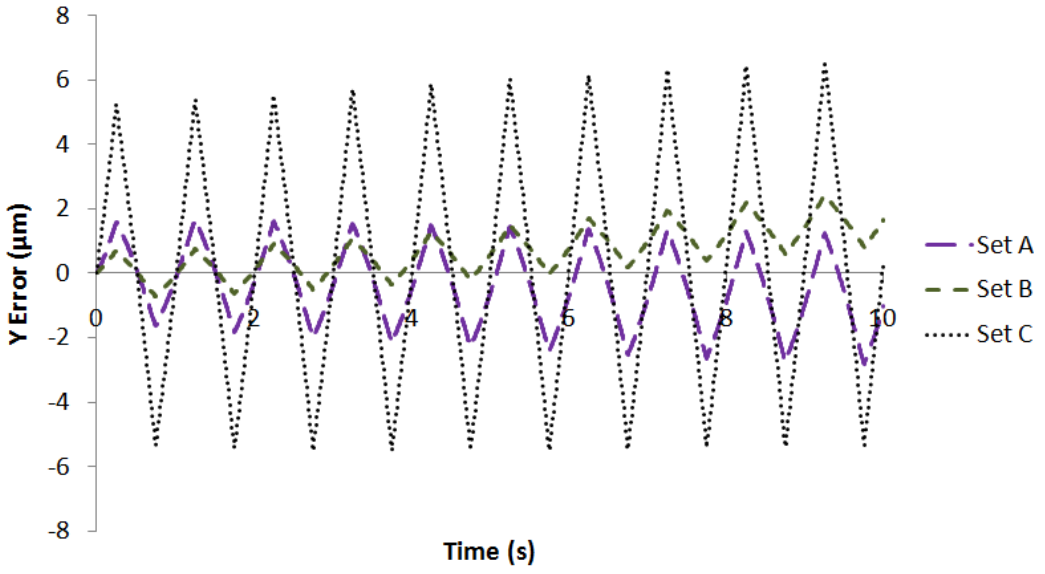

Figure 4-30a. Y Errors of Closed Loop Nonlinear System without Electrode Dislocation using OFC (Set A – Set C)

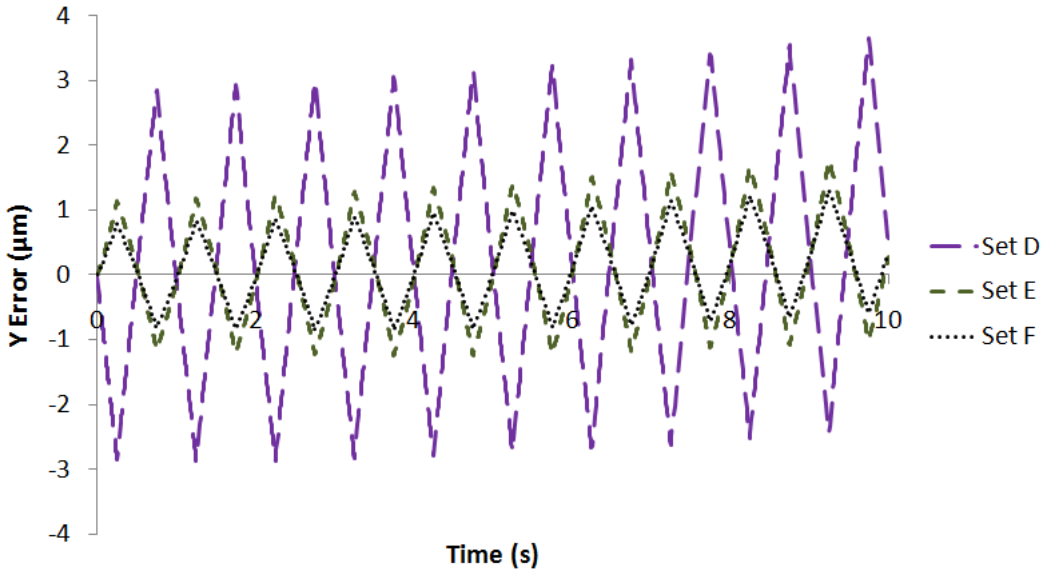

Figure 4-30b. Y Errors of Closed Loop Nonlinear System without Electrode Dislocation using OFC (Set D – Set F)

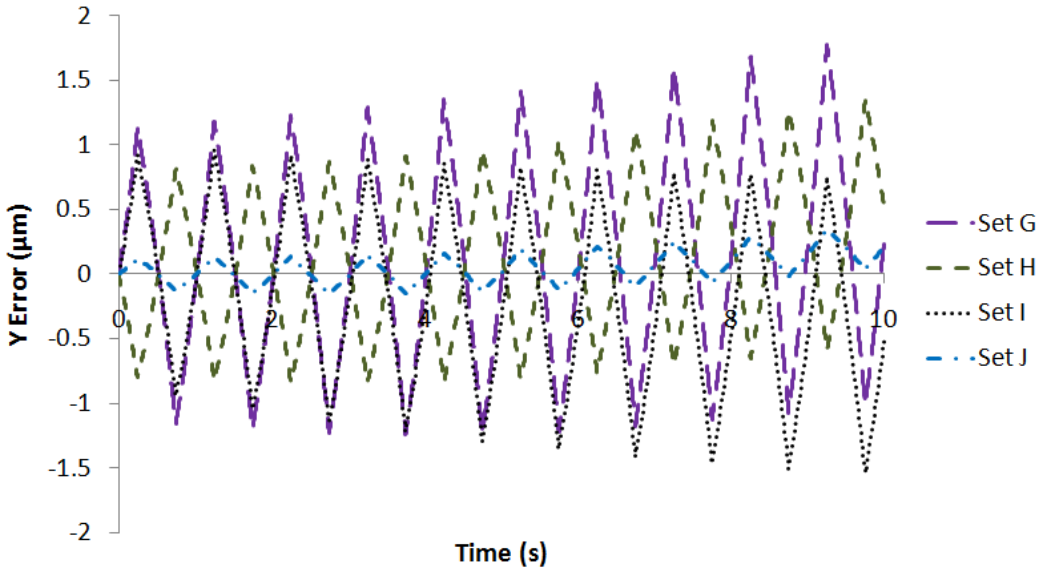

Figure 4-30c. Y Errors of Closed Loop Nonlinear System without Electrode Dislocation using OFC (Set G – Set J)

The tuning procedures involve trial-and-error method followed by interpolation and the tuned gains construct the Set J. First, in Fig. 4-27b, it is observed from the X displacement of the closed loop nonlinear system without

electrode dislocation using the controller gains (the Set E and the Set F) that when k_{XX} increases from 10×10^6 to 100×10^6, the amplitude of the ninth tip of the triangular pattern decreases from about 31 μm to about 21 μm. By interpolating k_{XX} of the Set E and the Set F, the amplitudes of the ninth peak and the desired amplitude (24 μm), k_{XX} of the Set J is calculated as 73×10^6 and the approximated value 70×10^6 is taken. Second, k_{XY} determines the monotonic increase rate of X displacement theoretically. However, in Fig. 4-27b and Fig. 4-27c, it is observed from the X displacement of the closed loop nonlinear system without electrode dislocation using the controller gains (the Set E and the Set G) that the effect of change of k_{XY} from -10×10^6 to -0.5×10^6 is not significant. There is no monotonic increase rate observed using $k_{XY}=-10\times10^6$ and $k_{XY}=-0.5\times10^6$. Therefore, a value in between which is $k_{XY}=-1\times10^6$ is chosen. Third, in Fig. 4-28b and Fig. 4-28c, it is observed from the Y displacement of the closed loop nonlinear system without electrode dislocation using the controller gains (the Set E and the Set H) that when k_{YX} increase from -10×10^6 to 10×10^6, the amplitude of the ninth tip of the triangular pattern decreases from about 2.3 μm to about 0.25 μm. Since the desired Y displacement at that moment is 1.25μm which is about mid-way of 2.3 μm and 0.25 μm, $k_{YX}=0$ is set in Set J. Fourth, in Fig. 4-28b and Fig. 4-28c, it is observed from the Y displacement of the closed loop nonlinear system without electrode dislocation using the controller gains (the Set E and the Set I) that k_{YY} determines the monotonic increase rate of the Y displacement. It is obvious that using the controller gains (the Set E and the Set I), the Y displacement decreases from about 3.5 μm to about 2.75 μm at 10 s when k_{YY} increases from 10×10^6 to 80×10^6. By interpolating k_{YY} of the Set E

and the Set I, the Y displacements of the closed loop nonlinear system without electrode dislocation using the OFC at 10 s (the Set E and the Set H) and the desired amplitude at 10 s (3.375 μm), k_{YY} of the Set J is calculated as 22×10^{6} and the approximated value 20×10^{6} is taken. The feedback gains of the Set J are constructed by the interpolated feedback gains. Change of $[N_{ff}]$ and change of $[k_{fb}]$ have similar effect on the X displacement and the Y displacement of the closed loop nonlinear system without electrode dislocation using the OFC. Since $[k_{fb}]$ has been tuned, the values of $[N_{ff}]$ used in the Set E to the Set I are adopted in the Set J. As a remark, the difference of change of $[N_{ff}]$ and change of $[k_{fb}]$ is that $[N_{ff}]$ which determines the feedforward signal affects the shape and the amplitude of the X displacement and the Y displacement while $[k_{fb}]$ which determines the feedback signal affects the dynamics of the closed loop system such as the tracking error convergence rate and the stability. Finally, in Fig. 4-31, it is observed from the X errors of the closed loop nonlinear system without electrode dislocation using the OFC with the Set A – Set J controller gains that all the X errors curves meet at the red crosses which are located at about 1 μm. The OFC with any feedforward and feedback controller gains cannot reduce the amplitude of the X error of the closed loop nonlinear system without electrode dislocation less than 1 μm. It is the limitation of the OFC on the system without electrode dislocation. In Fig. 4-29c, it is shown that k_{XX}, k_{XY}, N_{XX} and N_{XY} of the Set J can reduce the X error to about this level and no further tuning on N_{XX} and N_{XY} is required. Therefore, the Set J of the OFC gains is chosen for performance

investigation in the closed loop nonlinear system with electrode dislocation.

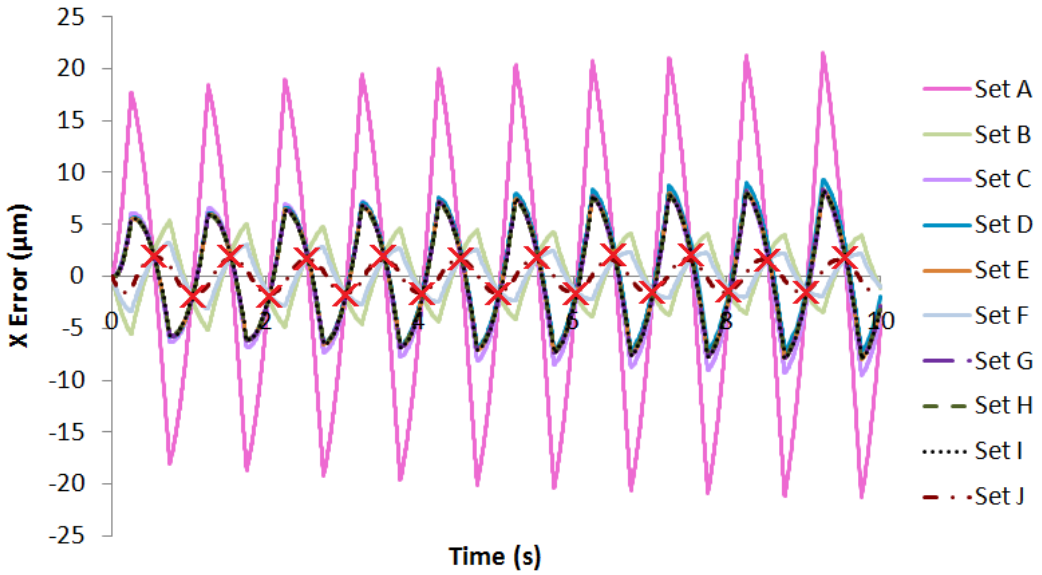

Figure 4-31. X Errors of Closed Loop Nonlinear System without Electrode Dislocation using OFC (Set A – Set J)

The Set J controller gains are used in the OFC to investigate the case that the piezoelectric tube actuator has electrode dislocation. The X input and the Y input to the closed loop nonlinear system with electrode dislocation using the OFC generated by Eq. (4.3a) are shown in Fig. 4-32 and Fig. 4-33 respectively. The X displacement and the Y displacement of the closed loop nonlinear system with electrode dislocation using the OFC are shown in Fig. 4-34 and Fig. 4-35 respectively. The X error and the Y error of the closed loop nonlinear system with electrode dislocation using the OFC are shown in Fig. 4-36 and Fig. 4-37 respectively. The X RMSE and the Y RMSE of the closed loop nonlinear system with electrode dislocation using the OFC are shown in Table 4-3.

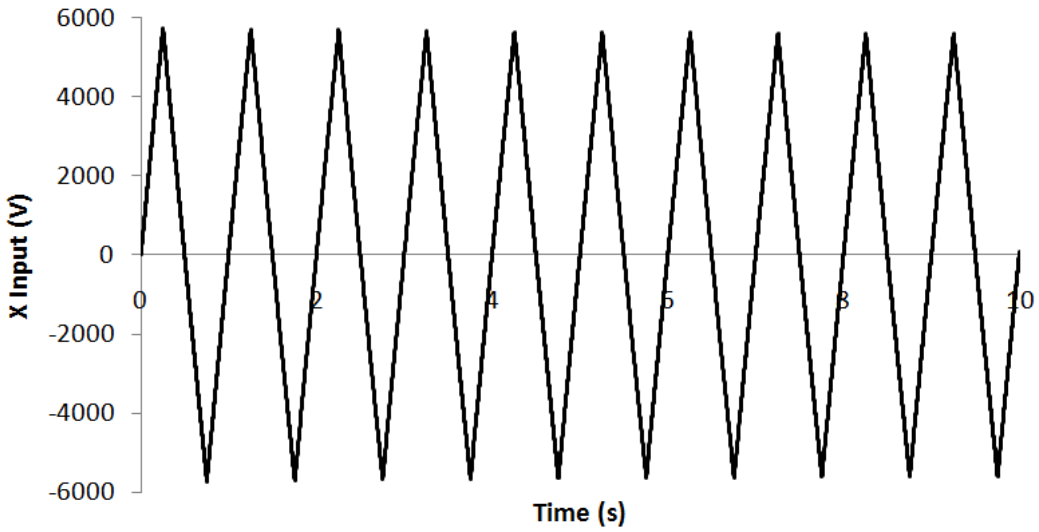

Figure 4-32. X Input of Closed Loop Nonlinear System with Electrode Dislocation using OFC

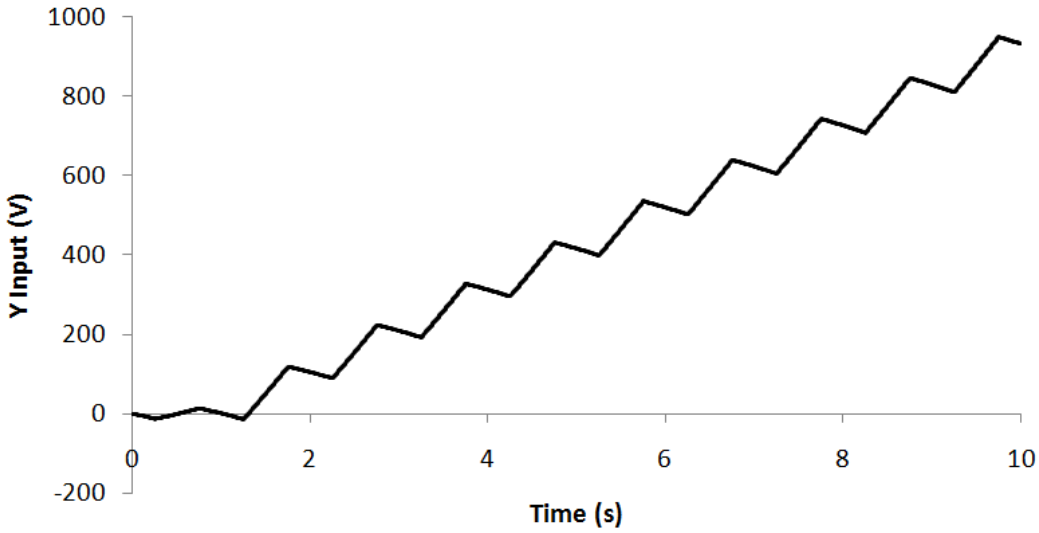

Figure 4-33. Y Input of Closed Loop Nonlinear System with Electrode Dislocation using OFC

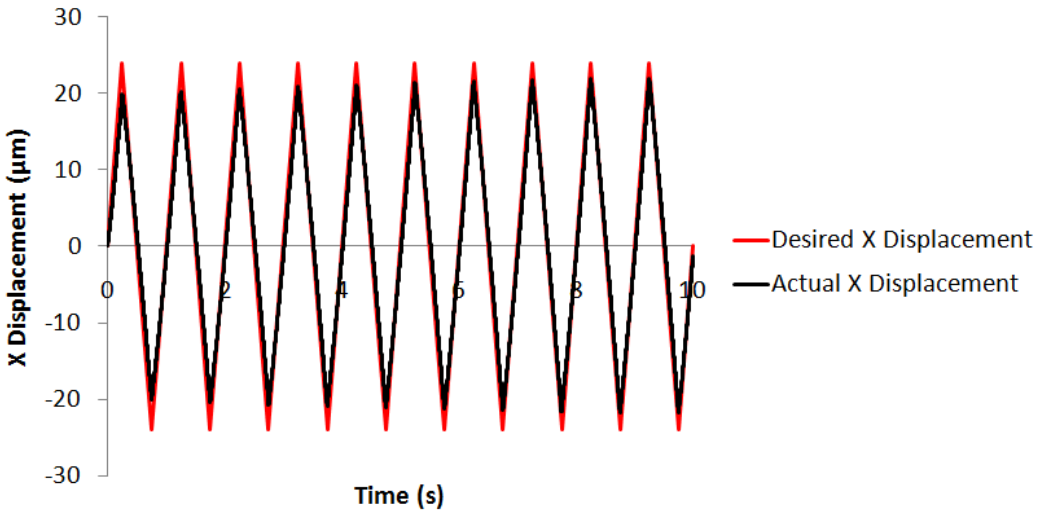

Figure 4-34. X Displacement of Closed Loop Nonlinear System with Electrode Dislocation using OFC

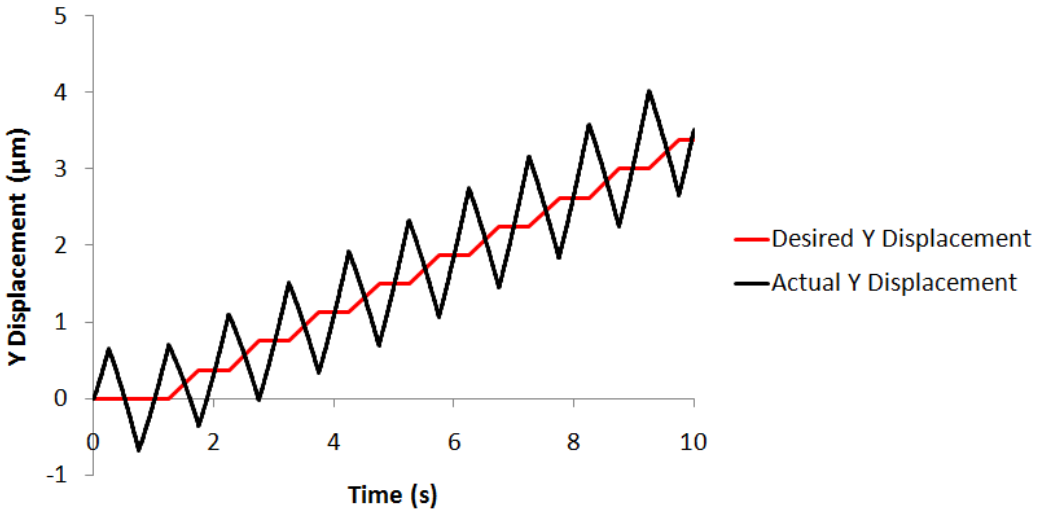

Figure 4-35. Y Displacement of Closed Loop Nonlinear System with Electrode Dislocation using OFC

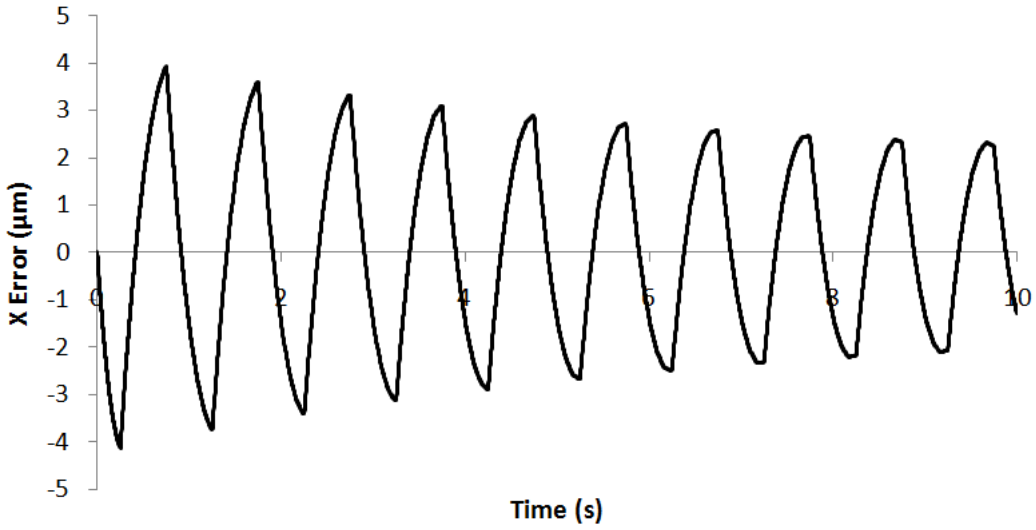

Figure 4-36. X Error of Closed Loop Nonlinear System with Electrode Dislocation using OFC

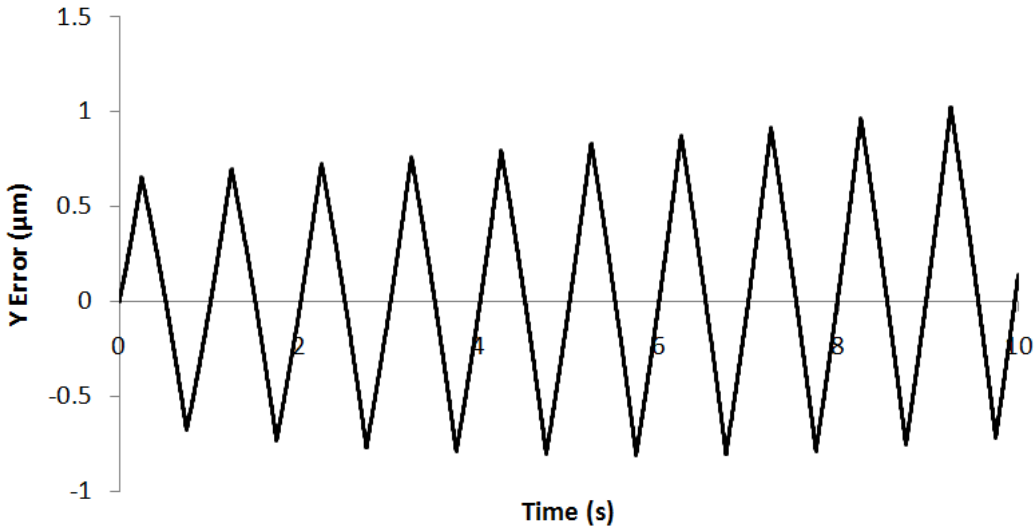

Figure 4-37. Y Error of Closed Loop Nonlinear System with Electrode Dislocation using OFC

In Fig. 4-34, it is observed that the amplitude of the X displacement of the closed loop nonlinear system with electrode dislocation using the OFC is reduced and it is smaller than that of the open loop nonlinear system with electrode dislocation shown in Fig. 4-6. The X RMSE of the closed loop nonlinear system

with electrode dislocation using the OFC (2.003 μm in Table 4-3) is smaller than that of the open loop nonlinear system with electrode dislocation (5.619 μm in Table 4-1). In Fig. 4-35, it is observed that the amplitude of the triangular pattern due to coupling effect exhibited in the Y displacement of the closed loop nonlinear system with electrode dislocation using the OFC is smaller than that of the open loop nonlinear system with electrode dislocation shown in Fig. 4-7. Therefore, it is observed in Fig. 4-9 and Fig. 4-37 that the peak-to-peak amplitude of the triangular pattern of the Y error of the closed loop nonlinear system with electrode dislocation using the OFC controller (1.5 μm) is smaller than that of the open loop nonlinear system with electrode dislocation (2.3 μm). It is concluded that the OFC can reduce the tracking error induced by coupling effect and hysteresis. In Table 4-1 and Table 4-3, it is shown that comparing to the open loop nonlinear system with electrode dislocation, the X RMSE of the closed loop nonlinear system with electrode dislocation using the OFC reduced from 5.619 μm to 2.003 μm and the Y RMSE of the closed loop nonlinear system with electrode dislocation using the OFC reduced from 0.678 μm to 0.465 μm. In Fig. 4-36, the X error of the closed loop nonlinear system with electrode dislocation using the OFC converges. Therefore, the closed loop nonlinear system with electrode dislocation using the OFC is more stable than the open loop system with electrode dislocation. Overall, the OFC improves the stability and reduces the error induced by coupling effect and hysteresis.

In Fig. 4-22 and Fig. 4-36, it is observed that the amplitude of the X error of the closed loop nonlinear system with electrode dislocation using the OFC is smaller than that of the closed loop nonlinear system with electrode dislocation using the PI controller. In Table 4-3, the X RMSE of the closed loop nonlinear

system with electrode dislocation using the OFC (2.003 μm) is smaller than that of the closed loop nonlinear system with electrode dislocation using the PI controller (2.908 μm). It shows that the OFC has a better ability of reducing the tracking error caused by hysteresis. In Fig. 4-21 and Fig. 4-35, it is observed that the triangular pattern of the Y displacement of the closed loop nonlinear system with electrode dislocation using the PI controller is smaller than that of the closed loop nonlinear system with electrode dislocation using the OFC. Therefore, it is observed in Fig. 4-23 and Fig. 4-37 that the peak-to-peak amplitude of the triangular pattern the Y error of the closed loop nonlinear system with electrode dislocation using the PI controller (0.6 μm) is smaller than that of the closed loop nonlinear system with electrode dislocation using the OFC controller (1.5 μm). It is demonstrated that the PI controller has a better ability of reducing the tracking error caused by coupling effect. However, it is observed in Fig. 4-23 and Fig. 4-37 that the Y error of the closed loop nonlinear system with electrode dislocation using the PI controller increases in negative direction and the Y error of the closed loop nonlinear system with electrode dislocation using the OFC diverges.

It is concluded that both the typical controllers can compensate coupling effect and hysteresis, and improve the stability of the piezoelectric tube actuator with electrode dislocation. According to compensation of hysteresis, the OFC is better than the PI controller. According to compensation of coupling effect, the PI controller is better than the OFC. However, the typical controllers cannot compensate creep. Although they can improve the stability of the piezoelectric tube actuator with electrode dislocation in X direction, the Y errors of the closed loop nonlinear system using the typical controllers diverge. Therefore, the PI controller

and the OFC are not perfect controllers.

Other than the PI controller and the OFC, the feedforward plus PI controller is an alternative choice. The structure of the feedforward plus PI controller is similar to the OFC. The difference is that the former one does not have the coupling term and the latter one does not have the integral term. It is deduced that the feedforward term allows the PI controller to perform similar to the OFC. In other words, it can improve the performance of the PI controller on mitigating the error caused by creep and hysteresis but degrade the performance on mitigating the error caused by coupling effect.

4.5 SUMMARY

The above findings can be summarized as follows:

(i) The X displacement is distorted in wave pattern due to hysteresis. Hysteresis causes the system gain to be larger and varying. The X RMSE of the open loop nonlinear system without electrode dislocation is 5.693 μm.

(ii) The Y error increases with time due to creep. Creep causes the system gain to increase with time.

(iii) When electrode dislocation exists, the X input affects the Y displacement significantly due to coupling effect. The peak-to-peak amplitude of the triangular pattern of the Y error of the open loop nonlinear system with electrode dislocation (2.3 μm) is larger than that of the open loop nonlinear system without electrode dislocation (0.4 μm).

(iv) The open loop nonlinear system is unstable in both X direction and Y direction. The performance of the open loop nonlinear system is unsatisfactory.

(v) Both the PI controller and the OFC can compensate hysteresis. The X RMSE of the closed loop nonlinear system with electrode dislocation using the PI controller is 2.908 μm and that of the closed loop nonlinear system with electrode dislocation using the OFC is 2.003 μm. Both of them are smaller than that of the open loop nonlinear system with electrode dislocation which is 5.619 μm. The data also show that the OFC is better than the PI controller regarding the compensation of hysteresis.

(vi) Both the PI controller and the OFC can compensate coupling effect. The peak-to-peak amplitude of triangular pattern of the Y error of the closed loop nonlinear system with electrode dislocation using the PI controller is 0.6 μm and that of the closed loop nonlinear system with electrode dislocation using the OFC is 1.5 μm. Both of them are smaller than that of the open loop nonlinear system with electrode dislocation which is 2.3 μm. The data also show that the PI is better than the OFC controller regarding the compensation of coupling effect.

(vii) Both of the PI controller and the OFC can improve the stability of the system in X direction. However, the Y error of the closed loop nonlinear system with electrode dislocation using the PI controller and the OFC diverge. Also, both of them cannot compensate creep. The PI controller and the OFC are not perfect.

CHAPTER 5

DEVELOPMENT AND PERFORMANCE OF ADAPTIVE SLIDING MODE CONTROLLER

5.1 INTRODUCTION

In the previous chapter, the performance of the PI controller and the OFC has been discussed. In this chapter, an advanced controller called the ASMC is developed. Since the piezoelectric tube actuator is influenced by coupling effect, creep and hysteresis, it can be characterized as a MIMO nonlinear time-varying system with uncertainty. In this thesis, it is simply called a nonlinear system because of convenience. The performance of the proposed sliding mode controller on forcing the error to converge to zero for such system is investigated in this chapter. Unlike the PI controller and the OFC, the ASMC belongs to the class of nonlinear controller. The structure of the sliding mode controller changes according to the sliding surface. Therefore, the performance of the ASMC is expected to be better than that of the PI controller and the OFC when it is adopted in the piezoelectric tube actuator.

The ASMC is designed based on the reduced order nonlinear FE model in state space form (Eq. (3.62b) and Eq. (3.63)) derived in Chapter 3. A continuous-time dynamic model of backlash-like hysteresis is adopted in the controller design process in order to enhance the performance on compensation of hysteresis. The reference model is established by optimal control for track following. The reference model is built because it provides more information for controller design. The PI sliding surface is stated on which the ASMC is insensitive to the matched uncertainty. The control law is then developed by unit vector nonlinear control together with equivalent control. The unit vector nonlinear control drives the system onto the sliding surface. The equivalent control forces the error to converge to zero when the system is on the sliding surface. A sliding mode observer called Walcott Zak observer is applied to estimate the unmeasurable states. Therefore, the degree of freedom of the ASMC is free to be chosen. Lyapunov criterion is stated to guarantee the stability of the closed loop system theoretically. The adaptive laws which can search appropriate controller gains automatically are also developed in the Lyapunov criterion. The initial controller gains are calculated by known information of the reduced order nonlinear FE model (Eq. (5.4ℓ)) instead of a guess in order to reduce the initial difference between the initial value and the true value. The responses of the closed loop nonlinear system with electrode dislocation using the ASMC are simulated and compared with those of the closed loop nonlinear system with electrode dislocation using the PI controller and the OFC which have been obtained in Chapter 4. The error minimization ability and the stability improvement ability of those controllers are discussed.

5.2 ASSUMPTIONS AND CONDITIONS

The ASMC is developed based on the following assumptions:

(1) The bounded time varying nonlinear uncertainty $[D_1]$ can match with the true modified input matrix $[B_1]$ such that $[D_1]=[B_1][D_{1m}]$.

(2) The overall uncertainty $[D_2]$ can match with the modified input matrix for controller design $[\bar{B}_1]$ such that $[D_2]=[\bar{B}_1][D_{2m}]$.

(3) The system of the piezoelectric tube actuator is reachable. It means that some eigenvalues of $\{[A]-[B][K_m]\}$ can be changed. The unchangeable eigenvalues are in the negative-half of the complex plane.

(4) The system of the piezoelectric tube actuator is detectable. It means that some eigenvalues of $\{[A]-[L_o][C]\}$ can be changed. The unchangeable eigenvalues are in the negative-half of the complex plane.

The following conditions should be satisfied:

(1) The design matrix for the reference states $[Q_m]$, the design matrix for the input to the reference model $[R_m]$, Lyapunov matrix for estimation errors of control gains of equivalent control $[M_1]$, $[M_2]$, $[M_3]$ and the design matrix for the observer $[Q]$ are positive definite.

(2) $\{[A]-[L_o][C]\}$ is Hurwitz by tuning the observer gain $[L_o]$. The observer error $[\varepsilon_o]$ converges to zero with this condition being satisfied.

5.3 CONTROLLER DESIGN

5.3.1 Hysteresis Model for Controller Design

The method of implementing the Prandtl-Ishlinskii hysteresis model into the ASMC design process has been proposed by Su *et al*. (2005). The Prandtl-Ishlinskii hysteresis model is fused in the control law aiming to release a signal to cancel the creep and the hysteresis influencing the error dynamics. The control gain of the Prandtl-Ishlinskii hysteresis model is adapted through the Prandtl-Ishlinskii hysteresis model itself and the sliding surface. Another method for enhancing the ability of the controller in hysteresis compensation has been developed by Su *et al*. (2000). A continuous-time dynamic model of backlash-like hysteresis which can model the backlash-like hysteresis such as the type of hysteresis exhibiting in piezoelectric material (Bashash *et al.*, 2009) has been proposed. According to this model, the hysteresis can be approximated by dividing it into a linear part and a bounded time-varying uncertain part which is shown in Eq. (5.1a). The error caused by the bounded time-varying uncertain part of hysteresis will converge to zero when the system reaches the sliding surface. Comparing these two methods, the benefit of the method proposed in Su *et al*. (2005) is that since the hysteresis is not considered as an uncertainty, the controller reaching gain ρ_c and the observer reaching gain ρ_o are smaller. It reduces the amplitude of the high frequency unit vector control signal; hence, the risk of exciting high frequency dynamics is reduced. The benefit of the method proposed in Su *et al*. (2000) is that the full knowledge of the parameters of the hysteresis model proposed by Su *et al*. (2000)

shown in Eq. (5.1b) in the thesis are not required. The necessary known information is the slope of the linear part k_h and the uniform bound of the bounded time-varying uncertain part $d_h(u_h)$ in order to determine the settings of the controller reaching gain ρ_c and the observer reaching gain ρ_o. Also, online computation of the outputs of the hysteresis models is not required so the computational effort is reduced.

The method proposed by Su *et al*. (2000) is adopted in the controller design of this thesis. The continuous-time dynamic model of backlash-like hysteresis is given (Su *et al.*, 2000):

$$H(t) = k_h u_h(t) + d_h(u_h), \tag{5.1a}$$

where

$$\begin{aligned} d_h(u_h) = {} & \left[H(0) - k_h u_h(0)\right] e^{-\alpha_h (u_h(t) - u_h(0)) \operatorname{sgn}(\dot{u}_h(t))} \\ & + e^{-\alpha_h u_h(t) \operatorname{sgn}(\dot{u}_h(t))} \int_{u_h(0)}^{u_h(t)} (\kappa_h - k_h) e^{\alpha_h \upsilon_h \operatorname{sgn}(\dot{u}_h(t))} d\upsilon_h . \end{aligned} \tag{5.1b}$$

$H(t)$, k_h and $d_h(u_h)$ denote the output, the slope of the linear part and the bounded time-varying uncertain part of the continuous-time dynamic model respectively. κ_h denotes threshold of the continuous-time dynamic model. α_h denotes switching rate of the continuous-time dynamic model. Since (Su *et al.*, 2000):

$$\lim_{u_h \to \infty} d_h(u_h) = -\frac{(k_h - \kappa_h)}{\alpha_h} \tag{5.2a}$$

$$\lim_{u_h \to -\infty} d_h(u_h) = \frac{(k_h - \kappa_h)}{\alpha_h}. \tag{5.2b}$$

$d_h(u_h)$ is shown to be bounded. $H(t)$ switches between $\frac{(k_h - \kappa_h)}{\alpha_h}$ and $-\frac{(k_h - \kappa_h)}{\alpha_h}$ with the switching rate α_h. The backlash-distance is determined by $\frac{(k_h - \kappa_h)}{\alpha_h}$. Changing κ_h can alter the backlash distance. $\kappa_h < k_h$ should be satisfied. The slope of the linear part of the continuous-time dynamic model k_h is equivalent to the proportional constant for the Prandtl-Ishlinskii hysteresis operator b_j. Superposition of a number of the Prandtl-Ishlinskii operators is adopted in simulation, therefore:

$$k_h = \sum_{j=1}^{N_J} b_j \ . \tag{5.3}$$

In practice, the value of k_h is obtained by observing the slope of the hysteresis loop with periodic input.

5.3.2 Adaptive Sliding Mode Controller

First of all, the controller is designed based on the nonlinear state space equation of the piezoelectric tube actuator developed in Chapter 3. Recall the state equation of the state space model given by Eq. (3.62b):

$$[\dot{x}] = [A][x] + [B][u_E] + [G][\chi] + [K_g] \ . \tag{5.4a}$$

Eq. (5.1a) is substituted into Eq. (5.4a):

$$[\dot{x}] = [A][x] + [B][u_E] + [G]\begin{bmatrix} \varepsilon_{cVX} \\ \varepsilon_{cVY} \\ k_h V_{EX} + d_{hVX} \\ p_{VY} \end{bmatrix} + [K_g]. \tag{5.4b}$$

Since the remnant polarization due to voltage at X-pair electrodes p_{VX} exhibits hysteresis with periodic input, it can be modelled by the continuous-time dynamic model. In contrary, the Y input is a dominant pseudo-step. The remnant polarization due to voltage at Y-pair electrodes p_{VY} can be ignored ($p_{VY} \approx 0$). The linear part and the bounded time-varying uncertain part are separated (Su *et al.*, 2000):

$$[\dot{x}] = [A][x] + [B][u_E] + \left\{ [G]\begin{bmatrix} 0 & 0 \\ 0 & 0 \\ k_h & 0 \\ 0 & 0 \end{bmatrix} \right\} [u_E] + [G]\begin{bmatrix} \varepsilon_{cVX} \\ \varepsilon_{cVY} \\ d_{hVX} \\ 0 \end{bmatrix} + [K_g] \tag{5.4c}$$

$$[\dot{x}] = [A][x] + [B_1][u_E] + [D_1] + [K_g], \tag{5.4d}$$

where

$$[B_1] = [B] + [G]\begin{bmatrix} 0 & 0 \\ 0 & 0 \\ k_h & 0 \\ 0 & 0 \end{bmatrix} \tag{5.4e}$$

$$[D_1] = [G][\varepsilon_{cVX} \quad \varepsilon_{cVY} \quad d_{hVX} \quad 0]^T. \tag{5.4f}$$

$[B_1] \in \Re^{n\times 2}$ denotes the true modified input matrix. $[D_1] \in \Re^n$ denotes the bounded time varying nonlinear uncertainty. d_{hVX} denotes the bounded time varying nonlinear uncertainty of the continuous-time dynamic model due to voltage at X-pair electrode. It is assumed that the bounded time varying nonlinear uncertainty $[D_1]$ can match with the true modified input matrix $[B_1]$ (Chapter 5

Assumption 1) such that (Perruquetti and Barbot, 2002):

$$[D_1] = [B_1][D_{1m}], \tag{5.4g}$$

where $[D_{1m}] \in \Re^2$ denotes the matched bounded time varying nonlinear uncertainty. Therefore, Eq. (5.4d) becomes:

$$[\dot{x}] = [A][x] + [B_1][u_E] + [B_1][D_{1m}] + [K_g]. \tag{5.4h}$$

Due to the electrode dislocation, there is a difference between the true modified input matrix of $[B_1]$ and the modified input matrix for controller design $[\overline{B}_1] \in \Re^{n\times 2}$. The perturbation for the modified input matrix $[\Delta B_1] \in \Re^{n\times 2}$ is introduced to the state equation Eq. (5.4d). The perturbation for the constant term due to gravity $[\Delta K_g] \in \Re^n$ is also introduced to Eq. (5.4d) for bias estimation such that:

$$[B_1] = [\overline{B}_1] + [\Delta B_1] \tag{5.4i}$$

$$[K_g] = [\overline{K}_g] + [\Delta K_g], \tag{5.4j}$$

where $[\overline{K}_g] \in \Re^n$ is the constant term due to gravity for controller design. Eq. (5.4i) and Eq. (5.4j) are substituted into Eq. (5.4d):

$$[\dot{x}] = [A][x] + [\overline{B}_1][u_E] + [\Delta B_1][u_E] + [D_1] + [\overline{K}_g] + [\Delta K_g] \tag{5.4k}$$

$$[\dot{x}] = [A][x] + [\overline{B}_1][u_E] + [D_2] + [\overline{K}_g], \tag{5.4ℓ}$$

where $[D_2] \in \Re^n$ denotes the overall uncertainty:

$$[D_2] = [\Delta B_1][u_E] + [D_1] + [\Delta K_g]. \tag{5.4m}$$

It is assumed that the overall uncertainty $[D_2]$ can match with the modified input

matrix for controller design $[\overline{B}_1]$ (Chapter 5 Assumption 2) (Perruquetti and Barbot, 2002):

$$[D_2] = [\overline{B}_1][D_{2m}], \tag{5.4n}$$

where $[D_{2m}] \in \Re^2$ is the matched overall uncertainties. Therefore, Eq. (5.4ℓ) becomes:

$$[\dot{x}] = [A][x] + [\overline{B}_1][u_E] + [\overline{B}_1][D_{2m}] + [\overline{K}_g]\ . \tag{5.4o}$$

Concerning the matching conditions shown in Eq. (5.4g) and Eq. (5.4n), it is pointed out that the terms $[\Delta B_1][u_E]$ and $[\Delta K_g]$ are matched with $[\overline{B}_1]$ and the nonlinear uncertainty $[D_1]$ is matched with both $[B_1]$ and $[\overline{B}_1]$.

The reference model is developed for track following. The objective of the ASMC is to force the states of the closed loop system to track the reference states instead of the desired output. The benefit of using reference model is that more information is available for controller design. The reference model is given as:

$$[\dot{x}_m] = [A_m][x_m] + [B_m][r] \tag{5.5a}$$

$$[y_m] = [C][x_m], \tag{5.5b}$$

where $[A_m] \in \Re^{n\times n}$ denotes the reference system matrix and $[B_m] \in \Re^{n\times 2}$ denotes the reference input matrix. $[x_m] \in \Re^n$ and $[y_m] \in \Re^2$ are the reference state vector and the reference output vector respectively. The best way to design the reference system matrix $[A_m]$ and the reference input matrix $[B_m]$ is making use of the reduced order linear FE model (Eq. (3.63) and Eq. (3.65)) without the constant term due to gravity $[K_g]$ of the piezoelectric tube actuator shown in Eq.

(3.65). However, the reference output $[y_m]$ may be unsatisfactory. It is necessary to apply the optimal control to tune the reference model and the detail is shown in Appendix D.

The state error vector is defined:

$$[e_s] = [x] - [x_m], \tag{5.6}$$

where $[e_s] \in \Re^n$ denotes the state error vector. The error dynamic equation is derived by subtracting Eq. (5.5a) from Eq. (5.4h):

$$[\dot{e}_s] = [A][x] + [B_1][u_E] + [B_1][D_{1m}] + [K_g] - [A_m][x_m] - [B_m][r] \tag{5.7a}$$

$$= [A_m][e_s] + [B_1][u_E] + [B_1][D_{1m}] + [K_g] + \{[A] - [A_m]\}[x] - [B_m][r] \ . \tag{5.7b}$$

The sliding surface is defined as (Fei and Batur, 2009):

$$[s] = [K_s][e_s] - \int_0^t [K_s][A_m][e_s] d\tau \ , \tag{5.8}$$

where $[s] \in \Re^2$ is the sliding surface and $[K_s] \in \Re^{2 \times n}$ is the sliding mode matrix. The derivative of the sliding surface is given:

$$[\dot{s}] = [K_s][\dot{e}_s] - [K_s][A_m][e_s] \tag{5.9a}$$

$$= [K_s]\{[A] - [A_m]\}[x] + [K_s][B_1][u_E] + [K_s][B_1][D_{1m}]$$

$$+ [K_s][K_g] - [K_s][B_m][r]. \tag{5.9b}$$

The equivalent control is derived by setting $[\dot{s}] = [0]$ (Perruquetti and Barbot, 2002):

$$[u_{eq}] = \{[K_s][B_1]\}^{-1}[K_s]\{[A_m] - [A]\}[x] + \{[K_s][B_1]\}^{-1}[K_s][B_m][r]$$

$$- \{[K_s][B_1]\}^{-1}[K_s][K_g] - [D_{1m}] \tag{5.10a}$$

$$= [K_1][x] + [K_2][r] + [K_3] - [D_{1m}], \tag{5.10b}$$

where

$$[K_1] = \{[K_s][B_1]\}^{-1}[K_s]\{[A_m] - [A]\} \tag{5.10c}$$

$$[K_2] = \{[K_s][B_1]\}^{-1}[K_s][B_m] \tag{5.10d}$$

$$[K_3] = -\{[K_s][B_1]\}^{-1}[K_s][K_g]. \tag{5.10e}$$

$[u_{eq}] \in \Re^2$ is the equivalent control. The values of the true control gains of the equivalent control $[K_1] \in \Re^{2\times n}$, $[K_2] \in \Re^{2\times 2}$ and $[K_3] \in \Re^2$ can be estimated through adaptive laws. The development of the adaptive laws will be shown in Section 5.3.4. By substituting Eq. (5.10a) into Eq. (5.7b) and using Eq. (5.10c) – Eq. (5.10e), the error dynamics on the sliding surface can be expressed as:

$$[\dot{e}_s] = [A_m][e_s]. \tag{5.11}$$

The detail of derivation of Eq. (5.11) is shown in Appendix E. The error dynamics in Eq. (5.11) implies that the error converges to zero on the sliding surface though the matched uncertainty exists. It is noted that the error dynamics of the closed loop system is still affected by matched uncertainty in the reaching phase. Reaching phase means that the sliding surface is not yet reached. Therefore, $[s] \neq [0]$.

The control signal of the ASMC is given:

$$[u_E] = [\hat{K}_1][x] + [\hat{K}_2][r] + [\hat{K}_3] + [w_c], \tag{5.12a}$$

where

$$[w_c] = -\rho_c \frac{[s]}{\|[s]\|}, \qquad [s] \neq [0] \tag{5.12b}$$

$[w_c]=[0]$, otherwise. (5.12c)

$\rho_c > 0$ is the controller reaching gain. $[\hat{K}_1] \in \Re^{2\times n}$, $[\hat{K}_2] \in \Re^{2\times 2}$ and $[\hat{K}_3] \in \Re^2$ are the estimates of the control gains of equivalent control $[K_1]$, $[K_2]$ and $[K_3]$ respectively. The overall control signal consists of two parts, the equivalent control and the unit vector nonlinear control $[w_c] \in \Re^2$. The unit vector nonlinear control takes action to force the system to enter onto the sliding surface when it is still in reaching phase $[s] \neq [0]$. The equivalent control is responsible to force the error to converge to zero (Eq. (5.11)) when the system is on the sliding surface of the controller $[s]=[0]$. Therefore, the error can be ensured to converge to zero with the combination of the equivalent control and the unit vector nonlinear control.

5.3.3 Sliding Mode Observer

Simple Luenberger observer is influenced by coupling effect, creep and hysteresis so it cannot function properly in the application of piezoelectric tube actuator. Instead, a Walcott Zak observer is implemented for observing the unmeasureable states in order that the degree of freedom of the controller can be increased and chosen freely by designer (Chen and Saif, 2006; and Fei and Batur, 2008). The sliding surface and the control signal are restated based on the estimated states.

The dynamics of the sliding mode observer is given as:

$$[\dot{\hat{x}}] = [A][\hat{x}] + [\overline{B}_1][u_E] - [L_o]\{[C][\hat{x}] - [y]\} + [\overline{K}_g] + [\overline{B}_1][w_o], \tag{5.13a}$$

where

$$[w_o] = -\rho_o \frac{[F_o][C][\varepsilon_o]}{\|[F_o][C][\varepsilon_o]\|}, \quad [F_o][C][\varepsilon_o] \neq [0] \tag{5.13b}$$

$$[w_o] = [0], \qquad \text{otherwise,} \tag{5.13c}$$

and $[\varepsilon_o] \in \Re^n$ denotes the observer error which is defined as:

$$[\varepsilon_o] = [\hat{x}] - [x]. \tag{5.14}$$

$[\hat{x}] \in \Re^n$ denotes the estimated state vector. $[L_o] \in \Re^{n\times 2}$ denotes the observer gain which determines the convergence rate of the observer error $[\varepsilon_o]$. $\rho_o > 0$ is the observer reaching gain. $[F_o] \in \Re^{2\times 2}$ is the observer sliding surface design matrix. $[w_o] \in \Re^2$ denotes the unit vector dynamics of the sliding mode observer which forces the system on the sliding surface of the observer. By subtracting Eq. (5.4o) from Eq. (5.13a), the observer error dynamics is derived as:

$$[\dot{\varepsilon}_o] = \{[A] - [L_o][C]\}[\varepsilon_o] + [\overline{B}_1][w_o] - [\overline{B}_1][D_{2m}]. \tag{5.15}$$

The system of the piezoelectric tube actuator is required to be detectable (Chapter 5 Assumption 4). $\{[A] - [L_o][C]\}$ is Hurwitz by tuning the observer gain $[L_o]$. The observer error $[\varepsilon_o]$ converges to zero with this condition satisfied (Chapter 5 Condition 2) and the convergence of the observer error $[\varepsilon_o]$ is proven in Section 5.3.4. The estimated error is given:

$$[\hat{e}_s] = [\hat{x}] - [x_m], \tag{5.16}$$

where $[\hat{e}_s] \in \Re^n$ is the estimated state error vector. Once the observer error $[\varepsilon_o]$

converges, the estimated error dynamic equation has the same structure as the error dynamic equation shown in Eq. (5.7b). The following estimated sliding surface can be adopted:

$$[\hat{s}] = [K_s][\hat{e}_s] - \int_0^t [K_s][A_m][\hat{e}_s]d\tau, \tag{5.17}$$

where $[\hat{s}] \in \Re^2$ denotes the estimated sliding surface. By following the same derivation from Eq. (5.8)-(5.11), the same conclusion in Section 5.3.2 is made such that the estimated error converges to zero on the estimated sliding surface of sliding mode controller. The control signal is restated:

$$[u_E] = [\hat{K}_1][\hat{x}] + [\hat{K}_2][r] + [\hat{K}_3] + [\hat{w}_c], \tag{5.18a}$$

where $[\hat{w}_c] \in \Re^2$ is the estimated unit vector nonlinear control given by:

$$[\hat{w}_c] = -\rho_c \frac{[\hat{s}]}{\|[\hat{s}]\|}, \qquad [\hat{s}] \neq [0] \tag{5.18b}$$

$$[\hat{w}_c] = [0], \qquad \text{otherwise.} \tag{5.18c}$$

By substituting Eq. (5.18a) into Eq. (5.13a), the following equation is obtained:

$$\begin{aligned}[\dot{\hat{x}}] = [A][\hat{x}] + [\overline{B}_1]\{[\hat{K}_1][\hat{x}] + [\hat{K}_2][r] + [\hat{K}_3] + [\hat{w}_c]\} - [L_o][C][\varepsilon_o] \\ + [\overline{K}_g] + [\overline{B}_1][w_o].\end{aligned} \tag{5.19}$$

Define:

$$[\tilde{K}_1] = [\hat{K}_1] - [K_1] \tag{5.20a}$$

$$[\tilde{K}_2] = [\hat{K}_2] - [K_2] \tag{5.20b}$$

$$[\tilde{K}_3] = [\hat{K}_3] - [K_3], \tag{5.20c}$$

where $[\tilde{K}_1] \in \Re^{2\times n}$, $[\tilde{K}_2] \in \Re^{2\times 2}$ and $[\tilde{K}_3] \in \Re^2$ denote the estimation errors of

the control gains of equivalent control $[K_1]$, $[K_2]$ and $[K_3]$ respectively. By substituting Eq. (5.4j), Eq. (5.10c) – Eq. (5.10e) and Eq. (5.20a) – Eq. (5.20c) into Eq. (5.19), the following equation can be derived:

$$\begin{aligned}[\dot{\hat{x}}] &= [A][\hat{x}] + [B_1][\tilde{K}_1][\hat{x}] + [B_1][K_1][\hat{x}] + [B_1][\tilde{K}_2][r] + [B_1][K_2][r] \\ &\quad + [B_1][\tilde{K}_3] + [B_1][K_3] - [\Delta B_1]\left\{[\hat{K}_1][\hat{x}] + [\hat{K}_2][r] + [\hat{K}_3]\right\} \qquad (5.21a) \\ &\quad + [\bar{B}_1][\hat{w}_c] - [L_o][C][\varepsilon_o] + [\bar{K}_g] + [\bar{B}_1][w_o] \\ &= [A_m][\hat{x}] + [B_m][r] \\ &\quad + [B_m]\left\{[K_2]^{-1}[\tilde{K}_1][\hat{x}] + [K_2]^{-1}[\tilde{K}_2][r] + [K_2]^{-1}[\tilde{K}_3]\right\} \\ &\quad - [\Delta B_1]\left\{[\hat{K}_1][\hat{x}] + [\hat{K}_2][r] + [\hat{K}_3]\right\} + [\bar{B}_1][\hat{w}_c] + [\bar{B}_1][w_o] \qquad (5.21b) \\ &\quad - [L_o][C][\varepsilon_o] - [\Delta K_g].\end{aligned}$$

The estimated error dynamic equation becomes:

$$\begin{aligned}[\dot{\hat{e}}_s] &= [A_m][\hat{e}_s] + [B_m]\left\{[K_2]^{-1}[\tilde{K}_1][\hat{x}] + [K_2]^{-1}[\tilde{K}_2][r] + [K_2]^{-1}[\tilde{K}_3]\right\} \\ &\quad - [\Delta B_1]\left\{[\hat{K}_1][\hat{x}] + [\hat{K}_2][r] + [\hat{K}_3]\right\} + [\bar{B}_1][\hat{w}_c] + [\bar{B}_1][w_o] \qquad (5.22) \\ &\quad - [L_o][C][\varepsilon_o] - [\Delta K_g].\end{aligned}$$

The derivative of the estimated sliding surface becomes:

$$\begin{aligned}[\dot{\hat{s}}] &= [K_s][\dot{\hat{e}}_s] - [K_s][A_m][\hat{e}_s] \qquad (5.23a) \\ &= [K_s][B_m]\left\{[K_2]^{-1}[\tilde{K}_1][\hat{x}] + [K_2]^{-1}[\tilde{K}_2][r] + [K_2]^{-1}[\tilde{K}_3]\right\}\end{aligned}$$

$$-[K_s][\Delta B_1]\left\{[\hat{K}_1][\hat{x}]+[\hat{K}_2][r]+[\hat{K}_3]\right\}+[K_s][\bar{B}_1][\hat{w}_c]+[K_s][\bar{B}_1][w_o]$$
$$-[K_s][L_o][C][\varepsilon_o]-[K_s][\Delta K_g]. \tag{5.23b}$$

5.3.4 Lyapunov Criterion

Lyapunov equation is developed for exhibiting the theoretical stability of the proposed ASMC. Moreover, the adaptive laws for estimating the controller gains of the control signal are established.

The Lyapunov candidate is selected as:

$$V_L=\frac{1}{2}[\hat{s}]^T[\hat{s}]+\frac{1}{2}tr\left\{[\tilde{K}_1]^T[M_1]^{-1}[\tilde{K}_1]\right\}+\frac{1}{2}tr\left\{[\tilde{K}_2]^T[M_2]^{-1}[\tilde{K}_2]\right\}$$
$$+\frac{1}{2}tr\left\{[\tilde{K}_3]^T[M_3]^{-1}[\tilde{K}_3]\right\}+\frac{1}{2}[\varepsilon_o]^T[P_o][\varepsilon_o]>0, \tag{5.24a}$$

where

$$[M_1]=[K_2][C_1] \tag{5.24b}$$

$$[M_2]=[K_2][C_2] \tag{5.24c}$$

$$[M_3]=[K_2][C_3]. \tag{5.24d}$$

V_L is Lyapunov function. $[C_1]\in\Re^{2\times2}$, $[C_2]\in\Re^{2\times2}$ and $[C_3]\in\Re^{2\times2}$ are the adaptive gains to suit the adaptation speed of $[K_1]$, $[K_2]$ and $[K_3]$ respectively. $[M_1]\in\Re^{2\times2}$, $[M_2]\in\Re^{2\times2}$ and $[M_3]\in\Re^{2\times2}$ denote the Lyapunov matrix for the estimation errors of control gains of equivalent control $[\tilde{K}_1]$, $[\tilde{K}_2]$ and $[\tilde{K}_3]$

respectively. The adaptive gains $[C_1]$, $[C_2]$ and $[C_3]$ should be designed to satisfy the condition that $[M_1]$, $[M_2]$ and $[M_3]$ are positive definite (Chapter 5 Condition 1). $[P_o] \in \Re^{n \times n}$ denotes the Lyapunov matrix for the observer error $[\varepsilon_o]$. $[P_o]$ is positive definite and it is solved by Eq. (5.27). The derivative of Lyapunov equation is shown:

$$\begin{aligned} \dot{V}_L = & [\hat{s}]^T [\dot{\hat{s}}] + tr\left\{[\tilde{K}_1]^T [M_1]^{-1} [\dot{\tilde{K}}_1]\right\} + tr\left\{[\tilde{K}_2]^T [M_2]^{-1} [\dot{\tilde{K}}_2]\right\} \\ & + tr\left\{[\tilde{K}_3]^T [M_3]^{-1} [\dot{\tilde{K}}_3]\right\} + \frac{1}{2}\left\{[\varepsilon_o]^T [P_o][\dot{\varepsilon}_o] + [\dot{\varepsilon}_o]^T [P_o][\varepsilon_o]\right\}, \end{aligned} \tag{5.25}$$

where $tr\{\bullet\}$ denotes trace. By using Eq. (5.15), the last term of Eq. (5.25) can be expressed as follows:

$$-\frac{1}{2}[\varepsilon_o]^T [Q][\varepsilon_o] + [\varepsilon_o]^T [P_o][\overline{B}_1][w_o] - [\varepsilon_o]^T [P_o][\overline{B}_1][D_{2m}], \tag{5.26}$$

where the design matrix for the observer $[Q] \in \Re^{n \times n}$ is expressed:

$$[Q] = -\{[P_o]\{[A] - [L_o][C]\} + \{[A] - [L_o][C]\}^T [P_o]\}. \tag{5.27}$$

The design matrix for the observer $[Q]$ should be designed to be positive definite (Chapter 5 Condition 1). The Lyapunov matrix for the observer error $[P_o]$ is solved out and only the positive definite solution is selected. By differentiating Eq. (5.20a) – Eq. (5.20c), the following relations are obtained:

$$\left[\dot{\tilde{K}}_1\right] = \left[\dot{\hat{K}}_1\right] \tag{5.28a}$$

$$\left[\dot{\tilde{K}}_2\right] = \left[\dot{\hat{K}}_2\right] \tag{5.28b}$$

$$\left[\dot{\tilde{K}}_3\right] = \left[\dot{\hat{K}}_3\right]. \tag{5.28c}$$

By using Eq. (5.23b), Eq. (5.24b) – Eq. (5.24d), Eq. (5.26) and Eq. (5.28a) – Eq. (5.28c), Eq. (5.25) can be expressed:

$$\begin{aligned}
\dot{V}_L = & \left\{ tr\left\{\left[\tilde{K}_1\right]^T [M_1]^{-1}[C_1]^T [B_m]^T [K_s]^T [\hat{s}][\hat{x}]^T\right\} + tr\left\{\left[\tilde{K}_1\right]^T [M_1]^{-1}\left[\dot{\hat{K}}_1\right]\right\}\right\} \\
& + \left\{ tr\left\{\left[\tilde{K}_2\right]^T [M_2]^{-1}[C_2]^T [B_m]^T [K_s]^T [\hat{s}][r]^T\right\} + tr\left\{\left[\tilde{K}_2\right]^T [M_2]^{-1}\left[\dot{\hat{K}}_2\right]\right\}\right\} \\
& + \left\{ tr\left\{\left[\tilde{K}_3\right]^T [M_3]^{-1}[C_3]^T [B_m]^T [K_s]^T [\hat{s}]\right\} + tr\left\{\left[\tilde{K}_3\right]^T [M_3]^{-1}\left[\dot{\hat{K}}_3\right]\right\}\right\} \\
& + [\hat{s}]^T [K_s][\bar{B}_1][\hat{w}_c] + [\hat{s}]^T [K_s][\bar{B}_1][w_o] - [\hat{s}]^T [K_s][L_o][C][\varepsilon_o] \\
& - [\hat{s}]^T [K_s][\Delta K_g] - [\hat{s}]^T [K_s][\Delta B_1]\left\{[\hat{K}_1][\hat{x}] + [\hat{K}_2][r] + [\hat{K}_3]\right\} \\
& - \frac{1}{2}[\varepsilon_o]^T [Q][\varepsilon_o] + [\varepsilon_o]^T [P_o][\bar{B}_1][w_o] - [\varepsilon_o]^T [P_o][\bar{B}_1][D_{2m}].
\end{aligned} \tag{5.29}$$

The following adaptive laws are selected:

$$\left[\dot{\hat{K}}_1\right] = -[C_1]^T [B_m]^T [K_s]^T [\hat{s}][\hat{x}]^T \tag{5.30a}$$

$$\left[\dot{\hat{K}}_2\right] = -[C_2]^T [B_m]^T [K_s]^T [\hat{s}][r]^T \tag{5.30b}$$

$$\left[\dot{\hat{K}}_3\right] = -[C_3]^T [B_m]^T [K_s]^T [\hat{s}]. \tag{5.30c}$$

By using Eq. (5.13b), Eq. (5.18b) and Eq. (5.30a) – Eq. (5.30c), Eq. (5.29) can be reduced:

$$\dot{V}_L = -\frac{1}{2}[\varepsilon_o]^T [Q][\varepsilon_o] - \rho_c [\hat{s}]^T [K_s][B_1]\frac{[\hat{s}]}{\|[\hat{s}]\|}$$

$$
\begin{aligned}
&-\rho_o[\hat{s}]^T[K_s][\bar{B}_1]\frac{[F_o][C][\varepsilon_o]}{\|[F_o][C][\varepsilon_o]\|}-[\hat{s}]^T[K_s][L_o][C][\varepsilon_o]-[\hat{s}]^T[K_s][\Delta K_g]\\
&-[\hat{s}]^T[K_s][\Delta B_1]\{[\hat{K}_1][\hat{x}]+[\hat{K}_2][r]+[\hat{K}_3]\}-\rho_o\frac{[\varepsilon_o]^T[P_o][\bar{B}_1][F_o][C][\varepsilon_o]}{\|[F_o][C][\varepsilon_o]\|}\\
&-[\varepsilon_o]^T[P_o][\bar{B}_1][D_{2m}],
\end{aligned}
\tag{5.31}
$$

where $\|\bullet\|$ denotes Euclidean norm. $[F_o]$ is chosen to satisfy the following relation:

$$
[F_o][C]=[\bar{B}_1]^T[P_o]. \tag{5.32}
$$

By using the inequality property of norm and Eq. (5.32), the following relation is established:

$$
\begin{aligned}
\dot{V}_L \le &-\frac{1}{2}[\varepsilon_o]^T[Q][\varepsilon_o]-\rho_c\lambda_{\min}([K_s][B_1])\|[\hat{s}]\|+\rho_o\|[K_s][\bar{B}_1]\|\|[\hat{s}]\|\\
&+\|[\hat{s}]\|\|[K_s][L_o]\|\|[C][\varepsilon_o]\|+\|[\hat{s}]\|\|[K_s]\|\|[\Delta K_g]\|+\|[\hat{s}]\|\|[K_s]\|\|[\Delta B_1]\|\|[\hat{K}_1]\|\|[\hat{x}]\|\\
&+\|[\hat{s}]\|\|[K_s]\|\|[\Delta B_1]\|\|[\hat{K}_3]\|-\rho_o\|[F_o][C][\varepsilon_o]\|+\|[F_o][C][\varepsilon_o]\|\|[D_{2m}]\|,
\end{aligned}
\tag{5.33}
$$

where $\lambda_{\min}(\bullet)$ denotes the eigenvalue with minimum real part. The following property is used:

$$
\lambda_{\min}([K_s][B_1])\|[\hat{s}]\|^2 \le [\hat{s}]^T[K_s][B_1][\hat{s}]. \tag{5.34}
$$

Finally, the following inequality is obtained:

$$
\begin{aligned}
\dot{V}_L \le &-\frac{1}{2}[\varepsilon_o]^T[Q][\varepsilon_o]-\lambda_{\min}([K_s][B_1])\|[\hat{s}]\|\{\rho_c-\{\rho_o+\|[K_s][L_o]\|\|[C][\varepsilon_o]\|\\
&+\|[K_s]\|\|[\Delta K_g]\|+\|[K_s]\|\|[\Delta B_1]\|\|[\hat{K}_1]\|\|[\hat{x}]\|+\|[K_s]\|\|[\Delta B_1]\|\|[\hat{K}_2]\|\|[r]\|\\
&+\|[K_s]\|\|[\Delta B_1]\|\|[\hat{K}_3]\|\}/\delta\}-\|[F_o][C][\varepsilon_o]\|\{\rho_o-\|[D_{2m}]\|\},
\end{aligned}
\tag{5.35}
$$

where the design scalar δ should satisfy:

$$\delta \le \lambda_{\min}\left([K_s][B_1]\right). \tag{5.36}$$

To ensure $\dot{V}_L \le 0$, the following conditions should be satisfied:

$$[Q] \ge 0 \tag{5.37a}$$

$$\rho_o \ge \|[D_{2m}]\| \tag{5.37b}$$

$$\begin{aligned}\rho_c \ge \Big\{&\rho_o + \|[K_s][L_o]\|\|[C][\varepsilon_o]\| + \|[K_s]\|\|[\Delta K_g]\| + \|[K_s]\|\|[\Delta B_1]\|\|[\hat{K}_1]\|\|[\hat{x}]\| \\ &+ \|[K_s]\|\|[\Delta B_1]\|\|[\hat{K}_2]\|\|[r]\| + \|[K_s]\|\|[\Delta B_1]\|\|[\hat{K}_3]\|\Big\}/\delta .\end{aligned} \tag{5.37c}$$

V_L is positive definite and $\dot{V}_L$ is negative semi-definite implies that $[\hat{s}]$, $[\tilde{\hat{K}}_1]$, $[\tilde{\hat{K}}_2]$, $[\tilde{\hat{K}}_3]$ and $[\varepsilon_o]$ are all bounded in the sense of Lyapunov stability (Ioannou and Sun, 1996). According to Barbălat's lemma (Ioannou and Sun, 1996), $[\hat{s}]$ and $[\varepsilon_o]$ converge to zero. According to the persistent excitation theory (Ioannou and Sun, 1996), the estimates of control gains of equivalent control $[\hat{K}_1]$ and $[\hat{K}_2]$ converge to the true value if the estimated state vector $[\hat{x}]$ and the desired output vector $[r]$ are persistent excitation signals in the Eq. (5.30a) and Eq. (5.30b). Both of the patterns of the estimated state vector $[\hat{x}]$ (Fig. F-1 – Fig. F-4) and the desired output vector $[r]$ (Fig. 5-8 and Fig. 5-9) show shape angles which actually is the sum of sine waves with different frequencies. Hence, the signals contain enough information for adaptation.

In practice, most of the signals in the control system are discrete. The adaptive law shown in Eq. (5.30a) requires current value of $[\hat{x}]$ but only the past value is

available. This may affect the adaptation and the degree of the effect depends on the computational speed. In addition, ρ_c and ρ_o should be large enough to satisfy Eq. (5.37b) and Eq. (5.37c) to ensure stability. However, ρ_c and ρ_o should not be too large otherwise the input amplifier may saturate.

The actual motion on the sliding surface can be regarded as the superposition of a slow motion along the surface and a fast motion perpendicular to the surface. Such phenomenon is called chattering effect (Perruquetti and Barbot, 2002). Chattering effect may excite unmodelled high frequency modes which cause instability. The following modified input which is based on the one used by Fei and Batur (2009) establishes a neighborhood boundary near the sliding surface to provide a soft switching for eliminating the chattering effect:

$$[u_E] = [\hat{K}_1][\hat{x}] + [\hat{K}_2][r] + [\hat{K}_3] - \rho_c \frac{[\hat{s}]}{\|[\hat{s}]\| + \gamma_c}, \tag{5.38}$$

where γ_c is the chattering constant for the controller. The observer can be modified as follows (Chen and Saif, 2006):

$$\begin{aligned}[\dot{\hat{x}}] = {} & [A][\hat{x}] + [\overline{B}_1][u_E] - [L_o]\{[C][\hat{x}] - [y]\} + [\overline{K}_g] \\ & - \rho_o [\overline{B}_1] \frac{[F_o][C][\varepsilon_o]}{\|[F_o][C][\varepsilon_o]\| + \gamma_o},\end{aligned} \tag{5.39}$$

where γ_o is the chattering constant for the observer. However, the soft switching mechanism causes $[e_s]$ and $[\varepsilon_o]$ to reduce to some small values rather than zero (Bashash and Jalili, 2009). The block diagram of the closed system is shown in Fig. 5-1.

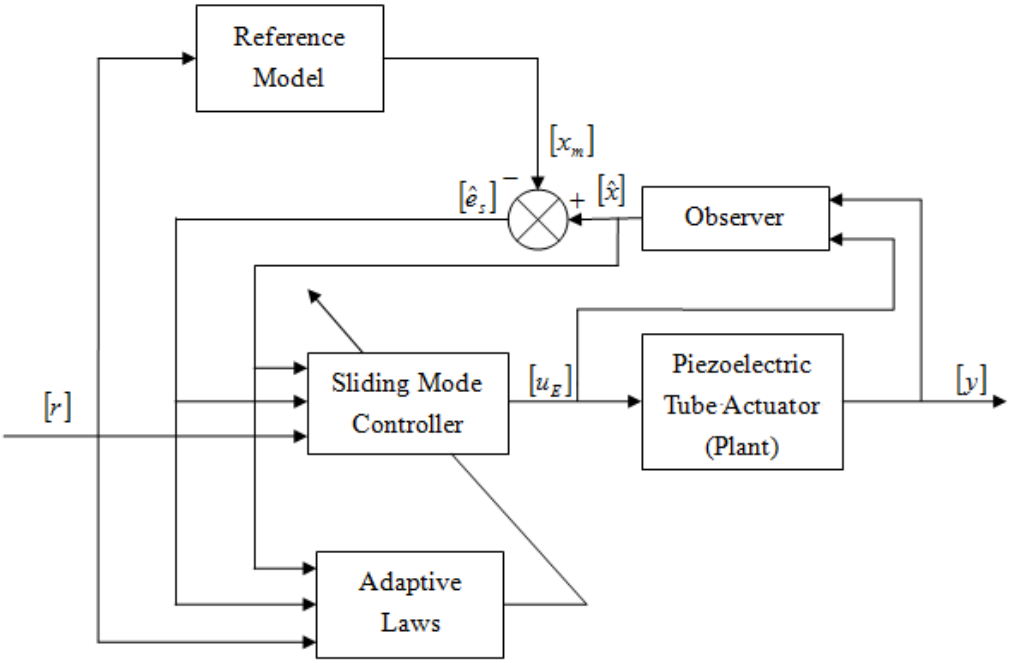

Figure 5-1. Block Diagram of Closed Loop System using ASMC

5.4 PROGRAM DEVELOPMENT

The simulation of the closed loop system using the ASMC is performed by MATLAB/SIMULINK 7.5. The connection of the blocks of the closed loop system using the ASMC is shown in Fig G-2 in Appendix F. The block connection of the plant model shown in Fig. G-1 is implemented into "Plant" block in Fig. G-2. The reference model (Eq. (5.5a) and Eq. (5.5b)) is implemented into "Reference Model" block. The estimated sliding surface (Eq. (5.17)) is implemented into "Sliding Surface" block. The adaptive laws (Eq. (5.30a) – Eq. (5.30c)) are implemented into "Adaptive Law 1" block, "Adaptive Law 2" block and "Adaptive Law 3" block respectively. The fourth term of the modified control law (Eq. (5.38)) is implemented into "Unit Vector Nonlinear Control" block. The modified sliding

mode observer (Eq. (5.39)) is implemented into "Observer" block. The block connection inside the "Observer" block is shown in Fig. G-3.

5.5 SIMULATION RESULTS OF CLOSED LOOP SYSTEM WITH ADAPTIVE SLIDING MODE CONTROLLER

In this section, the error minimization ability and the stability improvement ability of the ASMC on the reduced order nonlinear FE model (Eq. (3.62b) and Eq. (3.63)) with electrode dislocation are assessed. The performance of the ASMC is compared with that of the PI controller and the OFC. The simulations are based on the assumptions and conditions stated in Chapter 3 and the controller design of ASMC is based on the assumptions and the conditions stated in this chapter.

In practice, the dynamics of the model for controller design is an approximation of the real plant. Therefore, it is necessary to construct a controller with an order lower than that of the FE model of the plant in simulation. Referring to Chapter 3 Section 3.7, the reduced order nonlinear FE model (Eq. (3.62b) and Eq. (3.63)) with 35 retained states has the smallest RMSE (0.044 μm) and the reduced order nonlinear FE model (Eq. (3.62b) and Eq. (3.63)) with 20 retained states has the second smallest RMSE (0.099 μm). The reduced order nonlinear FE model (Eq. (3.62b) and Eq. (3.63)) with 20 retained states is used for controller design and the reduced order nonlinear FE model (Eq. (3.62b) and Eq. (3.63)) with 35 retained states is used as a plant in simulation.

The reduced order system matrix $[A]$, the reduced order input matrix $[B]$, the reduced order output matrix $[C]$, the nonlinear distribution matrix $[G]$ and the constant term due to gravity $[K_g]$ which can be found in the reduced order nonlinear FE model (Eq. (3.62b) and Eq. (3.63)) with 20 retained states are the known information for controller design. In addition, the slope of the linear part of the continuous-time dynamic model of backlash-like hysteresis k_h which can be obtained by observing the slope of the hysteresis loop with periodic input practically is also assumed to be known. Moreover, the reduced order input matrix $[B]$, the nonlinear distribution matrix $[G]$ and the slope of the linear part of the continuous-time dynamic model of backlash-like hysteresis k_h constitute the modified input matrix by Eq. (5.4e). Since it is assumed that the ASMC is designed based on the piezoelectric tube actuator without electrode dislocation, the reduced order input matrix $[B]$ should be obtained from the nonlinear FE model without electrode dislocation so the modified input matrix obtained by Eq. (5.4e) is the modified input matrix for controller design $[\overline{B}_1]$ which is not the true one. Also, the constant term due to gravity for controller design $[\overline{K}_g]$ adopts the constant term due to gravity $[K_g]$ obtained from the nonlinear FE model. Therefore, the modified input matrix for controller design $[\overline{B}_1]$ and the constant term due to gravity for controller design $[\overline{K}_g]$ are the known information. The values of the reduced order system matrix $[A]$, the modified input matrix for controller design $[\overline{B}_1]$, the constant term due to gravity for controller design $[\overline{K}_g]$, the reduced order output matrix $[C]$ and the slope of the linear part of the continuous-time dynamic model of backlash-like hysteresis k_h are given in Table 5-1.

Table 5-1. Model Parameters for Controller Design

$[A]$

$$\begin{bmatrix}
9.77 & 8.50 & 10.89 & 38.31 & 69.95 & -66.49 & -10.19 & 3.84 & -88.81 & 130.33 \\
-16.08 & 24.94 & 11.36 & 113.90 & -15.79 & -108.08 & 69.63 & -175.06 & -42.08 & -63.73 \\
-6.38 & 20.96 & 30.89 & 104.15 & 31.18 & -79.36 & -12.02 & -21.22 & 17.12 & 16.88 \\
5.37 & -6.31 & 5.96 & 23.15 & -9.29 & 2.68 & -0.65 & 69.89 & 15.18 & -31.49 \\
-2.59 & 5.63 & -5.69 & -33.89 & 11.45 & 36.53 & 6.72 & 3.99 & 84.92 & 46.79 \\
1.05 & 5.42 & 16.97 & 73.25 & -4.02 & -29.15 & 12.71 & 49.86 & 48.15 & -29.47 \\
-2.62 & 5.51 & -9.86 & -37.55 & 8.75 & 15.76 & 6.10 & -39.99 & 34.66 & 41.83 \\
-3.96 & 1.87 & -5.81 & -15.21 & -6.06 & 3.62 & 10.15 & -33.52 & -2.84 & -5.08 \\
1.68 & -3.39 & -1.91 & -12.56 & 0.92 & 6.79 & -9.23 & 4.11 & -12.03 & 11.21 \\
0.16 & -1.65 & 6.41 & 16.91 & -6.01 & -8.95 & -1.55 & 21.93 & -27.46 & -22.98 \\
3.15 & -0.26 & -6.37 & -11.70 & 3.40 & 5.57 & -6.84 & -2.45 & 8.45 & 17.67 \\
-0.42 & 2.13 & -3.38 & -13.49 & 0.66 & 11.05 & 13.83 & -13.96 & 0.93 & 9.31 \\
0.80 & 0 & 4.90 & 2.22 & 7.74 & -3.14 & -6.14 & 20.69 & -6.98 & 7.18 \\
1.04 & 2.61 & -0.60 & 1.50 & 5.91 & 1.65 & 9.37 & -9.18 & 3.81 & 17.43 \\
-0.66 & -1.84 & -3.38 & -11.18 & -5.83 & 10.21 & 6.82 & -7.05 & 1.35 & -3.78 \\
0.37 & 0.76 & 4.76 & 2.28 & 1.59 & -4.38 & -6.01 & 0.42 & 10.34 & -2.83 \\
-0.30 & -2.30 & -2.72 & -3.06 & -10.48 & 6.18 & 11.40 & -6.22 & 5.91 & -6.43 \\
-1.49 & 0.14 & 2.68 & 10.31 & 0.10 & -8.14 & 9.03 & 4.63 & -6.58 & 14.71 \\
-1.00 & 0.36 & 2.44 & 0.45 & 1.50 & 0.79 & 2.72 & 8.46 & -0.31 & -1.41 \\
-0.35 & -0.75 & -2.94 & -4.68 & 4.44 & 0.88 & -1.25 & 1.89 & 10.46 & 8.25
\end{bmatrix} \cdots$$

$$\cdots \begin{bmatrix}
37.26 & -64.37 & -81.32 & -14.83 & 33.58 & 19.72 & -13.22 & 26.56 & 1.46 & -7.85 \\
-48.93 & -25.06 & 21.16 & 26.97 & -17.46 & -5.53 & 9.97 & 39.31 & 3.67 & -16.18 \\
82.40 & 45.31 & 18.23 & -8.44 & 20.41 & -39.37 & -10.39 & 4.52 & 3.84 & 24.93 \\
-21.08 & 0.23 & -19.66 & -3.75 & 3.44 & 31.62 & -10.79 & -4.90 & 13.33 & -1.50 \\
21.70 & -18.68 & 25.01 & -21.98 & 31.99 & -5.36 & -5.36 & -8.17 & -44.16 & -32.84 \\
-14.81 & 6.13 & 0.85 & 5.94 & 16.19 & 27.22 & -17.30 & 8.56 & 29.42 & 12.63 \\
18.72 & -44.57 & 14.87 & 18.85 & 17.33 & -6.04 & -3.76 & -30.72 & 24.96 & 8.23 \\
-3.17 & -15.70 & 10.14 & 9.16 & -9.87 & -0.59 & 10.62 & -18.09 & -25.41 & -3.34 \\
7.73 & 9.83 & -5.19 & 1.84 & 0.40 & -4.45 & -12.23 & 9.08 & 0.89 & -12.03 \\
-8.11 & -4.53 & -0.93 & -23.47 & -4.10 & -3.09 & 9.93 & -44.47 & -9.21 & -13.72 \\
-4.00 & 0.27 & 3.63 & 47.03 & 17.02 & 9.06 & -31.01 & 31.45 & 76.57 & 24.27 \\
-9.98 & -10.64 & 17.03 & -33.75 & 15.64 & -13.41 & 10.82 & -37.63 & -1.11 & -16.31 \\
1.00 & -24.33 & 2.22 & -19.30 & -0.01 & 3.24 & 43.87 & -36.48 & -41.86 & -3.84 \\
-19.32 & 15.57 & 19.39 & -17.21 & 26.43 & -2.11 & -17.45 & -20.43 & -4.59 & -6.33 \\
-20.17 & 12.26 & -8.54 & -15.11 & -20.77 & 2.38 & 8.25 & 12.98 & -15.16 & 35.33 \\
4.51 & 6.74 & 2.74 & -3.47 & 19.45 & -7.23 & 3.98 & 8.59 & 69.81 & 5.64 \\
-3.17 & -9.67 & -23.19 & 11.56 & -13.83 & -3.13 & -11.00 & -2.76 & 5.03 & -6.73 \\
-6.49 & 2.33 & 15.72 & 18.25 & -13.04 & 7.07 & 6.82 & -8.40 & -25.57 & 10.20 \\
-13.72 & -15.85 & 13.43 & -0.23 & 9.82 & -29.26 & 1.76 & -10.26 & -10.80 & -17.40 \\
-8.08 & -2.45 & -28.85 & 3.61 & -26.96 & -5.84 & 1.46 & 19.15 & 21.71 & 7.22
\end{bmatrix} \times 10^4$$

$[\overline{B}_1]$	$\begin{bmatrix} -90.43 & 88.43 \\ 164.16 & -185.77 \\ 98.14 & -501.23 \\ 109.91 & 299.07 \\ -152.99 & 177.94 \\ 241.62 & 154.72 \\ 358.06 & -152.53 \\ 2.28 & -38.97 \\ 108.44 & 60.19 \\ -606.10 & -88.19 \\ 823.44 & -32.86 \\ -778.19 & -141.72 \\ -550.74 & -84.88 \\ -611.24 & -133.50 \\ -343.65 & -65.67 \\ 183.10 & -132.51 \\ 331.99 & 207.19 \\ -181.71 & -98.48 \\ -531.49 & -1.68 \\ 309.29 & 1.74 \end{bmatrix}$	$[C]$	$\begin{bmatrix} 0.64 & -1.25 \\ -1.55 & 4.05 \\ -3.28 & 3.51 \\ -12.05 & 18.95 \\ 1.08 & 4.00 \\ 3.37 & -18.41 \\ -1.03 & 5.68 \\ -6.73 & -17.07 \\ -14.07 & -9.00 \\ 6.74 & 2.10 \\ -2.24 & 1.21 \\ -6.17 & -3.51 \\ 4.91 & -2.29 \\ 1.14 & 0.45 \\ -3.26 & 1.61 \\ 0.16 & -1.36 \\ 1.90 & -0.55 \\ 0.09 & 4.91 \\ -1.76 & 1.35 \\ -0.92 & -1.28 \end{bmatrix}^T \times 10^{-6}$
$[G]$	$\begin{bmatrix} 18.99 & 34.83 & 3.06 & -2.63 \\ 0.98 & 25.54 & -5.55 & 5.36 \\ -30.92 & -1.57 & -3.28 & 16.26 \\ 53.39 & 12.13 & -3.71 & -10.74 \\ 59.18 & 41.17 & 5.12 & -4.08 \\ -41.11 & -10.23 & -8.15 & -6.63 \\ 20.67 & -4.38 & -12.04 & 3.47 \\ 116.04 & -6.19 & -0.08 & 1.33 \\ -72.24 & 3.27 & -3.65 & -2.02 \\ 91.84 & 0.37 & 20.40 & 4.45 \\ -314.07 & -32.01 & -27.71 & -2.38 \\ -25.86 & -12.36 & 26.20 & 7.25 \\ 226.22 & 15.85 & 18.53 & 4.54 \\ -238.54 & -61.20 & 20.58 & 6.28 \\ 67.54 & -43.26 & 11.58 & 3.26 \\ -166.89 & 15.43 & -6.15 & 3.31 \\ 119.71 & 26.51 & -11.17 & -7.85 \\ -18.46 & -82.28 & 6.10 & 3.69 \\ -89.13 & 22.41 & 17.87 & 1.92 \\ 15.65 & 28.69 & -10.42 & -1.61 \end{bmatrix} \times 10^{6}$	$[\overline{K}_g]$	$\begin{bmatrix} 243.06 \\ -56.94 \\ -34.22 \\ 349.11 \\ -870.17 \\ 530.06 \\ 879.37 \\ 177.11 \\ -88.09 \\ 261.39 \\ 543.88 \\ -16.12 \\ 82.41 \\ 1.69 \\ 185.38 \\ -29.81 \\ 153.36 \\ 124.78 \\ 60.88 \\ 77.71 \end{bmatrix} \times 10^{-6}$
k_h	-1.55×10^{-5}		

The control objective of the ASMC is to command the X and the Y displacements $[y]$ to track the reference X and the reference Y outputs $[y_m]$ shown in Fig. 5-2 and Fig. 5-3 respectively. Due to the dynamics of the reference

model, the reference displacement $[y_m]$ is different from the desired displacement $[r]$. The error between $[y_m]$ and $[r]$ should be minimized as much as possible by appropriate design for control gains of the reference model. The control parameters and the RMSEs for the reference model are shown in Table 5-2. It is shown in Fig. 5-2 and Fig. 5-3 that $[y_m]$ and $[r]$ are close to each other using the control parameters shown in Table 5-1. The feedback gain for the reference model $[K_m]$ in Eq. (D.16) can be calculated by MATLAB command "lqr". The X RMSE and the Y RMSE for the reference model (2.004 nm and 0.021 nm respectively) are small enough for tracking reference.

Table 5-2. Control Parameters and RMSEs for Reference Model

$[Q_m]$	$[I]_{20\times 20}$	$[K_m]$	$\begin{bmatrix} 0.09 & -1.85 \\ -3.57 & -9.34 \\ -1.98 & -10.18 \\ -11.47 & 10.73 \\ 9.33 & 3.61 \\ 24.85 & 5.58 \\ -11.71 & -3.41 \\ 37.90 & 6.97 \\ -7.45 & -16.62 \\ 4.40 & -5.75 \\ 5.78 & 2.26 \\ -3.06 & 1.10 \\ -9.82 & -9.28 \\ -7.13 & 7.82 \\ -5.12 & 5.31 \\ 8.64 & -8.01 \\ -4.63 & 10.42 \\ -4.24 & -10.78 \\ -5.91 & 1.22 \\ 1.24 & 3.30 \end{bmatrix}^T \times 10^{-2}$
$[R_m]$	$\begin{bmatrix} 0.1 & 0 \\ 0 & 0.1 \end{bmatrix}$		
$[N_m]$	$\begin{bmatrix} 3.88\times 10^8 & -1.8\times 10^7 \\ 9.62\times 10^6 & 2.63\times 10^8 \end{bmatrix}$		
X RMSE (nm)	2.004		
Y RMSE (nm)	0.021		

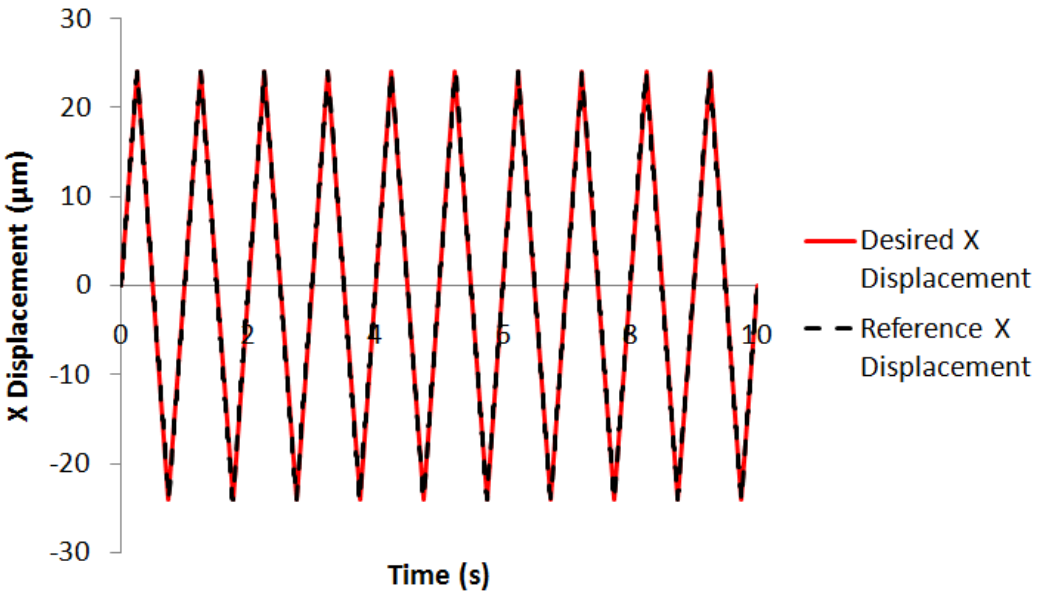

Figure 5-2. Desired and Reference X Displacements

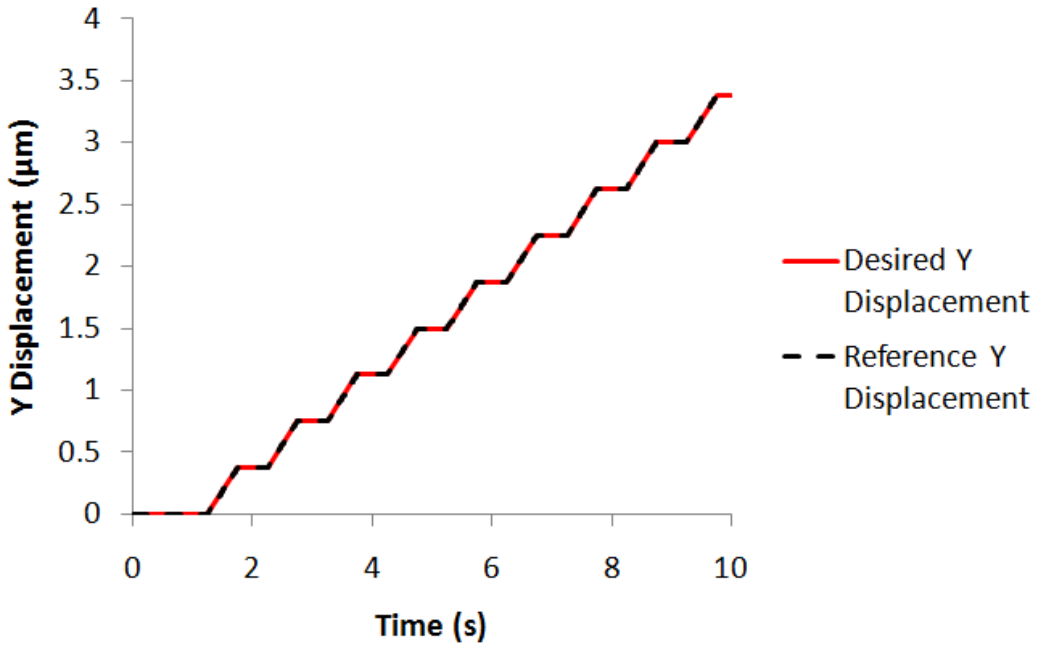

Figure 5-3. Desired and Reference Y Displacements

The settings of the ASMC and the Walcott Zak observer are shown in Table 5-3. The Lyapunov matrix for the observer error $[P_o]$ in Eq. (5.27) can be solved by MATLAB command "lyap". Since the dimension of $[P_o]$ is large, its values

are not given in this thesis. The initial estimates of control gains $\left[\hat{K}_1\right]_{initial} \in \Re^{2\times n}$, $\left[\hat{K}_2\right]_{initial} \in \Re^{2\times 2}$ and $\left[\hat{K}_3\right]_{initial} \in \Re^{2}$ are calculated based on the information of the reduced order FE model (Eq. (5.4*ℓ*)):

$$\left[\hat{K}_1\right]_{initial} = -\left\{\left[K_s\right]\left[\overline{B}_1\right]\right\}^{-1}\left[K_s\right]\left\{\left[A\right]-\left[A_m\right]\right\} \tag{5.40a}$$

$$\left[\hat{K}_2\right]_{initial} = \left\{\left[K_s\right]\left[\overline{B}_1\right]\right\}^{-1}\left[K_s\right]\left[B_m\right] \tag{5.40b}$$

$$\left[\hat{K}_3\right]_{initial} = -\left\{\left[K_s\right]\left[\overline{B}_1\right]\right\}^{-1}\left[K_s\right]\left[\overline{K}_g\right]. \tag{5.40c}$$

These choices of initial values allow the adaptation of the control gains starting at available values close to the true ones which are expressed in Eq. (5.10c) – Eq. (5.10e). This helps the estimated control gains to take less time to converge; hence, the transient response of the closed loop system is improved. The initial estimates of control gains are shown in Table 5-4.

Table 5-3. Settings for ASMC and Walcott Zak Observer

$[K_s]$	$\begin{bmatrix} 2.64 & 2.29 \\ 2.59 & 1.94 \\ 3.17 & 1.90 \\ 3.05 & 0.52 \\ 0.14 & 5.07 \\ 4.31 & 6.75 \\ 1.07 & 2.55 \\ 0.90 & 1.90 \\ 4.87 & 3.72 \\ 1.67 & 2.11 \\ 1.37 & 2.05 \\ 0.75 & 0.54 \\ 1.52 & 0.93 \\ 1.18 & 0.81 \\ 0.26 & 0.02 \\ 7.60 & 3.67 \\ 3.22 & 0.74 \\ 0.15 & 2.19 \\ 0.98 & 2.26 \\ 3.46 & 1.22 \end{bmatrix}^T \times 10^{-3}$	$[L_o]$	$\begin{bmatrix} 0.01 & 0.01 \\ 0.01 & 0.01 \\ 0.01 & 0.01 \\ 0.01 & 0.01 \\ 0.01 & 0.01 \\ 0.01 & 0.01 \\ 0.01 & 0.01 \\ 0.01 & 0.01 \\ 0.01 & 0.01 \\ 0.01 & 0.01 \\ 0.01 & 0.01 \\ 0.01 & 0.01 \\ 0.01 & 0.01 \\ 0.01 & 0.01 \\ 0.01 & 0.01 \\ 0.01 & 0.01 \\ 0.01 & 0.01 \\ 0.01 & 0.01 \end{bmatrix}$
$[C_1]$	$\begin{bmatrix} 4.1 & 2.2 \\ 2.1 & 3.9 \end{bmatrix} \times 10^{-5}$	$[Q]$	$[I]_{20\times 20}$
$[C_2]$	$\begin{bmatrix} 4.1 & 2.2 \\ 2.1 & 3.9 \end{bmatrix} \times 10^{7}$	$[F_o]$	$\begin{bmatrix} 0.04 & 2.86 \\ -4.18 & -1.88 \end{bmatrix} \times 10^{3}$
$[C_3]$	$\begin{bmatrix} 4.1 & 2.2 \\ 2.1 & 3.9 \end{bmatrix} \times 10^{-7}$	ρ_c	25×10^{4}
		γ_c	5×10^{-2}
		ρ_o	1×10^{3}
		γ_o	5×10^{-2}

Table 5-4. Initial Estimates of Control Gains

$\left[\hat{K}_1\right]_{initial}$	$\begin{bmatrix} -0.59 & 18.56 \\ 23.12 & 19.52 \\ 12.82 & 100.75 \\ 74.17 & -113.44 \\ -60.37 & -31.09 \\ -160.72 & -42.42 \\ 75.72 & 27.76 \\ -245.13 & -48.32 \\ 48.19 & 162.17 \\ -28.48 & 59.91 \\ -37.38 & -19.45 \\ 19.81 & -12.63 \\ 63.52 & 87.53 \\ 46.15 & 82.02 \\ 33.13 & -55.85 \\ -55.88 & 84.72 \\ 29.96 & -106.70 \\ 27.40 & 105.50 \\ 38.21 & -15.42 \\ -8.05 & -32.29 \end{bmatrix}^T \times 10^{-3}$	$\left[\hat{K}_2\right]_{initial}$	$\begin{bmatrix} 2.51 & -0.12 \\ -0.11 & 2.64 \end{bmatrix} \times 10^8$
		$\left[\hat{K}_3\right]_{initial}$	$\begin{bmatrix} 0.51 \\ 2.35 \end{bmatrix}$

The X input and the Y input of the closed loop nonlinear system with electrode dislocation using the ASMC generated by Eq. (5.38) are shown in Fig. 5-4 and Fig. 5-5 respectively. The estimated sliding surfaces which are expressed in Eq. (5.17) are shown in Fig. 5-6. The (1,1) elements of estimates of the control gains of equivalent control $\left[\hat{K}_1\right]$, $\left[\hat{K}_2\right]$ and $\left[\hat{K}_3\right]$ generated by Eq. (5.30a) – Eq. (5.30c) are shown in Fig. 5-7a – Fig. 5-7c. Since the dimensions of $\left[\hat{K}_1\right]$, $\left[\hat{K}_2\right]$ and $\left[\hat{K}_3\right]$ are large, only their (1,1) elements are shown. The X displacement and the Y displacement of the closed loop nonlinear system with electrode dislocation using the ASMC are shown in Fig. 5-8 and Fig. 5-9. For comparison, the X error and the Y error of the open loop nonlinear system with electrode dislocation, and the closed loop nonlinear system with electrode dislocation using the ASMC, the PI

controller and the OFC are plotted together in Fig. 5-10 and Fig. 5-11 respectively. The X RMSE and the Y RMSE of the closed loop nonlinear system with electrode dislocation using the ASMC are shown in Table 5-5.

Table 5-5. RMSEs of Open Loop Nonlinear System and Closed Loop Nonlinear System with Electrode Dislocation

	X RMSE (μm)	Y RMSE (μm)
Open Loop	5.619	0.678
ASMC	1.762	0.420
PI Controller	2.908	0.409
OFC	2.003	0.465

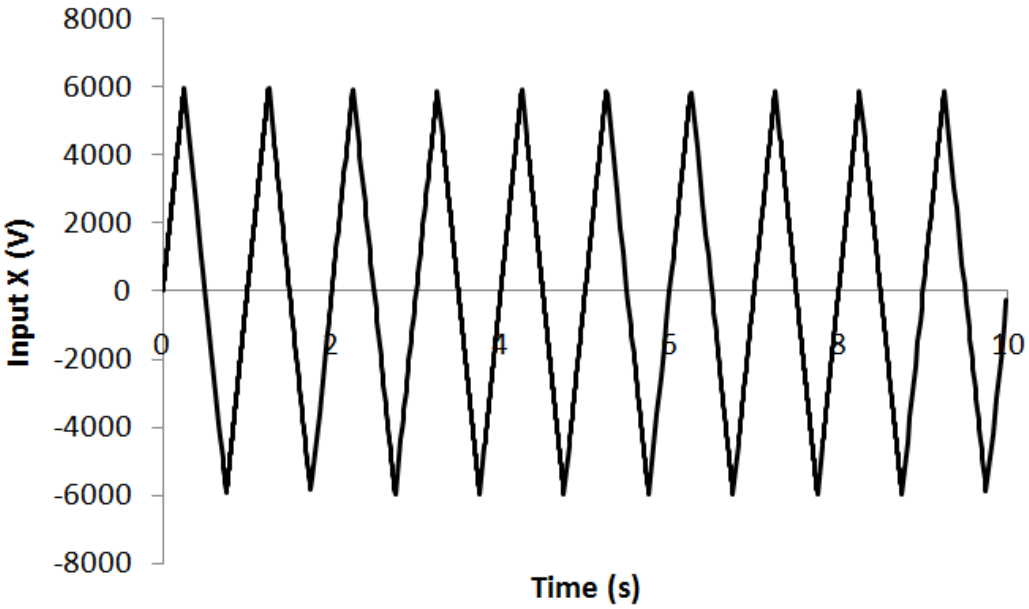

Figure 5-4. X Input of Closed Loop Nonlinear System with Electrode Dislocation using ASMC

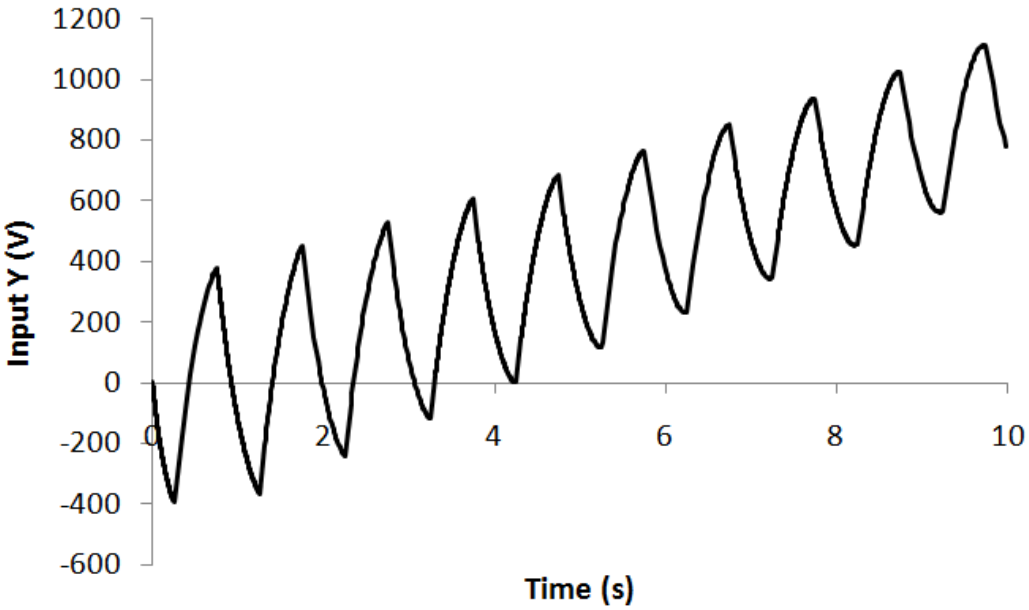

Figure 5-5. Y Input of Closed Loop Nonlinear System with Electrode Dislocation using ASMC

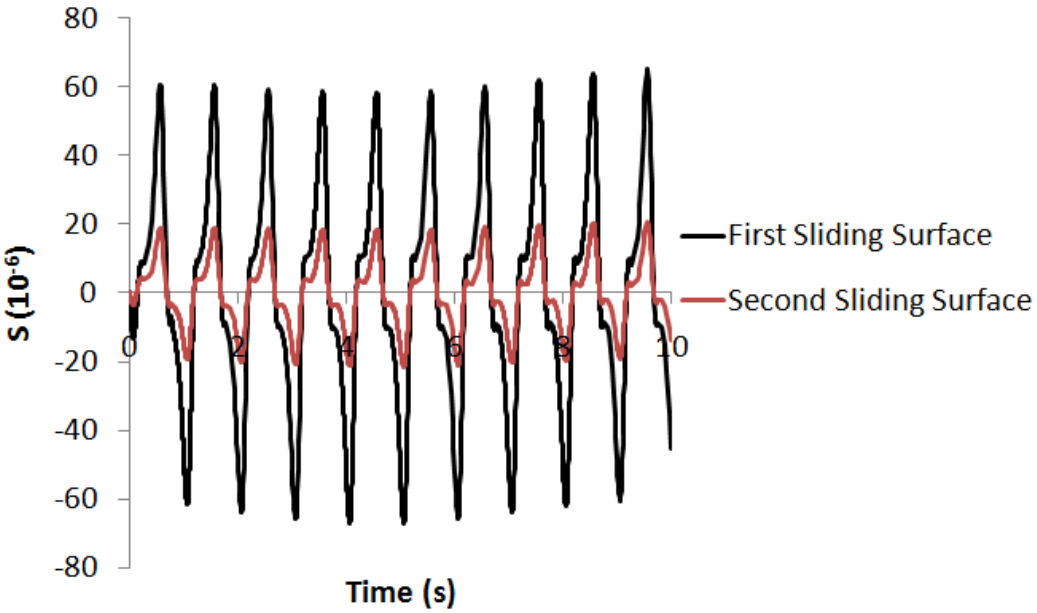

Figure 5-6. Estimated Sliding Surfaces of ASMC

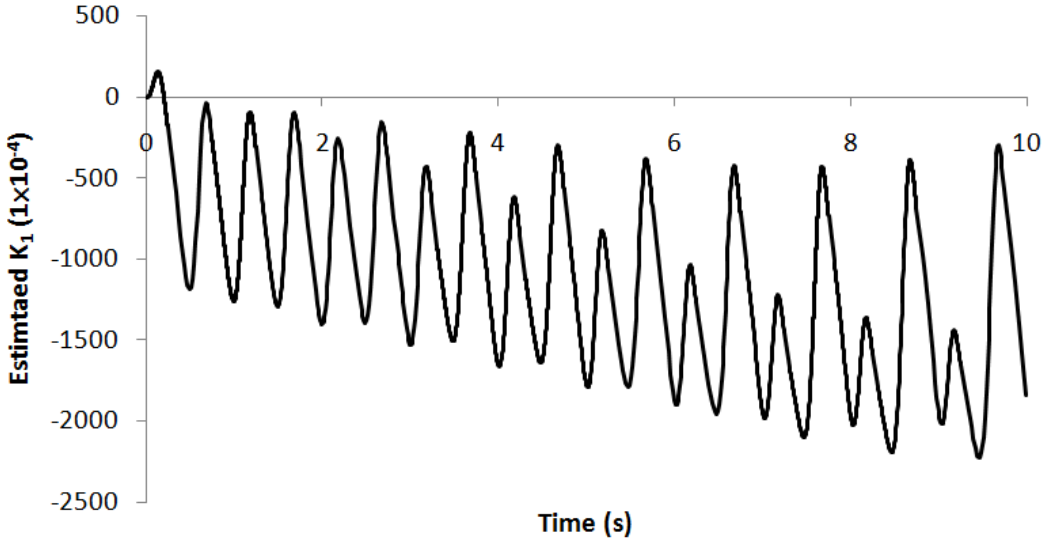

Figure 5-7a (1,1) Element of Estimates of Control Gains of Equivalent Control $\left[\hat{K}_1\right]$

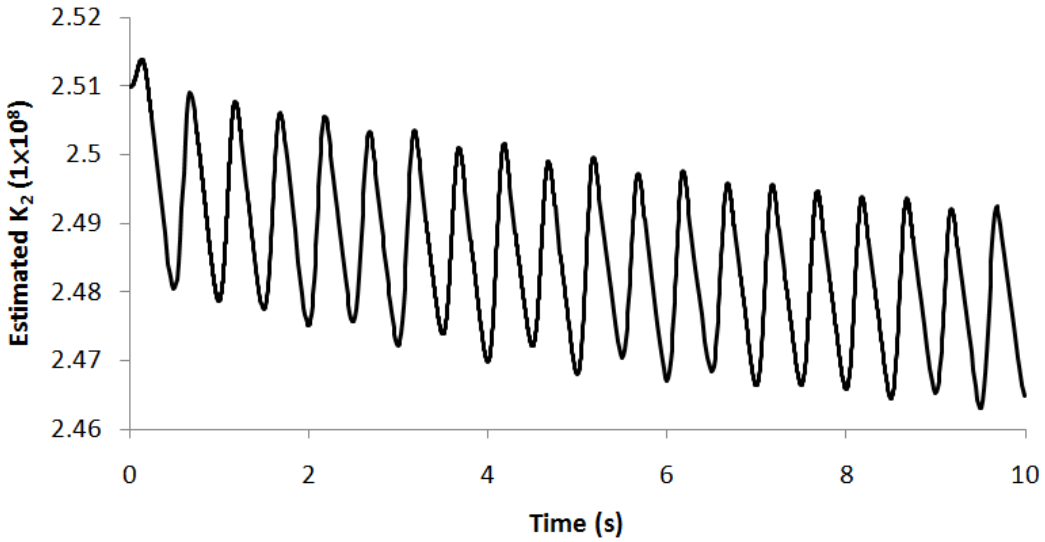

Figure 5-7b (1,1) Element of Estimates of Control Gains of Equivalent Control $\left[\hat{K}_2\right]$

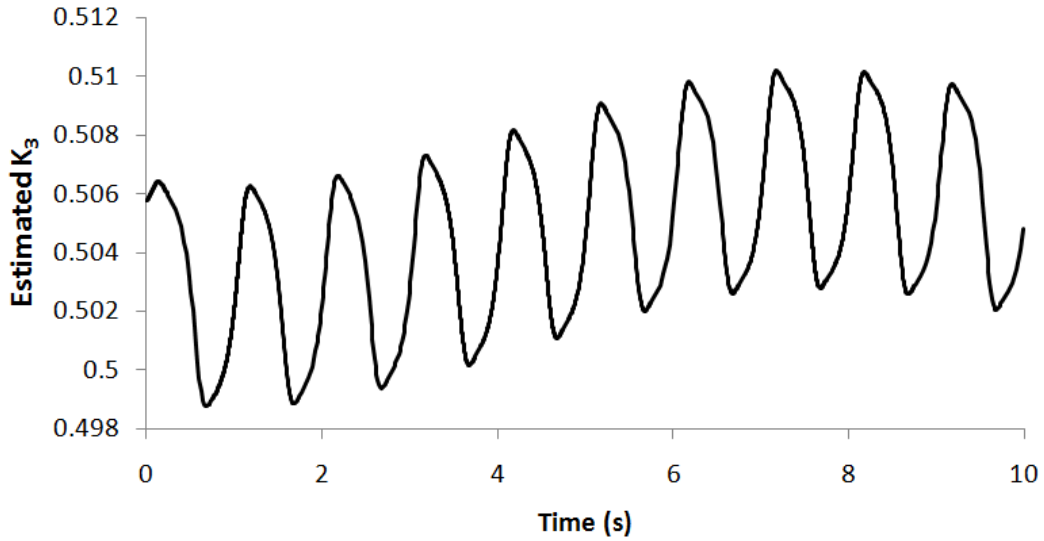

Figure 5-7c (1,1) Element of Estimates of Control Gains of Equivalent Control $\left[\hat{K}_3\right]$

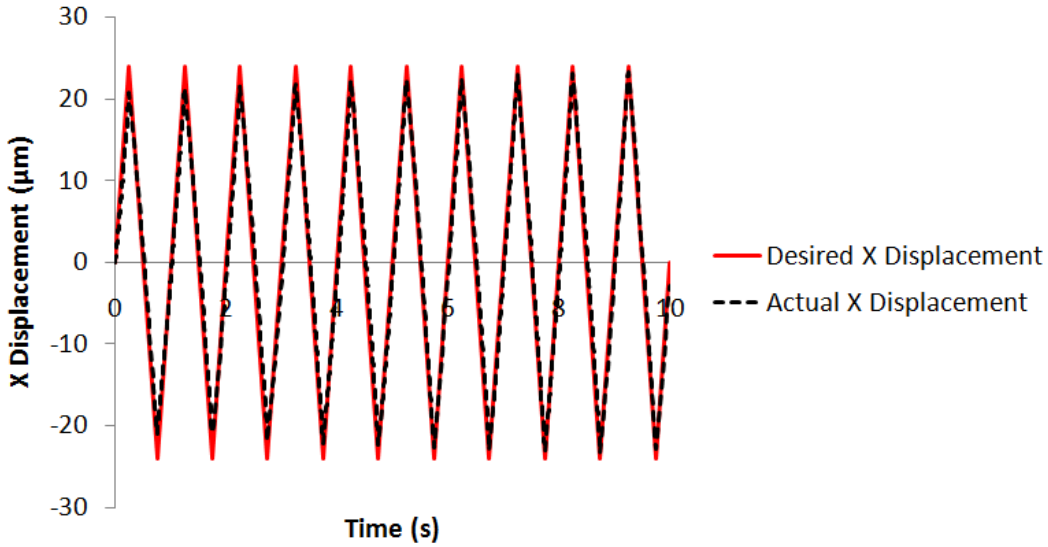

Figure 5-8. X Displacement of Closed Loop Nonlinear System with Electrode Dislocation using ASMC

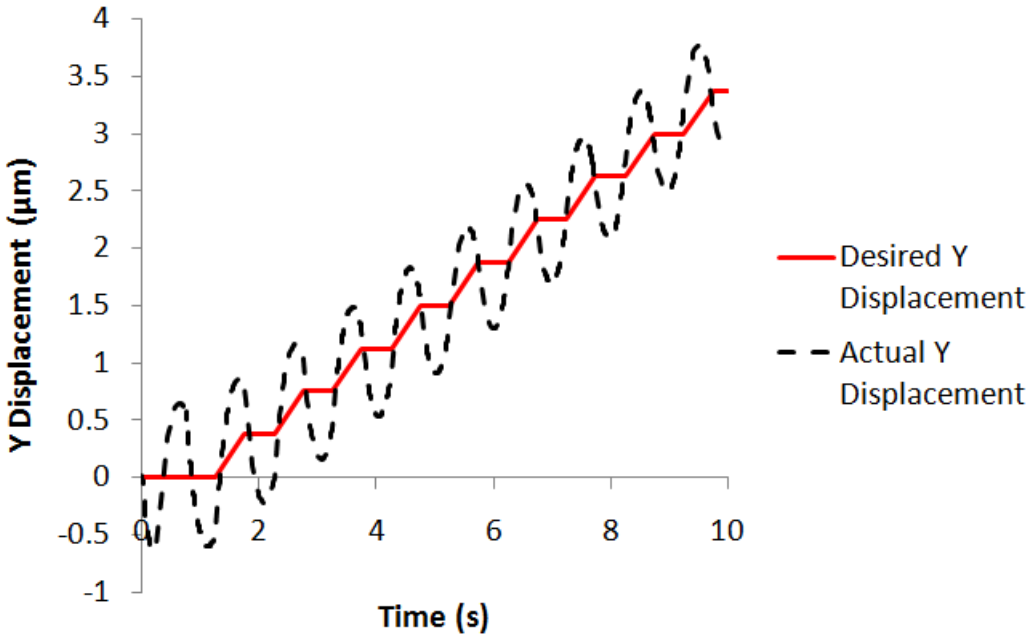

Figure 5-9. Y Displacement of Closed Loop Nonlinear System with Electrode Dislocation using ASMC

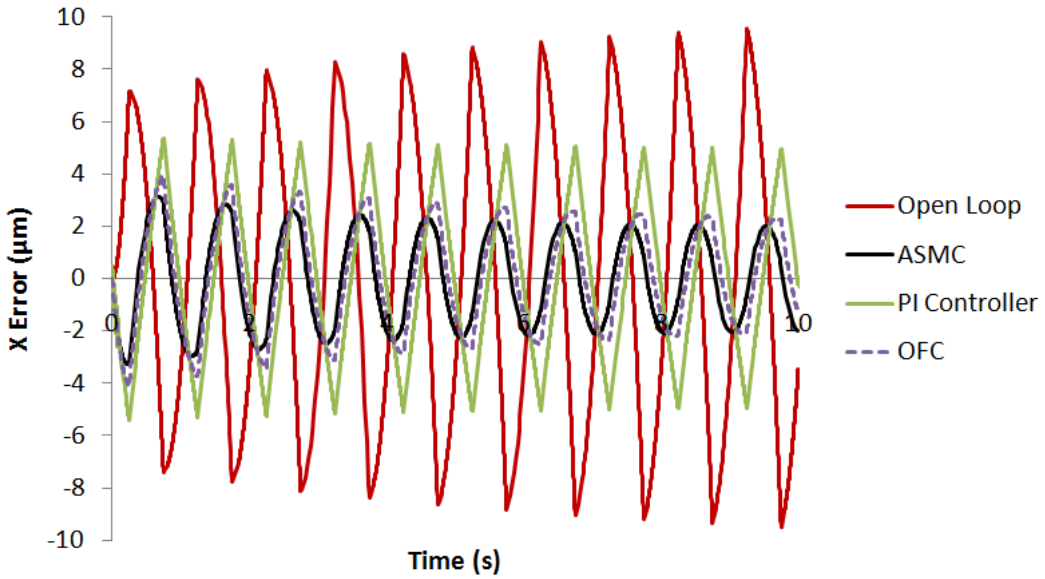

Figure 5-10. X Error of Open Loop and Closed Loop Nonlinear System with Electrode Dislocation

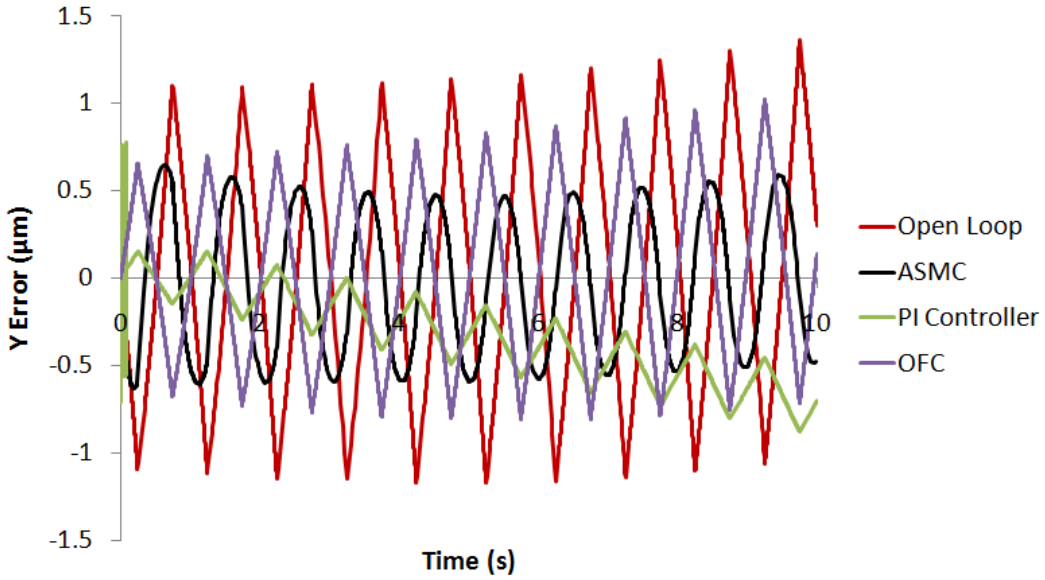

Figure 5-11. Y Error of Open Loop and Closed Loop Nonlinear System with Electrode Dislocation

As depicted in Fig. 5-8, the amplitude of the X displacement of the closed loop nonlinear system with electrode dislocation using the ASMC is reduced comparing to that of the open loop nonlinear system with electrode dislocation shown in Fig. 4-6. In Table 5-5, the X RMSE of the closed loop nonlinear system with electrode dislocation using the ASMC (1.762 µm) is smaller than that of the open loop nonlinear system with electrode dislocation (5.619 µm). It implies that the ASMC can reduce the tracking error due to hysteresis. Also, as depicted in Fig. 5-10, the peak-to-peak amplitude of the wave pattern of the X error of the closed loop nonlinear system with electrode dislocation using the ASMC (4 µm at steady state) is significantly smaller than that of the closed loop nonlinear system with electrode dislocation using the PI controller (10 µm) and is slightly smaller than that of the closed loop nonlinear system with electrode dislocation using the OFC (4.5 µm at steady state). In Table 5-5, the X RMSE of the closed loop nonlinear system with electrode dislocation using the ASMC (1.762 µm) is smallest. It is revealed the ability of the ASMC to reduce tracking error caused by hysteresis is

the best among the controller candidates.

As shown in Fig. 5-11, the peak-to-peak amplitude of the wave pattern of the Y error of the closed loop nonlinear system with electrode dislocation using the ASMC (1.1 μm) is smaller than that of the triangular pattern of the Y error of the open loop nonlinear system with electrode dislocation (2.3 μm). It implies that the ASMC can reduce the tracking error due to coupling effect. Also, as depicted in Fig. 5-11, the peak-to-peak amplitude of the wave pattern of the Y error of the closed loop nonlinear system with electrode dislocation using the ASMC (1.1 μm) is smaller than that of the triangular pattern of the Y error of the closed loop nonlinear system with electrode dislocation using the OFC (1.5 μm). It is revealed that the ability of the ASMC to reduce tracking error caused by coupling effect is better than that of the OFC. In Fig. 5-11, the peak-to-peak amplitude of the triangular pattern of the Y error of the closed loop nonlinear system with electrode dislocation using the PI controller (0.6 μm) is smaller than that of the wave pattern of the Y error of the closed loop nonlinear system with electrode dislocation using the ASMC (1.1 μm). It is revealed that the ability of the PI controller to reduce tracking error caused by coupling effect is better than that of the ASMC. In Table 5-5, the Y RMSE of the closed loop nonlinear system with electrode dislocation using the ASMC is 0.420 μm.

In Fig. 5-11, the Y error of the closed loop nonlinear system with electrode dislocation using the ASMC increases slower than that of the open loop nonlinear system with electrode dislocation in positive direction. It is revealed that the ASMC can reduce the tracking error caused by creep. In Fig. 5-7a – Fig. 5.7c, it is

observed that the (1,1) elements of estimates of the control gains of equivalent control $\left[\hat{K}_1\right]$, $\left[\hat{K}_2\right]$ and $\left[\hat{K}_3\right]$ are varying because the tracking error is not steady due to creep.

It is observed in Fig. 5-10 that the X error of the closed loop nonlinear system with electrode dislocation using the ASMC converges while that of the open loop nonlinear system with electrode dislocation diverges. Also, the convergence rate of the X error of the closed loop nonlinear system with electrode dislocation using the ASMC is highest among the controller candidates. In Fig. 5-11, it is observed that the increase rate of the Y error of the closed loop nonlinear system with electrode dislocation using the ASMC is lower than that of the open loop nonlinear system with electrode dislocation. The Y error of the closed loop nonlinear system with electrode dislocation using the OFC diverges quickly and that of the closed loop nonlinear system with electrode dislocation using the PI controller increases in negative direction quickly comparing to increase rate of the Y error of the closed loop nonlinear system with electrode dislocation using the ASMC. It implies that the relative stability of the piezoelectric tube actuator with electrode dislocation is improved by the ASMC. Also, the stability improvement ability of the ASMC is best among the controller candidates.

It is observed in Fig. 5-10 and Fig. 5-11 that the X error and the Y error of the closed loop nonlinear system with electrode dislocation using the ASMC do not converge to zero because the soft switching mechanism is adopted and the unmatched uncertainties is present.

It is concluded that the overall performance of the ASMC is better than those of the PI controller and the OFC because creep and hysteresis compensation ability, and stability improvement ability of the ASMC are the best among the controller candidates. However, coupling effect compensation ability of the ASMC is not as good as that of the PI controller.

5.6 SUMMARY

The works of this chapter can be summarized as follows:

(i) The ASMC has been successfully developed for the piezoelectric tube actuator. The theoretical stability of the closed loop nonlinear system with electrode dislocation using this controller is stated by the Lyapunov criterion.

(ii) The ASMC can minimize the tracking error of the piezoelectric tube actuator with electrode dislocation due to coupling effect. The peak-to-peak amplitude of the wave pattern of the Y error of the piezoelectric tube actuator with electrode dislocation is reduced from 2.3 μm to 1.1 μm. It can also minimize the tracking error of the piezoelectric tube actuator with electrode dislocation due to creep. The Y error of the piezoelectric tube actuator with electrode dislocation increases slower in positive direction. Also, it can minimize the tracking error of the piezoelectric tube actuator with electrode dislocation due to hysteresis. The X RMSE of the piezoelectric tube actuator with electrode dislocation is reduced from 5.619 μm to 1.762 μm. The ASMC can improve the stability of the piezoelectric tube actuator with electrode dislocation. The X error of the piezoelectric tube actuator with electrode dislocation converges

and the Y error of the piezoelectric tube actuator with electrode dislocation increases slower in positive direction.

(iii) The overall performance of the ASMC is the best among the controller candidates chosen in this research according to creep and hysteresis compensation ability, and stability improvement ability. The peak-to-peak amplitude of the wave pattern of the X error of the closed loop nonlinear system with electrode dislocation using the ASMC (4 μm at steady state) is significantly smaller than that of the closed loop nonlinear system with electrode dislocation using the PI controller (10 μm) and is slightly smaller than that of the closed loop nonlinear system with electrode dislocation using the OFC (4.5 μm at steady state). The convergence rate of the X error of the closed loop nonlinear system with electrode dislocation using the ASMC is higher than those of the closed loop nonlinear system with electrode dislocation using the PI controller and the OFC, and the Y error of the closed loop nonlinear system with electrode dislocation using the PI controller increases in negative direction quickly and that of the closed loop nonlinear system with electrode dislocation using the OFC diverges quickly comparing to increase rate of the Y error of the closed loop nonlinear system with electrode dislocation using the ASMC.

(iv) Due to the soft switching mechanism and the unmatched uncertainties, the tracking error of the piezoelectric tube actuator with electrode dislocation using the ASMC does not converge to zero.

CHAPTER 6

PERFORMANCE OF CONTROLLERS UNDER VARIOUS NONLINEARITY PROPERTIES

6.1 INTRODUCTION

In the previous chapter, the performance of the ASMC applied on the piezoelectric tube actuator with electrode dislocation has been investigated. In this chapter, the simulations on the closed loop system with altered creep and hysteresis properties using the ASMC are performed aiming to explore the ASMC's tolerance of various nonlinearity properties. The reasons for investigation are given as follows. Firstly, it probably has a bias measure of the hysteresis slope k_h in reality. k_h is important information for the proposed ASMC design in this thesis. Secondly, hysteresis is rate dependent. Hysteresis slope can decrease by 9% and the backlash distance can increase by 10% when the operating frequency increases from 1 Hz to 20 Hz (Yu *et al.*, 2002). Thirdly, creep is thermal dependent. The step response exhibits creep 15% more when the temperature increases from 25˚C to 49˚C (Motamedi *et al.*, 2009). Lastly, piezoelectric tube actuator having different treatment may have different creep and hysteresis properties. Therefore, it is

important to study the effect of various creep and hysteresis properties on the closed loop nonlinear system. Although it is shown in Chapter 5 that the overall performance of the ASMC is better than that of the typical controllers, the influences of altered creep and hysteresis properties on the responses of the closed loop nonlinear system with electrode dislocation using the typical controllers are also given in the chapter for comparison and reference to demonstrate whether the performance of the ASMC is still better than that of the typical controllers.

6.2 SIMULATION CONDITIONS

The simulations of the closed loop nonlinear system with electrode dislocation using the ASMC, the PI controller and the OFC are performed with the same controller settings adopted in previous chapters. The simulations are based on the assumptions and the conditions stated in Chapter 3 and the controller design of the ASMC is based on the assumptions and the conditions stated in Chapter 5. In order to characterize the system with changed hysteresis slope and changed hysteresis backlash-distance in simulation, the proportional constant for the Prandtl-Ishlinskii hysteresis operator b_j in Eq. (3.17) and threshold κ_j in Eq. (3.16a) – Eq. (3.16c) should be changed respectively. In order to characterize the system with altered creep effect in simulation, the weighting factor of Kelvin-Voigt creep operator w_f in Eq. (3.11) and the proportional constant for the Kelvin-Voigt creep operator a_f in Eq. (3.12) should be changed. w_f and a_f are regarded as creep properties in this study.

6.3 SIMULATION RESULTS OF SYSTEMS WITH VARIOUS HYSTERESIS PROPERTIES

The performance of the controllers has been investigated for the input frequency of 1 Hz in the previous chapters. In this section, the simulations of the closed loop nonlinear system with electrode dislocation are performed at 10 Hz and 20 Hz.

When the input frequency is increased from 1 Hz to 10 Hz, the hysteresis slope is decreased by 8%. With the change, the X input and the Y input of the closed loop nonlinear system with electrode dislocation using the ASMC generated by Eq. (5.38), the PI controller generated by Eq. (4.1a) and Eq. (4.2a), and the OFC generated by Eq. (4.3a) are shown in Fig. 6-1 and Fig. 6-2 respectively. The X error and the Y error of the closed loop nonlinear system with electrode dislocation are shown in Fig. 6-3 and Fig. 6-4 respectively. The X RMSE and the Y RMSE of the open loop nonlinear system and the closed loop nonlinear systems with electrode dislocation are shown in Table 6-1.

Table 6-1. RMSEs of Open Loop Nonlinear System and Closed Loop Nonlinear System with Electrode Dislocation (Hysteresis Slope decreased by 8%)

	X RMSE (μm)	Y RMSE (μm)
Open Loop	4.566	0.635
ASMC	2.381	0.507
PI Controller	3.090	0.432
OFC	2.635	0.393

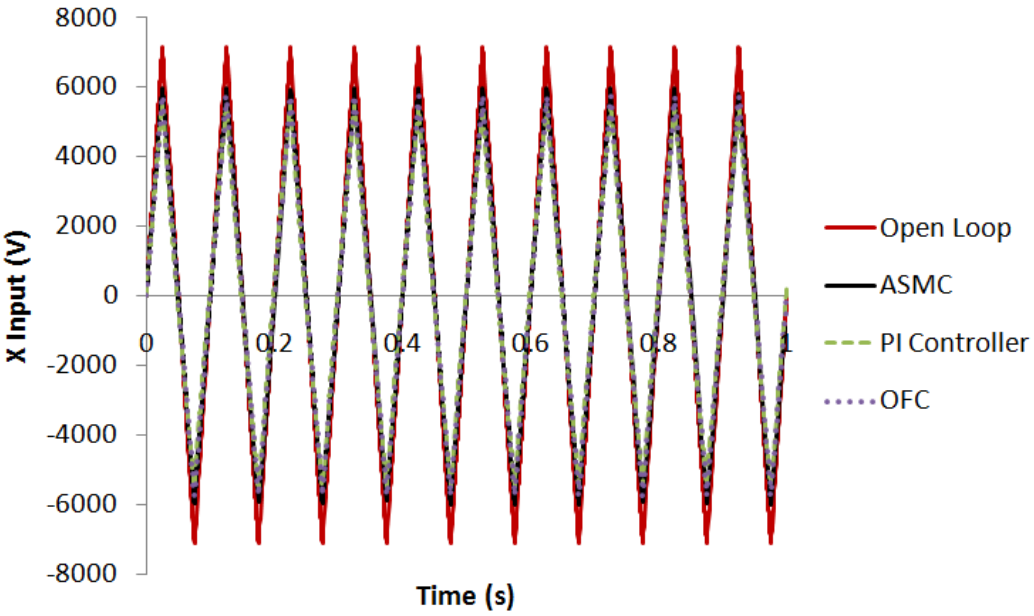

Figure 6-1. X Input of Closed Loop Nonlinear System with Electrode Dislocation (Hysteresis Slope decreased by 8%)

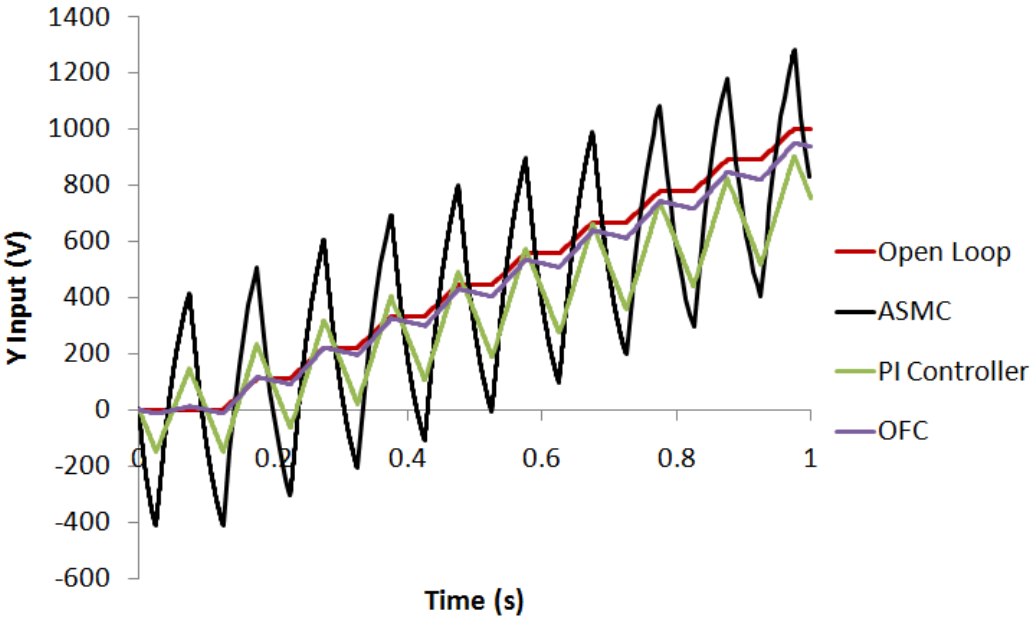

Figure 6-2. Y Input of Closed Loop Nonlinear System with Electrode Dislocation (Hysteresis Slope decreased by 8%)

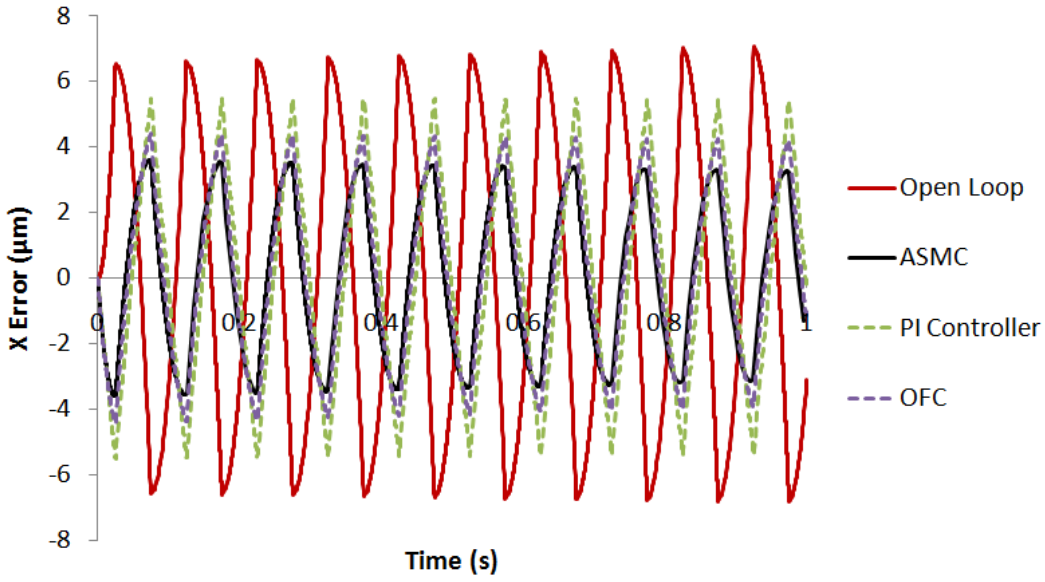

Figure 6-3. X Error of Closed Loop Nonlinear System with Electrode Dislocation (Hysteresis Slope decreased by 8%)

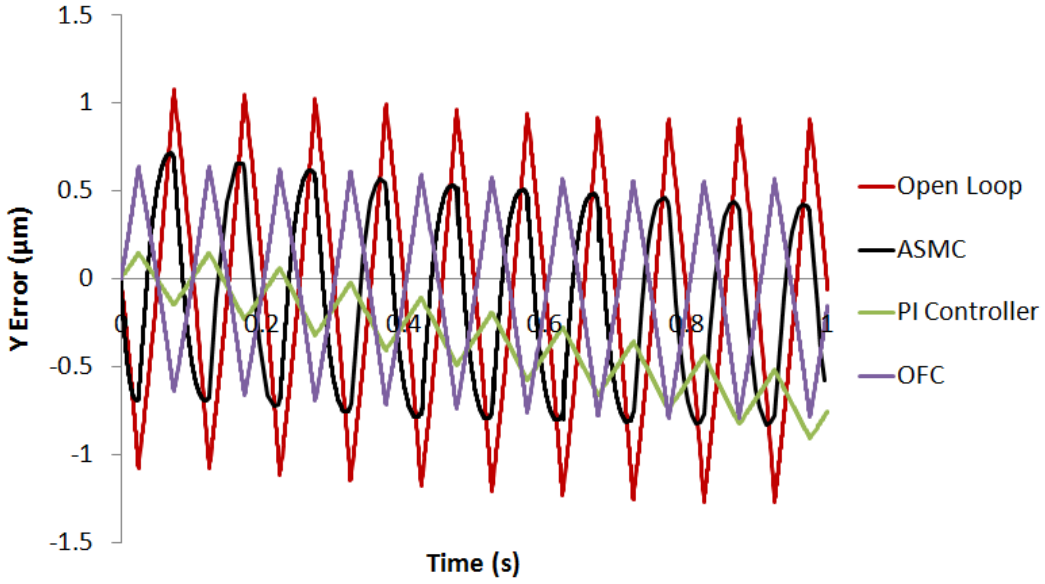

Figure 6-4. Y Error of Closed Loop Nonlinear System with Electrode Dislocation (Hysteresis Slope decreased by 8%)

When the input frequency is increased from 1 Hz to 20 Hz, hysteresis slope is decreased by 9% and the hysteresis backlash-distance is increased by 10%. With the change, the X input and the Y input of the closed loop nonlinear system with

electrode dislocation using the ASMC generated by Eq. (5.38) and the PI controller generated by Eq. (4.1a) and Eq. (4.2a), and the OFC generated by Eq. (4.3a), are shown in Fig. 6-5 and Fig. 6-6 respectively. The X error and the Y error of the closed loop nonlinear system with electrode dislocation are shown in Fig. 6-7 and Fig. 6-8 respectively. The X RMSE and the Y RMSE of the closed loop nonlinear system with electrode dislocation are shown in Table 6-2.

Table 6-2. RMSEs of Open Loop Nonlinear System and Closed Loop Nonlinear System with Electrode Dislocation (Hysteresis Slope decreased by 9% and Hysteresis Backlash-distance increased by 10%)

	X RMSE (μm)	Y RMSE (μm)
Open Loop	4.070	0.622
ASMC	2.535	0.536
PI Controller	3.113	0.434
OFC	2.786	0.383

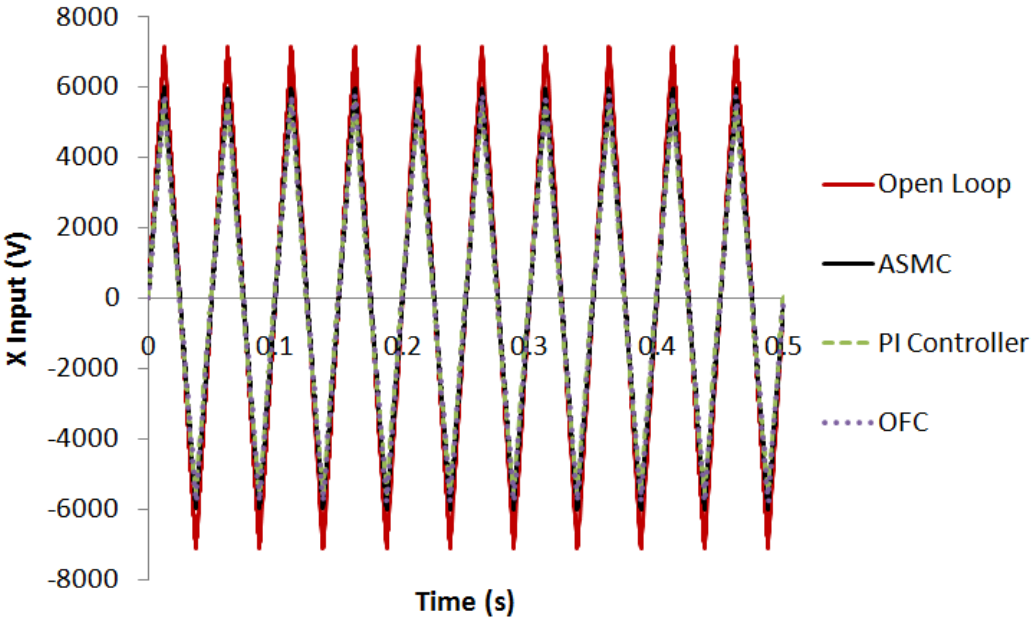

Figure 6-5. X Input of Closed Loop Nonlinear System with Electrode Dislocation (Hysteresis Slope decreased by 9% and Hysteresis Backlash-distance increased by 10%)

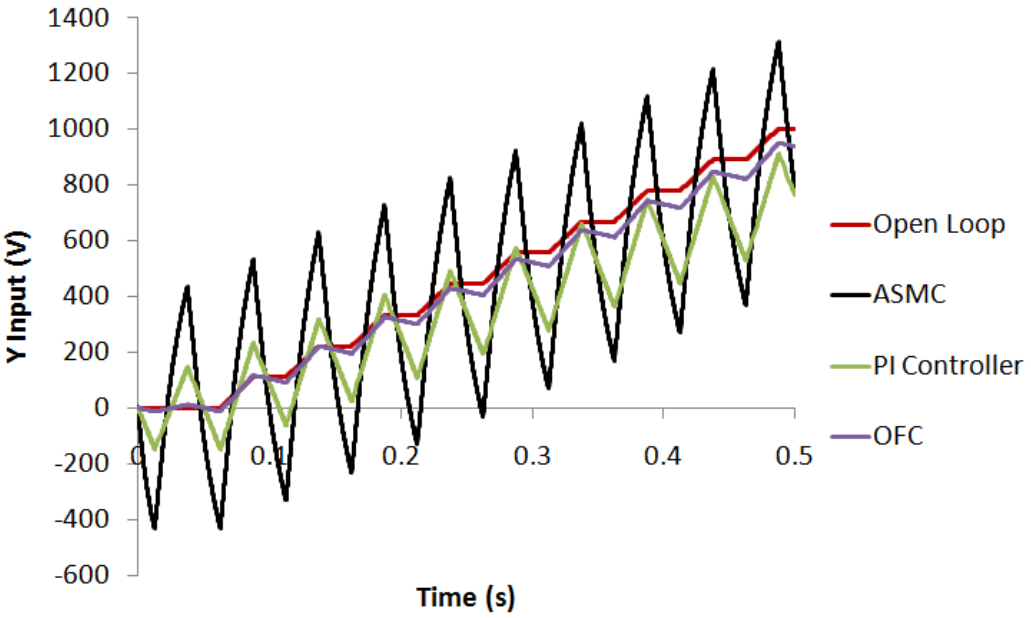

Figure 6-6. Y Input of Closed Loop Nonlinear System with Electrode Dislocation (Hysteresis Slope decreased by 9% and Hysteresis Backlash-distance increased by 10%)

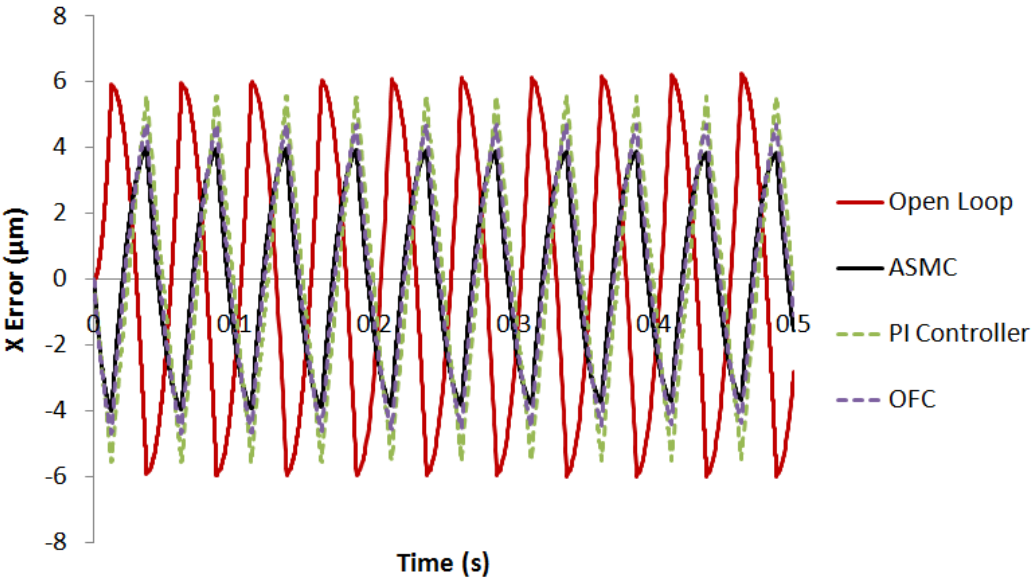

Figure 6-7. X Error of Closed Loop Nonlinear System with Electrode Dislocation (Hysteresis Slope decreased by 9% and Hysteresis Backlash-distance increased by 10%)

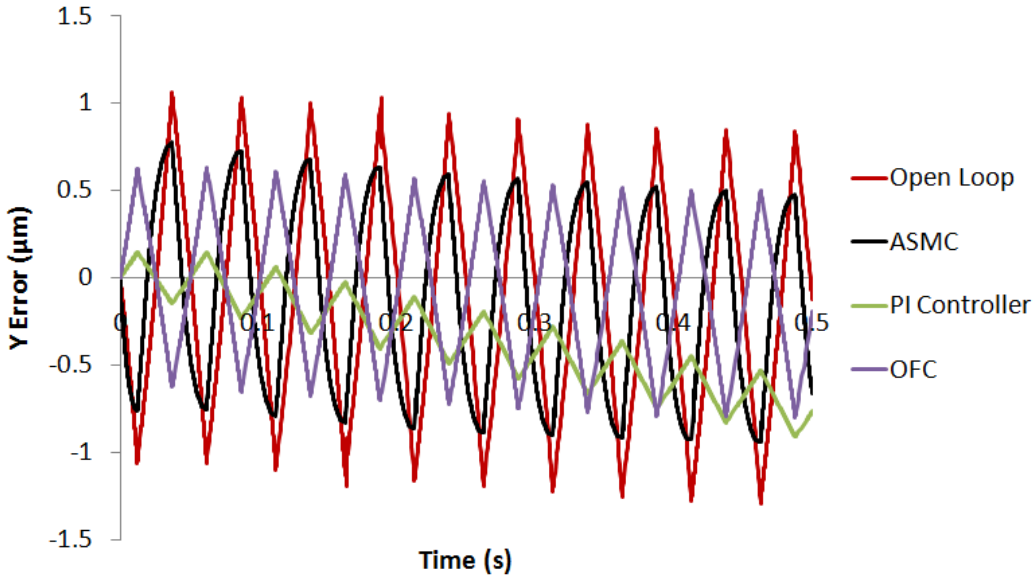

Figure 6-8. Y Error of Closed Loop Nonlinear System with Electrode Dislocation (Hysteresis Slope decreased by 9% and Hysteresis Backlash-distance increased by 10%)

As depicted in Fig. 6-3 and Fig. 6-7, the peak-to-peak amplitudes of the wave pattern of the X error of the closed loop nonlinear system with electrode dislocation using the ASMC (7 µm at 10 Hz and 20 Hz), the PI controller (11 µm at 10 Hz and 20 Hz) and the OFC (8 µm at 10 Hz and 9 µm at 20 Hz) are smaller than those of the open loop nonlinear system (13 µm at 10 Hz and 12 µm at 20 Hz). In Table 6-1, the X RMSEs of the closed loop nonlinear system with electrode dislocation using the ASMC (2.381 µm at 10 Hz and 2.535 µm at 20 Hz), using the PI controller (3.090 µm at 10 Hz and 3.113 µm at 20 Hz) and using the OFC (2.635 µm at 10 Hz and 2.786 µm at 20 Hz) are smaller than that of the open loop nonlinear system with electrode dislocation (4.566 µm at 10 Hz and 4.070 µm at 20 Hz). It implies that all controllers can compensate the error caused by hysteresis when hysteresis properties are changed. It is also shown that the peak-to-peak amplitudes of the wave pattern of the X error of the closed loop nonlinear system with electrode dislocation using the ASMC at 10 Hz and 20 Hz are smaller than those of closed

loop nonlinear system with electrode dislocation using the PI controller and the OFC. It reveals that the hysteresis compensation ability of the ASMC with hysteresis properties at 10 Hz and 20 Hz is the best among the controller candidates.

In Fig. 6-3, it is observed that the X error of the open loop nonlinear system with electrode dislocation diverges while those of the closed loop nonlinear system with electrode dislocation using the ASMC, the PI controller and the OFC converge at 10 Hz. In Fig. 6-7, it is observed that the X error of the open loop nonlinear system with electrode dislocation diverges at 20 Hz. The X errors of the closed loop nonlinear system with electrode dislocation using the PI controller and the OFC remain fluctuating without convergence and divergence at 20 Hz. The X error of the closed loop nonlinear system with electrode dislocation using the ASMC converges at 20 Hz. It is shown that the stability of the piezoelectric tube actuator with electrode dislocation can be improved by the ASMC, the PI controller and the OFC at 10 Hz and can be only improved by the ASMC at 20 Hz. Also, the convergence rate of the X errors of the closed loop nonlinear system with electrode dislocation using the ASMC is highest among the controller candidates at 10 Hz and 20 Hz. It reveals that the closed loop nonlinear system with electrode dislocation using the ASMC is most stable at 10 Hz and 20 Hz.

The maximum scanning frequency of AFM is 10 Hz which is covered in this simulation. Overall, the performance of the ASMC in tolerating the change of hysteresis properties is the best among the controller candidates in the operational frequency range of AFM.

6.4 SIMULATION RESULTS OF SYSTEMS WITH VARIOUS CREEP PROPERTIES

In this section, the simulations of the closed loop nonlinear system with electrode dislocation are performed with different creep effects. There are two cases investigated in this section: creep properties increased by 10% and by 25%.

For the case of creep properties increased by 10%, the X input and the Y input of the closed loop nonlinear system with electrode dislocation using the ASMC generated by Eq. (5.38), the PI controller generated by Eq. (4.1a) and Eq. (4.2a), and the OFC generated by Eq. (4.3a) are shown in Fig. 6-9 and Fig. 6-10 respectively. The X error and the Y error of the closed loop nonlinear system with electrode dislocation are shown in Fig. 6-11 and Fig. 6-12 respectively. The X RMSE and the Y RMSE of the closed loop nonlinear system with electrode dislocation are shown in Table 6-3.

Table 6-3. RMSEs of Open Loop Nonlinear System and Closed Loop Nonlinear System with Electrode Dislocation (Creep Parameters increased by 10%)

	X RMSE (μm)	Y RMSE (μm)
Open Loop	5.755	0.688
ASMC	1.705	0.424
PI Controller	2.778	0.406
OFC	1.905	0.482

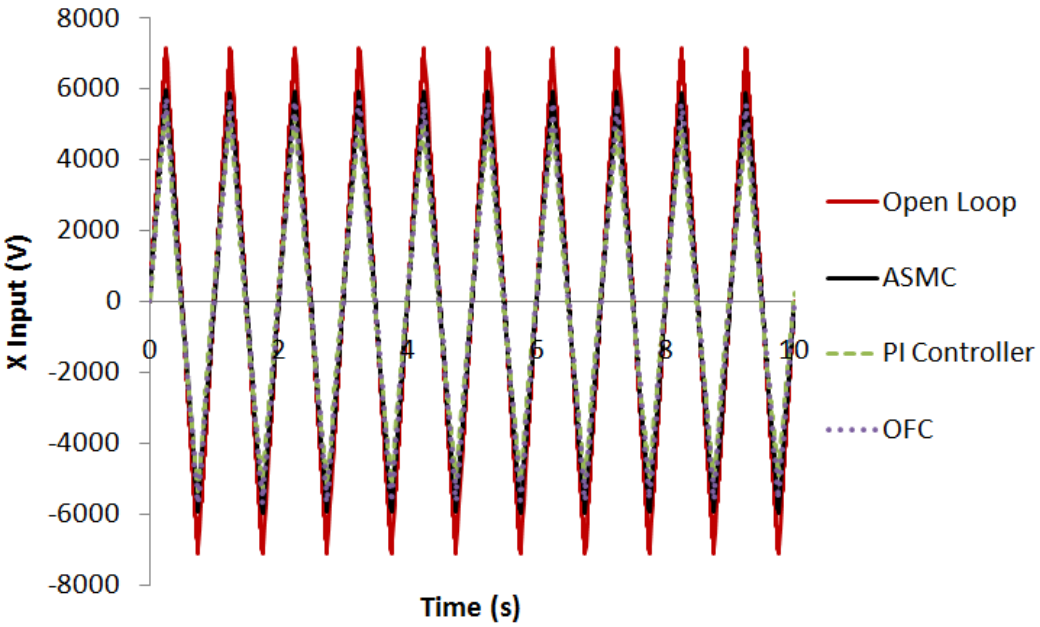

Figure 6-9. X Input of Closed Loop Nonlinear System with Electrode Dislocation (Creep Parameters increased by 10%)

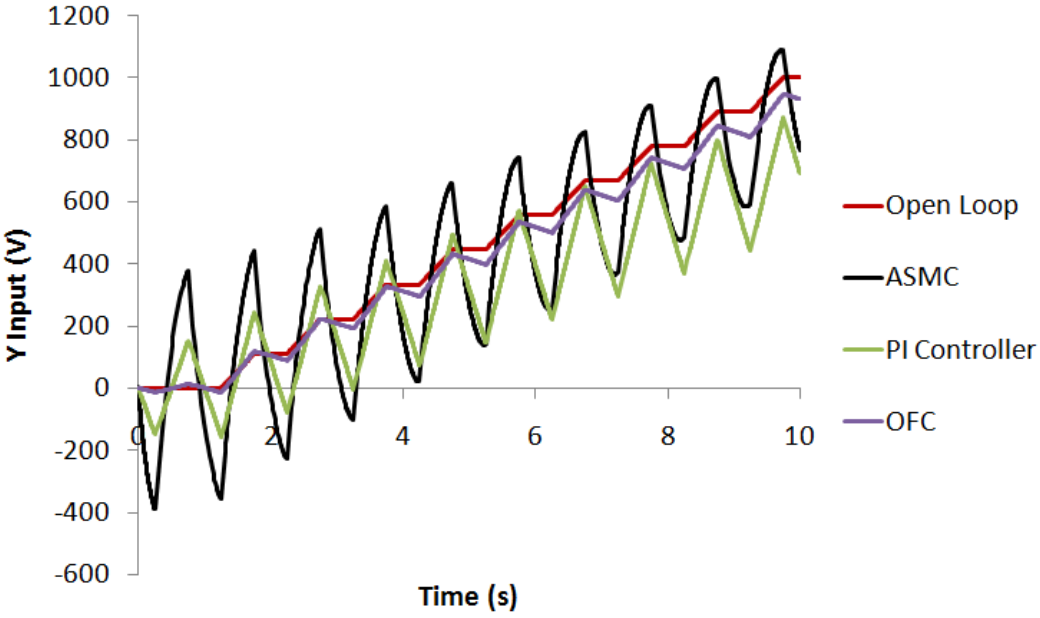

Figure 6-10. Y Input of Closed Loop Nonlinear System with Electrode Dislocation (Creep Parameters increased by 10%)

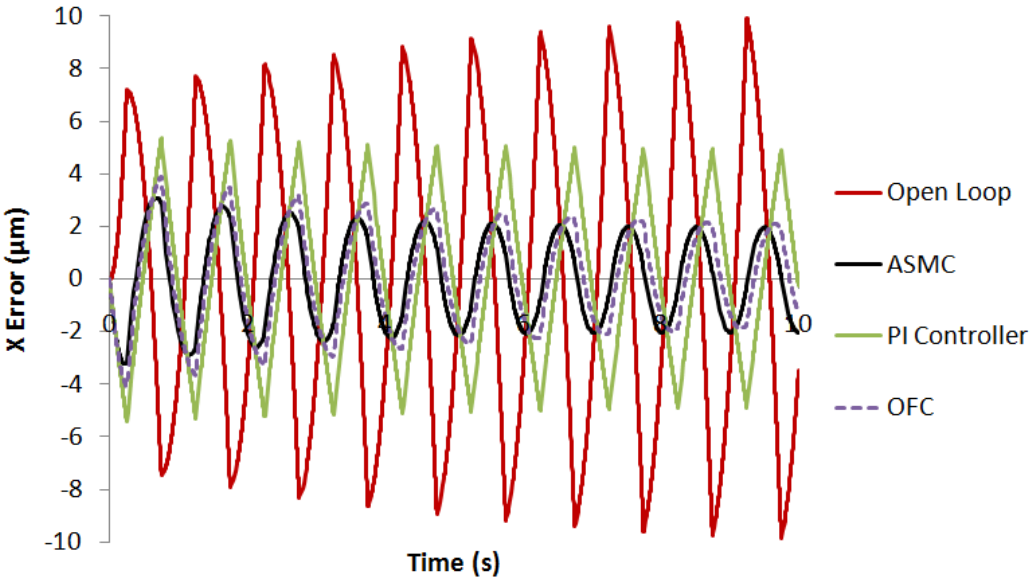

Figure 6-11. X Error of Closed Loop Nonlinear System with Electrode Dislocation (Creep Parameters increased by 10%)

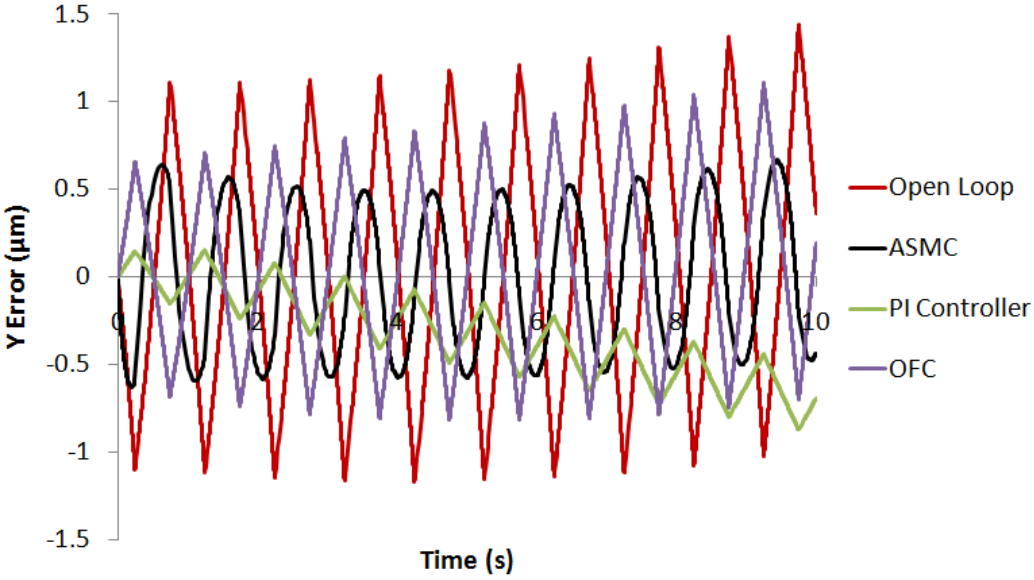

Figure 6-12. Y Error of Closed Loop Nonlinear System with Electrode Dislocation (Creep Parameters increased by 10%)

For the case of creep properties increased by 25%, the X input and the Y input of the closed loop nonlinear system with electrode dislocation using the ASMC generated by Eq. (5.38), the PI controller generated by Eq. (4.1a) and Eq. (4.2a),

and the OFC generated by Eq. (4.3a) are shown in Fig. 6-13 and Fig. 6-14 respectively. The X error and the Y error of the closed loop nonlinear system with electrode dislocation are shown in Fig. 6-15 and Fig. 6-16 respectively. The X RMSE and the Y RMSE of the closed loop nonlinear system with electrode dislocation are shown in Table 6-4.

Table 6-4. RMSEs of Open Loop Nonlinear System and Closed Loop Nonlinear System with Electrode Dislocation (Creep Parameters increased by 25%)

	X RMSE (μm)	Y RMSE (μm)
Open Loop	5.975	0.709
ASMC	1.651	0.446
PI Controller	2.711	0.399
OFC	1.761	0.510

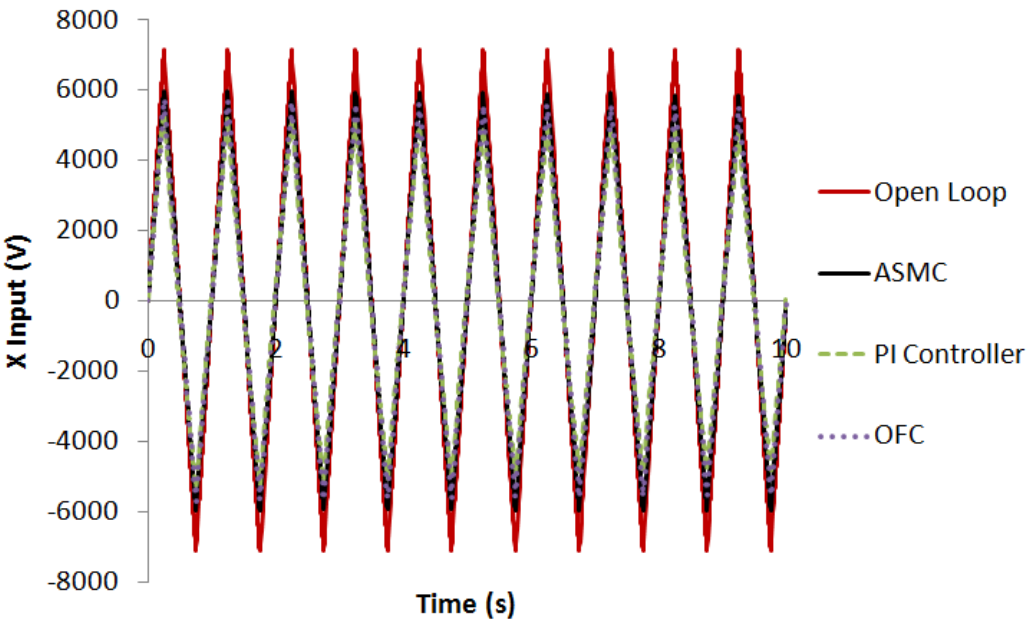

Figure 6-13. X Input of Closed Loop Nonlinear System with Electrode Dislocation (Creep Parameters increased by 25%)

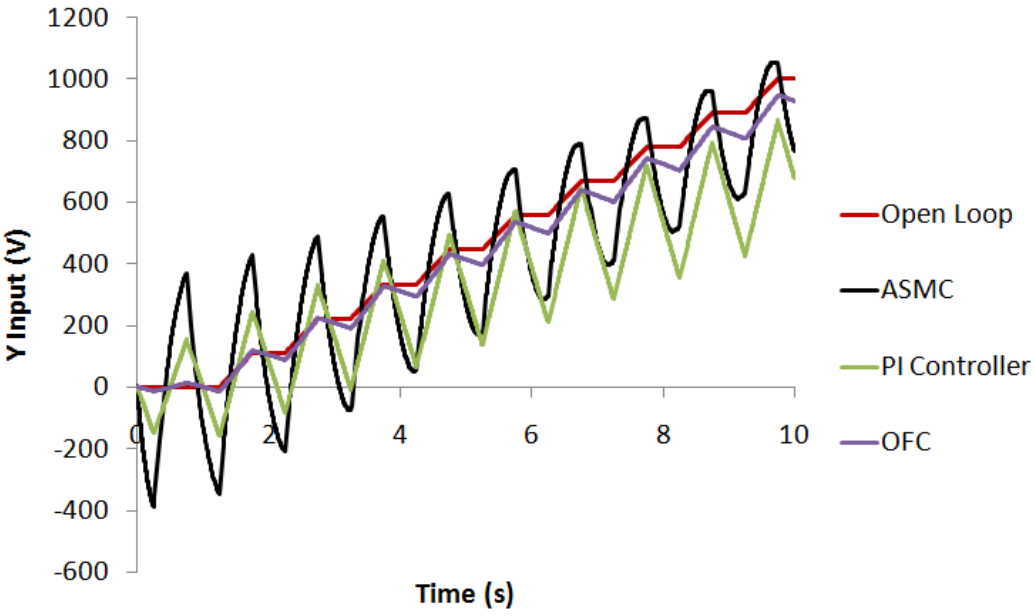

Figure 6-14. Y Input of Closed Loop Nonlinear System with Electrode Dislocation (Creep Parameters increased by 25%)

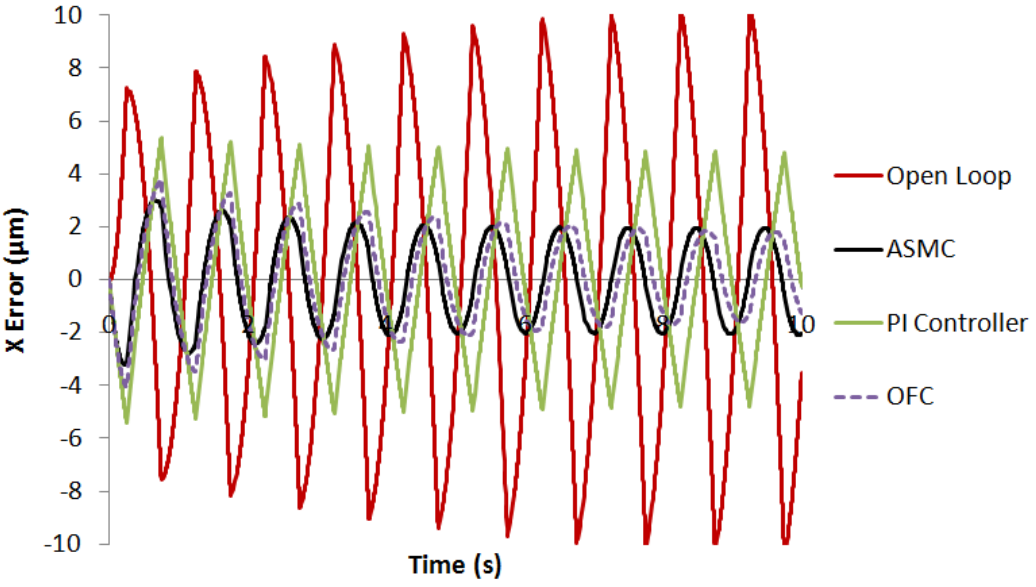

Figure 6-15. X Error of Closed Loop Nonlinear System with Electrode Dislocation (Creep Parameters increased by 25%)

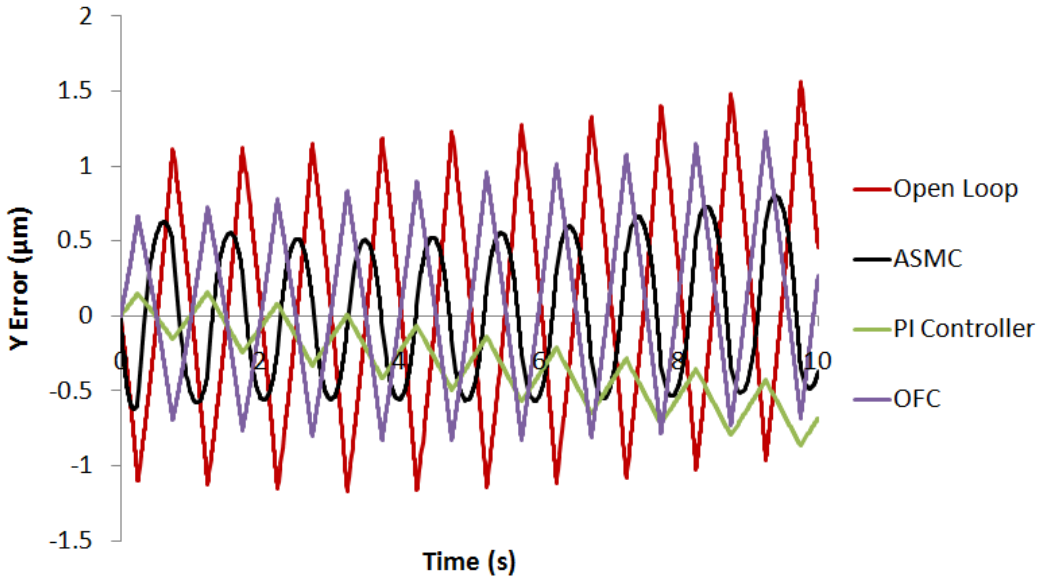

Figure 6-16. Y Error of Closed Loop Nonlinear System with Electrode Dislocation (Creep Parameters increased by 25%)

As depicted in Fig. 6-12, the increasing rate (in positive direction) of the Y error of the closed loop nonlinear system with electrode dislocation using the ASMC is smaller than that of the open loop nonlinear system with electrode dislocation. It implies that the error due to creep can be reduced by the ASMC when the creep properties increased by 10%. Also, it is observed in Fig. 6-12 that the Y error of the open loop nonlinear system with electrode dislocation and the closed loop nonlinear system with electrode dislocation using the OFC diverge quickly and the Y error of the closed loop nonlinear system with electrode dislocation using the PI controller increases quickly in the negative direction comparing to the increase rate of the Y error of the closed loop nonlinear system using the ASMC. It reveals that the closed loop nonlinear system with electrode dislocation using the ASMC is more stable than the open loop nonlinear system with electrode dislocation and the closed loop nonlinear system using the typical controllers when the creep properties are increased by 10%. It is implied that only the ASMC can tolerate the change of creep properties when creep properties are

increased by 10%.

As depicted in Fig. 6-16, the amplitude of the Y error of the closed loop nonlinear system with the ASMC diverges. It implies that the ASMC can no longer tolerate the creep effect when the increase of creep properties is 25%.

In Fig. 6-4, Fig. 6-8 and Fig. 6-12, it is observed that the peak-to-peak amplitude of the wave pattern of the Y error of the closed loop nonlinear system with electrode dislocation using the ASMC is larger than that using the PI controller and that using the OFC. It implies that the coupling effect is a main factor causing the ASMC not having the best results in the y direction.

For the ASMC, the error caused by coupling effect is reduced but still exists in the closed loop nonlinear system with electrode dislocation because the disturbance term related to the coupling effect $[\Delta B_1][u_E]$ may not match with $[\overline{B}]$ all the time. Therefore, the error caused by coupling effect cannot be fully eliminated by unit vector control.

In addition, it is observed that the monotonic increase rate of the Y error of the closed loop nonlinear system with electrode dislocation using the ASMC is smaller than that using the PI controller. This implies that the RMSE of the closed loop nonlinear system with electrode dislocation using the ASMC will be smaller than that using the PI controller when the scanning time is extended.

It is concluded that the ASMC can tolerate the changes of the hysteresis properties at 10 Hz and 20 Hz because it can reduce the peak-to-peak amplitude of the wave pattern of the X error and improve the relative stability of the piezoelectric tube actuator with electrode dislocation. The frequency range covers the maximum scanning frequency of AFM. Also, it is concluded that the ASMC can tolerate the changes of the creep properties when the increase of the creep properties is 10% because it can reduce the increasing rate (in positive direction) of the Y error and improve the relative stability of the piezoelectric tube actuator with electrode dislocation. The ASMC is not able to tolerate the creep effect when the increase of the creep properties is 25% since the amplitude of the Y error of the piezoelectric tube actuator with electrode dislocation diverges. By observing the performance of the controllers, the ASMC has a better tolerance of the changes of the creep properties and the hysteresis properties than the typical controllers.

6.5 SUMMARY

The above findings can be summarized as follows:

(i) The ASMC can reduce the peak-to-peak amplitudes of the wave pattern of the X error of the piezoelectric tube actuator with electrode dislocation from 13 μm to 7 μm at 10 Hz, and from 12 μm to 7 μm at 20 Hz. The ASMC can also improve the stability of the piezoelectric tube actuator with electrode dislocation at 10 Hz and 20 Hz. Therefore, the ASMC can tolerate the changes of the hysteresis properties at 10 Hz and 20 Hz.

(ii) The ASMC can reduce the increasing rate (in positive direction) of the Y error of the piezoelectric tube actuator with electrode dislocation when the increase

of the creep properties is 10%. It implies that the ASMC can still compensate creep effect. Therefore, the ASMC can tolerate the creep properties with this change.

(iii) The ASMC has a better tolerance of the changes of the creep properties and the hysteresis properties than the typical controllers because the ASMC shows better creep and hysteresis compensation abilities, and stability improvement ability than the typical controllers when the hysteresis exhibits at 10 Hz and 20 Hz, or the creep properties are increased by 10%.

CHAPTER 7

DISCUSSIONS AND CONCLUSIONS

7.1 DISCUSSIONS

In this thesis, an ASMC which can reduce the error caused by coupling effect, creep and hysteresis, and increase stability of the piezoelectric tube actuator with electrode dislocation was designed. Simulation results show that the ASMC performs better than the typical controllers. Therefore, ASMC can be a good candidate applied to the AFM. The main objective of this research is achieved. The major works done in this thesis are discussed below.

(i) In order to predict the dynamic behavior of the piezoelectric tube actuator, a mathematical model was built by FE method with implementation of superposition of Kelvin-Voigt creep operators and superposition of Prandtl-Ishlinskii hysteresis operators. The RMSE between the response of the full nonlinear FE model (Eq. (3.56) and Eq. (3.57)) and the simulation result obtained by Leang and Devasia (2007) was 0.362 μm. The order of the model was then reduced, and the model was expressed in state space form. The RMSE between the full nonlinear FE model (Eq. (3.56) and Eq. (3.57)) and the reduced order nonlinear FE model (Eq. (3.62b) and Eq. (3.63)) with 35 retained states was 0.044 μm. The RMSE between the full nonlinear FE model

(Eq. (3.56) and Eq. (3.57)) and the reduced order nonlinear FE model (Eq. (3.62b) and Eq. (3.63)) with 20 retained states was 0.099 μm. The comparisons reveal that the reduced order nonlinear FE models (Eq. (3.62b) and Eq. (3.63)) of 20 and 35 retained states were accurate enough for controller design and simulation purposes respectively.

(ii) The simulations of the open loop nonlinear system show that coupling effect, creep and hysteresis caused significant tracking error of the piezoelectric tube actuator. Hysteresis can distort the triangular pattern (the X displacement) and can increase the amplitude of the triangular pattern. The X RMSE of the open loop nonlinear system without electrode dislocation was 5.693 μm. Creep can cause the Y error to increase with time. Therefore, the system gain also increased with time. Due to coupling effect, the Y displacement also exhibited triangular pattern because the X input adversely affected the Y displacement. The peak-to-peak amplitude of the triangular pattern of the Y error of the open loop nonlinear system with electrode dislocation (2.3 μm) was larger than that of the open loop nonlinear system without electrode dislocation (0.4 μm). The X RMSE and the Y RMSE of the open loop nonlinear system with electrode dislocation were 5.619 μm and 0.678 μm respectively. The open loop nonlinear system was unstable in both X direction and Y direction. It was deduced that the accuracy of the AFM without controller implementation was not satisfactory.

(iii) Since the performance of the open loop nonlinear system with electrode dislocation was poor, typical controllers were adopted to the piezoelectric tube

actuator with electrode dislocation to investigate their improvement. Based on the nonlinear system without electrode dislocation, intensive tunings on the controller gains of the typical controllers were carried out. The simulations of the closed loop nonlinear system with electrode dislocation using the typical controllers with tuned controller gains were performed. Both the PI controller and the OFC can compensate hysteresis. The X RMSE of the closed loop nonlinear system with electrode dislocation using the PI controller was 2.908 μm and that of the closed loop nonlinear system with electrode dislocation using the OFC was 2.003 μm. Both of them were smaller than that of the open loop nonlinear system with electrode dislocation which was 5.619 μm. The data also show that the OFC was better than the PI controller regarding the compensation of hysteresis. Both the PI controller and the OFC can compensate coupling effect. The peak-to-peak amplitude of triangular pattern of the Y error of the closed loop nonlinear system with electrode dislocation using the PI controller was 0.6 μm and that of the closed loop nonlinear system with electrode dislocation using the OFC was 1.5 μm. Both of them were smaller than that of the open loop nonlinear system with electrode dislocation which was 2.3 μm. The data also show that the PI was better than the OFC controller regarding the compensation of coupling effect. Both of the PI controller and the OFC can improve the stability of the system in X direction. However, the Y error of the closed loop nonlinear system with electrode dislocation using the PI controller and the OFC diverged quickly. Also, both of them cannot compensate creep. The PI controller and the OFC were not perfect. There are two advantages for typical controllers: a) they can reduce the error induced by coupling effect and hysteresis; b) their structures

are simple so that it is easy to implement them in application. However, they also have disadvantages: a) the tuning process is time consuming and tedious; b) the theoretical stability of the closed loop system cannot be guaranteed due to the presence of coupling effect, creep and hysteresis; c) the controller gains found in the tuning process without electrode dislocation are not suitable for the controllers used in system with electrode dislocation; d) they cannot compensate creep.

(iv) An ASMC was developed for the piezoelectric tube actuator. The simulation of the closed loop nonlinear system with electrode dislocation using the ASMC was performed. Using the ASMC, the peak-to-peak amplitude of the wave pattern of the Y error of the piezoelectric tube actuator with electrode dislocation was reduced from 2.3 μm to 1.1 μm. The X error of the piezoelectric tube actuator with electrode dislocation converges and the Y error of the piezoelectric tube actuator with electrode dislocation increased slower in positive direction. The X RMSE of the piezoelectric tube actuator with electrode dislocation was reduced from 5.619 μm to 1.762 μm. It is evident that the ASMC can reduce error induced by coupling effect, creep and hysteresis, and improve the stability.

(v) The performance of the ASMC, the PI controller and the OFC was compared based on coupling effect, creep and hysteresis compensation ability, and the stability improvement ability. The peak-to-peak amplitude of the wave pattern of the X error of the closed loop nonlinear system with electrode dislocation using the ASMC (4 μm at steady state) was significantly smaller than that of the closed loop nonlinear system with electrode dislocation using the PI

controller (10 μm) and was slightly smaller than that of the closed loop nonlinear system with electrode dislocation using the OFC (4.5 μm at steady state). The peak-to-peak amplitude of the wave pattern of the Y error of the closed loop nonlinear system with electrode dislocation using the ASMC (1.1 μm) was smaller than that of the triangular pattern of the Y error of the closed loop nonlinear system with electrode dislocation using the OFC (1.5 μm) but larger than that of the closed loop nonlinear system with electrode dislocation using the PI controller (0.6 μm). The convergence rate of the X error of the closed loop nonlinear system with electrode dislocation using the ASMC was higher than those of the closed loop nonlinear system with electrode dislocation using the PI controller and the OFC. The Y error of the closed loop nonlinear system with electrode dislocation using the OFC diverged quickly and that of the closed loop nonlinear system with electrode dislocation using the PI controller increased in negative direction quickly comparing to increase rate of the Y error of the closed loop nonlinear system with electrode dislocation using the ASMC. It is concluded that: a) the performance of the PI controller on reducing the tracking error due to coupling effect was the best among the candidates; however, the performance on compensation of other adverse effects and stability improvement was poor; b) the performance of the OFC on reducing tracking error due to hysteresis was better than the PI controller and was nearly as good as that of the ASMC; however, the performance of creep compensation and stability improvement was poor. The OFC was quite sensitive to coupling effect due to electrode dislocation; c) the performance of the ASMC on reducing tracking errors due to creep and hysteresis, and stability improvement was the best among the controller

candidates. It is concluded that the ASMC can be a good candidate applied to AFM among the controllers in the research. The ASMC proposed in this thesis has the following advantages: a) hysteresis compensation is enhanced by implementing a continuous-time dynamic model of backlash-like hysteresis; b) with the observer, the order of the controller can be decided by the designer. Larger order of the controller improves the performance since the degree of the freedom is increased. Lower order of the controller allows shorter computation time of the control signal. Insufficient high computational speed can lead to instability. It is a trade-off; c) Lyapunov equation can be developed to state the theoretical stability of the ASMC influenced by coupling effect, creep and hysteresis; d) controller gains can be adapted automatically. However, the ASMC has the following disadvantages: a) a set of conditions should be satisfied in controller design process. Advanced engineering software such as MATLAB is necessary to solve some numerical problems such as Lyapunov equation, matrix inverse and division, and Riccati equation; b) the errors of the closed loop nonlinear system cannot be reduced to zero which is partly due to the soft switching mechanism and partly due to the unmatched uncertainties; c) the tracking error due to creep is reduced but not eliminated. Although the increasing rate (positive direction) of the Y error was reduced in the simulation, it was still present. The closed loop system cannot be regarded as a stable system as observed in the simulation result.

(vi) Further simulations were performed with different creep and hysteresis properties. The ASMC can reduce the peak-to-peak amplitudes of the wave pattern of the X error of the piezoelectric tube actuator with electrode

dislocation from 13 μm to 7 μm at 10 Hz, and from 12 μm to 7 μm at 20 Hz. Therefore, it can still compensate hysteresis with hysteresis exhibiting at 10 Hz and 20 Hz. The ASMC can also improve the stability of the piezoelectric tube actuator with electrode dislocation at 10 Hz and 20 Hz. It is evident that the ASMC can tolerate the changes of the hysteresis properties at 10 Hz and 20 Hz. The ASMC can reduce the increasing rate (in positive direction) of the Y error of the piezoelectric tube actuator with electrode dislocation when the increase of the creep properties is 10%. Therefore, it can still compensate creep effect with this change. It is evident that the ASMC can tolerate the changes of the creep properties when the increase of the creep properties is 10%. The ASMC has a better tolerance of the changes of the creep properties and the hysteresis properties than the typical controllers. The range of hysteresis tolerance of the ASMC was found to cover the maximum scanning frequency of AFM while the range of creep tolerance accounts for 10% change of its nominal parameter values of creep.

(vii) About the noise, if the experimental setup uses the PCI controller card (Brand Name: dSPACE, Model: DS1104), the voltage amplifier (Brand Name: TREK, Model: 10/40A) and the capacitive sensor (Brand Name: Lion Precision, Model: CPL290) with D Type 5 mm standard probe, the error caused by actuating noise and by measuring noise are about 5 nm rms and ± 5 nm respectively. It is small relative to the X RMSE and the Y RMSE of the closed loop nonlinear system.

7.2 CONCLUSIONS

The thesis is concluded as follows:

(1) The nonlinear FE model of the piezoelectric tube actuator has been successfully developed. Some assumptions and conditions were made to simplify the complexity of the model structure. The Kelvin-Voigt creep operator and the Prandtl-Ishlinskii hysteresis operator were implemented into the constitutive equations of piezoelectric material. The mathematical model formulated in this way facilitates the simulation of the dynamic response of the actuator with inherent creep and hysteresis characteristics. The balanced model truncation via Schur method was adopted to reduce the order of the model. The Rayleigh constants, the parameters of Kelvin-Voigt creep operators and the parameters of Prandtl-Ishlinskii hysteresis operators were identified by comparing the simulation results with the experimental ones from literature (Leang and Devasia, 2007). The full nonlinear FE model (Eq. (3.56) and Eq. (3.57)) and the reduced order nonlinear FE models (Eq. (3.62b) and Eq. (3.63)) have been validated by comparing their responses with the experimental ones from literature (Leang and Devasia, 2007) to show that the reduced order nonlinear FE models (Eq. (3.62b) and Eq. (3.63)) are accurate for controller design and simulation purposes.

(2) The ASMC has been developed for the piezoelectric tube actuator with electrode dislocation based on the reduced order nonlinear FE model (Eq. (3.62b) and Eq. (3.63)). Since coupling effect, creep and hysteresis were considered as uncertainties which were not fully known in controller design process, the ASMC which is insensitive to perturbations was a suitable choice for the piezoelectric tube actuator. A continuous-time dynamic model of backlash-like hysteresis was adopted to enhance compensation of hysteresis and the reduced order nonlinear FE model (Eq. (5.4ℓ)) was used for determining the initial values of controller gains in order to improve the transient response of the closed loop system. A Walcott Zak observer was adopted to estimate the unmeasurable states. Lyapunov equation ensured the theoretical stability of the closed loop system using the ASMC while some conditions should be satisfied. In addition, the adaptation laws of controller gains were developed by Lyapunov equation.

(3) The simulations of the open loop nonlinear model, and the closed loop nonlinear model with electrode dislocation using the ASMC, the PI controller and the OFC were performed aiming to track a raster pattern. The simulation results show that the ASMC was able to compensate coupling effect, creep and hysteresis, and improve the stability of the piezoelectric tube actuator with electrode dislocation simultaneously. The PI controller and the OFC cannot compensate creep, and their stability improvement ability was poorer than the ASMC's.

(4) Further simulations of the closed loop nonlinear system with electrode dislocation were performed for the cases when the creep properties or the hysteresis properties are altered. Simulation results show that the ASMC can tolerate the 10% increase of the creep parameters, or the hysteresis phenomenon exhibiting at 10Hz and 20Hz. The PI controller and the OFC had poorer error minimization ability and stability improvement ability.

7.3 CONTRIBUTIONS

(i) A reduced order nonlinear FE model (Eq. (3.62b) and Eq. (3.63)) of a piezoelectric tube actuator, capable of exhibiting creep and hysteresis, was successfully built up.

(ii) Effects of coupling due to electrode dislocation, creep and hysteresis on the responses of the open loop actuator system were investigated for tracking a raster pattern used in AFM.

(iii) An ASMC was developed for the piezoelectric tube actuator.

(iv) The performance, in terms of reduction of the tracking error induced by coupling effect, creep and hysteresis, and stability improvement, of the ASMC, the PI controller and the OFC was compared. The overall performance of the ASMC was found to be the best among the controller candidates.

(v) The performance of the ASMC using original settings for systems with altered creep and hysteresis properties was investigated. The controller can tolerate adverse effects in a certain range of biases.

7.4 SUGGESTIONS FOR FUTURE RESEARCH

This thesis systematically studies dynamic modelling problems and control problems of piezoelectric tube actuator and the simulation shows encouraging results for the ASMC. However, modelling and control of piezoelectric tube actuator are comprehensive fields and further investigation is needed. The problems listed below are set open.

(i) Coupling effect, creep and hysteresis have already been considered in this thesis. Nevertheless, it does not mean all the factors affecting the accuracy of the AFM have been taken account. Thermal drift is caused by internal heating of the AFM during operation or by external ambient temperature change leading to the dimensional change of AFM components including piezoelectric tube actuator. In practice, the ambient conditions can be well controlled; however, it is not a perfect solution because of internal heating. In current literature, phase-correlation method has been adopted for drift measurement. Hence, the thermal drift is compensated by neural network (Yang *et al.*, 2005) or gradient method (Zhan *et al.*, 2007). Yang and Jagannathan (2006) proposed combining phase-correlation method and neural network with the proportional-derivative controller to enhance ability on error

minimization; however, stability is difficult to be confirmed. It is a challenging task to develop a single controller which can compensate all effects including coupling, creep, hysteresis and thermal drift. First of all, a mathematical model which can take into account the thermal dynamics of piezoelectric tube actuator in addition to creep and hysteresis is built. One may refer to Kumar *et al.* (2008). Then, a controller with temperature feedback is designed based on such model. The difficulty of performing such tasks in this thesis is that there were not enough experimental results available for validation of model with thermal properties.

(ii) Vibration is a cause of tracking error and instability. There are a number of literature related to compensation of vibrations of AFM by controller design (Croft *et al.*, 2001), mechatronic design (Fleming and Moheimani, 2006) and combination of them (Schitter *et al.*, 2007; and Schitter, 2009). In fact, the operating frequency of AFM (10 Hz) is far below the first resonant frequency (about 850 Hz (Moheimani, 2008)) so the effect of vibration on the AFM operating at normal speed is not significant. The purpose of compensating errors due to vibration is to increase the limit of the scanning speed of AFM. Compensation of error due to vibration at high frequency together with coupling effect, creep and hysteresis is an interesting topic for research.

(iii) It is valuable to examine the performance of operator-based inverse feedforward controller plus ASMC since this kind of controller can further improve the ability of the ASMC on mitigating the error caused by nonlinearities.

(iv) The performance of the controllers was investigated by simulations in this thesis. Since there are numerous factors affecting the responses of the closed loop system, the controllers may perform differently in real-life situation. Applying the controllers to an industrial type piezoelectric tube actuator can reveal the actual performance. If possible, an experimental study of the performance of the controllers on an actual AFM is even more challenging.

APPENDIX A:
DERIVATION OF $[A]^e$ AND $[B]^e$

This appendix shows the derivation of $[A]^e$ and $[B]^e$. The nodal r coordinates of an element is given as:

$$[R]^e = [r_1 \quad r_2 \quad r_3 \quad r_4 \quad r_5 \quad r_6 \quad r_7 \quad r_8]^T, \tag{A.1}$$

where $[R]^e \in \Re^8$ denotes the nodal r coordinates of an element. r_i denotes the nodal r coordinate and the subscript of r_i specifies the i-th node. The r coordinate of an arbitrary point is given (Danielson and Noor, 1997):

$$r^e = N_1 r_1 + N_2 r_2 + N_3 r_3 + \cdots + N_8 r_8, \tag{A.2a}$$

where r^e denotes the r coordinate of an arbitrary point. Eq. (A.2a) can be rearranged as:

$$r^e = [n]^e [R]^e. \tag{A.2b}$$

The Jacobian is given (Danielson and Noor, 1997):

$$[J] = \begin{bmatrix} \dfrac{\partial r}{\partial \xi} & \dfrac{\partial \theta}{\partial \xi} & \dfrac{\partial z}{\partial \xi} \\ \dfrac{\partial r}{\partial \eta} & \dfrac{\partial \theta}{\partial \eta} & \dfrac{\partial z}{\partial \eta} \\ \dfrac{\partial r}{\partial \zeta} & \dfrac{\partial \theta}{\partial \zeta} & \dfrac{\partial z}{\partial \zeta} \end{bmatrix}. \tag{A.3a}$$

The Jacobian can be used for transformation of coordinates:

$$\begin{bmatrix} \frac{\partial}{\partial \xi}(\bullet) \\ \frac{\partial}{\partial \eta}(\bullet) \\ \frac{\partial}{\partial \zeta}(\bullet) \end{bmatrix} = [J] \begin{bmatrix} \frac{\partial}{\partial r}(\bullet) \\ \frac{\partial}{\partial \theta}(\bullet) \\ \frac{\partial}{\partial z}(\bullet) \end{bmatrix}, \tag{A.3b}$$

where "$\bullet$" is any function being partial differentiated. The following partial differentiations of assembly of shape functions are defined:

$$[\Lambda_1] = \begin{bmatrix} \frac{\partial [N]^e}{\partial \xi} & \frac{\partial [N]^e}{\partial \eta} & \frac{\partial [N]^e}{\partial \zeta} \end{bmatrix}^T \tag{A.4a}$$

$$[\Lambda_2] = \begin{bmatrix} \frac{\partial [n]^e}{\partial \xi} & \frac{\partial [n]^e}{\partial \eta} & \frac{\partial [n]^e}{\partial \zeta} \end{bmatrix}^T, \tag{A.4b}$$

where $[\Lambda_1] \in \Re^{9\times 24}$ and $[\Lambda_2] \in \Re^{3\times 8}$ are the partial differentiations of assembly of shape functions for interpolation of displacements and electric potentials respectively.

Each component of the strains of an element $[\varepsilon]^e$ in Eq. (3.6a) is given below:

$$\varepsilon_z = \frac{\partial u_z}{\partial z} \tag{A.5a}$$

$$= \left\{ \begin{bmatrix} 0 & 0 & 1 \end{bmatrix} [J]^{-1} \begin{bmatrix} 0 & 0 & 1 & 0 & 0 & 0 & 0 & 0 & 0 \\ 0 & 0 & 0 & 0 & 0 & 1 & 0 & 0 & 0 \\ 0 & 0 & 0 & 0 & 0 & 0 & 0 & 0 & 1 \end{bmatrix} [\Lambda_1] \right\} [q]^e \tag{A.5b}$$

$$= [\breve{A}_1]^e [q]^e \tag{A.5c}$$

$$\varepsilon_\theta = \frac{1}{r}\left(\frac{\partial u_\theta}{\partial \theta} + u_r \right) \tag{A.6a}$$

$$= \left\{ \frac{1}{r^e} \begin{bmatrix} 0 & 1 & 0 \end{bmatrix} [J]^{-1} \begin{bmatrix} 0 & 1 & 0 & 0 & 0 & 0 & 0 & 0 & 0 \\ 0 & 0 & 0 & 0 & 1 & 0 & 0 & 0 & 0 \\ 0 & 0 & 0 & 0 & 0 & 0 & 0 & 1 & 0 \end{bmatrix} [\Lambda_1] \right.$$

$$\left. + \frac{1}{r^e} \begin{bmatrix} 1 & 0 & 0 \end{bmatrix} [N]^e \right\} [q]^e \tag{A.6b}$$

$$= \left[\breve{A}_2 \right]^e [q]^e \tag{A.6c}$$

$$\varepsilon_r = \frac{\partial u_r}{\partial r} \tag{A.7a}$$

$$= \left\{ \begin{bmatrix} 1 & 0 & 0 \end{bmatrix} [J]^{-1} \begin{bmatrix} 1 & 0 & 0 & 0 & 0 & 0 & 0 & 0 & 0 \\ 0 & 0 & 0 & 1 & 0 & 0 & 0 & 0 & 0 \\ 0 & 0 & 0 & 0 & 0 & 0 & 1 & 0 & 0 \end{bmatrix} [\Lambda_1] \right\} [q]^e \tag{A.7b}$$

$$= \left[\breve{A}_3 \right]^e [q]^e \tag{A.7c}$$

$$\gamma_{\theta r} = \frac{\partial u_\theta}{\partial r} - \frac{u_\theta}{r} + \frac{1}{r} \frac{\partial u_r}{\partial \theta} \tag{A.8a}$$

$$= \left\{ \begin{bmatrix} 1 & 0 & 0 \end{bmatrix} [J]^{-1} \begin{bmatrix} 0 & 1 & 0 & 0 & 0 & 0 & 0 & 0 & 0 \\ 0 & 0 & 0 & 0 & 1 & 0 & 0 & 0 & 0 \\ 0 & 0 & 0 & 0 & 0 & 0 & 0 & 1 & 0 \end{bmatrix} [\Lambda_1] - \frac{1}{r^e} \begin{bmatrix} 0 & 1 & 0 \end{bmatrix} [N]^e \right.$$

(A.8b)

$$\left. + \frac{1}{r^e} \begin{bmatrix} 0 & 1 & 0 \end{bmatrix} [J]^{-1} \begin{bmatrix} 1 & 0 & 0 & 0 & 0 & 0 & 0 & 0 & 0 \\ 0 & 0 & 0 & 1 & 0 & 0 & 0 & 0 & 0 \\ 0 & 0 & 0 & 0 & 0 & 0 & 1 & 0 & 0 \end{bmatrix} [\Lambda_1] \right\} [q]^e$$

$$= \left[\breve{A}_4 \right]^e [q]^e \tag{A.8c}$$

$$\gamma_{zr} = \frac{\partial u_z}{\partial r} + \frac{\partial u_r}{\partial z} \tag{A.9a}$$

$$= \left\{ \begin{bmatrix} 1 & 0 & 0 \end{bmatrix} [J]^{-1} \begin{bmatrix} 0 & 0 & 1 & 0 & 0 & 0 & 0 & 0 & 0 \\ 0 & 0 & 0 & 0 & 0 & 1 & 0 & 0 & 0 \\ 0 & 0 & 0 & 0 & 0 & 0 & 0 & 0 & 1 \end{bmatrix} [\Lambda_1] \right.$$

$$+\begin{bmatrix}0 & 0 & 1\end{bmatrix}[J]^{-1}\begin{bmatrix}1&0&0&0&0&0&0&0&0\\0&0&0&1&0&0&0&0&0\\0&0&0&0&0&0&1&0&0\end{bmatrix}[\Lambda_1]\Bigg\}[q]^e \tag{A.9b}$$

$$=\left[\breve{A}_5\right]^e[q]^e \tag{A.9c}$$

$$\gamma_{z\theta}=\frac{\partial u_\theta}{\partial z}+\frac{1}{r}\frac{\partial u_z}{\partial \theta} \tag{A.10a}$$

$$=\Bigg\{\begin{bmatrix}0 & 0 & 1\end{bmatrix}[J]^{-1}\begin{bmatrix}0&1&0&0&0&0&0&0&0\\0&0&0&0&1&0&0&0&0\\0&0&0&0&0&0&0&1&0\end{bmatrix}[\Lambda] \tag{A.10b}$$

$$+\frac{1}{r^e}\begin{bmatrix}0 & 1 & 0\end{bmatrix}[J]^{-1}\begin{bmatrix}0&0&1&0&0&0&0&0&0\\0&0&0&0&0&1&0&0&0\\0&0&0&0&0&0&0&0&1\end{bmatrix}[\Lambda]\Bigg\}[q]^e$$

$$=\left[\breve{A}_6\right]^e[q]^e. \tag{A.10c}$$

Each component of the electric fields of an element $[E]^e$ in Eq. (3.9a) is given below:

$$E_z=-\frac{\partial \phi}{\partial z} \tag{A.11a}$$

$$=\Big\{-\begin{bmatrix}0 & 0 & 1\end{bmatrix}[J]^{-1}[\Lambda_2]\Big\}[\Phi]^e \tag{A.11b}$$

$$=\left[\breve{B}_1\right]^e[\Phi]^e \tag{A.11c}$$

$$E_\theta=-\frac{1}{r}\frac{\partial \phi}{\partial \theta} \tag{A.12a}$$

$$=\left\{-\frac{1}{r^e}\begin{bmatrix}0 & 1 & 0\end{bmatrix}[J]^{-1}[\Lambda_2]\right\}[\Phi]^e \tag{A.12b}$$

$$=\left[\breve{B}_2\right]^e[\Phi]^e \tag{A.12c}$$

$$E_r = -\frac{\partial \phi}{\partial r} \tag{A.13a}$$

$$= \left\{ -\begin{bmatrix} 1 & 0 & 0 \end{bmatrix} [J]^{-1} [\Lambda_2] \right\} [\Phi]^e \tag{A.13b}$$

$$= \left[\breve{B}_3\right]^e [\Phi]^e . \tag{A.13c}$$

Eq. (A.5c), Eq. (A.6c), Eq. (A.7c), Eq. (A.8c), Eq. (A.9c) and Eq. (A.10c) are assembled:

$$[\varepsilon]^e = \left[\left[\breve{A}_1\right]^e \quad \left[\breve{A}_2\right]^e \quad \left[\breve{A}_3\right]^e \quad \left[\breve{A}_4\right]^e \quad \left[\breve{A}_5\right]^e \quad \left[\breve{A}_6\right]^e \right]^T [q]^e . \tag{A.14a}$$

Defining:

$$[A]^e = \left[\left[\breve{A}_1\right]^e \quad \left[\breve{A}_2\right]^e \quad \left[\breve{A}_3\right]^e \quad \left[\breve{A}_4\right]^e \quad \left[\breve{A}_5\right]^e \quad \left[\breve{A}_6\right]^e \right]^T . \tag{A.14b}$$

Eq. (A.14a) has the form shown in Eq. (3.6c):

$$[\varepsilon]^e = [A]^e [q]^e . \tag{A.14c}$$

Similarly, Eq. (A.11c), Eq. (A.12c) and Eq. (A.13c) are assembled:

$$[E]^e = \left[\left[\breve{B}_1\right]^e \quad \left[\breve{B}_2\right]^e \quad \left[\breve{B}_3\right]^e \right]^T [\Phi]^e . \tag{A.15a}$$

Defining:

$$[B]^e = \left[\left[\breve{B}_1\right]^e \quad \left[\breve{B}_2\right]^e \quad \left[\breve{B}_3\right]^e \right]^T . \tag{A.15b}$$

Eq. (15a) has the form shown in Eq. (3.9c):

$$[E]^e = [B]^e [\Phi]^e . \tag{A.15c}$$

APPENDIX B:
FORMULATION OF $[Q_E]^e$

This appendix shows the formulation of $[Q_E]^e$. Considering an element with inner electrode attached, surface charges accumulate on the surface (1, 2, 5, 6) (Fig. (3-3)) when voltage is applied to the outer electrode. The charge supplied by the input voltage is uniform throughout the electrode (Chapter 3 Assumption 1). The elemental charge input vector $[Q_E]^e$ of an element with inner electrode attached is expressed:

$$[Q_E]^e = \frac{A_e}{4}[\rho_{inner} \quad \rho_{inner} \quad 0 \quad 0 \quad \rho_{inner} \quad \rho_{inner} \quad 0 \quad 0]^T, \tag{B.1}$$

where A_e is the area of the electrode attached surface of an element (m^2). ρ_{inner} is the surface charge density of the inner electrode (C/m^2). Similarly, considering an element with outer electrode attached, surface charges accumulate on the surface (3, 4, 7, 8) (Fig. 3-3) when voltage is applied to the outer electrode. The elemental charge input vector $[Q_E]^e$ of an element with outer electrode attached is expressed:

$$[Q_E]^e = \frac{A_e}{4}[0 \quad 0 \quad \rho_{outer} \quad \rho_{outer} \quad 0 \quad 0 \quad \rho_{outer} \quad \rho_{outer}]^T, \tag{B.2}$$

where ρ_{outer} is the surface charge density of the outer electrode (C/m^2).

The charges on the electrodes induced by the piezoelectric material are much less than those supplied by the external voltage (Chapter 3 Assumption 2). The

charges on the electrodes induced by the piezoelectric material are approximate one-fortieth of those supplied by the external voltage when piezoelectric tube actuator bends (Moheimani and Yong, 2008). Also, it is assumed that the deformation of the piezoelectric tube actuator is small so that cylindrical shape of the piezoelectric tube actuator does not distort seriously. Therefore, the total surface charge q_E on the electrode can be calculated by charge equation of the capacitor in cylindrical shape:

$$q_E = h \times 2\pi r_v \times \frac{\Theta}{2\pi} \times D_r \tag{B.3a}$$

$$\approx h r_v \Theta \varphi_{33} E_r , \tag{B.3b}$$

where h denotes height of piezoelectric tube actuator, r_v denotes radius of piezoelectric tube actuator and Θ denotes covering angle of electrode. The illustration of the parameters and the variables are shown in Fig. B-1.

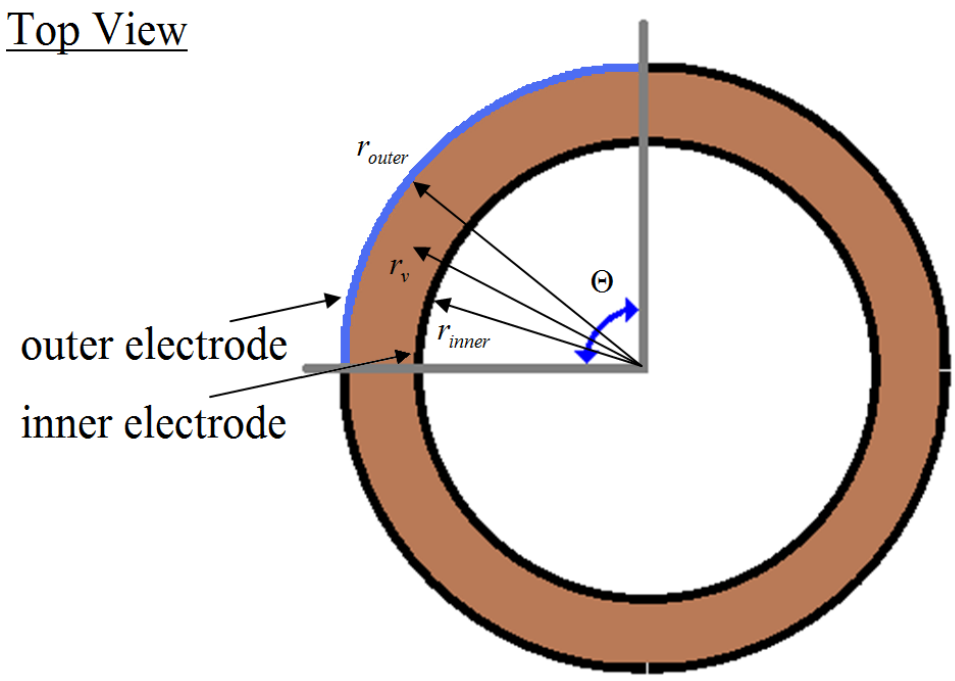

Fig. B-1 Illustration of r_{inner}, r_{outer}, r_v and Θ

The potential difference of the outer electrode and the inner electrode is expressed:

$$V_E = -\int_{r_{inner}}^{r_{outer}} E_r dr_v \ . \tag{B.4a}$$

Eq. (B.3b) is substituted into (B.4a):

$$V_E = -\int_{r_{inner}}^{r_{outer}} \frac{q_E}{r_v \Theta h \varphi_{33}} dr_v \tag{B.4b}$$

$$= \frac{q_E}{\Theta h \varphi_{33}} \ell n\left(\frac{r_{inner}}{r_{outer}}\right). \tag{B.4c}$$

The surface charge density of inner electrode is derived:

$$\rho_{inner} = \frac{q_E}{A_E} \tag{B.5a}$$

$$= \frac{q_E}{2\pi r_{inner} h \times \frac{\Theta}{2\pi}} \tag{B.5b}$$

$$= \frac{q_E}{r_{inner} h \Theta}, \tag{B.5c}$$

where ρ_{inner} denotes the surface charge density of inner electrode and A_E denotes the area of the electrode. Similarly, the surface charge density of outer electrode is derived:

$$\rho_{outer} = \frac{q_E}{r_{outer} h \Theta}, \tag{B.6}$$

where ρ_{outer} denotes the surface charge density of outer electrode. Eq. (B.5c) is substituted into Eq. (B.4c):

$$V_E = \frac{r_{inner} \rho_{inner}}{\varphi_{33}} \ell n\left(\frac{r_{inner}}{r_{outer}}\right). \tag{B.7a}$$

By rearranging Eq. (B.7a), the relation between the surface charge density of inner electrode is obtained:

$$\rho_{inner} = \frac{\varphi_{33}}{r_{inner}\ell n\left(\frac{r_{inner}}{r_{outer}}\right)} V_E . \tag{B.7b}$$

Similarly, the relation between the surface charge density of outer electrode is obtained:

$$\rho_{outer} = \frac{\varphi_{33}}{r_{outer}\ell n\left(\frac{r_{inner}}{r_{outer}}\right)} V_E . \tag{B.8}$$

Eq. (B.7b) is substituted into Eq. (B.1). The elemental charge input vector $[Q_E]^e$ of an element with inner electrode attached is obtained:

$$[Q_E]^e = \frac{\varphi_{33} A_e}{4 r_{inner}\ell n\left(\frac{r_{inner}}{r_{outer}}\right)} [V_E \quad V_E \quad 0 \quad 0 \quad V_E \quad V_E \quad 0 \quad 0]^T . \tag{B.9}$$

Similarly, Eq. (B.8) is substituted into Eq. (B.2). The elemental charge output vector $[Q_E]^e$ of an element with outer electrode attached is obtained:

$$[Q_E]^e = \frac{\varphi_{33} A_e}{4 r_{outer}\ell n\left(\frac{r_{inner}}{r_{outer}}\right)} [0 \quad 0 \quad V_E \quad V_E \quad 0 \quad 0 \quad V_E \quad V_E]^T . \tag{B.10}$$

APPENDIX C:

BALANCED MODEL TRUNCATION VIA SCHUR METHOD

The detail of the balanced model truncation via Schur method (Safonov and Chiang, 1989) is given in this appendix. Solving the Lyapunov equations:

$$[A_s][P_r]+[P_r][A_s]^T+[B_s][B_s]^T=[0] \tag{C.1}$$

$$[Q_o][A_s]+[A_s]^T[Q_o]+[C_s]^T[C_s]=[0], \tag{C.2}$$

the reachability Grammian $[P_r]\in\Re^{fo\times fo}$ and the observability Grammian $[Q_o]\in\Re^{fo\times fo}$ can be obtained. fo is the order of the full model. (A_s, B_s, C_s) is the full state space model defined by Eq. (3.56) and Eq. (3.57). The orthogonal real transformations $\Psi_A\in\Re^{fo\times fo}$ and $\Psi_D\in\Re^{fo\times fo}$ which order the Schur forms in ascending and descending order respectively are calculated by the following equations:

$$[\Psi_A]^T[P_r][Q_o][\Psi_A]=\begin{bmatrix}\lambda_1(P_rQ_o) & * & \cdots & \cdots & * \\ 0 & \lambda_2(P_rQ_o) & & & \vdots \\ \vdots & & \ddots & & \vdots \\ \vdots & & & \lambda_{fo-1}(P_rQ_o) & * \\ 0 & \cdots & \cdots & 0 & \lambda_{fo}(P_rQ_o)\end{bmatrix} \tag{C.3}$$

$$[\Psi_D]^T[P_r][Q_o][\Psi_D]=\begin{bmatrix}\lambda_{fo}(P_rQ_o) & * & \cdots & \cdots & * \\ 0 & \lambda_{fo-1}(P_rQ_o) & & & \vdots \\ \vdots & & \ddots & & \vdots \\ \vdots & & & \lambda_2(P_rQ_o) & * \\ 0 & \cdots & \cdots & 0 & \lambda_1(P_rQ_o)\end{bmatrix}, \tag{C.4}$$

where $\{\lambda_k(P_rQ_o) | k = 1, \cdots, fo\}$ are the eigenvalues of P_rQ_o. Hence, Ψ_A and Ψ_D are partitioned as follows:

$$[\Psi_A] = \left[\overbrace{[\Psi_{R,SMALL}]}^{fo-n} \middle| \overbrace{[\Psi_{L,BIG}]}^{n} \right] \tag{C.5}$$

$$[\Psi_D] = \left[\overbrace{[\Psi_{R,BIG}]}^{n} \middle| \overbrace{[\Psi_{L,SMALL}]}^{fo-n} \right], \tag{C.6}$$

where n is the order of the reduced model. The singular value decompositions of $[\Psi_{L,BIG}]^T[\Psi_{R,BIG}]$ which are $[\Omega_M] \in \Re^{n \times n}$ and $[U_M] \in \Re^{n \times n}$ are calculated by the following equation:

$$[\Psi_{L,BIG}]^T[\Psi_{R,BIG}] = [U_M][\Sigma_M][\Omega_M]^T, \tag{C.7}$$

where $[\Sigma_M] = diag(\sigma_{eig,1}(P_rQ_o) \cdots \sigma_{eig,n}(P_rQ_o))$ and $\sigma_{eig,k}(P_rQ_o) = \sqrt{\lambda_{eig,k}(P_rQ_o)}$. The left and right transformation $[S_{L,BIG}] \in \Re^{fo \times n}$ and $[S_{R,BIG}] \in \Re^{fo \times n}$ for the n-th reduced order model are calculated by the following equations:

$$[S_{L,BIG}] = [\Psi_{L,BIG}][U_M][\Sigma_n]^{-1/2} \tag{C.8}$$

$$[S_{R,BIG}] = [\Psi_{R,BIG}][\Omega_M][\Sigma_n]^{-1/2}. \tag{C.9}$$

$[\Sigma_n]$ is given by truncating the elements of diagonal matrix $[\Sigma_M]$ from $(n+1)$-th to fo-th row and column. The state space form of the reduced order model is given:

$$[A] = [S_{L,BIG}]^T[A_s][S_{R,BIG}] \tag{C.10}$$

$$[B_n] = [S_{L,BIG}]^T[B_s] \tag{C.11}$$

$$[C] = [C_s][S_{R,BIG}] \tag{C.12}$$

$$[D]=[D_s]=[0], \tag{C.13}$$

where $[A]\in\Re^{n\times n}$ denotes reduced order system matrix. $[B_n]\in\Re^{n\times 7}$ denotes reduced order input matrix with nonlinear distribution. $[C]\in\Re^{2\times n}$ denotes reduced order output matrix. $[D]\in\Re^{2\times 7}$ denotes reduced order feedforward matrix.

APPENDIX D:

OPTIMAL CONTROL FOR REFERENCE MODEL

It has been discussed in Chapter 5 Section 5.3.2 that the reference model can be designed based on the reduced order linear FE model (Eq. (3.63) and Eq. (3.65)) without the constant term due to gravity $[K_g]$ of the piezoelectric tube actuator shown in Eq. (3.65). As a remark, if the design of reference model is not based on the reduced order linear FE model (Eq. (3.63) and Eq. (3.65)) but by random selection of system matrix and input matrix, the difference of the dynamics of the reference model and the plant may be large. The states of the closed loop system cannot track the reference states easily.

First of all, the state equation of the reference model can be expressed:

$$[\dot{x}_m] = [A][x_m] + [B][u_m], \tag{D.1}$$

where $[u_m] \in \Re^2$ is the input to the reference model. It is remarked that $[u_m]$ is not a real input and it does not appear in the application. Since the dynamics of the linear model shown in Eq. (D.1) may not be satisfactory, optimal control is applied for adjustment. It is possible to focus on designing an optimal regulator first such that $[r] = [0]$ (Ogata, 2001). The feedback gain for the reference model $[K_m] \in \Re^{2\times n}$ is determined such that the following performance index is minimized:

$$J_c = \int_0^\infty \left([x_m]^T [Q_m][x_m] + [u_m]^T [R_m][u_m] \right) dt, \tag{D.2}$$

where $[Q_m] \in \Re^{n \times n}$ is the design matrix for the reference states and $[R_m] \in \Re^{2 \times 2}$ is the design matrix for the input to the reference model. $[Q_m]$ and $[R_m]$ should be designed to be positive definite (Chapter 5 Condition 1). For the optimal regulator, the input to the reference model $[u_m]$ is selected as:

$$[u_m] = -[K_m][x_m]. \tag{D.3}$$

Eq. (D.3) is substituted into Eq. (D.1), the following relation is obtained:

$$[\dot{x}_m] = \{[A] - [B][K_m]\}[x_m]. \tag{D.4}$$

Eq. (D.3) is substituted into Eq. (D.2) and the performance index becomes:

$$J_c = \int_0^\infty \left([x_m]^T \left([Q_m] + [K_m]^T [R_m][K_m] \right) [x_m] \right) dt. \tag{D.5}$$

The following relation is set:

$$[x_m]^T \left([Q_m] + [K_m]^T [R_m][K_m] \right) [x_m] = -\frac{d}{dt} \left([x_m]^T [P_m][x_m] \right), \tag{D.6}$$

where $[P_m] \in \Re^{n \times n}$ denotes the Riccati matrix. Using Eq. (D.4), Eq. (D.6) can be modified:

$$\{[A] - [B][K_m]\}^T [P_m] + [P_m]\{[A] - [B][K_m]\} = -\left([Q_m] + [K_m]^T [R_m][K_m] \right). \tag{D.7}$$

Since the design matrix for the input to the reference model $[R_m]$ is positive definite, it can be decomposed:

$$[R_m] = [T_c]^T [T_c], \tag{D.8}$$

where $[T_c] \in \Re^{2 \times 2}$ denotes a nonsingular matrix. Eq. (D.8) is substituted into Eq. (D.7) and the following equation is obtained:

$$[A]^T[P_m]+[P_m][A]$$

$$+\left\{[T_c][K_m]-\left\{[T_c]^T\right\}^{-1}[B]^T[P_m]\right\}^T\left\{[T_c][K_m]-\left\{[T_c]^T\right\}^{-1}[B]^T[P_m]\right\} \tag{D.9}$$

$$-[P_m][B][R_m]^{-1}[B]^T[P_m]+[Q_m]=[0].$$

The minimization of the performance index J_c with respect to $[K_m]$ requires minimization of the following equation:

$$[x_m]^T\left\{[T_c][K_m]-\left\{[T_c]^T\right\}^{-1}[B]^T[P_m]\right\}^T\left\{[T_c][K_m]-\left\{[T_c]^T\right\}^{-1}[B]^T[P_m]\right\}[x_m]. \tag{D.10}$$

The minimum occurs when the following relation is set:

$$[T_c][K_m]=\left\{[T_c]^T\right\}^{-1}[B]^T[P_m]. \tag{D.11}$$

Hence,

$$[K_m]=[T_c]^{-1}\left\{[T_c]^T\right\}^{-1}[B]^T[P_m] \tag{D.12a}$$

$$=[R_m]^{-1}[B]^T[P_m]. \tag{D.12b}$$

By substituting Eq. (D.11) into Eq. (D.9), the following reduced continuous algebraic Riccati equation is obtained:

$$[A]^T[P_m]+[P_m][A]-[P_m][B][R_m]^{-1}[B]^T[P_m]+[Q_m]=[0]. \tag{D.13}$$

In order to obtain the feedback gain for the reference model $[K_m]$, the Riccati matrix $[P_m]$ is solved by Eq. (D.13) first. It is noticed that it is probably that there are more than one solution of $[P_m]$ and only the positive definite one is selected. Then, the Riccati matrix $[P_m]$ is substituted into Eq. (D.12b) to solve out the feedback gain for the reference model $[K_m]$.

For tracking purpose, the input to the reference model $[u_m]$ is selected as:

$$[u_m] = [N_m][r] - [K_m][x_m], \tag{D.14}$$

where $[N_m] \in \Re^{2\times 2}$ is the feedforward gain for the reference model. The tuned reference model is obtained by substituting Eq. (D.14) into Eq. (D.1):

$$[\dot{x}_m] = \{[A] - [B][K_m]\}[x_m] + [B][N_m][r]. \tag{D.15}$$

By comparing Eq. (D.15) with Eq. (5.5a), the reference system matrix $[A_m]$ and the reference input matrix $[B_m]$ are given:

$$[A_m] = [A] - [B][K_m] \tag{D.16}$$

$$[B_m] = [B][N_m]. \tag{D.17}$$

$[N_m]$ can be tuned by trial-and-error method until the reference output $[y_m]$ is sufficiently close to the desired output $[r]$. The system is required to be reachable (Chapter 5 Assumption 3). $[A_m]$ can be ensured to be Hurwitz as it is found by the optimal control.

APPENDIX E:

DERIVATION OF ERROR DYNAMICS ON SLIDING SURFACE

In this appendix, the detail of the derivation of the error dynamics on the sliding surface is shown. By substituting the equivalent control Eq. (10a) into the error dynamic equation Eq. (5.7b), the following equation is obtained:

$$\begin{aligned}[\dot{e}_s] &= [A_m][e_s] + [B_1]\{[K_s][B_1]\}^{-1}[K_s]\{[A_m]-[A]\}[x] \\ &\quad + [B_1]\{[K_s][B_1]\}^{-1}[K_s][B_m][r] - [B_1]\{[K_s][B_1]\}^{-1}[K_s][K_g] \\ &\quad + [K_g] + \{[A]-[A_m]\}[x] - [B_m][r] \end{aligned} \tag{E.1a}$$

$$\begin{aligned} &= [A_m][e_s] + \{[I]-[B_1]\{[K_s][B_1]\}^{-1}[K_s]\}\{[A]-[A_m]\}[x] \\ &\quad - \{[I]-[B_1]\{[K_s][B_1]\}^{-1}[K_s]\}[B_m][r] + \{[I]-[B_1]\{[K_s][B_1]\}^{-1}[K_s]\}[K_g], \end{aligned} \tag{E.1b}$$

where $[I]$ denotes the identity matrix in appropriate size. Eq. (5.10a) – Eq. (5.10c) are rearranged:

$$[A]-[A_m] = -[B_1][K_1] \tag{E.2a}$$

$$[B_m] = [B_1][K_2] \tag{E.2b}$$

$$[K_g] = -[B_1][K_3]. \tag{E.2c}$$

By substituting Eq. (E.2a) – Eq. (E2c) into Eq. (E.1b), the error dynamic equation becomes:

$$[\dot{e}_s] = [A_m][e_s] - \{[I] - [B_1]\{[K_s][B_1]\}^{-1}[K_s]\}[B_1][K_1][x]$$
$$- \{[I] - [B_1]\{[K_s][B_1]\}^{-1}[K_s]\}[B_1][K_2][r] \quad \text{(E.3a)}$$
$$- \{[I] - [B_1]\{[K_s][B_1]\}^{-1}[K_s]\}[B_1][K_3].$$

Since:

$$\{[I] - [B_1]\{[K_s][B_1]\}^{-1}[K_s]\}[B_1] = [0], \quad \text{(E.4)}$$

the error dynamics of the closed loop system on the sliding surface is reduced to:

$$[\dot{e}] = [A_m][e]. \quad \text{(E.5)}$$

APPENDIX F:

PLOTTINGS OF ESTIMATED STATES

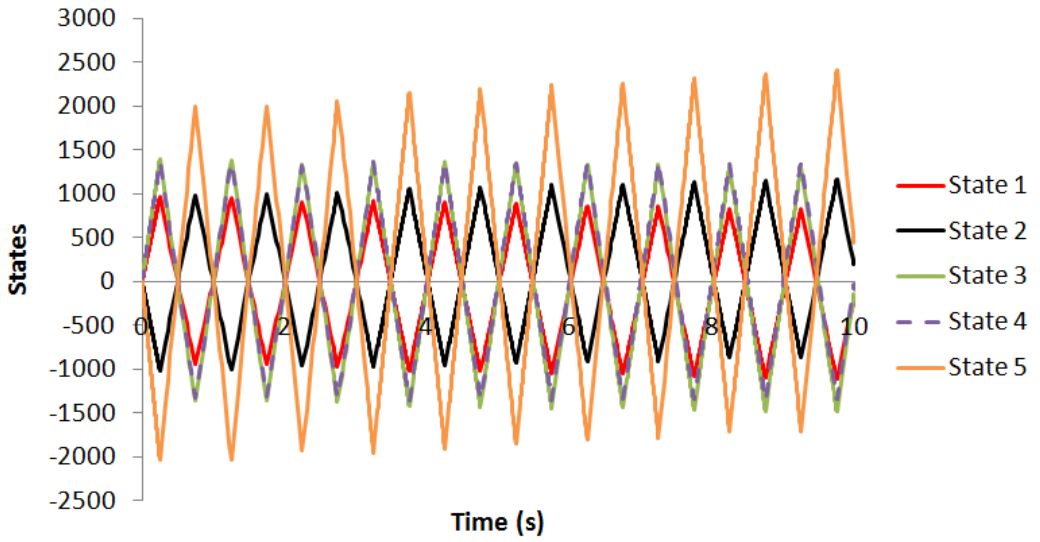

Figure F-1. Estimated States (State 1 – 5)

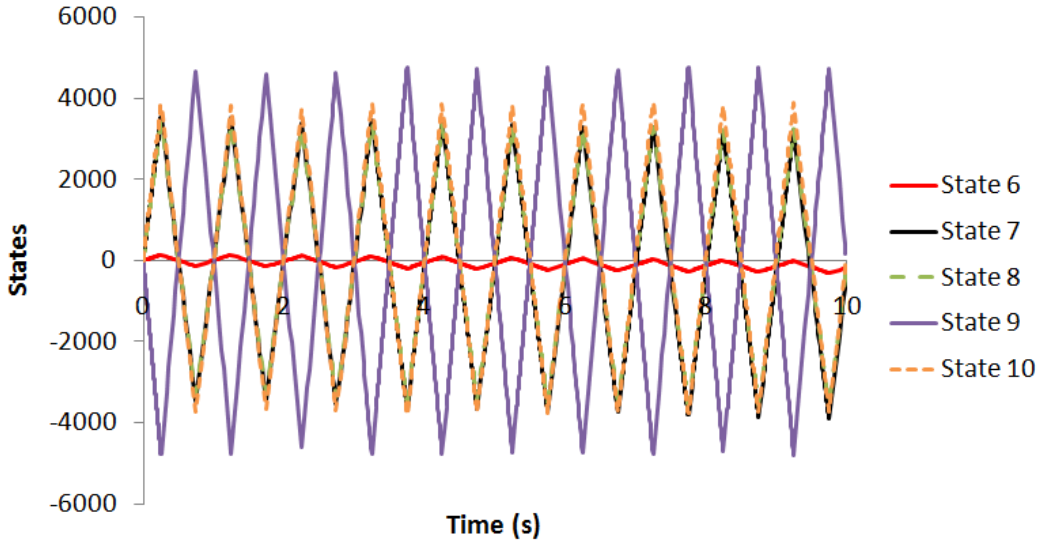

Figure F-2. Estimated States (State 6 – 10)

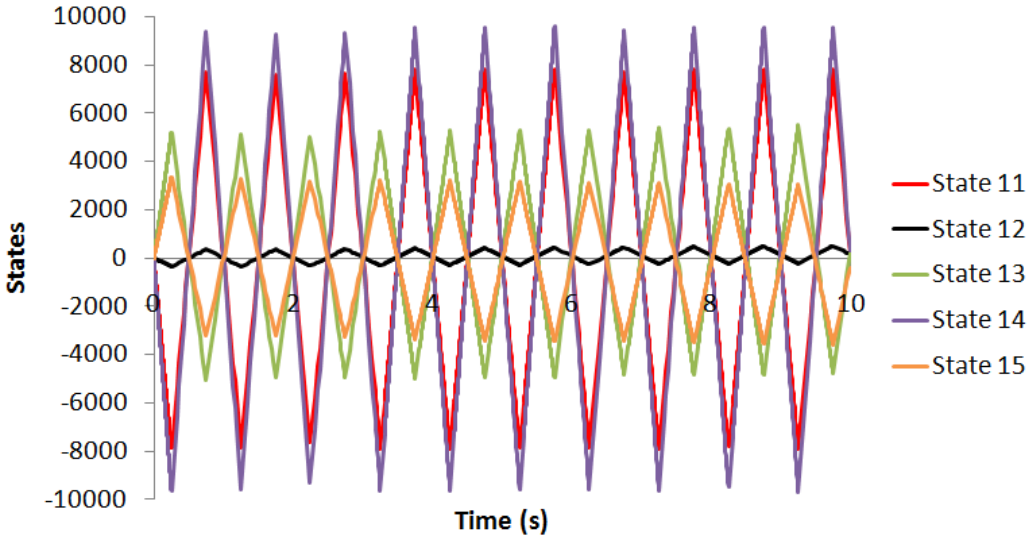

Figure F-3. Estimated States (State 11 – 15)

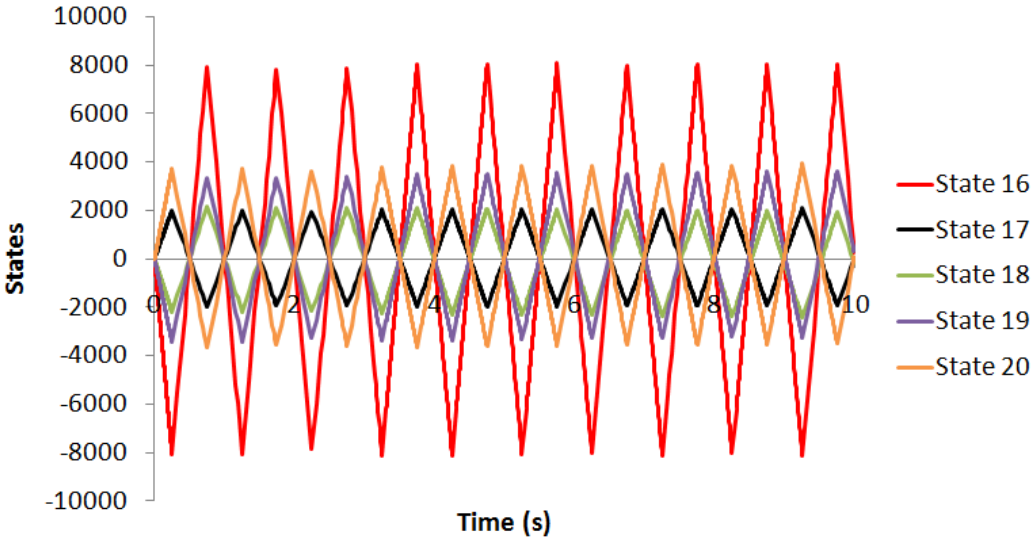

Figure F-4. Estimated States (State 16 – 20)

APPENDIX G:

BLOCK CONNECTIONS IN MATLAB/SIMULINK

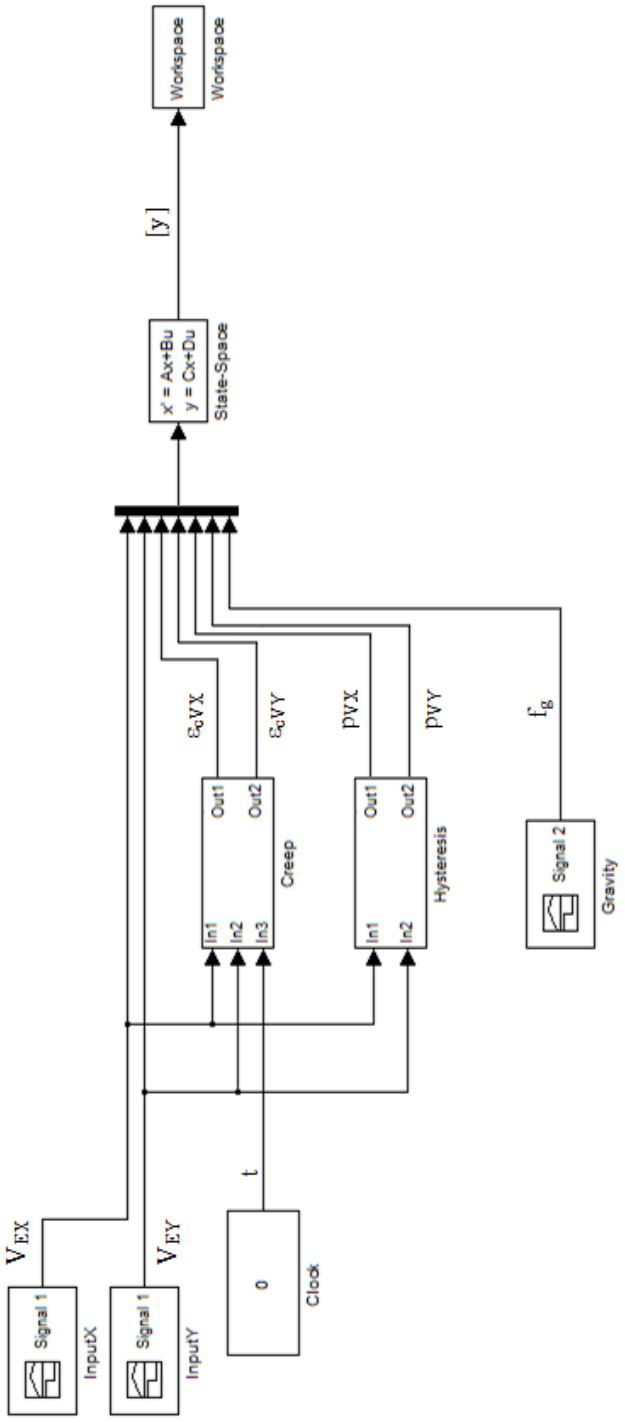

Figure G-1. Block Connection of Plant Model in MATLAB/Simulink

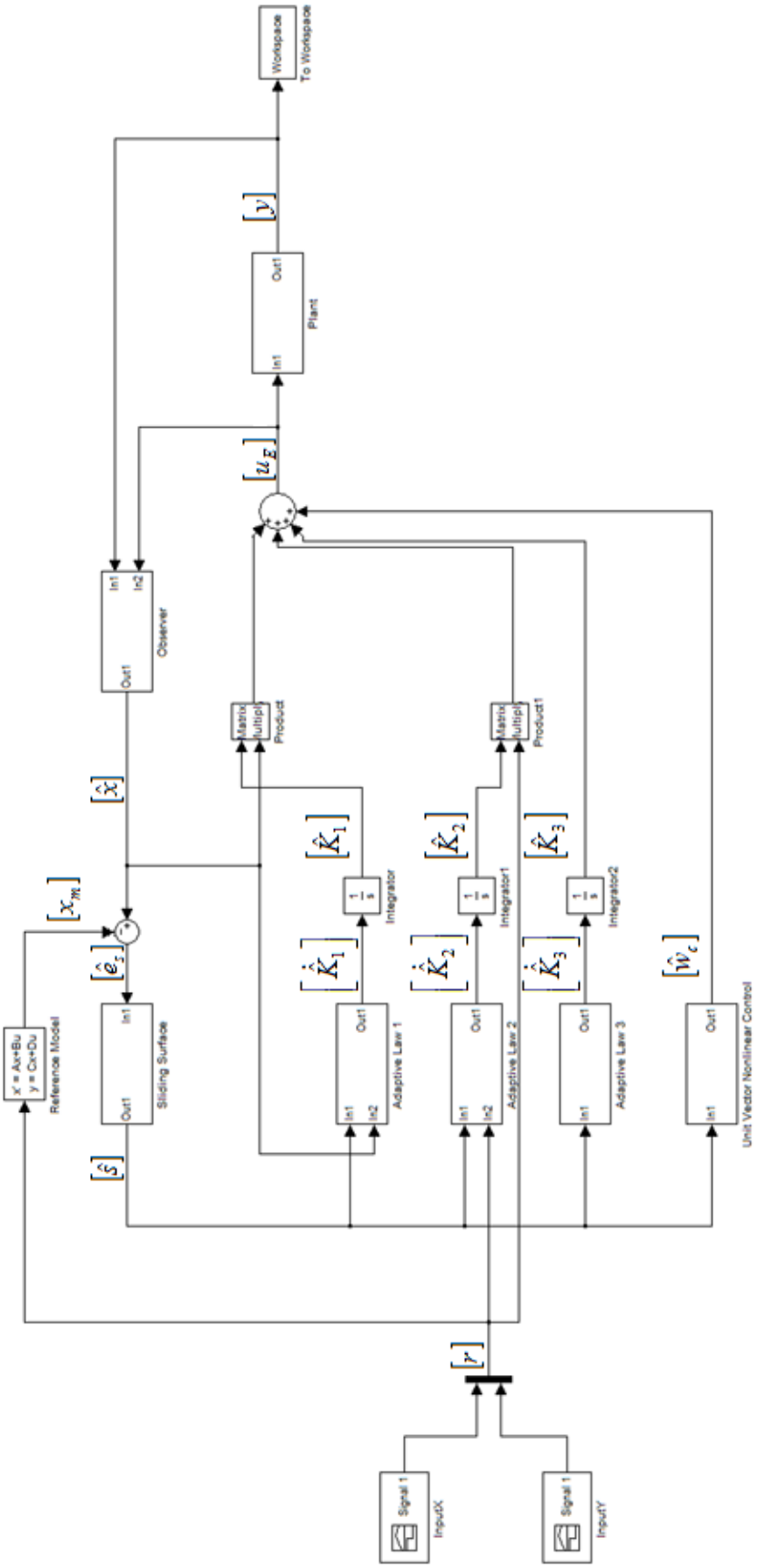

Figure G-2. Block Connection of Closed Loop System using ASMC in MATLAB/Simulink

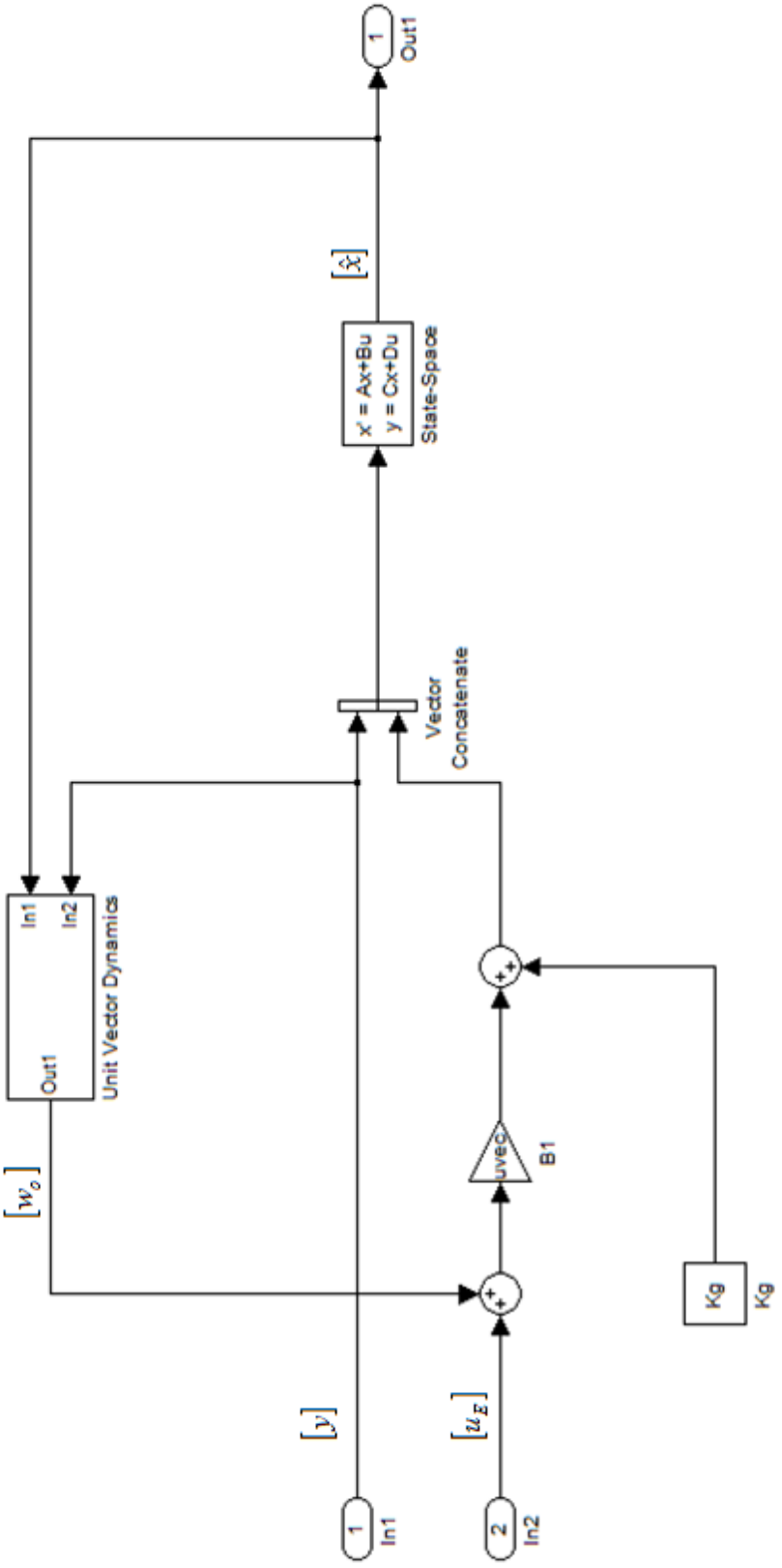

Figure G-3. Block Connection of Walcott Zak Observer in MATLAB/Simulink

APPENDIX H:

MAIN PROGRAM FOR FORMULATION OF REDUCED ORDER FINITE ELEMENT MODEL

```
%parameters
nel=192;
nnel=8;
ndof=4;
dndof=3;
phndof=1;
nnode=336;
dsdof=nnode*dndof;
dedof=nnel*dndof;
phsdof=nnode*phndof;
phedof=nnel*phndof;


%material properties of pzt-4
emodulus11=1.39e11;
emodulus12=7.7837e10;
emodulus13=7.4284e10;
emodulus22=1.39e11;
emodulus23=7.4284e10;
emodulus33=1.1541e11;
emodulus44=2.5641e10;
emodulus55=2.5641e10;
```

```
emodulus66=3.0581e10;
emodulus=[emodulus11 emodulus12 emodulus13 0 0 0;
emodulus12 emodulus22 emodulus23 0 0 0;
emodulus13 emodulus23 emodulus33 0 0 0;
0 0 0 emodulus44 0 0;
0 0 0 0 emodulus55 0;
0 0 0 0 0 emodulus66];

piezocoeff31=-5.2028;
piezocoeff32=-5.2028;
piezocoeff33=15.0804;
piezocoeff24=12.7179;
piezocoeff15=12.7179;
piezocoeff=[0 0 0 0 piezocoeff15 0;
0 0 0 piezocoeff24 0 0;
piezocoeff31 piezocoeff32 piezocoeff33 0 0 0];

dielecoeff11=6.7515e-9;
dielecoeff22=6.7515e-9;
dielecoeff33=7.4215e-9;
dielecoeff=[dielecoeff11 0 0; 0 dielecoeff22 0; 0 0 dielecoeff33];

poisson=0.34;
density=7500;

alpha=0.3*6.0416;
beta=0.015*4.056e-5;

hysteresis_weight=-3.33e-3/10000;
P_max=1.12*5.2;
```

```
%dimension of the piezoelectric tube actuator
or=(12.7e-3)/2;
wall=0.5e-3;
ir=or-wall;
length=25.4e-3;
unit_height_electrode_element=(length-2*2.8e-3)/4;


degree =90;


%global coordinate system
tempa=[17 1 2 18 65 49 50 66];
tempb=tempa;
for m=1:14
    tempb=[tempb;tempa+(m*1)];
end
tempb=[tempb;32 16 1 17 80 64 49 65];
tempb=[tempb;tempb+16];
glabel=tempb;
for m =1:5
    glabel=[glabel;tempb+(48*m)];
end
clear tempa tempb;


n=1;
z=0;
for r=0:1:2
    for th=0:2*pi/16:15/16*2*pi
            gcoor(n,1)=or-r*wall/2;
        if th==pi*2/8
            gcoor(n,2)=th+(degree-90)*pi/180;
```

```
        else
            gcoor(n,2)=th;
        end
        gcoor(n,3)=z;
        n=n+1;
    end
end

for z=2.8e-3:unit_height_electrode_element:length-2.8e-3
    for r=0:1:2
        for th=0:2*pi/16:15/16*2*pi
            gcoor(n,1)=or-r*wall/2;
          if th==pi*2/8
              gcoor(n,2)=th+(degree-90)*pi/180;
          else
              gcoor(n,2)=th;
          end
           gcoor(n,3)=z;
           n=n+1;
        end
    end
end

z=length;
for r=0:1:2
    for th=0:2*pi/16:15/16*2*pi
        gcoor(n,1)=or-r*wall/2;
        if th==pi*2/8
            gcoor(n,2)=th+(degree-90)*pi/180;
        else
```

```
            gcoor(n,2)=th;
          end
        gcoor(n,3)=z;
        n=n+1;
    end
end

%formulating the dynamic equations
Mg = createMg (glabel, gcoor, density, dsdof, dedof, nel);
Kqqg = createKqqg (glabel, gcoor, emodulus, dsdof, dedof, nel);
Dg=alpha.*Mg+beta.*Kqqg;
Kqphg = createKqphg (glabel, gcoor, piezocoeff, dsdof, dedof, phsdof,
phedof, nel);
Kphphg = createKphphg (glabel, gcoor, dielecoeff, dielecoeff, phsdof,
phedof, nel);
Fg = createFg_ss (glabel,gcoor,dsdof,dedof,nel);
[Mg Dg Kqqg Kqphg Fg Kphphg]=bc(Mg, Dg, Kqqg, Kqphg, Fg, Kphphg);
Kg = Kqqg+(Kqphg/Kphphg)*Kqphg.';

A11=zeros(864,864);
A12=eye(864);
A21=-Mg\Kg;
A22=-Mg\Dg;
A=[A11 A12;A21 A22];

[creep1g_pos_x creep3g_pos_x creep1g_neg_x creep3g_neg_x
creep1g_pos_y creep3g_pos_y creep1g_neg_y creep3g_neg_y] =
createcreepg_bd (glabel, gcoor, dsdof, dedof, phedof, phsdof, emodulus,
poisson, piezocoeff);
[Khg_pos_x Khg_neg_x Khg_pos_y Khg_neg_y] = createKhg_bd (glabel, gcoor,
```

```
phedof, phsdof);

B = form_B (glabel, gcoor, phsdof, phedof, ir, or, dielecoeff33,
unit_height_electrode_element, Mg, Kqphg, Kphphg, creep1g_pos_x,
creep3g_pos_x, creep1g_neg_x, creep3g_neg_x, creep1g_pos_y,
creep3g_pos_y, creep1g_neg_y, creep3g_neg_y, Fg, Khg_pos_x, Khg_neg_x,
Khg_pos_y, Khg_neg_y, degree);

C=zeros(2,1728);
C(1,721)=1;
C(2,757)=1;

D=zeros(2,11);

F=B(:,11);

g=ss(A,B,C,D);

%order reduction

order=35;
gred=schurmr(g,order);
[Ar,Br,Cr,Dr]=ssdata(gred);
```

REFERENCES

Abramovitch D Y, Andersson S B, Pao L Y and Schitter G 2007 A Tutorial on the Mechanisms, Dynamics, and Control of Atomic Force Microscopes *Proceedings of American Control Conference* 3488-502

Agarwal P and Salapaka M. V. 2008 Control and Systems Approaches to Atomic Force Microscopy *IFAC Proceedings Volumes* **17** 10456-67

Ashley S C, Aridoğan U, Riddle R and Leang K K 2008 Hysteresis Inverse Iterative Learning Control of Piezoactuators in AFM *IFAC Proceedings Volumes* **17** 8269-74

Barrett R C and Quate C F 1991a High-speed, Large-scale Imaging with Atomic Force Microscope *Journal of Vacuum Science & Technology B: Microelectronics and Nanometer Structures* **9** 302-6

Barrett R C and Quate C F 1991b Optical Scan-correction System Applied to Atomic Force Microscopy *Review of Scientific Instruments* **62** 1393-9

Bashash S and Jalili N 2009 Robust Adaptive Control of Coupled Parallel Piezo-flexural Nanopositioning Stages *IEEE/ASME Transactions on Mechatronics* **14** 11-20

Berg M, Hagedorn P and Gutschmidt S 2004 On the Dynamics of Piezoelectric Cylindrical Shells *Journal of Sound and Vibration* **274** 91-109

Berghuis H, Ortega R and Nijmeijer H 1993 A Robust Adaptive Robot Controller *IEEE Transactions on Robotics and Automation* **9** 825-830

Bhikkaji B, Ratnam M, Fleming A. J. and Moheimani S O R 2007 High-performance Control of Piezoelectric Tube Scanners *IEEE Transactions on Control Systems Technology* **15** 853-66

Binnig G, Quate C F and Gerber C 1986 Atomic Force Microscope *Physical Review Letters* **56** 930-3

Binnig G and Smith D P E 1986 Single-tube Three-dimensional Scanner for Scanning Tunneling Microscopy *Review of Scientific Instruments* **57** 1688-9

Birdi K S 2003 *Scanning Probe Microscopes: Applications in Science and Technology* (CRC Press LLC)

Carr R G 1988 Finite Element Analysis of PZT Tube Scanner Motion for Scanning Tunnelling Microscopy *Journal of Microscopy* **152** 379-85

Chandrupatla T R and Belegundu A D 2002 *Introduction to Finite Elements in Engineering* (Upper Saddle River, N. J.: Prentice Hall)

Chen C J 1992 In Situ Testing and Calibration of Tube Piezoelectric Scanners *Ultramicroscopy* **42-44** 1653-8

Chen W and Saif M 2006 Novel Sliding Mode Observers for a Class of Uncertain Systems *Proceedings of the American Control Conference* **2006** 2622-7

Chiu C S, Lian K Y and Wu T C 2004 Robust Adaptive Motion/Force Tracking Control Design for Uncertain Constrained Robot Manipulators *Automatica* **40** 2111-9

Clayton G M, Tien S, Fleming A J, Moheimani S O R and Devasia S 2008 Inverse-feedforward of Charge-controlled Piezopositioners *Mechatronics* **18** 273-81

Colton R J, Engel A, Frommer J E, Gaub H E, Gewirth A A, Guckenberger R, Rabe J, Heckl W M and Parkinson B 1998 *Procedures in Scanning Probe Microscopies* (John Wiley & Sons)

Croft D, Shed G and Davasia S 2001 Creep, Hysteresis, and Vibration Compensation for Piezoactuators: Atomic Force Microscopy Application *Journal of Dynamic Systems, Measurement and Control, Transactions of ASME* **123** 35-43

Danielson K T and Noor A K 1997 Three-dimensional Finite Element Analysis in Cylindrical Coordinates for Nonlinear Solid Mechanics Problems *Finite Elements in Analysis and Design* **27** 225-49

El Rifai O M and Youcef-Toumi K 1999 On Factors Affecting the Performance of Atomic Force Microscopes in Contact-Mode *IEEE/ASME International Conference on Advanced Intelligent Mechatronics* 21-6

El Rifai O M and Youcef-Toumi K 2003 Design and Control of Atomic Force Microscopes *Proceedings of the American Control Conference* **5** 3714-9

Fei J and Batur C 2008 Adaptive Sliding Mode Control with Sliding Mode Observer for a Microelectromechanical Vibratory Gyroscope *Proceedings of the Institution of Mechanical Engineers. Part I: Journal of Systems and Control Engineering* **222** 839-49

Fei J and Batur C 2009 A Class of Adaptive Sliding Mode Controller with Proportional-integral Sliding Surface *Proceedings of the Institution of Mechanical Engineers. Part I: Journal of Systems and Control Engineering* **223** 989-99

Fleming A J and Moheimani S O R 2005 Sensor-less Vibration Suppression and Scan Compensation for Piezoelectric Tube Nanopositioners *Proceedings of the 44th IEEE Conference on Decision and Control, and the European Control Conference* **2005** 1162-7

Fleming A J and Moheimani S O R 2006 Sensorless Vibration Suppression and Scan Compensation for Piezoelectric Tube Nanopositioners *IEEE Transactions on Control Systems Technology* **14** 33-44

Galinaitis W S and Rogers R C 1998 Control of a Hysteretic Actuator using Inverse Hysteresis Compensation *Proceedings of SPIE – The International Society for Optical Engineering* **3323** 267-77

Ge P and Jouaneh M 1996 Tracking Control of a Piezoceramic Actuator *IEEE Transactions on Control Systems Technology* **4** 209-16

Haertling G Hn 1999 Ferroelectric Ceramics: History and Technology *Journal of the American Ceramic Society* **82** 797-818

Hau L C and Fung H K 2004 Effect of ACLD Treatment Configuration on Damping Performance of a Flexible Beam *Journal of Sound and Vibration* **269** 549-67

Hsu S H and Fu L C 1999 Robust Output High-gain Feedback Controllers for the Atomic Force Microscope under High Data Sampling Rate *Proceedings of the 1999 IEEE International Conference on Control Applications* **2** 1626-31

Ioannou P A and Sun J 1996 *Robust Adaptive Control* (Prentice-Hall, Upper Saddle River)

Jairath A K 2008 *Control Systems: the State Variable Approach (Conventional and MATLAB)* (Boca Raton: CRC Press; New Delhi, India: Ane Books India)

Janocha H and Kuhnen K 2000 Real-time Compensation of Hysteresis and Creep in Piezoelectric Actuators *Sensors and Actuators, A: Physical* **79** 83-9

Jung H and Gweon D G 2000 Creep Characteristics of Piezoelectric Actuators *Review of Scientific Instruments* **71** 1896-900

Kamlah M and Bhle U 2001 Finite Element Analysis of Piezoceramic Components Taking into Account Ferroelectric Hysteresis Behavior *International Journal of Solids and Structures* **38** 605-33

Krejci P and Kuhnen K 2001 Inverse Control of Systems with Hysteresis and Creep *IEE Proceedings: Control Theory and Applications* **148** 185-92

Kumar R, Mishra B K and Jain S C 2008 Static and Dynamic Analysis of Smart Cylindrical Shell *Finite Elements in Analysis Design* **45** 13-24

Kusculuoglu Z K and Royston T J 2008 Nonlinear Modeling of Composite Plates with Piezoceramic Layers using Finite Element Analysis *Journal of Sound and Vibration* **315** 911-926

Landis C M 2004 Non-linear Constitutive Modeling of Ferroelectrics *Current Opinion in Solid State and Materials Science* **8** 59-69

Leang K K and Devasia S 2007 Feedback-linearized Inverse feedforward for Creep, Hysteresis, and Vibration Compensation in AFM Piezoactuators *IEEE Transactions on Control Systems Technology* **15** 927-35

Li Z, Ge S S and Adams M 2007 Adaptive Robust Motion/Force Control of Holonomic-constrained Nonholonomic Mobile Manipulators *IEEE Transactions on Systems, Man, and Cybernetics, Part B: Cybernetics* **37** 607-16

Li Z, Ge S S, Adams M and Wijesoma W S 2008a Robust Adaptive Control of Uncertain Force/Motion Constrained Nonholonomic Mobile Manipulators *Automatica* **44** 776-84

Li Z, Ge S S and Wang Z 2008b Robust Adaptive Control of Coordinated Multiple Mobile Manipulators *Mechatronics* **18** 239-50

Li Z, Lee E and Ben Amara F 2009 Performance Enhancement in High-Speed Contact-Mode Atomic Force Microscopy *IEEE Transactions on Control Systems Technology* **17** 1193-201

Lim Y H, Varadan V V and Varadan V K 1997 Finite-element Modeling of the Transient Response of MEMS Sensors *Smart Materials and Structures* **6** 53-61

Lim Y H, Gopinathan S V, Varadan V V and Varadan V K 1999 Finite Element Simulation of Smart Structures using an Optimal Output Feedback Controller for Vibration and Noise Control *Smart Materials and Structures* **8** 324-37

Low T S and Guo W 1995 Modeling of a Three-layer Piezoelectric Bimorph Beam with Hysteresis *Journal of Microelectromechanical Systems* **4** 230-7

Maess J, Fleming A J and Allgöwer F 2008a Model-based Vibration Suppression in Piezoelectric Tube Scanners through Induced Voltage Feedback *American Control Conference* 2022-7

Maess J, Fleming A J and Allgöwer F 2008b Simulation of Dynamic-coupling in Piezoelectric Tube Scanners by Reduced Order Finite Element Analysis *Review of Scientific Instruments* **79** Article Number 015105

Maess J, Becker J, Gaul L and Allgöwer F 2008c Two-degree-of-freedom Tracking Control of Piezoelectric Tube Scanners in Two-dimensional Scanning Applications *Proceedings of the 17th World Congress, the International Federation of Automatic Control* 8257-62

Magonov S N and Whangbo M H 1996 Surface Analysis with STM and AFM: Experimental and Theoretical Aspects of Image Analysis *VCH Verlagsgesellschaft mbH*

Mayergoyz I D 1991 *Mathematical Models of Hysteresis* (New York: Springer-Verlag)

Moheimani S O R 2008 Accurate and Fast Nanopositioning with piezoelectric tube scanners: Emerging Trends and Future Challenges *Review of Scientific Instruments*, **79**, Article Number 071101

Moheimani S O R and Yong Y K 2008 Simultaneous Sensing and Actuation with a Piezoelectric Tube Scanner *Reviews of Scientific Instruments* **79** Article number 073702

Mokaberi B and Requicha A A G 2008 Compensation of Scanner Creep and Hysteresis for AFM Nanomanipulation *IEEE Transactions on Automation Science Engineering* **5** 197-206

Motamedi M, Rezaei S M, Zareinejad M and Saadat M 2009 Robust Control of a Piezoelectric Stage under Thermal and External Load Disturbances *Proceedings of the American Control Conference* 2260-5

Niezrecki C, Brei D, Balakrishnan S and Moskalik A 2001 Piezoelectric Actuation: State of the Art *Shock and Vibration Digest* **33** 269-80

Oates W S and Smith R C 2006 Nonlinear Optimal Tracking Control of a Piezoelectric Nanopositioning Stage *Proceedings of SPIE – The International Society for Optical Engineering* **6166** Article Number 616616

Ogata K 2001 *Modern Control Engineering* (Prentice Hall)

Pantazi A, Sebastian A, Cherubini G, Lantz M, Pozidis H, Rothuizen H and Eleftheriou E 2007 Control of MEMS-based Scanning-probe Data-storage Devices *IEEE Transactions on Control Systems Technology* **15** 824-41

Payam A F and Abdel-Rahman E M 2009 A Hybrid PD-fuzzy Controller for Atomic Force Microscopes *Proceedings of ASME International Mechanical Engineering Congress and Exposition* **13** 481-8

Perruquetti W and Barbot J P 2002 *Sliding Mode Control in Engineering* (Marcel Dekker, INC)

Preumont A 2006 *Mechatronics: Dynamics of Electromechanical and Piezoelectric Systems* (Dordrecht: Springer)

Royston T J and Houston B H 1998 Modeling and Measurement of Nonlinear Dynamic Behavior in Piezoelectric Ceramics with Application to 1-3 Composites *Journal of the Acoustical Society of America* **104** 2814-27

Sabanovic A, Khan S, Elitas M and Jenernik K 2006 Sliding Mode Adaptive Controller for PZT Actuators *proceedings of IECON 2006 – 32nd Annual Conference on IEEE Industrial Electronics* 5209-5214

Safonov M G and Chiang R Y. 1989 A Schur Method for Balanced-truncation Model Reduction *IEEE Transactions on Automatic Control* **34** 729-33

Santos H, Mota Soares C M, Mota Soares C A and Reddy J N 2008 A Finite Element Model for the Analysis of 3D Axisymmetric Laminated Shells with Piezoelectric Sensors and Actuators: Bending and Free Vibration *Computers and Structures* **86** 940-7

Schitter G, Å ström K J, DeMartini B E, Thurner P J, Turner K L and Hansma P K 2007 Design and Modeling of a High-speed AFM-scanner *IEEE Transactions on Control Systems Technology* **15** 906-15

Schitter G 2009 Improving the Speed of AFM by Mechatronic Design and Modern Control Methods *Technisches Messen* **76** 266-73

Sebastian A, Gannepalli A and Salapaka M V 2007 A Review of the Systems Approach to the Analysis of Dynamic-mode Atomic Force Microscopy *IEEE Transactions on Control Systems Technology* **15** 952-9

Shakir H and Kim W J 2007 Multiscale Control for Nanoprecision Positioning Systems with Large Throughput *IEEE Transactions on Control Systems Technology* **15** 945-51

Shampine L F and Reichelt M W 1997 The MATLAB ODE Suite *Society for Industrial and Applied Mathematics* **18** 1-22

Shieh H J and Hsu C H 2007 An Integrator-backstepping-based Dynamic Surface Control Method for a Two-axis Piezoelectric Microelectric Micropositioning Stage *IEEE Transactions on Control Systems Technology* **15** 916-26

Sridhar S, Giannakopoulos A E, Suresh S and Ramamurty U 1999 Electrical Response during Indentation of Piezoelectric Materials: A New Method for Material Characterization *Journal of Applied Physics* **85** 380-7

Su C Y, Stepanenko Y, Svoboda J and Leung T P 2000 Robust Adaptive Control of a Class of Nonlinear Systems with Unknown Backlash-Like Hysteresis *IEEE Transactions on Automatic Control* **45** 2427-32

Su C Y, Wang Q Q, Chen X K and Rakheja S 2005 Adaptive Variable Structure Control of a Class of Nonlinear Systems with Unknown Prandtl-Ishlinskii Hysteresis *IEEE Transactions on Automatic Control* **50** 2069-74

Tamer N and Dahleh M 1994 Feedback Control of Piezoelectric Tube Scanners *Proceedings of the 33rd Conference on Decision and Control* 1826 -31

Tien S, Zou Q and Devasia S 2005 Iterative Control of Dynamic-coupling-caused Errors in Piezoscanners during High-speed AFM Operation *IEEE Transactions on Control Systems Technology* **13** 921-31

Utkin V I 1977 Variable Structure Systems with Sliding Mode *IEEE Transactions on Automatic Control* **22** 212-22

Wu C P and Syu Y S 2006 Asymptotic Solutions for Multilayered Piezoelectric Cylinders under Electromechanical Loads *Computers, Materials and Continua* **4** 87-107

Wu C P, Syu Y S and Lo J Y 2007 Three-dimensional Solutions of Multilayered Piezoelectric Hollow Cylinders by an Asymptotic Approach *International Journal of Mechanical Sciences* **49** 669-89

Wu Y and Zou Q 2007 Iterative Control Approach to Compensate for Both the Hysteresis and the Dynamics Effects of Piezo Actuators *IEEE Transactions on Control Systems Technology* **15** 936-44

Yang Q, Jagannathan S and Bohannan E W 2005 Block Phase Correlation-based Automatic Drift Compensation for Atomic Force Microscopes *Proceedings of 5th IEEE Conference on Nanotechnology* **1** 370-3

Yang Q and Jagannathan S 2006 Atomic Force Microscope-based Nanomanipulation with Drift Compenation *International Journal of Nanotechnology* **3** 527-44

Yu Y, Xiao Z, Naganathan N G and Dukkipati R V 2002 Dynamic Preisach Modelling of Hysteresis for the Piezoceramic Actuator System *Mechanism and Machine Theory* **37** 75-89

Zhan Z, Yang Y, Li W J, Dong Z, Qu Y, Wang Y and Zhou L 2007 AFM Operating-drift Detection and Analyses Based on Automated Sequential Image Processing *Proceedings of 7th IEEE International Conference on Nanotechnology – IEEE – NANO 2007* 748-53

Zhong J and Yao B 2008 Adaptive Robust Precision Motion Control of a Piezoelectric Positioning Stage *IEEE Transactions on Control Systems Technology* **16** 1039-46